

DEVELOPMENT OF TRANSITION METAL DOPED POLYCRYSTALLINE ZnO FOR SPINTRONICS APPLICATIONS

Thesis submitted in fulfillment of the requirements for the Degree of

DOCTOR OF PHILOSOPHY

By

NEHA KONDAL



DEPARTMENT OF PHYSICS AND MATERIALS SCIENCE

JAYPEE UNIVERSITY OF INFORMATION TECHNOLOGY
WAKNAGHAT, SOLAN, H.P., INDIA

JULY 2018

@ Copyright JAYPEE UNIVERSITY OF INFORMATION TECHNOLOGY, WAKNAGHAT
JULY 2018

ALL RIGHTS RESERVED

CONTENTS

ABSTRACT		xiii
LIST OF ACRONYMS AND ABBREVIATIONS		xv
LIST OF FIGURES		xvi-xx
LIST OF PUBLICATIONS		xxi
CHAPTER 1	INTRODUCTION	1-24
	<ul style="list-style-type: none"> 1.1 Introduction 1.2 Crystal Structure of ZnO 1.3 Native defects in ZnO <ul style="list-style-type: none"> 1.3.1 Oxygen vacancies 1.3.2 Zinc Interstitials 1.3.3 Zinc vacancies 1.3.4 Oxygen interstitials 1.3.5 Zinc antisite and Oxygen antisite 1.4 Electronic band structure of ZnO 1.5 Photoluminescence and EPR studies of ZnO 1.6 Spintronics: ZnO based dilute magnetic semiconductors 1.7 Theoretical models for explaining magnetism in DMS <ul style="list-style-type: none"> 1.7.1 Direct exchange interaction 1.7.2 Carrier mediated indirect exchange: RKKY interactions 1.7.3 Mean field Zener model 1.7.4 Double exchange mechanism 1.8 A prototype spin based light emitting diode References 	

CHAPTER 2	THERMAL AND TEMPORAL EVOLUTION OF MICROSTRUCTURE AND INTERFACE FORMATION OF GRAIN BY HIGH TEMPERATURE ANNEALING	25-57
	<ul style="list-style-type: none"> 2.1 Introduction 2.2 Experimental techniques for annealing <ul style="list-style-type: none"> 2.2.1 Conventional Annealing 2.2.2 Multistep Annealing 2.3 Result and Discussions <ul style="list-style-type: none"> 2.3.1 X-Ray Diffraction studies of CA ZnO nanoparticles 2.3.2 Morphological studies of CA ZnO 2.3.3 Theoretical model of grain growth 2.3.4 X-Ray Diffraction studies of MSA ZnO nanoparticles 2.3.5 Morphological studies of MSA ZnO 2.3.6 Raman studies of CA and MSA ZnO 2.4 Conclusion References 	
CHAPTER 3	ORIGIN OF POLYCHROMATIC EMISSION AND DEFECT DISTRIBUTION WITHIN ANNEALED NANO CRYSTALLINE ZnO AND THEIR EFFECT ON MAGNETIC PROPERTIES AND SPIN-SPIN INTERACTION	59-92
	<ul style="list-style-type: none"> 3.1 Introduction 3.2 Experimental details 3.3 Result and Discussions <ul style="list-style-type: none"> 3.3.1 Optical excitation and polychromatic emission 3.3.2 Sub band excitation and emissions 3.3.3 EPR measurements and magnetic studies 	

	<p>3.4 Conclusion</p> <p>References</p>	
CHAPTER 4	SELECTIVELY ENHANCED DIFFERENT DEFECT IN NANOCRYSTALLINE ZnO: A PATH TO MAKE P-TYPE ZnO WITHOUT DOPING BY MULTISTEP ANNEALING	93-114
	<p>4.1 Introduction</p> <p>4.2 Result and discussions</p> <p> 4.2.1 Optical excitation and polychromatic emission</p> <p> 4.2.2 Sub band excitation and emissions</p> <p> 4.2.3 EPR measurements and magnetic studies</p> <p>4.3 Comparative study of conventional and Multi step annealing</p> <p> 4.3.1 Mechanisms</p> <p> 4.3.2 Morphological studies</p> <p> 4.3.3 Photoluminescence studies</p> <p> 4.3.4 EPR and Magnetic studies</p> <p>4.4 Conclusion</p> <p>References</p>	
CHAPTER 5	DEVELOPMENT OF CoO AND NiO DOPED ZnO BASED DMS: A PROMISING MATERIAL FOR SPIN ALIGNER	115-135
	<p>5.1 Introduction</p> <p>5.2 Experimental details</p> <p>5.3 Result and discussions</p> <p> 5.3.1 X-Ray diffraction studies of $Zn_{1-x}Co_xO$</p> <p> 5.3.2 Magnetic properties of $Zn_{1-x}Co_xO$</p> <p> 5.3.3 Magnetic properties of $Zn_{1-x}Ni_xO$</p>	

	5.4 Conclusion References	
CHAPTER 6	CONCLUSION AND FUTURE SCOPE	137-142
	6.1 Summary 6.2 Future Scope	
	BIBLIOGRAPHY	143-152



JAYPEE UNIVERSITY OF INFORMATION TECHNOLOGY

(Established by H.P. State Legislative vide Act No. 14 of 2002)

Dumehar Bani, Kandaghat, Distt. Solan – 173234 (H.P.) INDIA

Website: www.juit.ac.in

Phone No. (91) 07192-257999 (30 Lines)

Fax: (91) 01792 245362

DECLARATION

I hereby declare that the work reported in Ph.D. thesis entitled “**Development of Transition Metal Doped Polycrystalline ZnO for Spintronics Applications**” submitted at **Jaypee University of Information Technology, Wagnaghat, India** is an authentic record of my work carried out under the supervision of **Dr. Sanjiv Kumar Tiwari**. I have not submitted this work elsewhere for any other degree or diploma. I am fully responsible for the contents of my Ph.D. Thesis.

Neha Kondal

Enrollment No. 146954

Department of Physics and Materials Science,
Jaypee University of Information Technology,
Wagnaghat, Solan, H.P. India-173234.

Date.....



JAYPEE UNIVERSITY OF INFORMATION TECHNOLOGY

(Established by H.P. State Legislative vide Act No. 14 of 2002)
Dumehar Bani, Kandaghat, Distt. Solan – 173234 (H.P.) INDIA

Website: www.juit.ac.in

Phone No. (91) 07192-257999 (30 Lines)

Fax: (91) 01792 245362

CERTIFICATE

This is to certify that the work reported in the Ph.D. thesis entitled “**Development of Transition Metal Doped Polycrystalline ZnO for Spintronics Applications**”, submitted by **Neha Kondal** at **Jaypee University of Information Technology, Wagnaghat, India** is a bonafide record of her original work carried out under my supervision. This work has not been submitted elsewhere for any other degree or diploma.

Supervisor:

Dr. Sanjiv Kumar Tiwari

Assistant Professor

Department of Physics and Materials Science,
Jaypee University of Information Technology,
Wagnaghat, Solan, H.P. India-173234.

Date.....

Dedicated
to
Mom & Dad

ACKNOWLEDGEMENT

Sometimes it is immensely difficult to put plethora of emotions into mere words. The same perplexity haunts my mind in penning down sincere thanks to all who have contributed in assorted ways in making this compilation a magnificent experience.

*Out of a deep seated conviction, it gives me immense pleasure to express my inveterate gratitude towards my Ph.D. supervisor **Dr. Sanjiv Kumar Tiwari** for his constructive criticism and proper visualization in a magniloquent way due to his professional acumen and fineness at every stage of this study. He has been in front of my eyes for more than three years motivating me, taking up my new challenges every day, tackling them with all his grit and determination and always thriving to come out victorious. His unflinching support has always encouraged me to go ahead especially when I felt it was not possible. He shall remain best teacher, my best adviser and my best friend with all my secrets. “Thank you Dr. Tiwari” I couldn’t have asked for better supervisor than you.*

*Besides, I owe gratuitous thanks to **Prof. P. B. Barman** who has always been there with his fatherly hand, whenever I needed it the most. His excellent monitoring and counseling has always energized me to work hard. Without his scolds it would have been impossible for this naughty child to be on track and compile this thesis.*

*I express my gratefulness to **Prof. Vinod Kumar Gupta** (Vice Chancellor), **Prof. Samir Dev** (Director and Academic Head) and **Maj Gen Rakesh Bassi** (Registrar) who had been very supportive and helpful throughout this journey. I have lots of praises and appreciation to all my learned teachers **Dr. Dheeraj Sharma, Dr. Pankaj Sharma, Dr. Vineet Sharma, Prof. Sunil Kumar Khah, Dr. Ragini Raj Singh, Dr. Surajit Kumar Hazra and Dr. Rajesh Kumar**, Department of Physics and Materials Science, JUIT. Heartfelt thanks to **Prof. Ghanshyam Singh, Dr. Neeru Sharma, Dr. Amol Vasudeva, Mr. Pramod Kumar & Deepak Singh** for being so compassionate and supportive though this journey.*

*I am extremely thankful to **Dr. Adrien Savoyant**, Aix-Marseille University, France with whom I initially collaborated to learn Easy Spin but finally ended up with new experimental findings. This work would have been incomplete without the low temperature measurements done in his lab. His suggestion and insightful comments always gave me new ways of thinking. I shall be*

indebted for his kind cooperation. I am grateful to **Prof. Ramesh Chandra** (IIT Roorkee) for all the characterizations facilities at IIT Roorkee. My heartfelt thanks to **Dr. Ragini Raj Singh** (JUIT) and **Dr. Pankaj Sharma** (JUIT) for the precious time they have invested in characterising my samples.

It gives me immense pleasure to thank and acknowledge my revered teachers **Prof. Mahavir Singh** (HPU), **Prof. P. K. Ahluwalia** (HPU), **Prof. Vir Singh Rangra** (HPU), **Prof. Nagesh Thakur** (HPU), **Dr. Sapna Sharma** (St. Bede's College), **Dr. Shyam** (HPU) & **Dr. Prikshit Gautam** (DU) who have been my constant motivators throughout this journey. Words are not enough to express the love and care **Dr. Sr. Molly Abraham** has given me. A big thank you my Lady love !

A good support system is important to survive and staying sane in Ph.D. A special thanks to my partners in crime of all the fun times **Rohit Sharma, Jonny Dhiman, Prashant Thakur, Dr. Priyam Dhani and Ritika Verma** without whose endless gossips and fights over cardamom (tea) this journey would never have been possible. I am grateful to my seniors and juniors for standing by me whenever I needed the most, **Dr. Sarita Kango, Dr. Shivani Sood, Dr. Richa Khokra, Dr. Rajender Singh, Dr. Bandna Bharti, Dr. Hitanshu, Dr. Rajinder Kumar, Dipti Rawat, Dhruv, Kanchan, Pooja, Shikha, Asha, Rajan, Ekta, Anuradha, Sanjay.** Special mention and love to my champs **Nikesh Chauhan, Parushi Sharma, Avinash Thakur, Vaishali, Himanshu Chauhan and Anubha.**

A special mention and credit is due to my lovely ladies **Aaruti Sood, Kriti Pathak and Vaishali Kashmiri** who have been always there during my tough times. Friends by chance, sisters by choice. Love you! Tonnes of thanks to my friends **Adv. Kritika Sharma, Himani Guleria, Apurva Pirta, Vidushi Stan, Vikas Dhiman, Amar, Kuldeep, Shammi, Ajay Verma, Jitender Thakur, Adv. Vinod Chauhan, Harish, Bandna, Jasbeer, Dr. Monika Negi, Ravi, Akshay Patial, & Saurabh.**

No matter how depressed I was in Ph.D. time it was my family, my cousins who knew how to cheer and make best out of me. Thanks a bunch **Manjula Thakur, Anjali Verma, Kavita Thakur, Simple Rohta, Gaurav Thakur, Dr. Aneesh Thakur, Ranju Thakur, Kirti Angra, Madan Verma, Sunil Rohta, Amritansh Thakur, Dushyant Thakur, Abhinav Narwal, Pawan Thakur,** for being

there always. I must not forget to mention the encouragement, love and support by Vandana Tiwari & my two musketeers Swapnil and Vedika. In you all I have found a family for keeps.

*My vocabulary fails and I actually become bankrupt when it comes to express my gratitude and thankfulness towards my mains, my father **Dr. M. R. Kondal** and mother **Mrs. Promila Kondal** and my younger sib **Adv. Aditya Kondal**. Whether it is the way you comforted me when I was down, or the way in which your hugs magically wiped out my frowns. Mom & dad, you have been there every moment, to make sure my life turned out this way. It is actually impossible to thank you adequately for everything you've done, from loving me unconditionally to raising me to this day. I could not have asked for better parents or role-models. Eddy thanks bro! I know a thanks won't work, I owe you a macbook now.*

Lastly, I want to state for any errors that may remain in this work, the responsibility is entirely my own while the expertise in this study belongs to those acknowledged above.

Neha Kondal

ABSTRACT

The tailoring of spins as well as charge in semiconductors is the central theme of era of spintronics. Prototype spintronics devices uses carrier dopant magnetic exchange interactions in magnetically doped semiconductors called Dilute Magnetic Semiconductors (DMS) to tailor either spin polarizations of host material or spin of the dopants itself. Zinc Oxide being a potential host material for DMS has attracted researchers for its various electronics and optoelectronic applications. In this work ZnO has been used as a host material for DMS with two dopants CoO and NiO. The study has been divided in four main objectives.

Firstly, ZnO has been explored by applying two annealing techniques i.e. conventional annealing and multistep annealing. These annealing techniques differ in their growth mechanisms and hence lead to different grain growth kinetics. Annealed samples have been structurally explored by X-Ray diffraction technique & Raman Spectroscopy. The diffusion equations have been solved to understand the grain growths and diffusion of intrinsic defects. A grain growth model has been briefly discussed in this objective.

Secondly, as grain growth kinetics was different in both the annealing techniques the defect distribution within the grain will also be different for both the cases. So, the defect distribution due to conventional annealing has been explored extensively by means of Photoluminescence spectroscopy, UV-Visible spectroscopy and Fluorescence imaging. The chemical nature of the defects has been investigated by means of Electron Paramagnetic Resonance. Further the magnetic properties were studied by Vibrating Sample Magnetometry. The undoped ZnO samples were found to exhibit room temperature ferromagnetism till annealing temperature 1000°C whereas a sharp diamagnetism has been observed at 1100°C. The distributions of defects from emissions and origin of ferromagnetism have been discussed in this objective.

Thirdly, the defect distributions due to multistep annealing have been studied. It was found that distributions of intrinsic defects within the grains are opposite to that in conventional annealing. The same characterization techniques have been employed for multistep annealed samples. Selectively enhanced emissions from defects are the major outcome of this objective.

Lastly, a material for spin aligner has been developed. ZnO has been doped with CoO and NiO using solid state reactions and has been explored extensively for structural and magnetic properties. Low temperature EPR measurements were performed to detect the effect of Co ion

and Ni ions introduced in the lattice of ZnO. The Co clustering has been reported in this objective and unwanted Mn and Co in Ni doped samples.

LIST OF ACRONYM & ABBREVIATIONS

E _a	Activation Energy
BMP	Bound Magnetic Polaron
CB	Conduction Band
CBM	Conduction Band Minima
CA	Conventional annealing/annealed
CF	Crystal field
DLE	Deep level emission
DAP	Donor acceptor pair
FESEM	Field Emission Scanning Electron Microscopy
FWHM	Full Width at Half Maxima
LDA	Local density approximation
LED	Light Emitting Diode
MSA	Multistep annealing/annealing
NBE	Near Band Emission
PL	Photoluminescence
PEG	Polyethylene glycol
PVA	Polyvinyl alcohol
SO	Spin Orbit
TM	Transition Metal
UV	Ultra violet
VB	Valence Band
VBM	Valence Band Maxima
w.r.t	with respect to
XRD	X-Ray Diffraction

LIST OF FIGURES

Figure No.	Caption	Page No.
Figure 1.1	Hexagonal wurtzite structure of ZnO	3
Figure 1.2	Ball & stick illustration of the local atomic relaxations around the V_o , V_o^+ and V_o^{2+}	6
Figure 1.3	Ball & stick illustration of the local atomic relaxations around the V_{Zn}	8
Figure 1.4	Splitting of VB in three twofold degenerate VB	9
Figure 1.5	Band structure & symmetry of wurtzite ZnO	9
Figure 1.6	Splitting of energy levels in presence of magnetic field & absorption of MW energy	11
Figure 1.7	Schematics of defects and their surroundings	14
Figure 1.8	Schematic for (a) Dopant, (b) Non magnetic host semiconductor, (c) Dilute Magnetic semiconductor	16
Figure 1.9	Variation of J with interatomic radii r multiplied by radius of the Fermi sphere K_f	18
Figure 1.10	A prototype Design of spin light emitting diode	20
Figure 2.1	Schematic of Conventional annealing and Multistep annealing	28
Figure 2.2	Ideal hexagonal wurtzite ZnO structure undoped and pristine	31
Figure 2.3	XRD patterns of CA ZnO at various temperatures; inset show the Voigt and Lorentzian fits to the experimental data points	31
Figure 2.4	Shift of [002] peak with various CA temperatures	33
Figure 2.5	Variation of ratio of intensity of peak [002]/[101] and stress with annealing temperature	34
Figure 2.6	Grain size and surface to volume ratio of grains versus annealing temperature	35
Figure 2.7	FESEM images of (a) Pristine ZnO, (b) CA ZnO annealed at 200°C, (c) CA ZnO annealed at 400°C, (d) CA ZnO annealed at 600°C, (e) CA ZnO annealed at 800°C, (f) CA ZnO annealed at 1000°C, (g) CA ZnO annealed at 1100°C	36, 37

Figure 2.8	Variation of $-\ln \left[1 - \left(\frac{x}{x_m} \right)^2 \right]$ with inverse of annealing temperature (CA)	40
Figure 2.9	Schematic of grain growth model and defects distribution within Conventional annealed ZnO nanoparticles	41
Figure 2.10	XRD pattern of MSA ZnO nanoparticles at different temperatures	42
Figure.2.11	Shift of [002] peak with various Multistep annealing temperatures	42
Figure 2.12	Variation of Stress and intensity ratio of peak [002]/[101] versus annealing temperature of MSA	43
Figure 2.13	Grain size of Multistep annealed ZnO versus annealing temperature fitted with kinetics equation	44
Figure 2.14	FESEM image of (a) Pristine ZnO nanoparticles, (b) MSA ZnO at 400°C, (c) MSA ZnO at 600°C, (d) MSA ZnO at 800°C	45
Figure 2.15	(a) FESEM image of Pristine ZnO highlighting grain with colored marker, (b) Pristine ZnO cylindrical grains fitted with lognormal fit, (c) Pristine ZnO hexagonal grains fitted with lognormal fit, (d) Pristine ZnO spherical shaped grains with Gaussian fit	46, 47, 48
Figure 2.16	The lognormal and Gaussian fits of (a) MSA at 400°C ZnO cylindrical shaped grains, (b) MSA at 400°C ZnO spherical shaped grains	48
Figure 2.17	(a) The lognormal fit of MSA at 600°C ZnO spherical shaped grains, (b) The evolutions of spherical shaped grains from cylindrical ones	49, 50
Figure 2.18	Raman spectra for CA ZnO samples	52
Figure 2.19	Raman spectra for MSA ZnO samples	52
Figure 2.20	(a) Raman spectra for CA ZnO samples before and after the breaking of grains (Pristine, 800°C and 1100°C, (b) Raman spectra for MSA ZnO samples before and after the breaking of grains (Pristine, 400°C and 800°C	54
Figure 3.1	Square of absorption coefficient (α) plotted with photon energy	63
Figure 3.2	PL spectra of CA ZnO samples at excitation energy 3.54eV	65

Figure 3.3	(a) Deconvoluted Photoluminescence spectra of 400°C CA ZnO at excitation wavelength 370nm, (b) Deconvoluted Photoluminescence spectra of 1000°C CA ZnO at excitation wavelength 370nm, (c) Deconvoluted Photoluminescence spectra of 1100°C CA ZnO at excitation wavelength 370nm	66, 67
Figure 3.4	Variation of ratio of PL peak intensity of NBE/ Zn to O vacancy with annealing temperature.	68
Figure 3.5	Variation of I_{NBE}/I_{Zn} and I_{NBE}/I_{Oxygen} with inverse of annealing temperature; dotted line shows the Arrhenius fit.	69
Figure 3.6	Schematic of visible emission transitions from ZnO.	70
Figure 3.7	(a) PL spectra of CA 1000°C A capped with PEG and surface modified ZnO at different excitations, (b) PL spectra of CA 1000°C A capped with PVA and surface modified ZnO at different excitations	71, 72
Figure 3.8	(a) PL spectra at 400nm excitation energy, (b) Extended spectra of 400°C CA samples, (c) PL spectra at excitation 450nm excitation energy, (d) Extended spectra of 450°C CA samples	73, 74
Figure 3.9	Spatial distribution of defects and their emissions within the grains	76
Figure 3.10	Fluorescence image of ZnO with various excitations (a) DAPI, (b) FITC, (c) TRITC, (d) Combined fluorescence image of grain	77
Figure 3.11	(a) Room temperature EPR spectra of Pristine ZnO, (b) Room temperature EPR spectra of CA sample at 1000°C, (c) EPR spectra obtained at 100K with reference DPPH, inset shows enhanced spectra	78, 79, 80
Figure 3.12	M-H curve of CA sample at 200°C, 800°C and 1100°C	81
Figure 3.13	(a)Low temperature ESR spectra of CA at 400°C, (b) Deconvoluted shows the low temperature ESR spectra of CA at 400°C, (c) Deconvoluted shows the low temperature ESR spectra of CA at 400°C	82, 83
Figure 3.14	Low temperature ESR spectra of 800°C	84
Figure 3.15	(a) Low temperature ESR spectra of 800°C, (b) Deconvoluted ESR spectra at 125K	85, 86
Figure 3.16	The g value of Zn_i plotted with temperatures	87

Figure 3.17	The g value of V_o plotted with temperatures	87
Figure 4.1	Square of absorption coefficient (α) versus with incident photon energy	96
Figure 4.2	Photoluminescence spectra of MSA samples	97
Figure 4.3	(a) Deconvoluted PL spectra of 400°C MSA sample, (b) Deconvoluted PL spectra of 800°C MSA sample	98, 99
Figure 4.4	Variation of Intensity ratio of defect complexes with respect to NBE versus multistep annealing temperature	100
Figure 4.5	PL spectra at excitation wavelength of 450 nm	101
Figure 4.6	M-H curve of all the MSA samples	102
Figure 4.7	Magnetization versus MSA temperature	103
Figure 4.8	(a) ESR spectra of 400°C MSA sample from 275K to 125K. (b) ESR spectra of 800°C MSA sample from 275K to 125K	103, 104
Figure 4.9	(a) Variation of peak to peak intensity of MSA 400°C and 800°C with temperature. (b) Variation of line width of MSA 400°C And MSA 800°C with temperature	104, 105
Figure 4.10	ESR spectra at 200K for 400°C and 800°C MSA sample	105
Figure 4.11	Schematic of distribution of defects within the grains in CA and MSA process	107
Figure 4.12	(a) FESEM image of CA 400°C, (b) FESEM image of MSA 400°C, (c) FESEM image of CA 600°C, (d) FESEM image of MSA 600°C, (e) FESEM image of CA 800°C, (f) FESEM image of MSA 800°C	108
Figure 4.13	(a) PL spectra of CA and 400°C MSA sample (b) PL spectra of CA and 600°C MSA sample, (c) PL spectra of CA and MSA at 800°C.	109, 110
Figure 4.14	EPR spectra of CA and MSA at 400°C and 800°C	111
Figure 4.15	M-H curve of MSA and CA of 800°C and 1100°C	112
Figure 5.1	XRD pattern for undoped and CoO doped ZnO annealed conventionally at 1100°C.	119
Figure 5.2	Variation of peak 100 with 2θ of all $Zn_{1-x}Co_xO$ ($x = 0, 2, 4, 6, 8, 10\%$) samples.	119

Figure 5.3	(a) Variation of lattice parameter a and c with CoO doping, (b) Variation of ratio of c/a with CoO doping %; Inset shows the variation of volume with % doping.	120
Figure 5.4	Microscopic picture of Co clustering, when Co occupied tetrahedral position in ZnO.	121
Figure 5.5	M-H curve of $Zn_{1-x}Co_xO$ at x = 2, 4, 6, 8, 10%.	122
Figure 5.6	Normalized room temperature ESR spectra of CoO doped ZnO. Dotted lines show constant resonance (No g shift with doping (a) All doping percentages (b) CoO doping 2%, 4% & 8%: inset shows EPR spectra for 1% doping (c) CoO doping 6% & 10%.	123, 124
Figure 5.7	EPR spectra of Co doping at 1% performed at 5K.	127
Figure 5.8	(a) EPR spectra of Co doping at 1% for g_{\perp} performed at 5K and 25K, (b) EPR spectra of Co doping at 1% for g_{\parallel} performed at 5K, 25K, 45K, 65K and 85K.	128
Figure 5.9	(a) Raman spectra with increasing doping percentage, (b) De-convoluted of 2% CoO doped sample, (c) De-convoluted of 10% CoO doped sample in 350-600 cm^{-1} range, (d) De-convoluted of 10% CoO doped sample in 200-400 cm^{-1} range.	130, 131
Figure 5.10	M-H curve of $Zn_{1-x}Ni_xO$ at x = 0.5, 1, 1.5, 2, 2.5, 3 and 3.5 %.	132
Figure 5.11	EPR spectra for Ni doping at 0.5% at 15K, 25K, 45K and 65K.	133

LIST OF PUBLICATIONS

- **International Journals**

- [1] **Neha Kondal** and Sanjiv Kumar Tiwari, “Selectively enhanced oxygen vacancies in undoped polycrystalline ZnO as a consequence of Multi-Step Sintering”, **Ceramic International**, vol. 43, no. 13, pp. 10347–10352, 2017.
- [2] **Neha Kondal** and Sanjiv Kumar Tiwari, “Origin of polychromatic emission and defect distribution within annealed ZnO nanoparticles”, **Material Research. Bulletin**, vol. 88, no. December, pp. 156–165, 2017.

- **Conference Proceedings**

- [3] **Neha Kondal** and S. K. Tiwari, “Thermal and temporal evolution of microstructure in polycrystalline ZnO”. **AIP Conference Proceedings**, vol. 1728, 2016.

- **International/ National Conferences/ Workshops**

- [1] National Workshop on X-Ray Powder Diffraction (NXRD-2017) held in Department of SAIF/CIL, Panjab University, Chandigarh & Institute of Nano Science and Technology (INST), Mohali.
- [2] Presented a paper “Controlled variation of Zinc interstitials as a result of Multi step Sintering” National Conference on Advances in Basic & Applied Sciences (ABAS-2017) held in Hamirpur, HP, 2017.
- [3] Presented a paper “Effect of Multistep sintering on defect distribution in polycrystalline ZnO” in National Seminar on Innovation and challenges in Basic & Applied Sciences (ICBAS-2017) Maharaja Agrasen University, March 4, 2017.
- [4] Presented a paper “Thermal and temporal evolution of microstructure in polycrystalline ZnO” in International Conference on Condensed Matter and Applied Physics, ICC, Organized by Department of Physics, GEC Bikaner, October 31, 2015.

CHAPTER 1

“INTRODUCTION”

1.1 Introduction

There has been a great deal of interest in Zinc Oxide (ZnO) semiconductor as a prominent host for Dilute Magnetic Semiconductor (DMS) because of its optoelectronic applications. Its direct wide band gap of 3.37 eV at low temperatures and 3.34 eV at room temperature (RT) makes it a promising candidate for blue-ultraviolet and white light emitting diode. It is a multifunctional material and possesses potential applications in diverse areas like varistors, piezoelectric transducers, transparent conduction films, light emitting diodes etc [1-4]. ZnO has a large exciton binding energy of 60 meV which makes it more suitable than GaN (24.7 meV), ZnS (36 meV) and ZnSe (21 meV) for applications based on excitonic effects at room temperatures [5]. The most practical advantage of ZnO from industrial point of view is its abundant availability, low cost and low toxic behavior. Due to the low toxicity it is also used as diet supplement in animal feeds [6]. ZnO is not really a new-fangled material for research but has been explored by many groups for decades. Research in ZnO followed a roller coaster pattern as there is no clear consensus on its grain growth and defect distributions.

1.2 Crystal Structure of ZnO

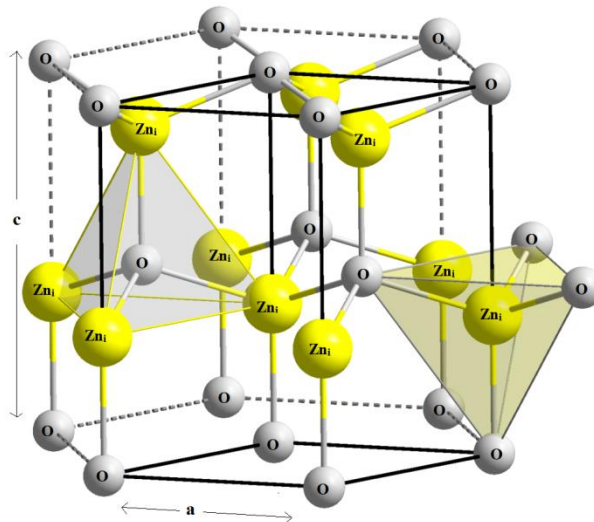


Figure 1.1: Hexagonal wurtzite structure of ZnO (<https://www.wikipedia.org/>).

Zinc oxide crystallizes in three forms: Hexagonal Wurtzite, Cubic Zinc blende and Rocksalt. Under ambient conditions the thermodynamically stable structure of ZnO is Hexagonal wurtzite structure as shown in figure 1.1. The electro negativity values of O^{-2} and Zn^{+2} are 3.44 and 1.65, respectively resulting in very strong ionic bonding between Zn^{+2} and O^{-2} . It has two lattice constants a, c where $a = 3.25\text{\AA}$ and $c = 5.2\text{\AA}$; and their ratio $c/a \approx 1.60$ which is close to the ideal value of hexagonal cell i.e. $c/a = 1.633$. The wurtzite structure belongs to space group P63mc. The Zn and O share typically sp^3 hybridized covalent bonds. Each sub lattice includes 4 atoms per unit cell & each atom one kind (group II) is surrounded by 4 atoms of the other kind i.e. (Group IV) and vice versa.

1.3 Native defects in ZnO

Intrinsic defects of the crystal are its imperfections which arises from migration, diffusion or removal the constituent elements from their original sites. First type of intrinsic defects consists of atoms missing at the respective lattice sites i.e. creation of vacancies like Oxygen Vacancies (V_o) and Zinc vacancies (V_{Zn}). Secondly, extra atoms occupying the interstitial positions in the unit cell are called interstitial defects like Zinc interstitials (Zn_i) and Oxygen interstitials (O_i). Thirdly, an atom occupying the original lattice site of other atom are called antisite defects as in case of ZnO, O occupying the Zn lattice or vice versa called antisite Zinc or antisite Oxygen (Zn_o or O_{Zn}). These defects affect the optical, electrical and the magnetic properties of semiconductor. All the intrinsic defects depend on the growth kinetic and processing techniques of the material. The native defect V_o & Zn_i has been often believed to be the source of unintentional n type conductivity [7]. ZnO has a direct band gap where its conduction band (CB) is formed out of 4s level of Zn and valence band (VB) is made up of 2p orbital of O. The electronic levels of all the intrinsic defects has been studied extensively by local density approximation (LDA) along with Hubbard parameter (U) and density functional theory (DFT) but there exist no firm consensus on their origins and their locations in the band gap.

Jannotti reported the native defects of ZnO theoretically and calculated their formation energies in Zn rich conditions using different approaches LDA and LDA+U as shown in Table I [8].

Defect	Charge state	$E^{LDA}(eV)$	$E^{LDA+U}(eV)$
V_o	0	0.69	1.34
	+1	0.64	0.81
	+2	-0.37	-0.60
Zn_i	0	2.76	3.62
	+1	1.32	1.56
	+2	-0.10	-0.45
V_{Zn}	0	5.94	6.39
	-1	6.02	6.49
	-2	6.31	6.94
O_i	0	6.36	6.83
	-1	6.63	6.83
	-2	7.49	8.28
Zn_o	0	3.43	4.98
	+1	1.81	2.74
	+2	0.22	0.53
	+3	0.48	0.44
	+4	0.14	-0.13
O_{Zn}	0	9.94	10.04
	-1	10.53	10.88
	-2	11.08	11.76

Table I: Formation energies of intrinsic defects in Zn rich conditions [8].

1.3.1 Oxygen vacancies

V_o can be believed as O atom being missing from its original lattice site. Electrons which seems bound to the missing O atoms can be viewed as coming from 4 nearest Zn atoms. From table-I we can see that formation energy of V_o^+ even under Zinc rich condition is 0.81 eV which is small

as compared to other defects. This means that V_o can be easily formed and concentration of V_o^+ will be more under equilibrium conditions.

Electronic structure of V_o comprises of four dangling bonds (sp^3) and two electrons. V_o exist in 3 charged states i.e. neutral V_o , V_o^{+1} and V_o^{+2} , where V_o and V_o^{2+} are more stable than V_o^+ . In neutral charged state of V_o the 4 neighboring Zn shifts inward by around 12% of equilibrium Zn-O bond length as shown in figure 1.2.

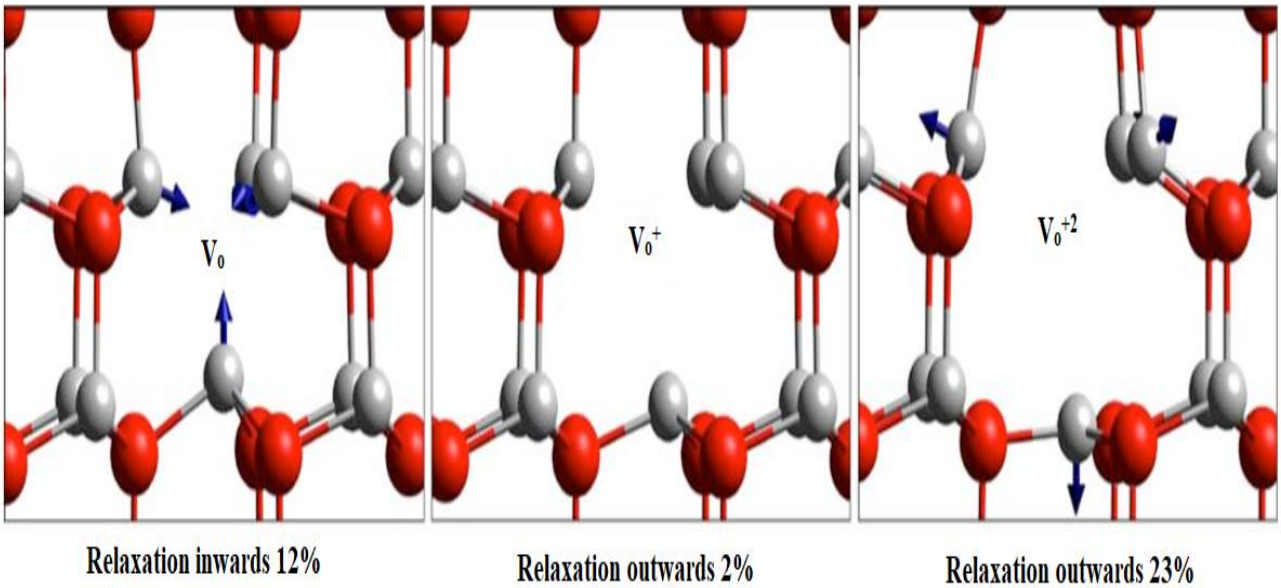


Figure 1.2: Ball & stick illustration of the local atomic relaxations around the V_o , V_o^+ and V_o^{2+} [10].

In case of V_o^+ charged state the Zn atoms relax in outward direction by 2% and for V_o^{2+} charged states by 23% respectively as shown in figure 1.2. Based on theoretical calculations of Janotti the neutral V_o has low formation energy of $\approx 1.34\text{eV}$. They found that in n-type ZnO migration barrier of V_o is 2.4eV. Erhart and Albe also reported that migration barriers of V_o is 2.55eV (out of plane) and 1.87eV (in plane) [9]. The high migration barrier of 2.4eV meaning that V_o undergoes little diffusion at room temperature but annealing at higher temperatures may lead to rigorous movement of V_o . The emission of V_o in the visible region is positioned in green region as predicted by many authors.

1.3.2 Zinc Interstitials

Zn_i are believed as Zn atoms on the interstitial positions. Zn_i are shallow donors and their position lie 0.5eV below the conduction band minima (CBM). The formation energy of Zn_i^+ is 1.56 eV and Zn_i is 3.62 eV, which is quite high even under Zn rich conditions whereas the migration barriers as predicted by them are low of the order of 0.57 eV. This theoretical value of migration barrier is also in good agreement with experimental migration barrier of 0.55 eV as reported by Thomas who heated the crystals in the Zinc vapors followed by rapid quenching [11]. The migration of Zn_i^+ is also predicted to be isotropic as the difference of 0.05eV was found for paths parallel and perpendicular to c axis of the hexagonal wurtzite structure. The lower value of migration barrier means that Zn_i have less possibility to occur as isolated Zn_i . It is likely that they either diffuse out of the material or bind with other intrinsic defects centers or impurities.

Electronically speaking there are two major lattice sites for Zn_i in Hexagonal Wurtzite ZnO i.e. Tetrahedral and octahedral sites. The Zn_i usually occupies octahedral sites as they are more stable than tetrahedral sites. Stability of the Zn_i is brought about by the fact that, at the tetrahedral site, it is situated at a distance of roughly $0.833 d_0$. d_0 is the bond length of Zn–O along c-axis) and has one Zn and one O as the nearest neighbors, while in the octahedral site, it is at a distance of approximately $1.07d_0$ and has three Zn and three O atoms as nearest neighbors [12]. Based on size considerations, the Zn interstitial is expected to be stable on the octahedral site because of less geometrical constraints.

1.3.3 Zinc vacancies

The removal of Zn from its lattice site to an interstitial position results in V_{Zn} . They introduce partially occupied states in the band gap. The electronic structure of V_{Zn} is made up of dangling bonds of four oxygen atoms. The dangling bonds of O combines to form a doubly charged symmetric state located somewhere deep in VB and induce 3 partially occupied states. Hence V_{Zn} has three states, V_{Zn} , V_{Zn}^{-1} , V_{Zn}^{-2} . The formation energy of V_{Zn} under Zn rich conditions is as high as 6.39 eV whereas under O rich conditions it is 3.7 eV. The four O atoms around V_{Zn} shifts outwards by 10% with respect to equilibrium ZnO bond length. The isotropic migration energy barrier for the zinc vacancy in the -2 charge state is 1.4eV. Taylor et al reported the signal in

electron paramagnetic resonance from V_{Zn} in range of $g = 2.0018-2.056$ in irradiated single crystals [13].

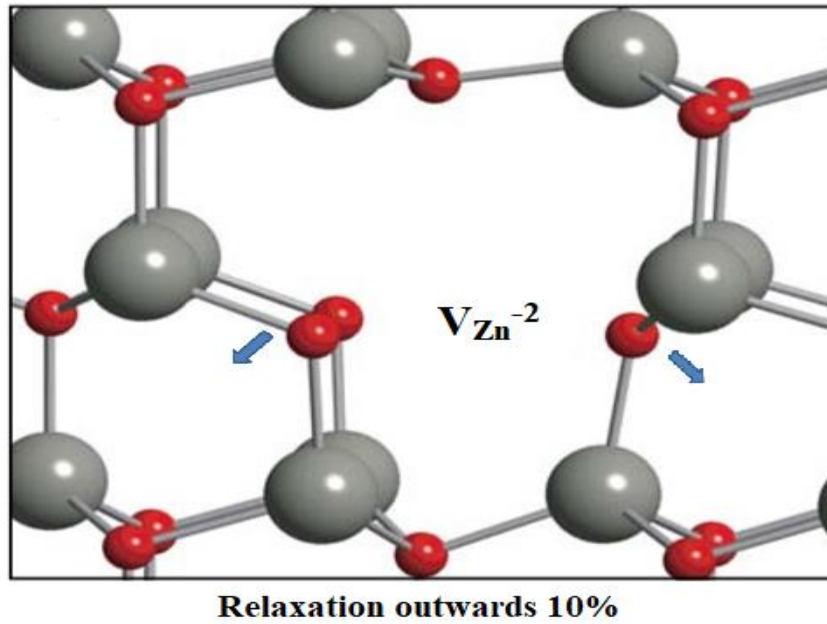


Figure 1.3: Ball & stick illustration of the local atomic relaxations around the V_{Zn} [10].

1.3.4 Oxygen interstitials

Excess O atoms in lattice, sitting at interstitial positions are believed as O_i and have very large formation energies as 6.83eV. The migrations barriers are of O_i are 0.9eV whereas for O_i^{-2} along the c axis of the crystal lattice is 1.1eV.

1.3.5 Zinc antisite and Oxygen antisite

Zn sitting on a wrong lattice site i.e. sitting on an O site is called Zinc antisite. Similarly an O atom sitting at Zn site is called Oxygen antisite. The formation energy of both Zn_o & O_{zn} is 4.98eV and 10.04eV which is quite high as compared to other defects.

1.4 Electronic band structure of ZnO

ZnO has a direct band gap where CB is mainly s-type and VB is p-type. The spin orbit (SO) coupling further leads to partial lifting of valence band degeneracy. Without SO coupling the crystal field (CF) causes splitting of p state into Γ_5 and Γ_1 state as shown in figure 1.4. CF and SO coupling together give rise to 3 twofold degenerate VB. These band states are denoted by A (Γ_7 symmetry), B (Γ_9 symmetry) and C (Γ_7 symmetry) in figure 1.5. The theoretical negative value of SO coupling as predicted by Thomas and Hopfield was experimentally confirmed by Rowe et al. Because of this reason $j = 1/2$ is higher than $j = 3/2$ [14-15].

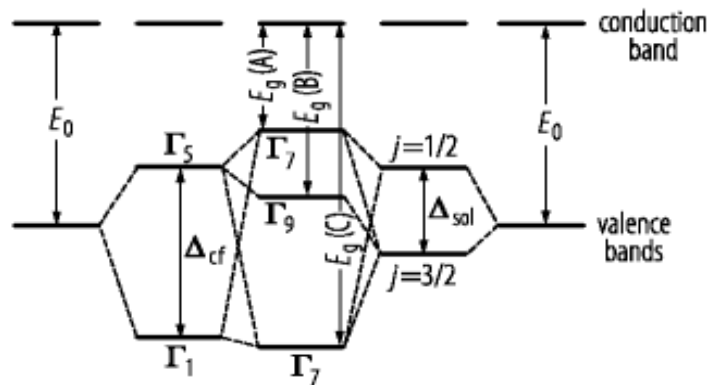


Figure 1.4: Splitting of VB in three twofold degenerate VB [15].

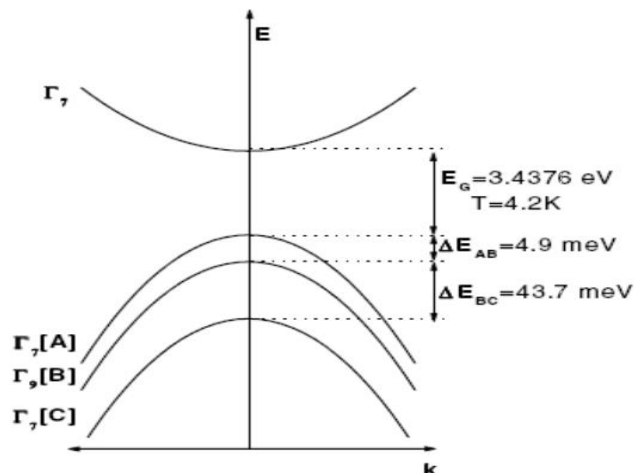


Figure 1.5: Band structure & symmetry of wurtzite ZnO [37].

1.5 Photoluminescence and EPR studies of ZnO

Photoluminescence (PL) is a process of absorption of photon, exciting its one or more electron to higher excited state and then transition of that electron to ground state by a radiation of photon. PL is the widely used technique to study the wide band gap materials like ZnO and ZnSe. It reveals information about band structure, crystal field splitting, spin orbit coupling, defect related emissions and their states in the band gap. PL work on the basis of detecting the radiative transitions in the process. There are basically two types of transitions in PL i.e. free excitonic transition and bound excitonic transition. When the transition decays radiative and the energy of photon coming out is of order of the E_g of the material it is called the free excitonic transition else if it gets trapped at defect site it is called bound exciton. For any luminescent material, it is inevitable to investigate and find out the origins of luminescent centers. The electrical & optical properties of a semiconductor material can be controlled & modified by controlling the nature, concentration and distributions of defects present in it. These defects can be introduced and relocated during growth or by post growth treatments like annealing, sintering or ion implantation. The understanding of their position, ionic nature and distribution becomes vital to understand the conduct of these defects.

The room temperature PL is characterized by an ultraviolet emission so called Near Band Edge (NBE) and at least one broad band emission in the visible region attributed to deep levels called deep level emissions (DLE). The DLE region extends from 400nm to 750nm in the PL spectrum. Different reports have suggested that visible region emission is attributed to the intrinsic defects lying within the band gap.

The green luminescence in PL spectra has been most debatable emission in ZnO. Many authors have attributed it to V_o present in the sample [16-17]. Zhao et al in his report on ZnO implanted with Zn and O concluded that V_{Zn} are responsible for green emissions in ZnO [18]. Kohan also predicted green luminescence because of V_{Zn} [19]

The blue emissions centered at 427nm are because of Zn defects i.e. Zn_i [20]. The yellow-orange emission in the regions has been attributed to antisite Zinc/oxygen, and O_i [21]. PL is indeed an effective way to investigate the electronic states of defects in the sample but does not give idea

about the ionic nature of the defects. To get insights of the ionic and chemical nature of defects a spectroscopy called Electronic Paramagnetic Spectroscopy has been widely used.

EPR is a magnetic resonance technique which is based on the interaction of unpaired electron spins with applied magnetic field. The spin of an electron is a purely quantum mechanical phenomenon and is usually characterized by the spin quantum number $S = \frac{1}{2}$. Its magnetic moment can be written as

$$\mu_e = -g_e \cdot \beta_e \cdot S$$

Where, $g_e = 2.0023$; the electron g-factor or Landé-factor, $\beta_e =$ Bohr magneton number.

In the presence of external magnetic field B , there exist two different energy states for an electron as shown in figure 1.6.

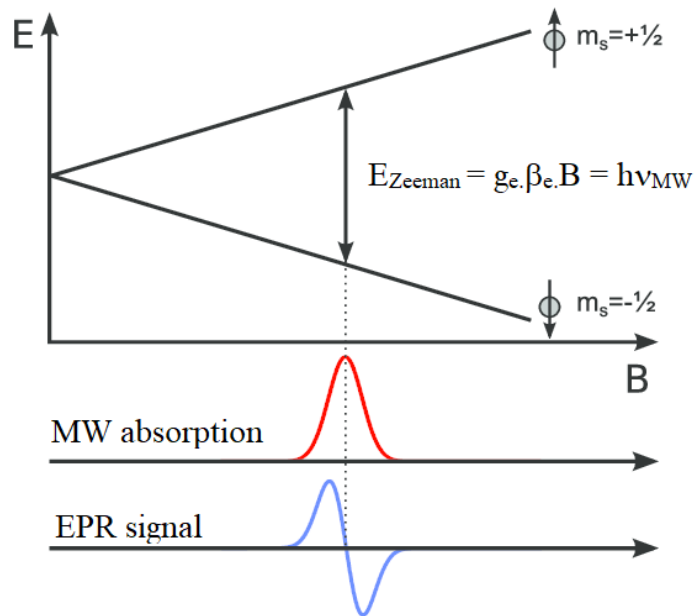


Fig 1.6: Splitting of energy levels in presence of magnetic field & absorption of MW energy [38].

Hence, interaction between electron magnetic moment and applied field can be expressed by the following Hamiltonian:

$$H_{ZI} = -\mu_e \cdot B = g_e \cdot \beta_e \cdot S_z$$

In resonance condition the microwave energy must be equal to Zeeman energy i.e.:

$$\Delta E = h \cdot \nu = g_e \cdot \beta_e \cdot B_o$$

Where, ν is the microwave frequency. Hence the typical EPR signal consist of following following contributions:

(a) In systems like ZnO, an unpaired electron is related with its spin motion and orbital motion which in turn give rise to spin magnetic moment and orbital magnetic moment. This can be described as following Hamiltonian [22]:

$$H = \beta_e \cdot B(L + g_e S) + \lambda \cdot L \cdot S = \beta_e \cdot B \cdot g \cdot S$$

Where, λ is the SO coupling constant,

g is the effective Lande`s g factor.

The magnetic moment has two major influences i.e. SO coupling & orbital magnetic field interaction. These fundamentals give the reason why g is no longer remains equal to 2.0023 and anisotropic. The departure of the principal g values from the free electron i.e. 2.0023 carries information SO coupling, crystal field, and more important the local filed exchange interaction.

(b) The magnetic moment of the unpaired electron will also interact with local magnetic fields originating from non-zero nuclear spins. This interaction is known as the nuclear hyperfine interaction and is given by:

$$H_{HF} = I \cdot A \cdot S$$

Where, A is the hyperfine coupling tensor.

(c) In nuclei with nuclear spins greater than one possesses an electric quadrupole moment Q_e because of the non-spherical charge distribution in the nucleus. The interaction with such nuclei can be expressed as:

$$H_Q = I \cdot Q \cdot I$$

Where, Q is the quadrupole coupling tensor. (d) As in the case of the magnetic moment of the electron, also the magnetic moment of the nucleus interacts with the magnetic field B. This causes a new term in the spin Hamiltonian

$$H_{NZ} = -g_N \beta_N \cdot I$$

Where β_N is the nuclear magneton,

g_N is the nuclear g-factor.

If the system consist of two or more unpaired electrons, i.e. total spin $S > 1/2$, then electrons in the surroundings creates a local electric field called as crystal field. It induces a splitting in the ground state of electron even in absence of B and hence is called Zero field splitting. This interaction results in a line splitting in the ESR spectrum and this interaction can be described by the following Hamiltonian:

$$H_{FS} = S \cdot D \cdot S$$

Where, D is the axial fine structure parameter.

Therefore, the electron in a magnetic field experiences mainly four interactions i.e. Zeeman Interaction, Nuclear hyperfine interaction, Electrostatic quadrupole interaction and Zero field splitting. Hence, the total spin Hamiltonian can be written as

$$H_T = \beta_e \cdot B \cdot g \cdot S + I \cdot A \cdot S + I \cdot Q \cdot I + S \cdot D \cdot S$$

In case of ZnO, the nuclear spin is zero, so one can neglect the contribution of hyperfine interaction and quadrupole interaction term from the total spin Hamiltonian.

The electrons trapped at defects sites will hence produce a different value of Lande's g factor corresponding to their surroundings (different from that of free electron 2.0023) as shown in figure.1.7.

Taking the spin-orbit interaction and electronic calculations, deviation from g of free electron is given as [23].

$$g^* = g_e - \left(\frac{2}{3}\right) \left[\frac{p^2 \Delta_{SO}}{E_g (E_g + \Delta_{SO})} \right]$$

Where, p^2 is the interband mixing coefficient which describes the (20eV for ZnO),

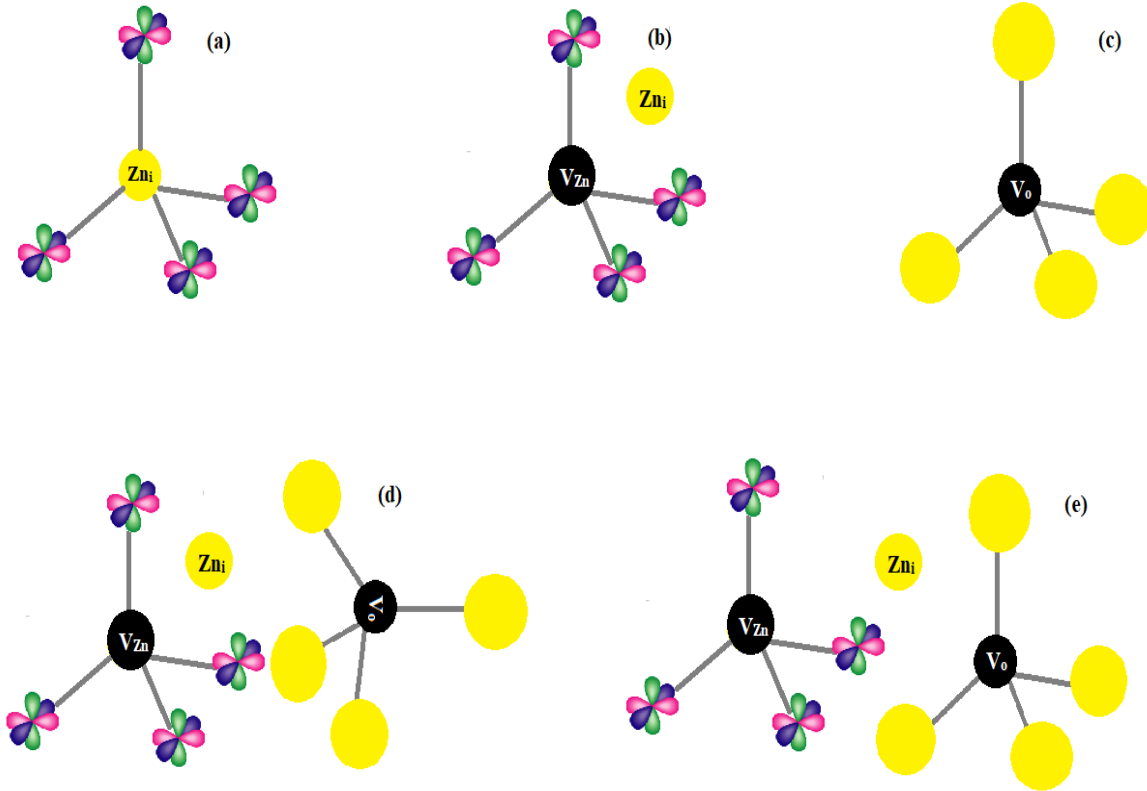


Figure 1.7: Schematics of defects and their surroundings.

E_g is the band gap energy,

Δ_{SO} is the spin orbit coupling.

This means more the spin-orbit coupling more will be the deviation from the ideal Lande's g value of free electron. Hence, characteristics signal in EPR spectra of ZnO at $g= 2.0155$, $g = 2.0024$ and $g = 2.0165$ has been attributed to V_{Zn} [24-25]. Signal centered at $g = 1.96$ is assigned to V_o . Signal assigned to $g = 1.9640$ is assigned to Zn_i [26]. Morazzini et al reported signal $g =$

1.955 and $g = 1.958$ to Zn^+ and V_o^+ [27]. This collectively means that defects will experience different SO coupling & CF, and therefore will amount to different g value depending on their respective environments and will lead to tailoring of magnetic properties as shown in figure 1.7. Therefore, techniques like annealing/ sintering which leads to diffusion and migration of intrinsic defects without external doping in turn tailor the magnetic properties to large extent.

1.6 Spintronics: ZnO based dilute magnetic semiconductors

“Spintronics” spin and charge coupled electronics in an emerging field of research in solid state physics. After the development of transistors in the electronic industry microelectronics industry has made fantastic progress in integrating chips on a single wafer which have numerous applications in today`s technological aspects. The basis of the electronic industry was charge of electron. In 1965, Gordon E Moore predicted that number of transistors that would fit on a given area of silicon chip would double every year. In this way more computing power would be obtained for the same price and electronic devices would be less expensive and will perform better. But there will be a certain time approximated in early 2015`s when the size of individual gates will approach the dimensions of atoms and will not be reduced further. At that time size would finitely approach a scale of few nanometres where the realms of classical physics will stop working and new quantum mechanical effects will begin. At that point of time there will be a search of new degree of freedom which will serve the cause and will lead to drastic advancement in the upcoming technology. Hence, that new degree of freedom will be spin of electron which is intrinsic angular momentum of electrons. The foundation of spintronics industry would rely on manipulation of spin and charge controlled magnetic nanostructures.

The 1st generation spintronics devices were based on passive magneto resistance sensors and memory elements which used electrodes made from alloys of ferromagnetic 3d metals. This lead to development of giant magneto resistance in multi layers and tunnelling magneto resistance [28, 29] Direct use of magnetic material & metal contacts to make Giant Magneto Resistance devices has resulted in poor efficiency due to conductivity and lattice mismatch that exist at the interface of metal/ insulator or metal/semiconductor. Therefore development of next generation of spintronics devices are expected work on manipulation of spin polarised electrons in host

semiconductor matrix and the interfaces of the contacts [30]. For the operational devices, spin polarised electrons need to preserve their polarization as they travel through interface. The study of interaction of spin polarised electrons with random spin polarised electrons of semiconducting layer becomes vital. Therefore a design of material combining both semiconducting and ferromagnetic properties becomes very necessary for the development of such spintronics devices. This leads to the study of dilute magnetic semiconductors (DMS). DMS are the materials exhibiting both semiconducting and magnetic properties. They are semiconductors in which fraction of cations in the lattice are replaced by magnetic ions. Figure.1.8. shows the schematic for DMS which indicates the substitution of very small concentration of host ions with the dopant ions. Dopants are usually transition metals with partially filled d orbital like Fe, Co, Mn, Ni etc.

The interest in the field started with possibilities to tailor many interesting properties like band gap, lattice parameters and electrical properties. In addition magnetic properties which arise from electrons of d orbital give rise to many different properties like magneto transport and magneto optical properties. The field progressed a lot since then and widely used host compounds till date are GaN, GaAs and ZnO with different transition metals which have been found to have Curie temperature well above the room temperature.

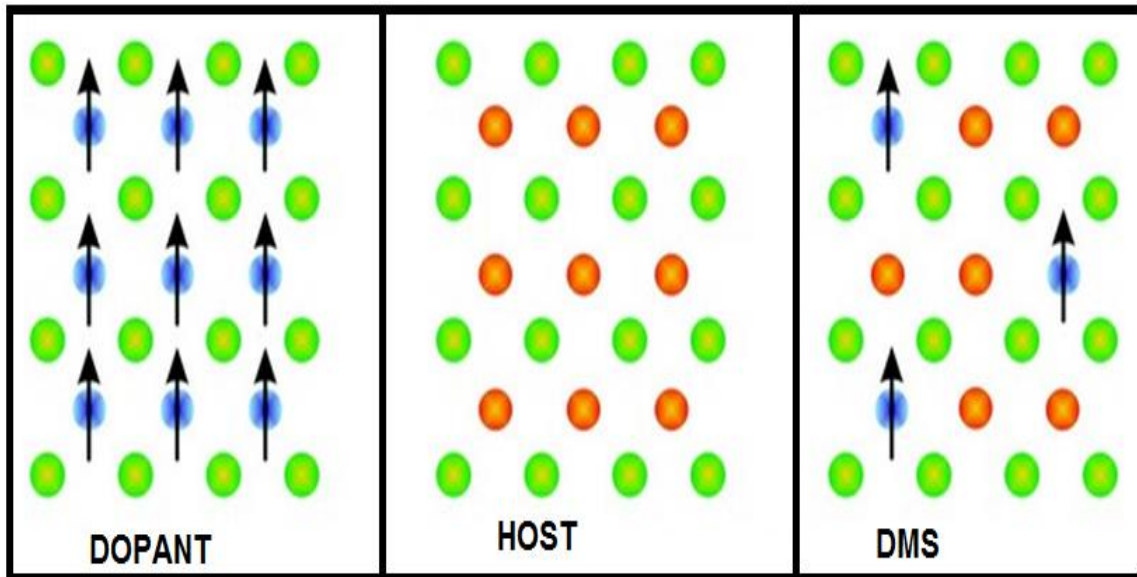


Figure 1.8: Schematic for (a) Dopant (b) Non magnetic host semiconductor (c) Dilute Magnetic semiconductor [39].

1.7 Theoretical models for explaining magnetism in DMS

The literature of DMS, proposes different models of origin of magnetism in DMS. Few models have been discussed here in short based on the exchange interactions between spin-spin. These interactions are mainly are direct interaction, RKKY interactions, double exchange, mean field Zener model etc

1.7.1 Direct exchange interaction

This type of exchange interaction involves the direct coupling of magnetic ions via overlapping of magnetic orbitals. The direct exchange interaction coupling of the spins can be described by the Heisenberg Hamiltonian [31]:

$$H = - \sum_{ij} J_{ij} S_i S_j$$

Where, J_{ij} is the exchange integral and is given as

$$J_{ij} = \frac{1}{2} (E_s - E_t)$$

Where, $(E_s - E_t)$ represents the small difference between the triplet and singlet states. If the value of J_{ij} is positive, it leads to ferromagnetic exchange whereas if J_{ij} is negative it is antiferromagnetic exchange.

1.7.2 Carrier mediated indirect exchange: RKKY interaction

If the distance between the magnetic ions are large then interaction between them involves a free carrier present in the system and such an interaction is called Carrier mediated indirect exchange. As the name suggest Dilute magnetic semiconductor, the word “dilute” signifies the large distance between the magnetic ions hence no direct interaction between them. There are very few types of exchange interactions like, RKKY interaction, Mean field Zener Model, Double exchange mechanism, Bound magnetic polaron model etc. The indirect exchange was proposed long ago by Ruderman-Kittel-Kasuya-Yosida (RKKY) [32]. For two spins sitting at i and j site, the interaction is mediated by polarization of conduction electrons. The characteristics for this interaction is an oscillatory behavior of exchange integral J . This J_{ij} is given as

$$J_{ij}^{RKKY} = \frac{J^2 k_F^6}{\varepsilon_F} \frac{\hbar^2 V^2}{N^2 (2\pi)^3} F(2k_F R_{ij})$$

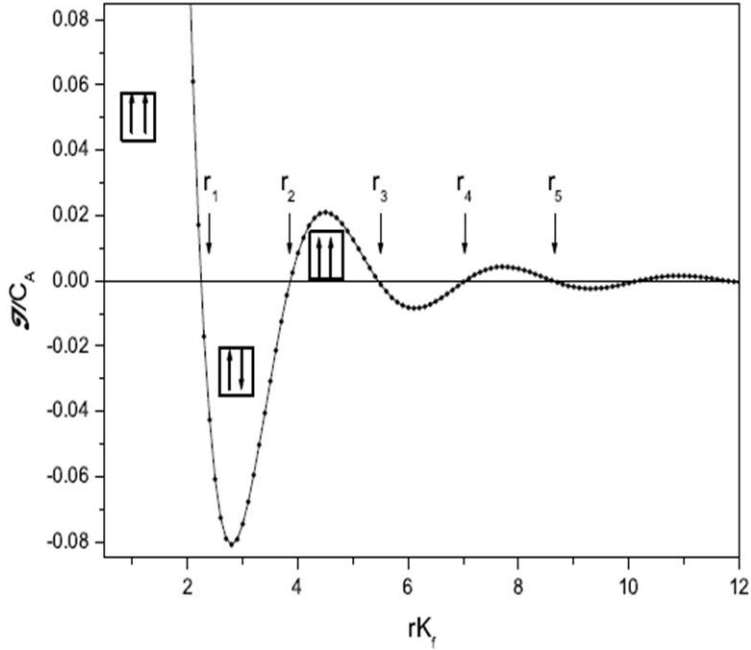


Figure.1.9: Variation of J with interatomic radii r multiplied by radius of the Fermi sphere K_f [32].

Exchange integral changes its sign as function of distance between localized moments as shown in figure.1.9.

1.7.3 Mean field Zener model

Mean field Zener Model by Dietl et al. is based on the original model of Zener and the RKKY interaction. In this model, the delocalized hole acts as mediator in RKKY like interaction among localized transition metal ions resulting in ferromagnetism [33, 34]. In comparison to the RKKY interaction, this model takes into account the complex valence-band structure of semiconductors. In the process, it reveals the important effect of the SO coupling in the VB in determining the magnitude of the Curie temperature T_C and the direction of the easy axis in p-type ferromagnetic semiconductors.

1.7.4 Double exchange mechanism

The double exchange mechanism also projected by Zener is explained by hopping of electron between two neighboring magnetic ions. In case of TM 3d levels are split by the crystal field into lower energy doublet and higher energy triplet levels. In $\text{Zn}_{1-x}\text{Co}_x\text{O}$ the low energy spin up 3d-states are strongly hybridized with O 2p states [35, 36]. Besides that, high energy spin-down states of Co ions are located close to the CBM of host ZnO. If the magnetic moments of neighboring Co ions are aligned parallel, electrons in the partially filled 3d-orbitals of the Co ions are allowed to hop from one ion to the other and stabilize the ferromagnetic ground state.

1.8 A prototype spin based light emitting diode

One of the goals is to build spin-based light emitting diodes (LED) that generate left or right circularly polarized light. LED's are optoelectronic devices that, upon application of a forward electrical bias, favors the radiative recombination of electrons and holes resulting in emission of light (electroluminescence).

In order to implement this idea the fundamental requirement is electron-spin injection, manipulation and detection in host semiconductor as discussed above. Practically, spin manipulation is relatively straight forward, but injecting and detecting these spin under practical condition is a challenging task because one need to find spin-polarized material (Spin aligner) in which most of the electron spins are aligned in a particular direction at room temperature e.g. room temperature ferromagnetism is essential. A promising material for this purpose could be transition metal doped ZnO based dilute magnetic semiconductors (DMS), e.g. $\text{Zn}_x\text{M}_{1-x}\text{O}$ (M= Co, Ni,) as spin aligner, and nonmagnetic p-and n-type ZnO as base and recombinant material respectively. The advantage of choosing transition metal oxide over other oxides is that those magnetic ions will be incorporated is electronically, thus providing localized magnetic moments without altering the crystal structure and carriers doping. Transition metal spins in undoped or n-type ZnO are usually coupled by large exchange energy and, at low doping concentration and low temperature, the sp-d exchange interaction leads to a large Lande's g factor (more than twice as compared to free electron) which results in large Zeeman splitting of band edge related states. We exploit this enhanced Zeeman splitting to align the spins within the magnetic layer of ZnO. Subsequently, these spin-polarized electrons will be passed into the non-magnetic n-type ZnO.

Depending on spin de-phasing times (which is of the order of nanosecond), the preferential spin orientation will survive up to a distance of 50-100 nanometer: therefore, by making a second ZnO nano-structured layer of thickness of about 100 nm, ZnO based spintronics device can be made. A prototype design of this type of device is shown in figure 1.10.

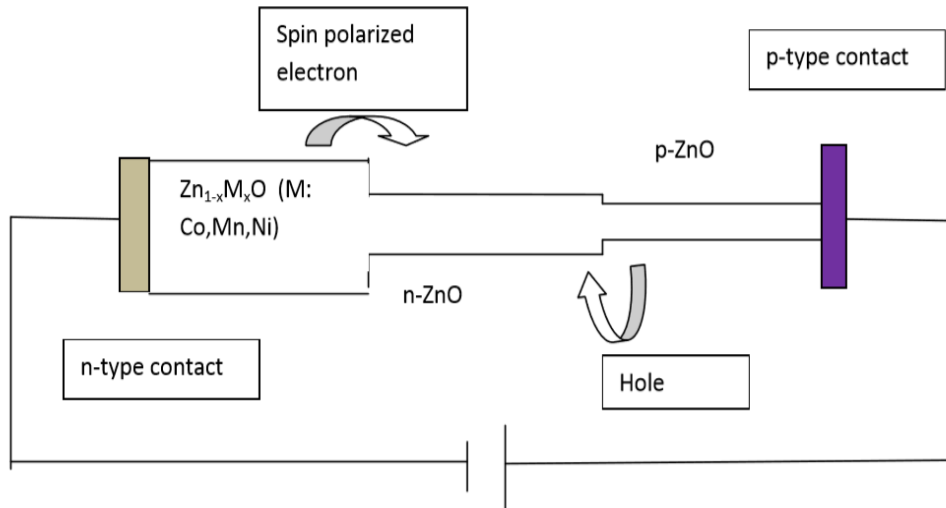


Figure 1.10: A prototype design of spin light emitting diode.

From scientific point of view, ideally p-type and n-type ZnO has almost same optical band gap so that it is way easy to transfer electrons and holes from each other. A spin aligner material is ferromagnetic at room temperature. On biasing polarized electron will transfer from spin aligner to n type ZnO and will recombine with the hole there and will emit a circularly polarized light.

Based on this spin LED few problems have been intended as follows:

- (a) Effect of spin-spin, and spin-lattice interaction at the interface of grains, and p-type and n-type ZnO has not been studied to the best of our knowledge.
- (b) P-type ZnO means existence of excess zinc vacancies in sample, and interaction of these defects with Zn interstitial will result in donor-acceptor pair (DAP) formation. The effect of DAP on magnetic properties has not been studied. Although, DAP signal has been reported in low temperature photoluminescence and core-shell type structure.

(c) Similar to point (a) effect of interface of single crystalline CoO and NiO doped ZnO with polycrystalline ZnO has not been studied. This is because SO interaction strength in polycrystalline ZnO is $\sim 20\text{meV}$ which is almost same as L-S coupling strength of Co^{+2} ions.

Hence, based on these four objectives have been framed:

Chapter 2. “Thermal and temporal evolution of microstructure and interface formation of grain by high temperature annealing”.

Chapter 3. “Origin of polychromatic emission and defect distribution within annealed nanocrystalline ZnO and their effect on magnetic properties and spin-spin interaction”.

Chapter 4. “Selectively enhanced shallow and deep donor defect in nanocrystalline ZnO: A path to make p-type ZnO without doping by multistep annealing”.

Chapter 5. “Development of CoO and NiO doped ZnO based DMS: A promising material for spin aligner”.

REFERENCES

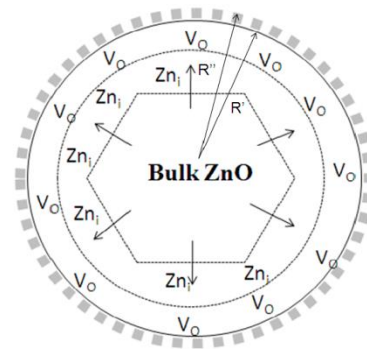
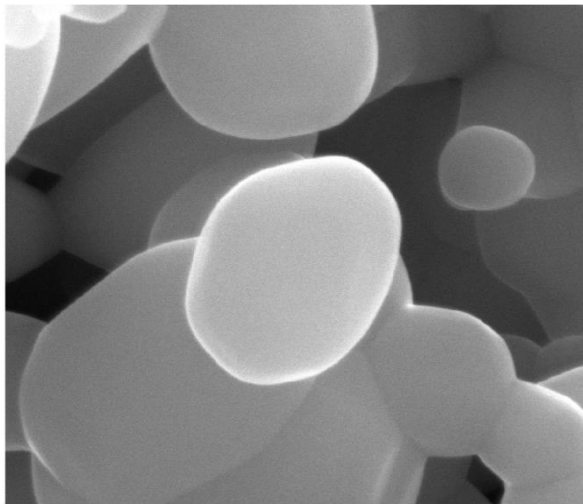
1. J. Xie, H. Deng, Z. Q. Xu, Y. Li, and J. Huang, “Growth of ZnO photonic crystals by self-assembly”, *Journal of Crystal Growth*, vol. 292, no. 2, pp. 227–229, 2006.
2. M. Law, L. E. Greene, J. C. Johnson, R. Saykally, and P. Yang, “Nanowire dye-sensitized solar cells”, *Nature materials*, vol. 4, no. 6, pp. 455–459, 2005.
3. Z. P. Wei, Y. M. Lu, D. Z. Shen, Z. Z. Zhang, B. Yao, B. H. Li, J. Y. Zhang, D. X. Zhao, X. W. Fan, and Z. K. Tang, “Room temperature p-n ZnO blue-violet light-emitting diodes”, *Applied Physics Letters*, vol. 90, no. 4, pp. 4–7, 2007.
4. K. Rainey, J. Chess, J. Eixenberger, D. A. Tenne, C. B. Hanna, and A. Punnoose, “Defect induced ferromagnetism in undoped ZnO nanoparticles”, *Journal of Applied Physics*, vol. 115, no. 17, 2014.
5. Yu P Y and Cardona M 2005 *Fundamentals of Semiconductors* 3rd edition (Berlin: Springer).
6. J. W. Smith, M. D. Tokach, R. D. Goodband, J. L. Nelssen, and B. T. Richert, “Effects of the Interrelationship between Zinc Oxide and Copper Sulfate on Growth Performance of Early-Weaned Pigs”, *Journal of Animal science*, vol. 75, no. 7, pp. 1861–1866, 1997.
7. S. E. Harrison, “Conductivity and Hall effect of ZnO at low temperatures”, *Physical Review*, vol. 93, no. 1, pp. 52–62, 1954.
8. A. Janotti and C. G. Van De Walle, “Native point defects in ZnO”, *Physical Review B*, vol. 76, no. 16, pp. 1–22, 2007.
9. P. Erhart and K. Albe, “First-principles study of migration mechanisms and diffusion of oxygen in zinc oxide”, *Physical Review B*, vol. 73, no. 11, p. 115207, 2006.
10. A. Janotti and C. G. Van De Walle, “Oxygen vacancies in ZnO”, *Applied. Physics. Letters*, vol. 87, no. 12, pp. 1–3, 2005.
11. D. G. Thomas, “Interstitial Zinc in Zinc Oxide”, *Journal of Physics and Chemistry of Solids*, vol. 3, pp. 229–237, 1957.
12. C. H. Henry and D. V. Lang, “Non radiative capture and recombination by multiphonon emission in GaAs and GaP”, *Physical Review B*, vol. 15, no. 2, pp. 989-1016, 1977.
13. A. L. Taylor, G. Filipovich, and G. K. Lindeberg, “Electron paramagnetic resonance associated with Zn vacancies in neutron-irradiated ZnO”, *Solid State Communications*, vol. 8, no. 17, pp. 1359–1361, 1970.

14. X. L. Wu, G. G. Siu, C. L. Fu, and H. C. Ong, “*Photoluminescence and cathodoluminescence studies of stoichiometric and oxygen-deficient ZnO films*”, Applied Physics Letters, vol. 78, no. 16, pp. 2285–2287, 2001.
15. D. G. Thomas, “*The exciton spectrum of zinc oxide*”, Journal of Physics and Chemistry of Solids, vol. 15, no. 1–2, pp. 86–96, 1960.
16. T. M. Børseth, B. G. Svensson, A. Y. Kuznetsov, P. Klason, Q. X. Zhao, and M. Willander, “*Identification of oxygen and zinc vacancy optical signals in ZnO*”, Applied Physics Letters, vol. 89, no. 26, 2006.
17. A. B. Djurisic and Y. H. Leung, “*Optical properties of ZnO nanostructures*”, Small, vol. 2, no. 8–9, pp. 944–961, 2006.
18. Q. X. Zhao, P. Klason, M. Willander, H. M. Zhong, W. Lu, and J. H. Yang, “*Deep-level emissions influenced by O and Zn implantations in ZnO*”, Applied Physics Letters, vol. 87, no. 21, pp. 1–3, 2005.
19. Kohan A. F., Ceder G. , D. Morgan, and C. G. Van de Walle, “*First-principles study of native point defects in ZnO*”, Physical Review B, vol. 61, no. 22, pp. 15019–15027, 2000.
20. B.Lin, Z. Fu, and Y. Jia, “*Green luminescent center in undoped zinc oxide films deposited on silicon substrates*”, Applied Physics Letters, vol. 79, no. 7, pp. 943–945, 2001.
21. Weckhuysen, Bert M, Ralf Heidler, and Robert A. Schoonheydt. "*Electron spin resonance spectroscopy.*" *Characterization I*. Springer, Berlin, Heidelberg, 2004. 295-335.
22. X. L. Wu, G. G. Siu, C. L. Fu, and H. C. Ong, “*Photoluminescence and cathodoluminescence studies of stoichiometric and oxygen-deficient ZnO films*”, Applied Physics Letters, vol. 78, no. 16, pp. 2285–2287, 2001.
23. K. M. Whitaker, S. T. Ochsenein, V. Z. Polinger, and D. R. Gamelin, “*Electron Confinement Effects in the EPR Spectra of Colloidal n-Type ZnO Quantum Dots*”, Journal of Physical Chemistry C, vol. 98195, pp. 14331–14335, 2008.
24. L. Koudelka, J. Horák, and P. Jariabka, “*Morphology of polycrystalline ZnO and its physical properties*”, *J. Mater. Sci*, vol. 29, no. 6, pp. 1497–1500, 1994.
25. D. Galland and A. Herve, “*Temperature dependence of the ESR spectrum of the zinc vacancy in ZnO*”, *Solid State Communication*, vol. 14, no. 10, pp. 953–956, 1974.
26. N.G.Kakazey, T. V. Srećković, and M. M. Ristić, “*Electronic paramagnetic resonance investigation of the evolution of defects in zinc oxide during tribophysical activation*”, Journal of materials science, vol. 32, no. 17, pp. 4619–4622, 1997.
27. F. Morazzoni, R. Scotti, P. Dinola, C. Milani, and D. Narducci, “*Electron-Paramagnetic*

- Resonance Study of the Interaction of the ZnO Surface with Air and Air Reducing Gas-Mixtures*”, Journal of the Chemical Society, Faraday Transactions, vol. 88, no. 12, pp. 1691–1694, 1992.
28. M. N. Baibich, J. M. Broto, A. Fert, F. N. Van Dau, F. Petroff, P. Eitenne, G. Creuzet, A. Friederich, and J. Chazelas, “*Giant magnetoresistance of (001)Fe/(001)Cr magnetic superlattices*”, Physical review letters, vol. 61, no. 21, pp. 2472–2475, 1988.
 29. C. Chappert, A. Fert, and F. N. Van Dau, “*Spin storage: the convergence of spin electronics and magnetic recording*”, vol. 3, no. 1, pp. 1–36, 1988.
 30. T. Bland, L. Kiyong, and S. Steinmüller, “*The spintronics challenge*”, Physics World, vol. 21, no. 1, pp. 24–28, 2008.
 31. P.W. Anderson “*Magnetism*” ed G Rado and H Suhl (New York) Chapter 2 (1963) 25
 32. Yosida K, —Theory of Magnetism, Springer, Berlin, 1996.
 33. T. Dietl, H. Ohno, F. Matsukura, J. Cibert, and D. Ferrand, “*Zener model description of ferromagnetism in zinc-blende magnetic semiconductors*”, Science, vol. 287, no. 5455, pp. 1019–1022, 2000.
 34. C. Zener, “*Interaction between the d shells in the transition metals*”, Physical Review, vol. 81, no. 3, pp. 440–444, 1951.
 35. Sato K, Yoshida H.K, “*Material Design for Transparent Ferromagnets with ZnO-Based Magnetic Semiconductors Express Letter Material Design for Transparent Ferromagnets with ZnO-Based Magnetic Semiconductors*”, Japanese Journal of Applied Physics. vol. 39, no. 6B, pp. 555–558, 2000.
 36. Sato K, Yoshida H.K, “*First principles materials design for semiconductor spintronics*”, *Semiconductor Science and Technology*”, vol. 17, pp. 367-376, 2002.
 37. Meyer B.K, Alves H, Hofmann D.M, Kriegseis W, Forster D, Bertram F, Christen J, Hoffmann A, Straßburg M, Dworzak M, and Haboeck U, "Bound exciton and donor–acceptor pair recombinations in ZnO." *Physica status solidi (b)*” vol 241.2, pp 231-260,2004.
 38. Sperlich A, "Electron paramagnetic resonance spectroscopy of conjugated polymers and fullerenes for organic photovoltaics." (2013).
 39. Ohno H, “*Making Nonmagnetic Semiconductors Ferromagnetic*”, Control and uses of facts vol. 281, Issue 5379, pp. 951-956.

CHAPTER 2

“THERMAL AND TEMPORAL EVOLUTION OF MICROSTRUCTURE AND INTERFACE FORMATION OF GRAIN BY HIGH TEMPERATURE ANNEALING”



2.1 Introduction

Annealing is the process of heating a material to a particular temperature, maintaining it at that temperature for some particular duration and then letting it cool down to RT naturally or by maintaining some heating gradient. Increase in temperature leads to agglomeration, grain coarsening and exaggerated grain growth [2]. Therefore, it is very important to understand the evolution of grains and microstructures on annealing. Annealing by means of thermal activation, increases the mobility of defects within the grains which leads to grain growth. The defects or impurities migrate and diffuse with their respective diffusion coefficients within the grain leading to redistribution of defects. This redistribution in turn lead to tailoring of various defect related properties viz optical, electrical and magnetic properties. The annealing process is usually characterised by its annealing temperature and annealing time. The process is initiated by choosing a constant heating rate and then raising the temperature from RT to desired temperature. This step is called as step of “Thermal evolution”. After reaching the annealing temperature a hold of some optimised annealing time is kept. This step of holding the temperature for particular annealing time is called step of “Temporal evolution”. Therefore, in order to explore its microstructures and defect distributions, two techniques conventional and multistep annealing with different kinetics and mechanisms have been chosen to anneal the ZnO. In conventional annealing the activation energies, heating rate and diffusion coefficient remain same where as in case of multistep annealing they become variable in each step. This chapter introduces with two different annealing techniques CA and MSA. Their grain growth mechanisms and the grain growth model based structural analysis of the samples and different morphologies of grains have been discussed in this chapter.

2.2 Experimental Techniques of Annealing

To redistribute defects, understand and control microstructures in pure ZnO, two annealing techniques has been adopted i.e.

- a) Conventional Annealing (CA)
- b) Multi step annealing (MSA)

as shown by schematic in fig.2.1.

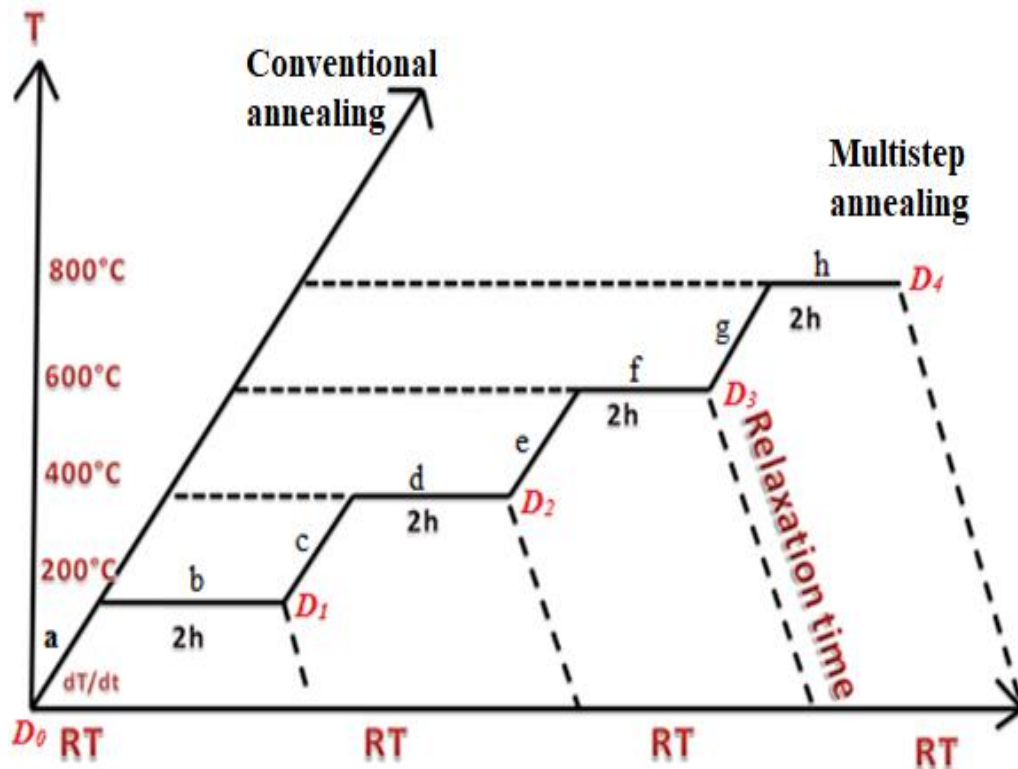


Figure 2.1: Schematic of Conventional annealing and Multi step annealing [1].

ZnO powder (99.99%) pure was purchased from Sigma Aldrich. The powder was first crushed in mortar and pestle for 3 hours. All the experiments were performed in air atmosphere in a muffle furnace. The furnace was initially optimized for heating rate and samples were annealed in alumina crucibles. For CA the pure ZnO powder was annealed at heating rate, $\frac{dT}{dt} = 100^\circ\text{C}/\text{min}$ at chosen temperatures 200, 400, 600, 800, 1000 and 1100°C respectively. The temperature was raised from RT to particular desired annealing temperature at i.e. step of thermal evolution. Then after achieving the desired temperature it is kept to evolve temporally for two hours. The heating was constant all the way through process. The sample was then naturally cooled to room temperature.

Multi step annealing as the name suggests is annealing in steps. For Multi step annealing the ZnO powder was annealed stepwise in step of two hours at heating rate = $100^\circ\text{C}/\text{min}$ at 200, 400, 600 and 800°C . The desired temperature in MSA was achieved by step by step rising of the

temperature and holding time. MSA consists of many thermal and temporal evolutions steps. In figure 2.1 step “a”, “c”, “e” & “g” are called the steps of thermal evolutions and step “b”, “d”, “f” & “h” are steps of temporal evolutions. For example, we take a case of annealing a sample at 400°C for 2 hours. The temperature of furnace is raised from RT to 200°C at first and a hold of 2 hours is maintained there. After these 2 hours i.e. step “b”, the sample is not allowed to cool down instead the temperature is raised to 400°C and finally a hold of 2 hours is maintained. After these 2 hours the sample is allowed to cool naturally to RT. The difference in the mechanisms starts at step “c” where, activation energies and diffusion coefficients of defects become very different from that of step “a”.

To investigate the structural deformations, grain size and stress evolved during of conventional and multistep annealed ZnO powder RT X-ray diffraction (XRD) technique was employed. XRD spectra were recorded for all the samples in range of 20°-80° at scanning speed of 0.02/min by means of Copper K_{α} radiation of wavelength 1.5406 Å. To see morphologies and shapes of the nanoparticles Field Emission Scanning Electron Microscopy (FESEM) was performed. Raman spectroscopy was performed to get structural insights of the sample.

2.2.1 Conventional Annealing

The kinetics of grain growth during CA suggests that grain size depend on annealing temperature and annealing time as: $d - d_o = Kt^n$, Where, d = average grain size after annealing time t,

d_o = is initial grain size, $K = K_o e^{\left(-\frac{Q}{RT}\right)}$, Q = activation energy of the defects, R = gas constant, T = annealing temperature [3].

In CA rate of change of grain size with annealing temperature is proportional to annealing time and heating rate; $\frac{dD}{dT} \propto t^{n-1} \left(\frac{dT}{dt}\right)^{-1}$ which are constant [5].

Heating rate $\frac{dT}{dt}$ and the activation energies (Q) of various defects remains constant. Hence, the grain growth is dependent only on the temporal evolutions i.e. the annealing time. Therefore we can bring to a close, that in CA, though the defects starts migrating and diffusing during thermal

evolutions but the grain growth occurs only when the sample is allowed evolve with annealing time at constant temperature.

2.2.2 Multi step Annealing

Since, the diffusion of defects depends on the environment they are surrounded. Hence the activation energy and diffusion coefficients become different for each step and play an important role in redistributing the defects. In MSA, the controlled steps lead to different grain growth mechanisms. The rate of change of grain size with temperature in MSA now becomes proportional to different activation energies of the defects in each step, the annealing temperature which is divided in steps, the annealing time and the heating rate which is a quasi constant.

$\frac{dd}{dT} \propto K_0 e^{\left(\frac{-Q}{RT}\right)} t^{n-1} \left(\frac{dT}{dt}\right)^{-1}$. Hence, for MSA the grain growth depends equally on thermal as well as temporal evolutions.

Both the processes CA and MSA differ in their mechanism of evolution of microstructures and grain growth. Hence, they will lead to a different distribution of defects inside or within a sample, which will lead to different defects related structural, optical and magnetic properties within pure ZnO without any extrinsic doping.

2.3. Results and Discussions

2.3.1 X ray diffraction studies of CA ZnO nanoparticles

The structure of ZnO is hexagonal wurtzite structure as discussed previously with two lattice parameters a and c where $\frac{c}{a} = 1.633$ Is shown in figure 2.2. Zn is tetrahedral coordinated to four O and vice versa in sp³ bonding. This is an ideal structure of undoped and pristine ZnO All the annealed samples will be observed in reference to this ideal structure whose XRD spectra is given by spectra B in figure 2.3.

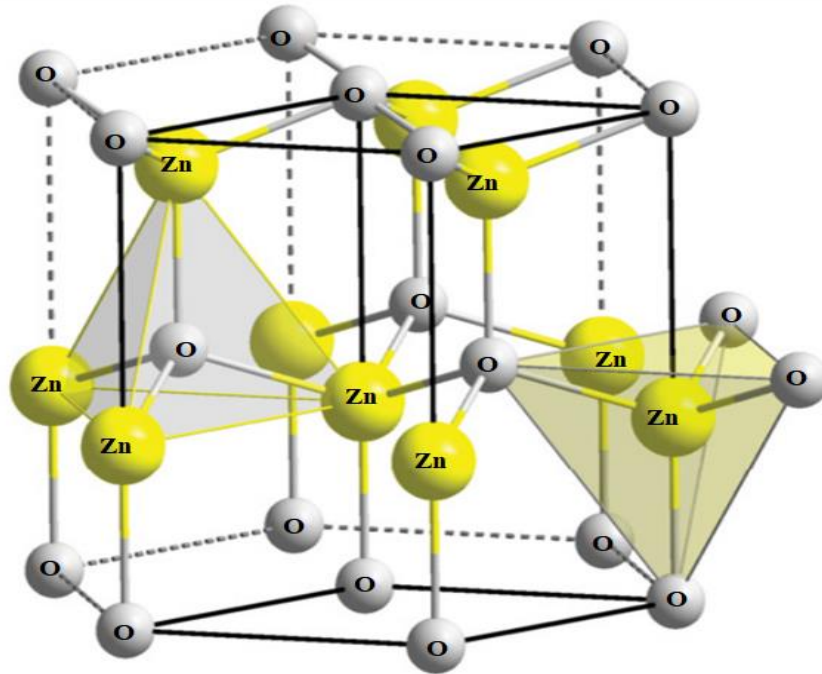


Figure 2.2: Ideal hexagonal wurtzite ZnO structure undoped and pristine (<https://www.wikipedia.org>).

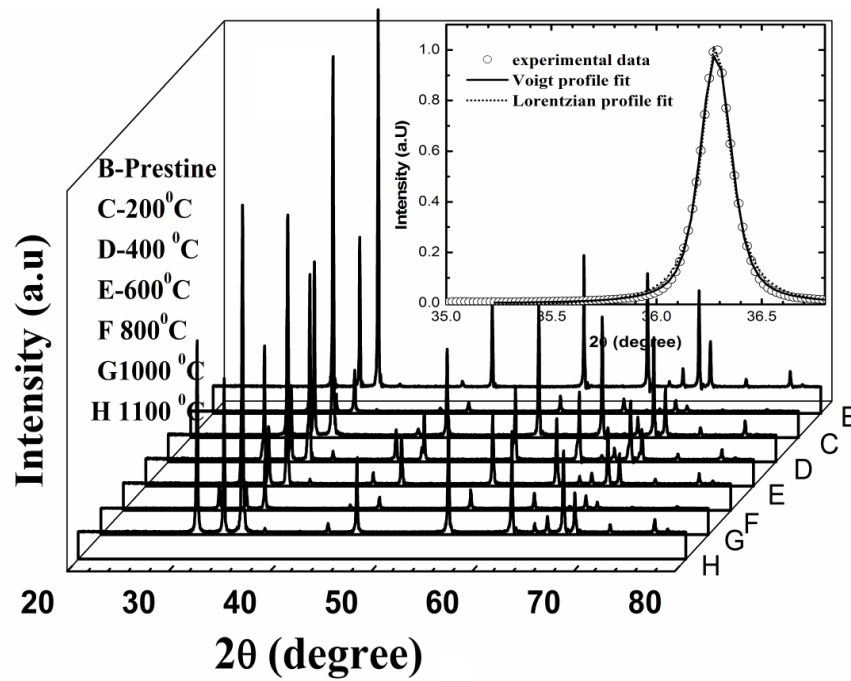


Figure 2.3: XRD patterns of CA ZnO at various temperatures; inset show the Voigt and Lorentzian fits to the experimental data points.

Figure 2.3 is the X-Ray diffraction pattern of ZnO samples annealed conventionally at temperatures 200, 400, 600, 800, 1000 and 1100°C respectively. The XRD peaks were individually indexed with the wurtzite phase of pure Zinc oxide in reference to “JCPDS Card Number. 361451”. The XRD peaks were broad and the broadening consisted of contribution - from instrumental factors, non uniform strain and grain size [6]. The instrumental broadening which arises due to instrumentation needs to be removed before calculating the actual grain size. Full width at Half Maxima (FWHM) is typically used to measure the width the XRD peak. There are many methods to remove instrumental broadening. David and Matthewman did modelling of experimental XRD line profile by using Voigt function and assigned Lorentzian and Gaussian component to size effect and instrumental broadening from the XRD instrument [7]. Similarly we used the Voigt, Lorentzian and Gaussian line profiles to remove the instrumental broadening. The distribution of strain within the sample is a natural and has a Gaussian distribution whereas X-Rays line profile is Lorentzian is nature. Lorentzian line profile implies $\beta_{exp} = \beta + \beta_{instr}$,

Gaussian line profile implies $\beta_{exp}^2 = \beta^2 + \beta_{instr}^2$ and Voigt implies $\beta_{exp} = \beta + \frac{\beta_{instr}^2}{\beta_{exp}}$ where β_{exp} is

the measured FWHM from XRD spectra, β_{instr} is the instrumental broadening contribution and β is the actual FWHM arising only from the sample. To remove the instrumental broadening each and every peak of XRD spectra was individually fitted with Lorentzian, Gaussian and Voigt fits and final FWHM of sample was given as: $\beta = (2\beta_L - \beta_V) \pm (5\beta_V^2 - 4\beta_L\beta_V)^{1/2} / 2$.

The inset of Figure 2.3 shows the Lorentzian and Gaussian fits to the experimental data. The Integral breadth method (peak area/ peak position) was used to calculate FWHM of the peaks and grain size was calculated by Scherer’s formula given by: $d = \frac{k\lambda}{\beta \cos \theta}$, where, d is grain size in Å, k is a shape factor (in general taken as 0.9), λ is X Ray wavelength (taken as 1.54 Å for Cu-K α) [8-9]. During air annealing, diffusion of Zn is usually isotropic w.r.t orientation/direction of the crystal. The activation of diffusion of Zn along a, b and c axis is 131 kJ-mol⁻¹ and 116 kJ-mol⁻¹. Therefore, Zn is said to have equal probability for diffusion in all crystal directions [10]. Therefore, we chose to examine the variation of XRD peak along c-axis and observed its variation with annealing temperature.

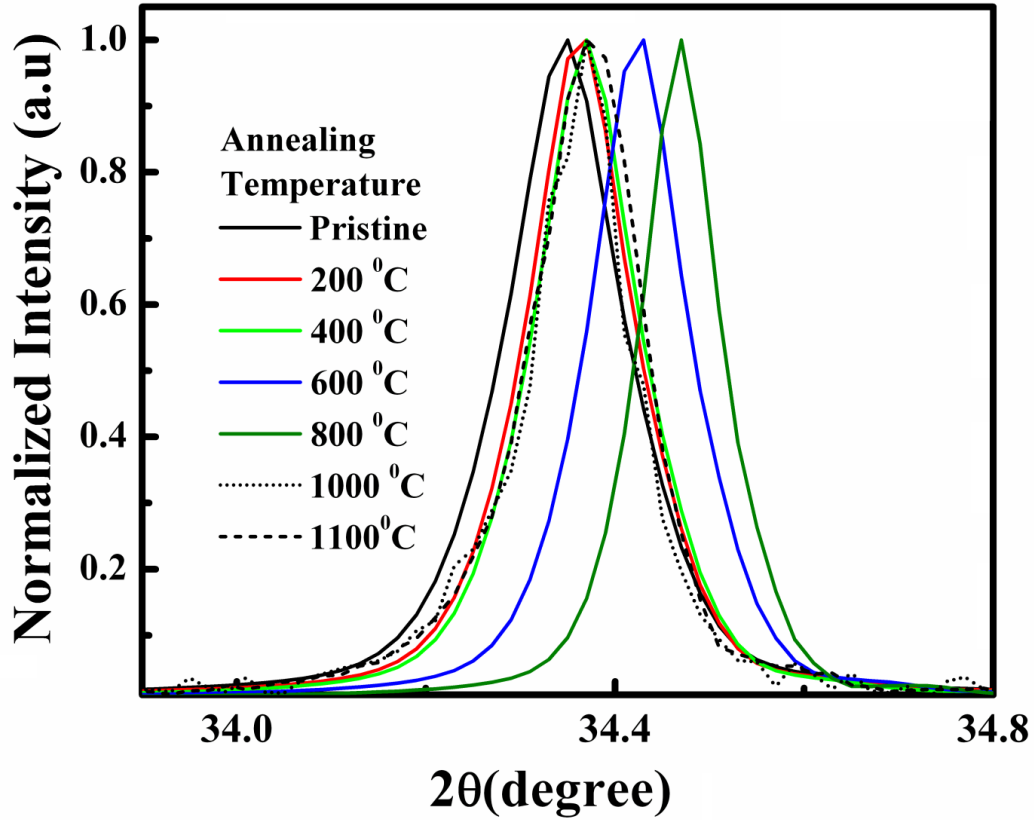


Figure 2.4: Shift of [002] peak with various CA temperatures.

Figure 2.4. show the variation of position of [002] peak of CA ZnO samples with different annealing temperatures. It is evident from figure 2.4 that with increase in temperature XRD peaks shift towards higher values of diffraction angle till 800°C after that relaxes to lower value for 1000°C and 1100°C CA samples. The shift towards higher and lower angles is because of high concentration of Zn defects i.e. Zn_i inside the ZnO grains. This in turn generates a uniform stress within the grains with tensile component parallel to c-axis. Analysis of diffraction formula ($2d \sin\theta = n\lambda$ or $\Delta d/d \tan\theta = -\Delta\theta$) indicates that strain is compressive in nature as $\Delta\theta$ is positive. The relaxation of peak towards lower angles at 1000°C and 1100°C signifies the lessening concentration of oxygen vacancies & showed a steady progress of compressive towards tensile stress.

Stress generated from diffusion of Zn_i along c-axis was calculated as:

$$\sigma = -453.6 * \left[\frac{c-c_0}{c_0} \right] \quad (2.1)$$

Where, $c_0 = 5.205 \times 10^{-10}m$ is stress free lattice constant [11].

The variation of the uniaxial stress has been plotted with different annealing temperature as shown in figure 2.5.

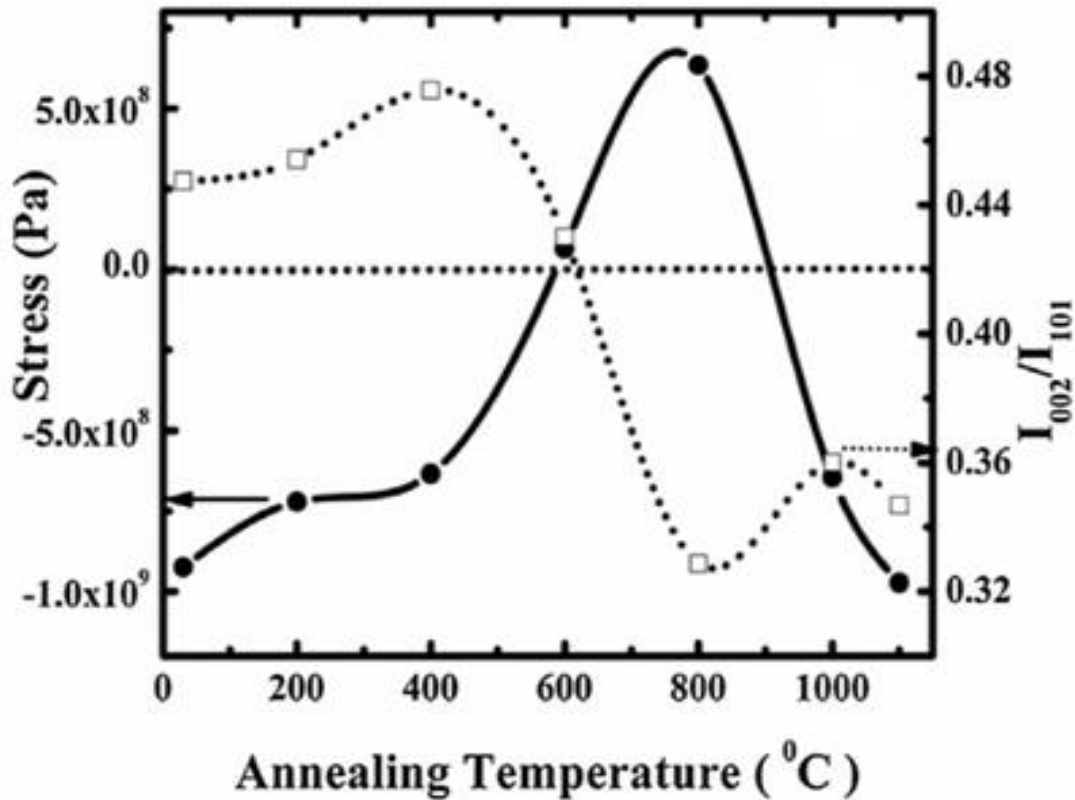


Figure 2.5: Variation of ratio of intensity of peak [002]/[101] and stress with annealing temperature.

It is clear from the graph that stress changes from compressive to tensile and strain increases at annealing till 800°C and decreases after that. The variation of concentration of Zn_i with annealing temperature was observed by analyzing intensity ratio of peak [002]/[101] in XRD spectra as its diffusion is isotropic, hence we can choose to observe diffusion in any direction. The dotted line in figure 2.5 shows the variation of intensity ratio of diffraction peak [002]/[101] versus annealing temperature. It is a generally accepted that size of grain increase with temperature because of agglomeration & coagulation of numerous tiny grains into bigger ones. We noticed an abrupt drop off in grain size for temperature > 800°C. The grain size and surface to volume ratio of grains (S_{GB}) versus temperature has been plotted in figure 2.6. The grain size was initially 67nm, then increased to 93nm at 800°C and then decreased to 65 nm at 1100°C.

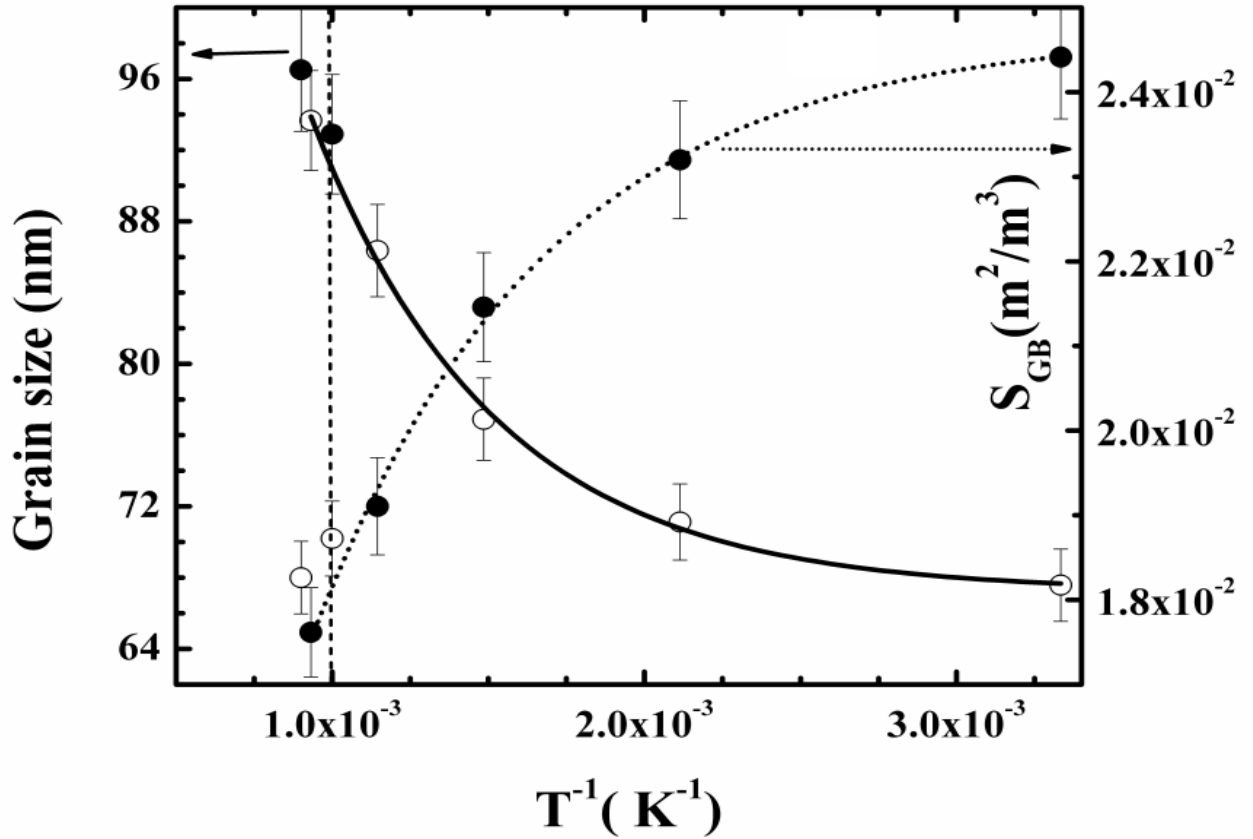


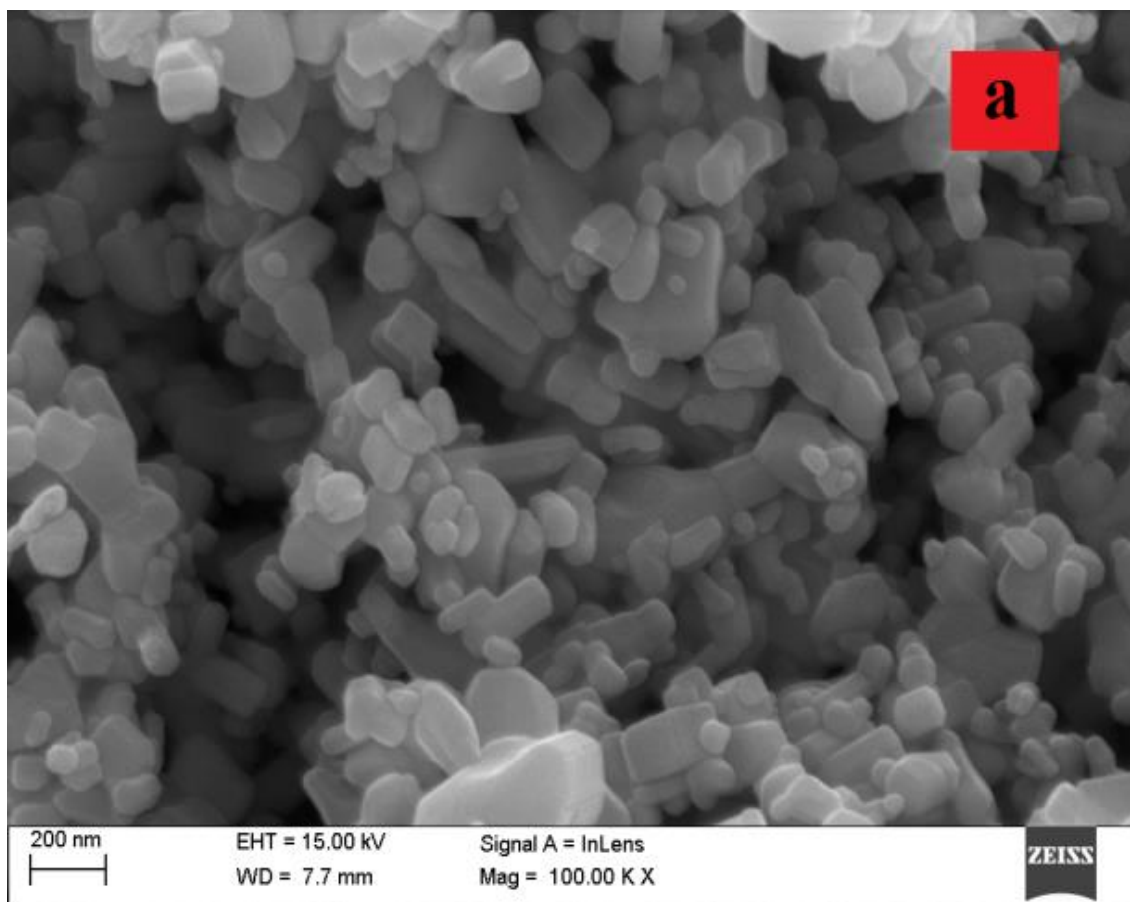
Figure 2.6: Grain size & S_{GB} of grains versus CA temperature.

Arrhenius equation $d = d_0 \exp\left(\frac{-Q}{kT}\right)$ was used to estimate the activation energy the fitting to grain size versus annealing temperature yielded $Q = 385 \text{ kJ}\cdot\text{mol}^{-1}$. This value of Q for grain growth is near to the diffusion barrier of Zn and O in ZnO annealed at heating rate $100^\circ\text{C}\cdot\text{min}^{-1}$ [12]. Rodolfo et al. has claimed that Q is strongly dependent on heating rate. Q was found to be 388, 254 and $280 \text{ kJ}\cdot\text{mol}^{-1}$ for heating rate of 50, 75 and $100^\circ\text{C}\cdot\text{min}^{-1}$ [13]. It substantiate that annealing leads to diffusion of Zn_i and Oxygens and hence redistributions of defects inside the crystal. The diffusion of defects during annealing takes place according to their migration barriers. Zn_i are fast diffusers and O defects are slow diffusers. The dominant growth of grain along c axis leads to deformation of the shape of nanoparticles. Surface to volume ratio of grains was calculated using $\frac{1.65}{\langle d \rangle}$ & figure 2.6 shows its variation with CA temperature [14]. With the rise in grain size surface to volume ratio decrease, which indicates large surface area. Hence, one

can conclude that smaller particles are rich in defects which reside on the surface as compared to bigger particles. Therefore, collectively from results of structural variations, development of stress along with increase in surface to volume ratio on CA signify that CA undoped ZnO nanoparticles are rich in surface defects.

2.3.2 Morphological studies of CA ZnO

The morphology of the annealed grains was investigated by FESEM images. Figure 2.7 shows the FESEM images of pristine and CA ZnO at 200 °C, 400 °C, 600°C, 800°C, 1000°C and 1100°C.



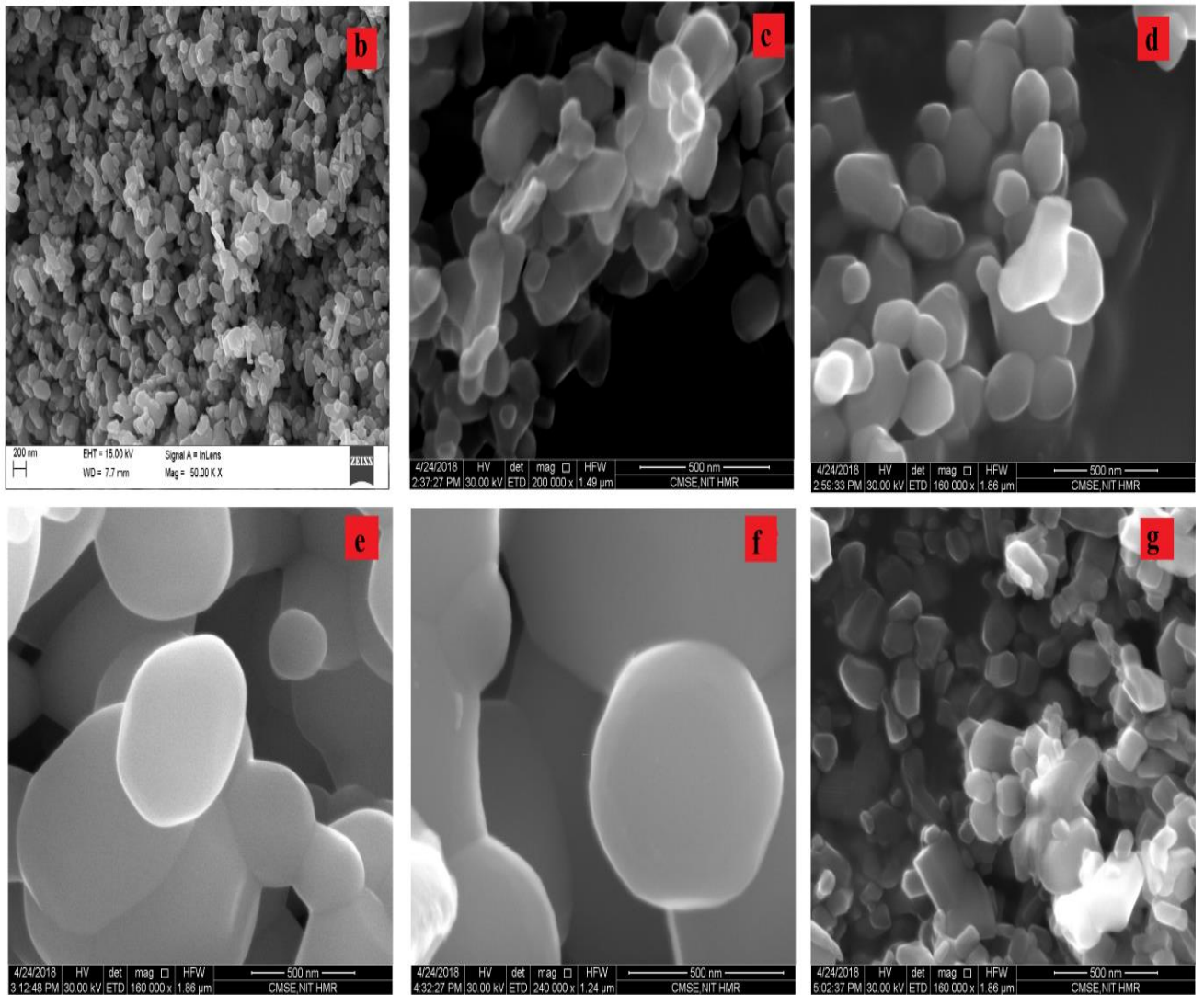


Figure 2.7: FESEM images (a) Pristine ZnO (b) CA ZnO annealed at 200°C (c) CA ZnO annealed at 400°C (d) CA ZnO annealed at 600°C (e) CA ZnO annealed at 800°C (f) CA ZnO annealed at 1000°C (g) CA ZnO annealed at 1100°C.

In the pristine sample the grains were of different shapes like cylindrical, spherical and hexagonal. With increase in CA temperatures shapes transformation took place and the shape of grains at CA temperature 600°C and 800°C became almost spherical in shape. It transforms to almost perfect spherical shape at 1000°C with the formation of grain boundaries at 1100°C. To explore the diffusion of intrinsic defects during annealing, diffusion equation was solved in spherical polar coordinates system.

2.3.3 Theoretical model for grain growth

To model the defect distributions in ZnO suppose a particle with radii “R”. The diffusion equation for surplus Zn_i within the grain is given as,

$$\nabla^2 C = \frac{1}{D} \frac{\partial C}{\partial t} \quad (2.2)$$

Where, C designates the “concentration” and D the “diffusion coefficient” of Zn_i .

In spherical polar coordinates equation 2.2 can be written as:

$$\frac{1}{r^2} \frac{\partial}{\partial r} \left(r^2 \frac{\partial C}{\partial r} \right) + \frac{1}{r^2 \sin \theta} \frac{\partial}{\partial \theta} \left(\sin \theta \frac{\partial C}{\partial \theta} \right) + \frac{1}{r^2 \sin^2 \theta} \frac{\partial^2 C}{\partial \phi^2} = \frac{1}{D} \frac{\partial C}{\partial t} \quad (2.3)$$

We presume isotropic radial diffusion of Zinc interstitial & confine calculation towards radial growth only. Spherical harmonic part of equation 2.3 plays a vital role in growth of nanowire and nanorods. Hence, above equation can be modified as

$$\frac{\partial^2 C}{\partial r^2} + \frac{2}{r} \frac{\partial C}{\partial r} = \frac{1}{D} \frac{\partial C}{\partial t} \quad (2.4)$$

The boundary conditions are “ $C(r,0) = C_0$ ” & “ $C(r,t) = C_s$ ”, Where, C_0 represents bulk concentration of Zn_i , C_s represents surface concentration of Zn_i . Solution of equation 2.4 yields,

$$C(r,t) = C_s + \frac{4R}{\pi r} (C_0 - C_s) \sum_{n=0}^{\infty} \left(\frac{1}{2n+1} \right) \sin \left\{ \frac{(2n+1)\pi r}{R} \right\} \exp \left\{ -D \left(\frac{2n+1}{R} \pi \right)^2 t \right\} \quad (2.5)$$

Where “ $n = 0, 1, 2, 3$ ”.....

Equation 2.5 then suggest if concentration of Zn_i at the surface and the core becomes equal i.e. $C_0 = C_s$ then “ $C(r,t) = C_s$ ”, means particle will not grow further. Meaning thereby whenever the chemical balance is sustained by CA in dissimilar environment viz O, Zn, H or N, surface

defects will be tailored but grain size remains unaffected. For this reason, one can conclude that size of grain increases because formation of new layer of oxidized Zn_i on pristine grain, further, keep on the formation of a “new oxidized layer” on outer surface of the first layer and so on. Hence size of the grain increases monotonically with temperature. This growth continues till Zn_i diffuses throughout the newly formed oxidized layer. Once the diffusion is stopped & annealing is continued, grains densification starts and newly oxidized layer detaches from grains. This elucidate X-Ray diffraction results which suggests the reduction in stress & smaller grain size as that of pristine grain after annealing at 1000°C and 1100°C. Differentiating equation (2.5) gives radial concentration gradient in newly formed layer of ZnO.

$$\left(\frac{\partial C}{\partial r}\right)_{r=R'} = -\frac{4}{R'}(C_0 - C_s) \sum_{n=0}^{\infty} \exp\left\{-D\left(\frac{2n+1}{R}\pi\right)^2 t\right\} \quad (2.6)$$

“Taking into account the mass balance of Zn_i crossing the oxidized surface layer and assuming thickness (x) of new layer smaller than grain size (x << R’)” it is written as:

$$x^2 = 2\left(\frac{2R'}{\pi}\right)^2 \left(\frac{C_0 - C_s}{\sigma}\right) \sum_{n=0}^{\infty} \frac{1}{(2n+1)^2} \left[1 - \exp\left\{-D\left(\frac{2n+1}{R}\pi\right)^2 t\right\}\right] \quad (2.7)$$

Where $[x = R'^2 - R^2]$, “R’” corresponds to radii of new formed layer. “ $\sigma = \rho_s (M_{Zn}/M_{ZnO})$ ”, here, ρ_s , M_{Zn} , and M_{ZnO} represent density of ZnO at surface, atomic weight of Zn and molecular weight of ZnO respectively. For the case of large annealing time ($t \rightarrow \infty$) and maximum oxidized layer thickness ($x \rightarrow x_m$) equation 2.7 modifies to

$$-\ln\left[1 - \left(\frac{x}{x_m}\right)^2\right] - \ln\frac{\pi^2}{8} = D\left(\frac{\pi}{R}\right)^2 t \quad (2.8)$$

D depend on annealing temperature as $D = D_o \exp\left(-\frac{Q}{kT}\right)$. Figure 2.8 shows the plot of $-l$

$n \left[1 - \left(\frac{x}{x_m} \right)^2 \right]$ with inverse of annealing temperature.

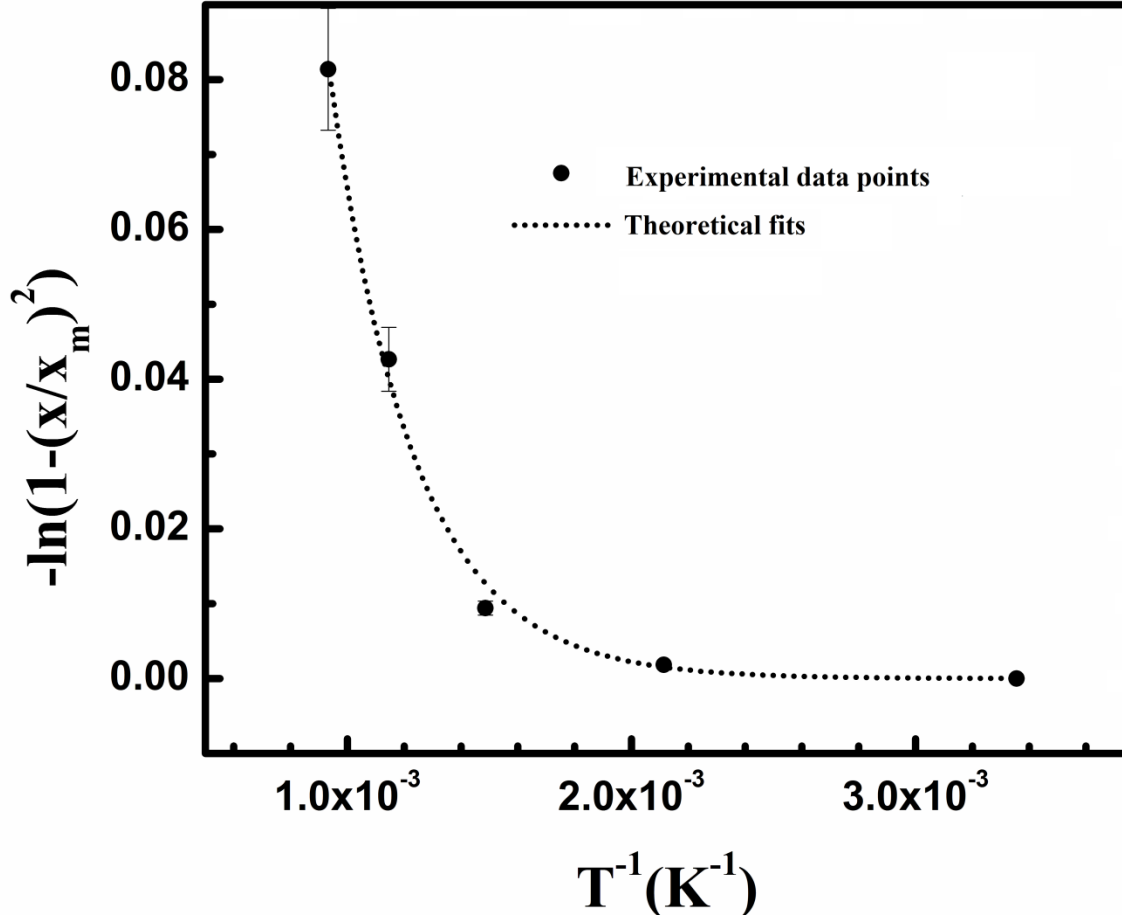


Figure 2.8: Variation of $-l n \left[1 - \left(\frac{x}{x_m} \right)^2 \right]$ with inverse of annealing temperature (CA).

The theoretical fit of equation 2.8 was then fitted to the experimental result gives D_o of order of $10^{-18} m^2 sec^{-1}$. It is in agreement to DFT calculations when combined with climbing image-nudged elastic band method of diffusion of Zn_i and V_o [15]. Based on the theoretical and experimental results the schematic of distribution of defects in CA is shown in figure 2.9.

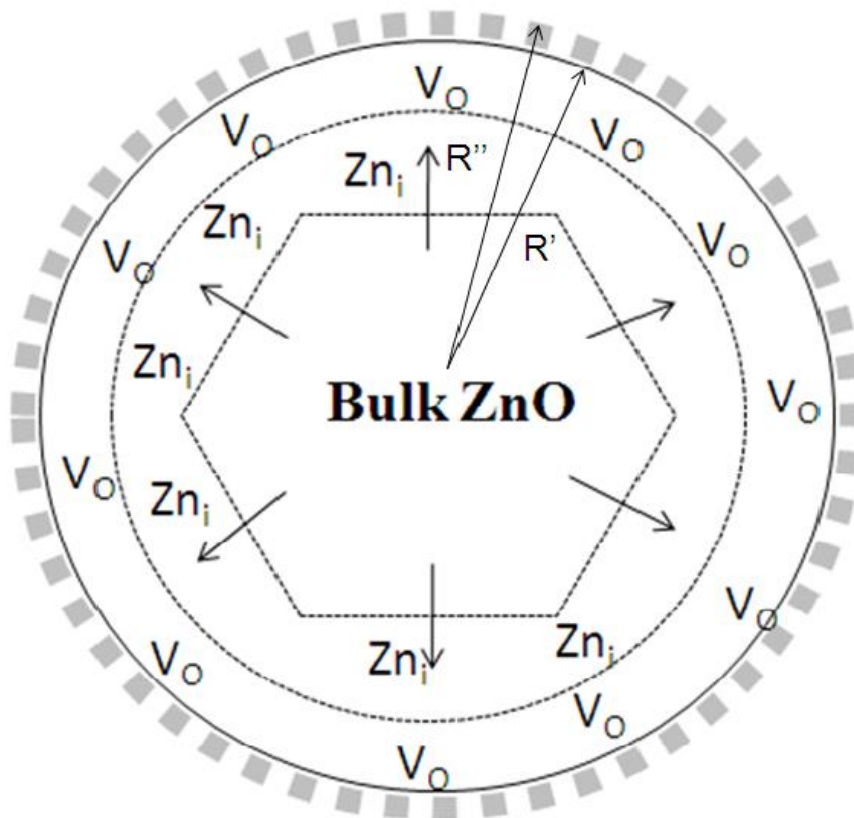


Figure 2.9: Schematic of grain growth model and defects distribution within Conventional annealed ZnO nanoparticles.

The Zn_i on the surface reacts with oxygen in the air atmosphere and form a layer of ZnO as shown by shaded grey region in the figure 2.9. When at high annealing temperature the concentration of Zn_i on the surface becomes equivalent to the concentration at core, the particle growth is inhibited and densification start taking place. When the annealing temperature is further increased the grain sheds its surface layer and breaks down to smaller grain.

2.3.4 X Ray diffraction studies of MSA ZnO nanoparticles

Figure 2.10 shows the XRD pattern for multistep annealed ZnO nanoparticles. After removing the instrumental broadening all the peaks were analyzed individually for calculations.

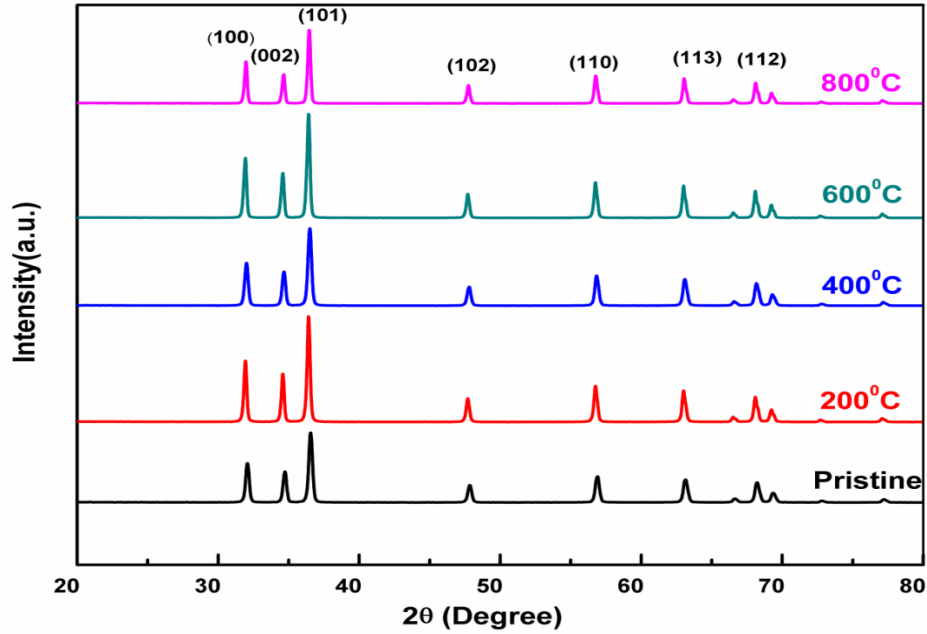


Figure 2.10: XRD pattern of MSA ZnO nanoparticles at different temperatures.

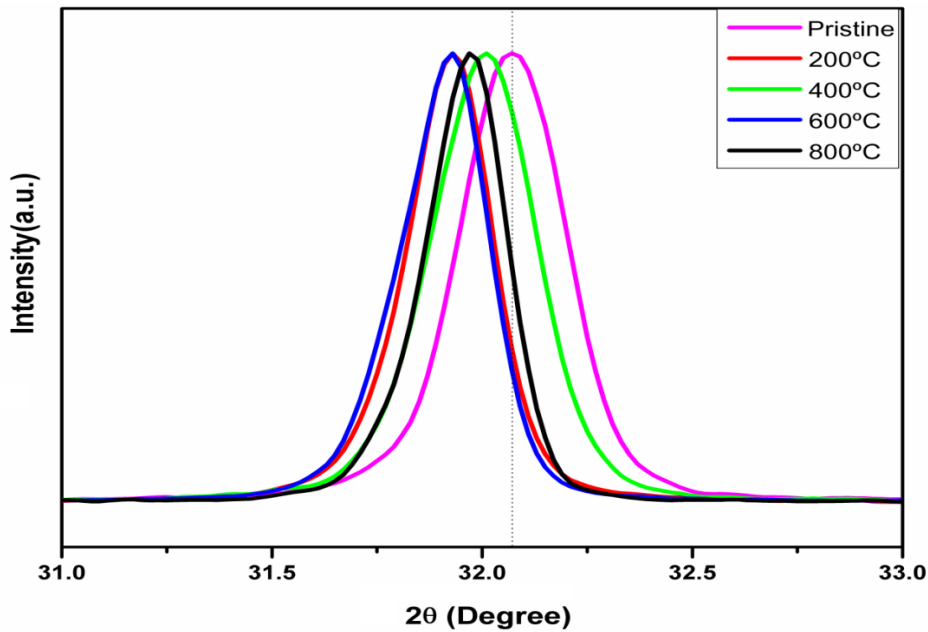


Figure 2.11: Shift of [002] peak with various Multistep annealing temperatures.

The peak [002] shift toward lower 2θ values w.r.t pristine ZnO is shown in figure 2.11. The shift towards lower θ implies the existence of tensile stress in the MSA samples. The variation of [002] plane in MSA seems very different from CA. As the grain growth mechanism and defect distributions are different in both the cases the stress distribution in the grains will also be very

different. To see the variation of stress we calculated the uniaxial stress along c axis as shown in figure 2.12 using equation 2.1. The trend of variation of stress was oscillatory in nature with MSA temperatures. The intensity of [002]/ [101] peak was plotted to see the diffusion of Zn_i within the grains due to MSA. It was found that the variation of diffusion of Zn_i was almost same as that in case of CA with respect to figure. 2.5.

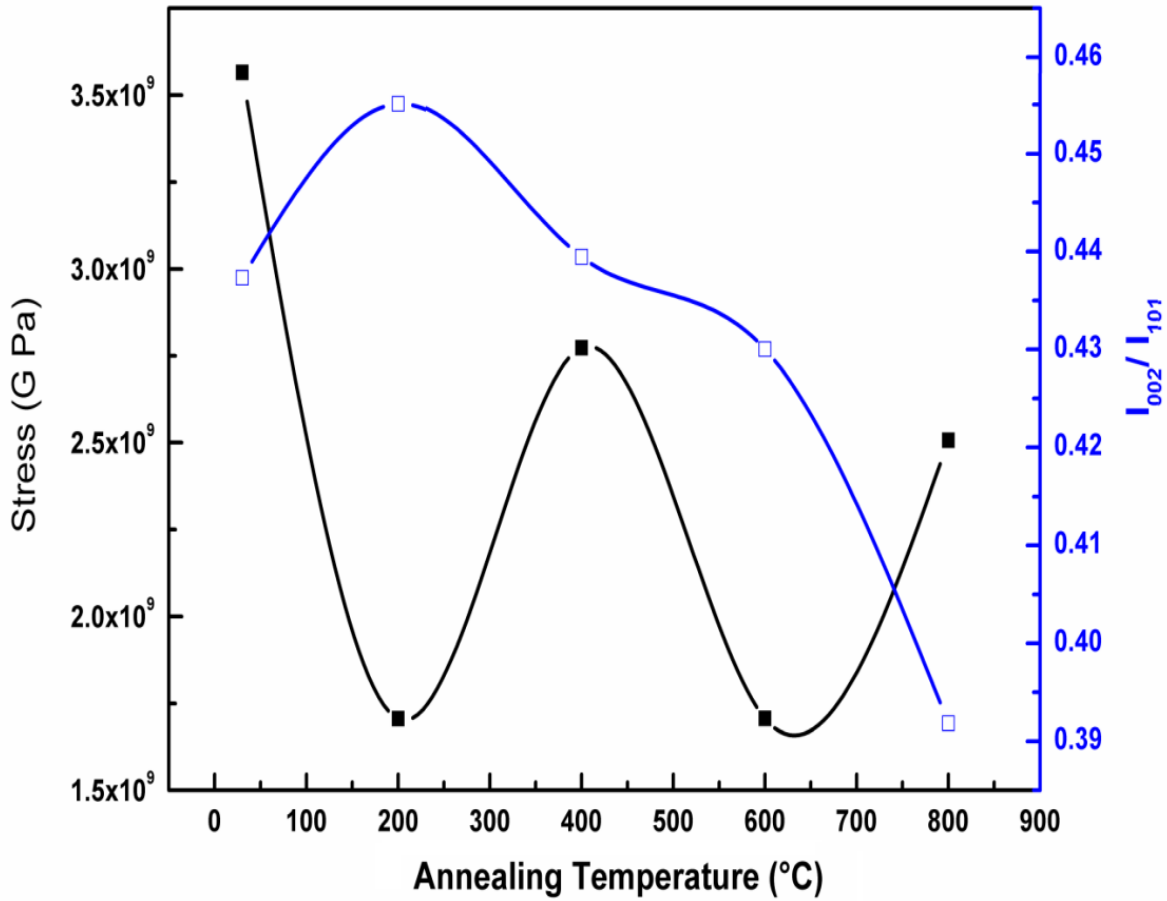


Figure 2.12: Variation of Stress and intensity ratio of peak [002]/[101] versus annealing temperature of MSA.

The kinetic equation for MSA which involves both thermal and temporal evolutions together i.e. includes the concurrent effect of time & temperature is given in equation 2.9:

$$d = d_o \exp\left\{\ln(t^n) + \frac{Q}{R\left(\frac{1}{303} - \frac{1}{T}\right)}\right\} \quad (2.9)$$

Where; d is average grain size, d_0 = initial grain size, Q = activation energy of defects, T = annealing temperature, t = annealing time.

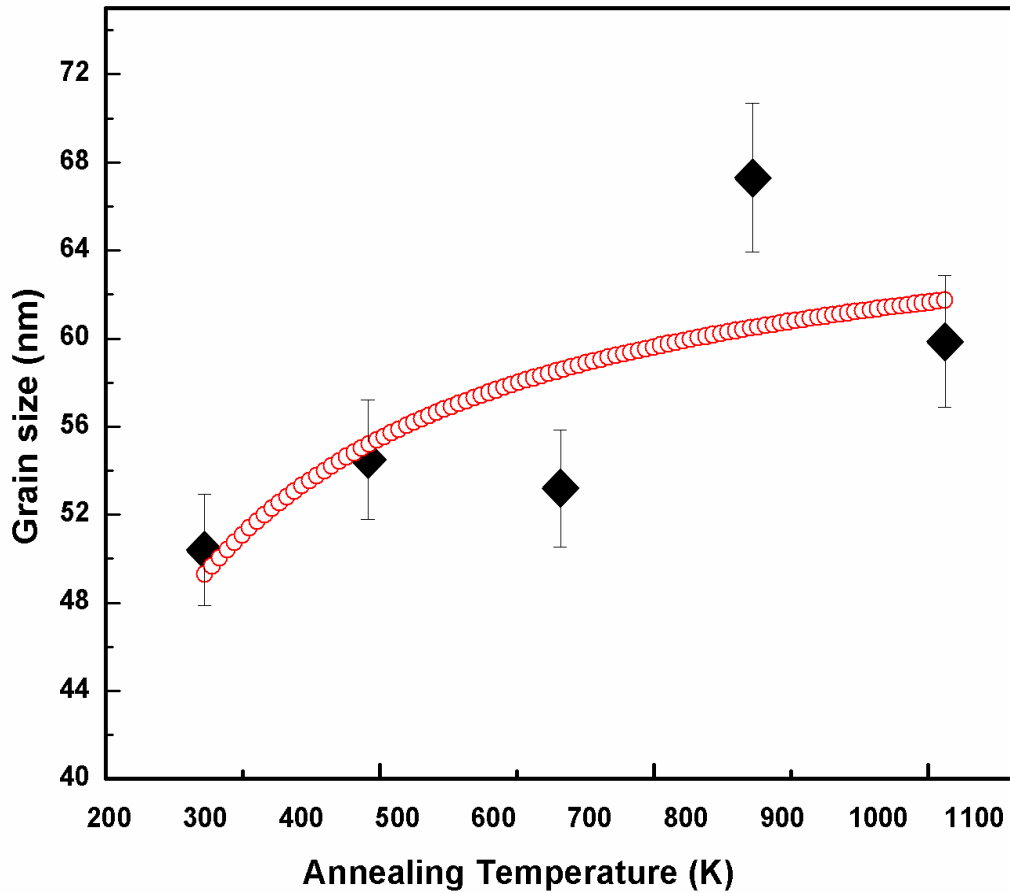


Figure 2.13: Grain size of Multistep annealed ZnO versus annealing temperature fitted with kinetics equation.

The equation 2.9 when fitted with experimental grain size was found to be in good agreement with theoretical fundamentals proposed for MSA as shown in figure 2.13. This implies that grain growth depended on annealing time and annealing temperature both simultaneously.

2.3.5 Morphological studies of MSA ZnO

To see the distribution of defects and shape transformations of nanoparticles FESEM was performed.

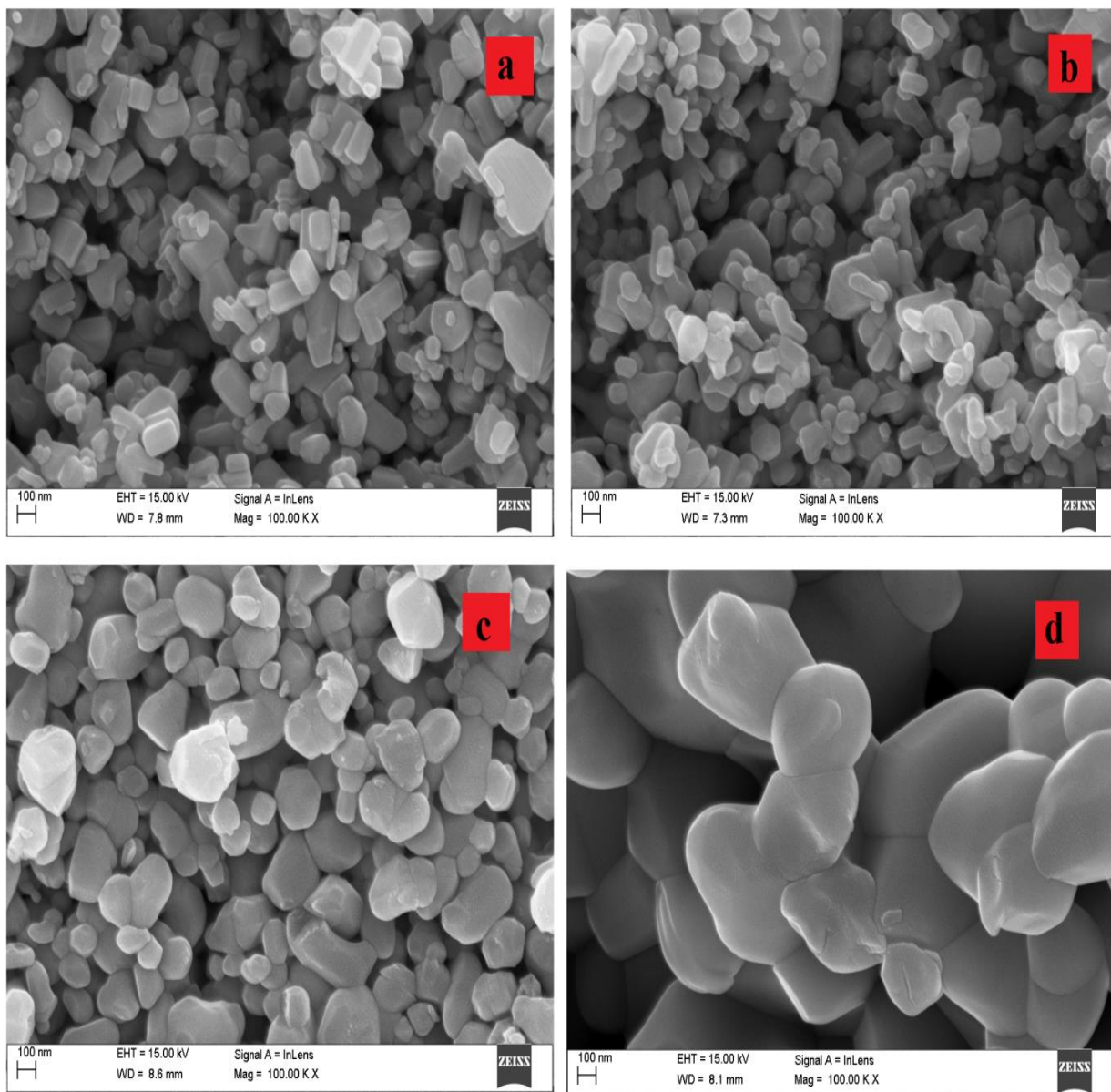
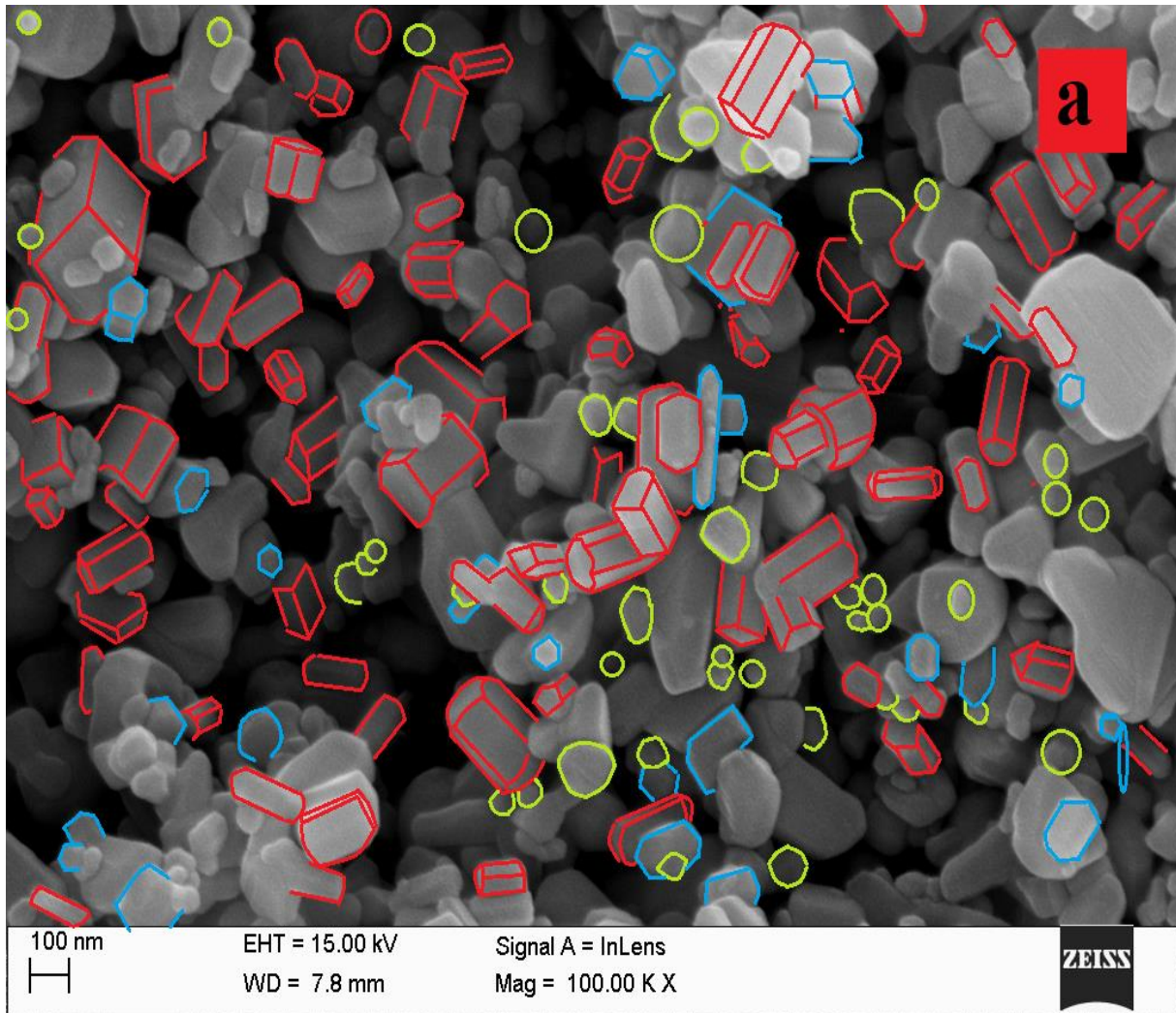
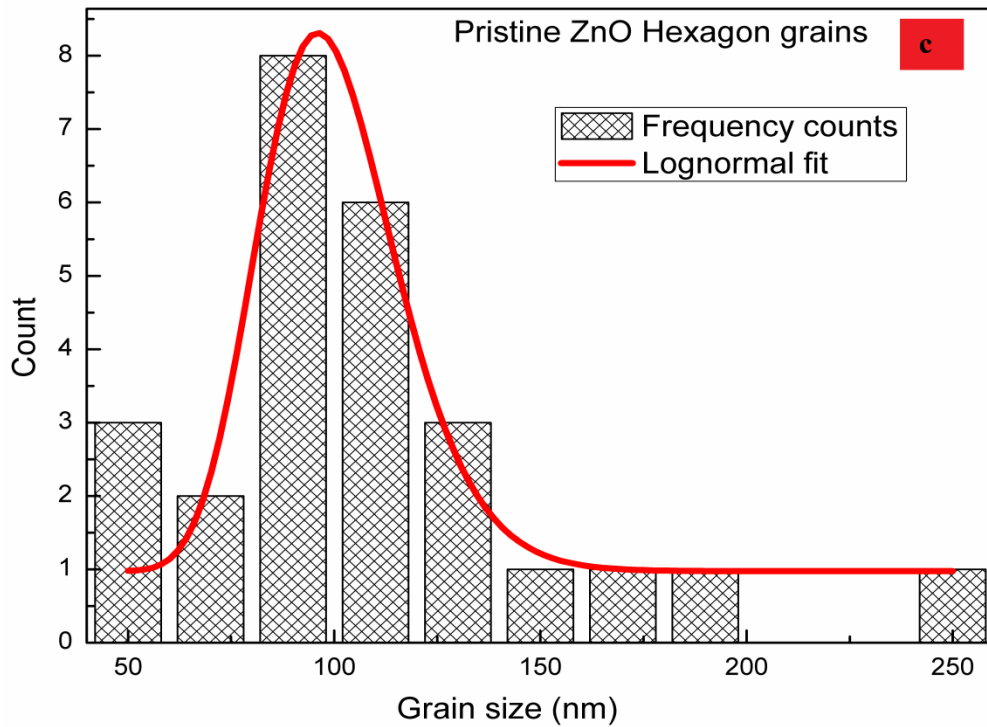
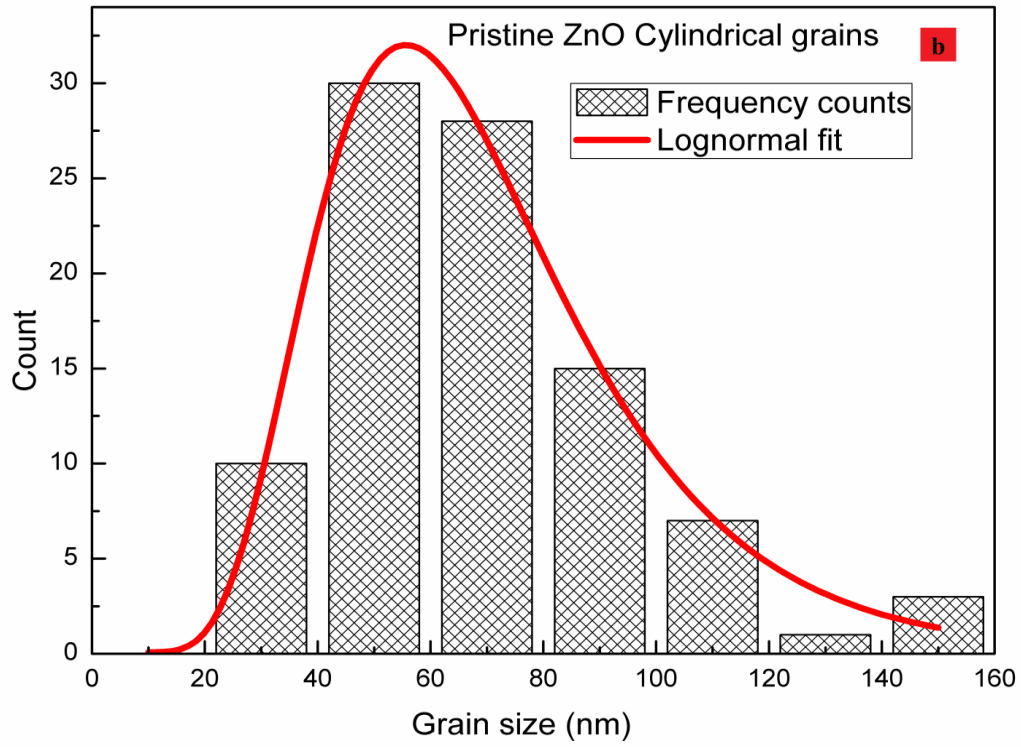


Figure 2.14: FESEM image of (a) Pristine ZnO nanoparticles, (b) MSA ZnO at 400°C, (c) MSA ZnO at 600°C, (d) MSA ZnO at 800°C.

Figure 2.14 shows the morphology of ZnO nanoparticles, pristine and annealed at 400°C, 600°C, and 800°C. It is evident from the images that pristine ZnO consist of different shapes like cylindrical, hexagons and spherical shaped grains.



The various shapes of pristine ZnO were separately fitted with lognormal fits as shown in figure 2.16 (b, c, d). It was observed that the 52% structures were cylindrical shaped grains with diameter 50nm. The spherical shaped grains were 33% with diameter 55nm and only 26% left grains were hexagon shaped with diameter 80nm. .



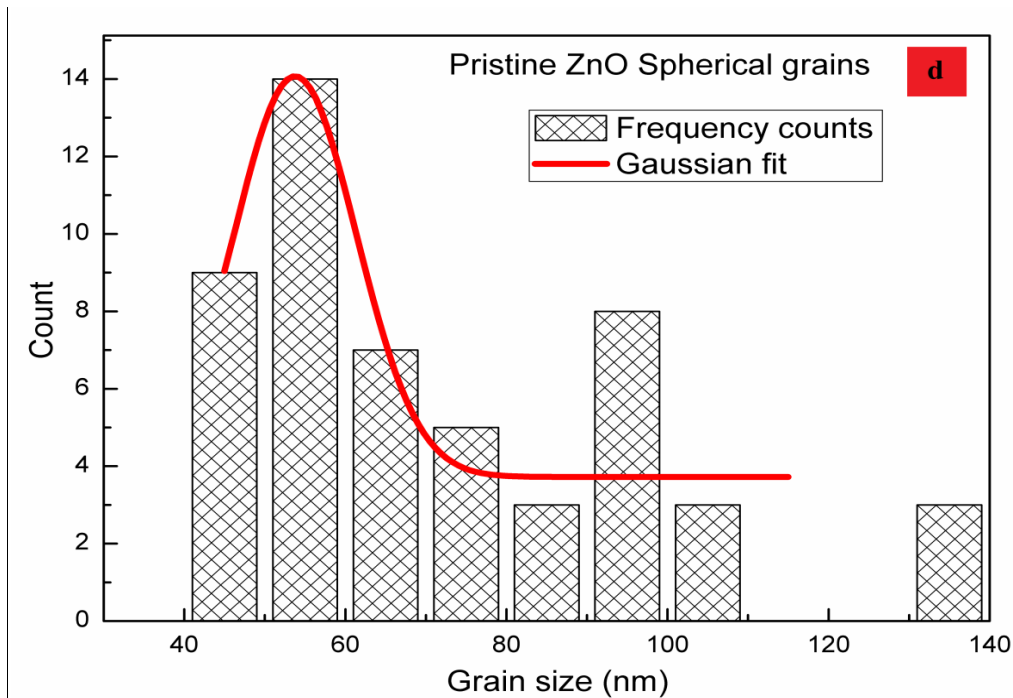


Figure 2.15: (a) FESEM image of Pristine ZnO highlighting grain with colored marker, (b) Pristine ZnO cylindrical grains fitted with lognormal fit, (c) Pristine ZnO hexagonal grains fitted with lognormal fit , (d) Pristine ZnO spherical shaped grains with Gaussian fit.

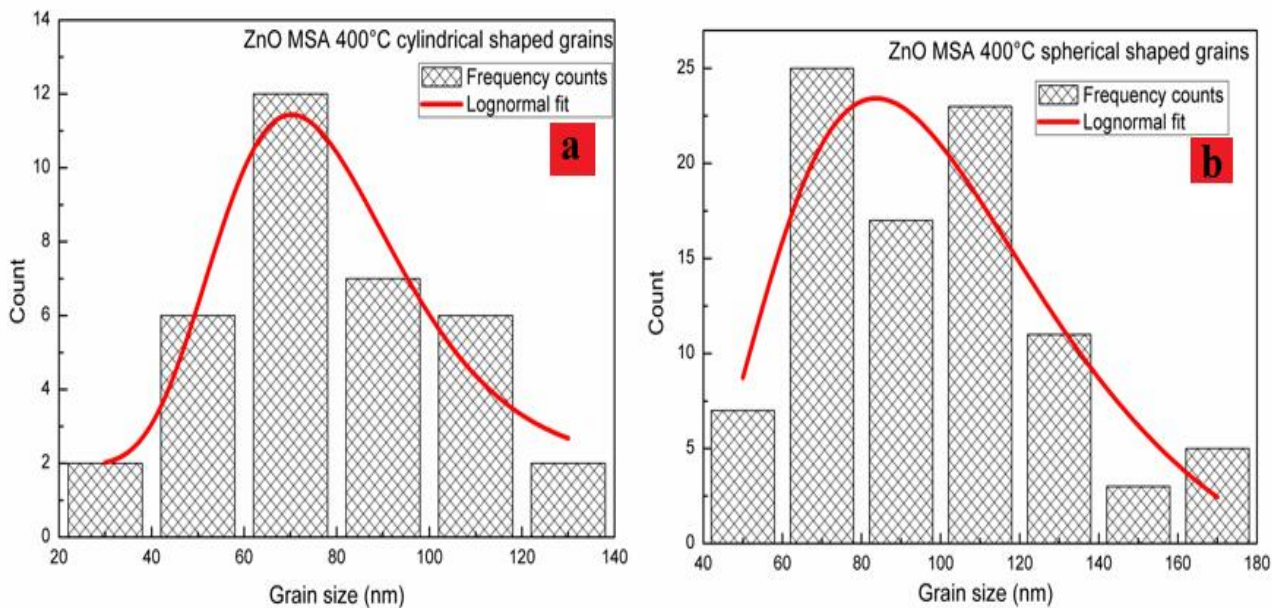
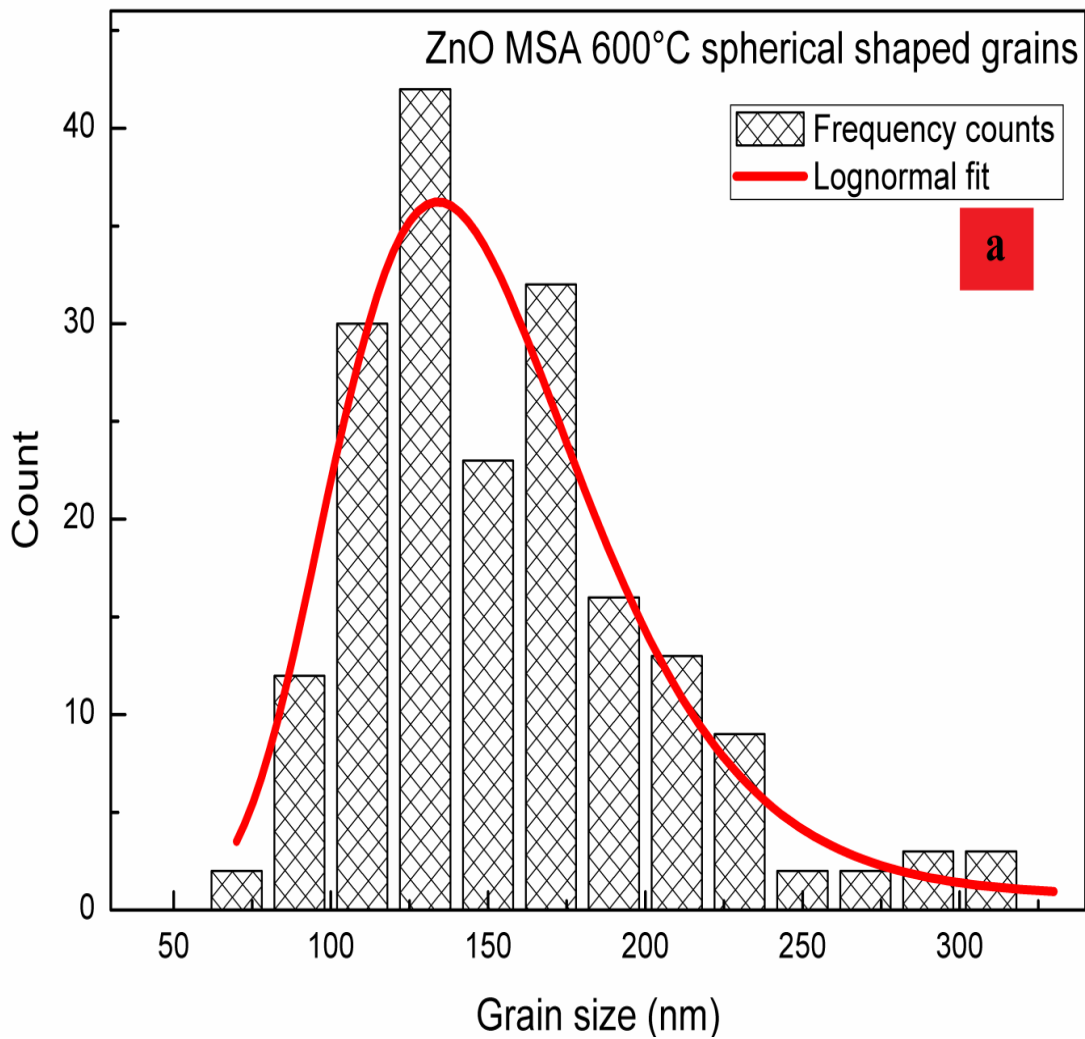


Figure 2.16: The lognormal and Gaussian fits of (a) MSA at 400°C ZnO cylindrical shaped grains, (b) MSA at 400°C ZnO spherical shaped grains

In figure 2.16 MSA temperature 400°C, cylindrical grains reduced to 27% with increased diameter of 75nm. The spherical shaped grains increased to 72% with diameter 70nm and 110nm but hexagon shaped grains completely vanished. The diameters of cylindrical shaped grains increased with annealing temperature but length did not increase. The length (l)/radii(r) was initially greater than 1 but later on reaching temperatures of 600°C this l/r was approximately 1. Meaning there by that rods were getting thicker and thicker, and when the thickness was approximately equal to length of rods they transformed into spherical shapes. At 600°C the cylindrical shaped grains and hexagons vanished and spherical shapes persisted as shown in figure 2.17 (a).



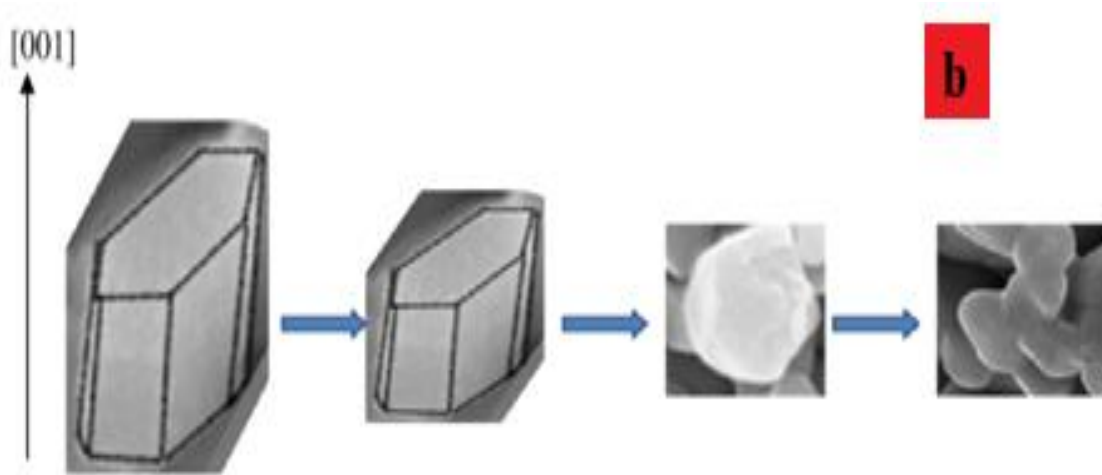


Figure 2.17: (a) The lognormal fit of MSA at 600°C ZnO spherical shaped grain, (b) The evolutions of spherical shaped grains from cylindrical ones.

At 800°C the grains continued to be spherical and grain boundary formation took place. Hence figure 2.17 (b) reveals that most of the particles were cylindrical in shape initially and then transformed to spheres at higher temperature, diffusion equation was solved in cylindrical coordinates. Diffusion equation for MSA can be written as same as in case of CA i.e.

$$\nabla^2 C = \left(\frac{1}{D}\right) \left(\frac{\partial C}{\partial t}\right) \quad (2.10)$$

$$\frac{\partial C}{\partial t} = D \nabla^2 C \quad (2.11)$$

When diffusion constant is not isotropic then it is convenient to break equation 2.11 in flux formulation i.e.

$$\frac{\partial C}{\partial t} = \left(\frac{\partial}{\partial x_i}\right) \left(D_{ij}\right) \left(\frac{\partial C}{\partial x_j}\right) \quad (2.12)$$

Where, $(D_{ij})\left(\frac{\partial c}{\partial x_j}\right)$ indicate flux it is important to mention here that this case is due to concentration gradient of defects along j direction. (j = r, θ , φ). (D_{ij}) is now diffusion tensor and can be written as

$$D_{ij} = \begin{pmatrix} D_{rr} & D_{r\theta} & D_{rz} \\ D_{\theta r} & D_{\theta\theta} & D_{\theta z} \\ D_{\theta r} & D_{\theta z} & D_{zz} \end{pmatrix} \quad (2.13)$$

Or
$$\frac{\partial}{\partial x_j} = \left(\frac{\partial}{\partial r} \hat{r}, \frac{\partial}{r\partial\theta} \hat{\theta}, \frac{\partial}{\partial z} \hat{z} \right) \quad (2.14)$$

For ease of calculation we assumed diffusion along r direction only and neglecting off diagonal terms and anti symmetric terms (which are relevant at higher temperatures \approx melting temperature. The diffusion constant breaks like

$$D_{ij} = (D_{\text{parallel}} - D_{\text{perpendicular}}) b_i b_j + D_{\text{perpendicular}} \delta_{ij} \quad (2.15)$$

Where, $b_i b_j$ represent driving forces; along perpendicular and parallel axis. Here parallel means driving force along c axis and perpendicular means driving force along a,b axis. Driving force may be chemical potential difference or some external perturbations like electric field, magnetic field or defects in potential.

We only consider the chemical potential difference in defects in concentrations in bulk of grains and at surface of grains. Hence, considering along one direction we get:

$$\frac{\partial c}{\partial t} = \left(\frac{1}{r} \right) \frac{\partial}{\partial t} \left(r D \frac{\partial c}{\partial r} \right) \quad (2.16)$$

The solution of this equation contains Bessel's function hence defects should be distributed oscillatory in MSA.

2.3.6 Raman Studies of CA and MSA ZnO

Raman Spectroscopy is a common practice based of the inelastic scattering on monochromatic light within the sample accompanied by generation and annihilation of elementary excitations i.e. lattice vibrations (phonons). Raman spectroscopy is used to study the

lattice dynamics of the sample and therefore imparts information about the structural properties of the system.

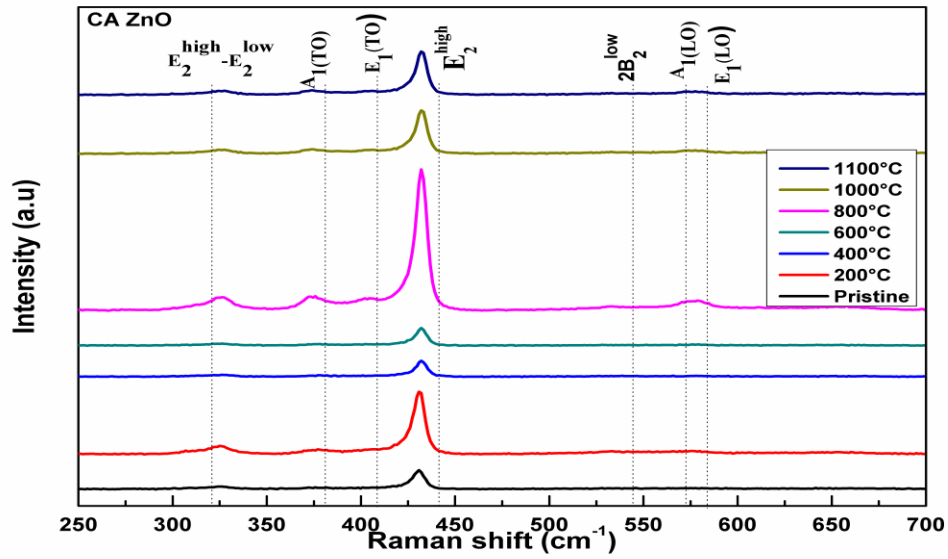


Figure 2.18: Raman spectra for CA ZnO samples.

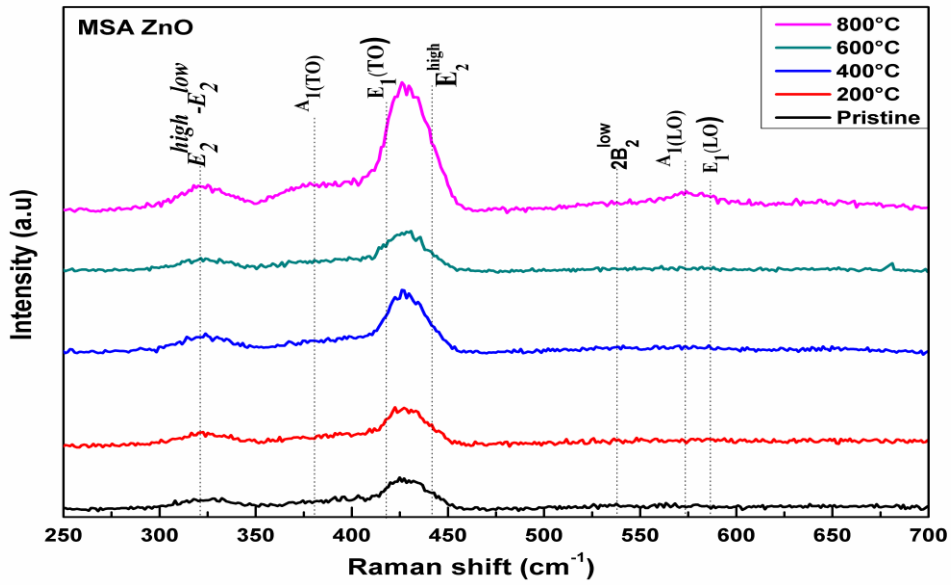


Figure 2.19: Raman spectra for MSA ZnO samples.

Figure 2.18 & figure 2.19 shows the Raman spectra for CA and MSA annealed samples. Hexagonal wurtzite type lattice structure belonging to the space group C_{6v}^4 ($P6_3mc$) implies basic unit of four atoms in unit cell. The number of phonon modes are $3n = 12$, being 9 optical modes (three longitudinal (LO) and six transverse, TO) and 3 acoustic modes (1 longitudinal (LA) and 2 transverse (TA)). At Γ point of the Brillouin zone the optical phonons have following irreducible representations: $\Gamma_{opt} = A_1 + E_1 + 2E_2 + 2B_1$ [16]. Where, B_1 modes are silent i.e. IR and Raman inactive and E_2 vibrations are only Raman active (non polar). The nonpolar phonon modes with symmetry E_2 have two frequencies: E_2^{high} (437cm^{-1}) associated with motion of O atoms and E_2^{low} associated with Zn sub lattice. E_2^{high} phonon mode is distinctive Raman mode of ZnO. The atoms move perpendicular to c-axis and in each sub lattice and neighboring ion move to opposite to each other. Hence, displacement of ions sums to zero i.e. no net polarization. For these reason two modes are defined as non polar modes. Further, Raman and IR active phonons A_1 and E_1 are polar.

On contrary to this A_1 and E_1 phonon that are oxygen dominated are polar modes. The atoms move parallel or perpendicular to c-axis for A_1 and E_1 symmetry in such a way that displacement of Zn atom with respect to O atoms induces net polarization. As a consequence A_1 and E_1 splits into longitudinal optical (LO) and transverse optical (TO). The associated Raman peaks become four i.e. $A_1(\text{TO})$ (380cm^{-1}), $A_1(\text{LO})$ (574cm^{-1}), $E_1(\text{TO})$ (407cm^{-1}), and $E_1(\text{LO})$ (583cm^{-1}). The change in line shape broadening and a little shift to higher and lower wave number depicts the compressive and tensile strain & electron phonon interaction as a result of annealing. The electron-phonon interactions are important and play a significant role in Raman scattering. Two types on interactions must be considered inevitably, the deformation potential interaction, due to the modulation of crystal periodic potential by relative atomic displacements of the phonons and the Frohlich interaction. The Frohlich interactions are because of the macroscopic electric field generated by relative displacement of oppositely charged atoms within the unit cell which concerns only the LO phonons. Therefore the two LO phonon modes i.e. $A_1(\text{LO})$ and $E_1(\text{LO})$ have very close wave numbers (574cm^{-1} and 583cm^{-1}). These peaks are often merged in a single band called LO band. Their low intensity is attributed to electron-phonon coupling.

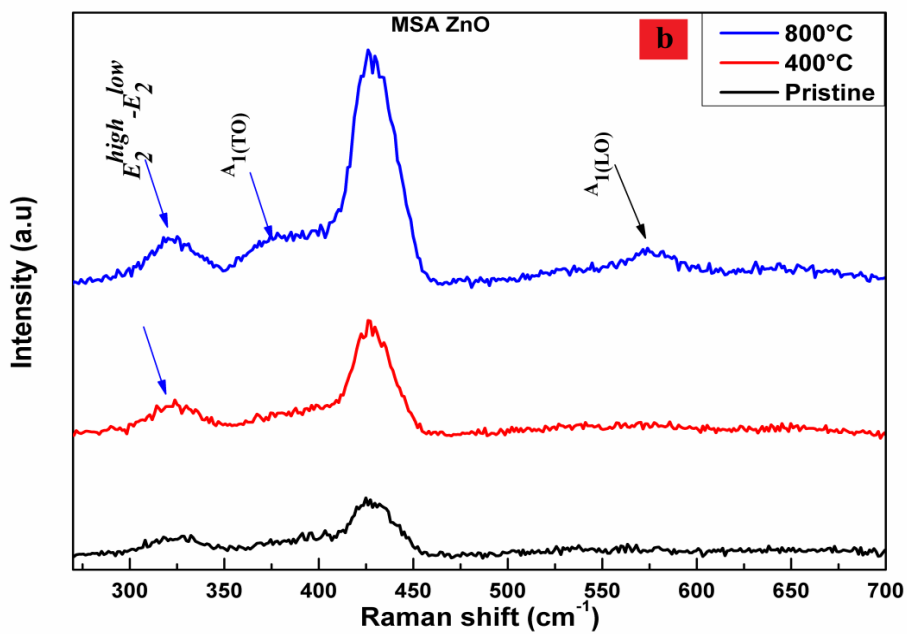
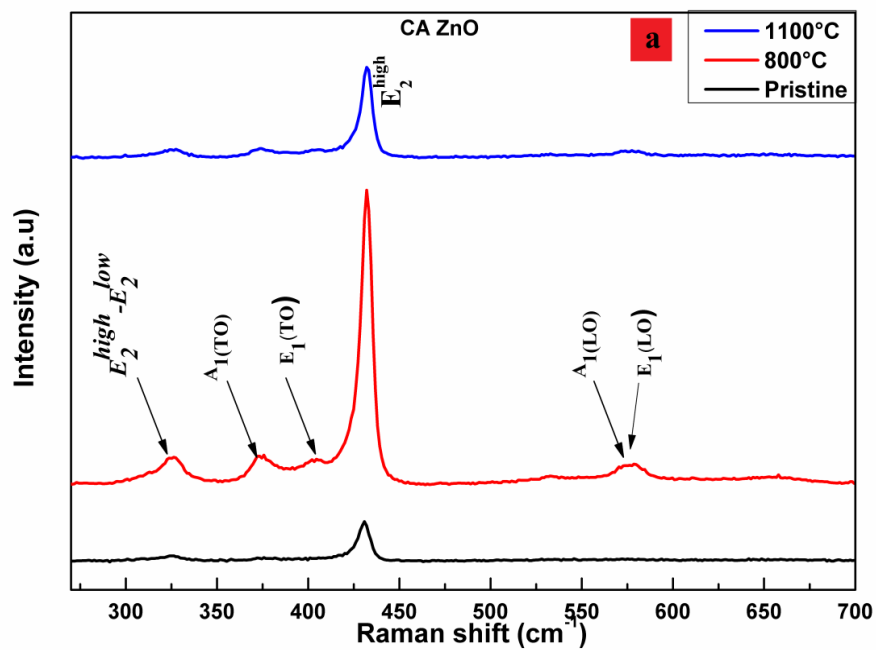


Figure 2.20: (a) Raman spectra for CA ZnO samples before and after the breaking of grains (Pristine, 800°C and 1100°C), (b) Raman spectra for MSA ZnO samples before and after the breaking of grains (Pristine, 400°C and 800°C).

Figure 2.20 (a) and (b) shows the Raman spectra for CA and MSA ZnO pristine, 800°C and 1100°C. The appearance of low intensity of LO band in CA and MSA signifies the existence of V_o in the sample due to high temperature annealing.

2.4 Conclusion

Two different annealing techniques CA and MSA has been discussed in this Chapter. These techniques differ in the mechanisms and hence the respective grain growth and micro structural evolution are very different to each other. The grain growth in both these cases takes place differently as in case of CA the grain growth is attributed to layer by layer model of the nanoparticles. The shapes of nanoparticles in CA was almost spherical where as in case of MSA it transformed from cylindrical to spherical with annealing temperature. The diffusion equation has been solved in spherical polar coordinates in case of CA where as it is solved in cylindrical polar coordinates for MSA to predict the diffusion of defects due to annealing. It was found that Zn_i being fast diffuser migrate toward surface and V_o remain somewhere in the core of the grain in case of CA whereas in case of MSA the Zn_i moves towards surface but remains in the core as well. The core Zn_i interacts with the V_o and form complexes. The defects reside differently in grains and hence also lead to different structural properties also studied by Raman Spectroscopy.

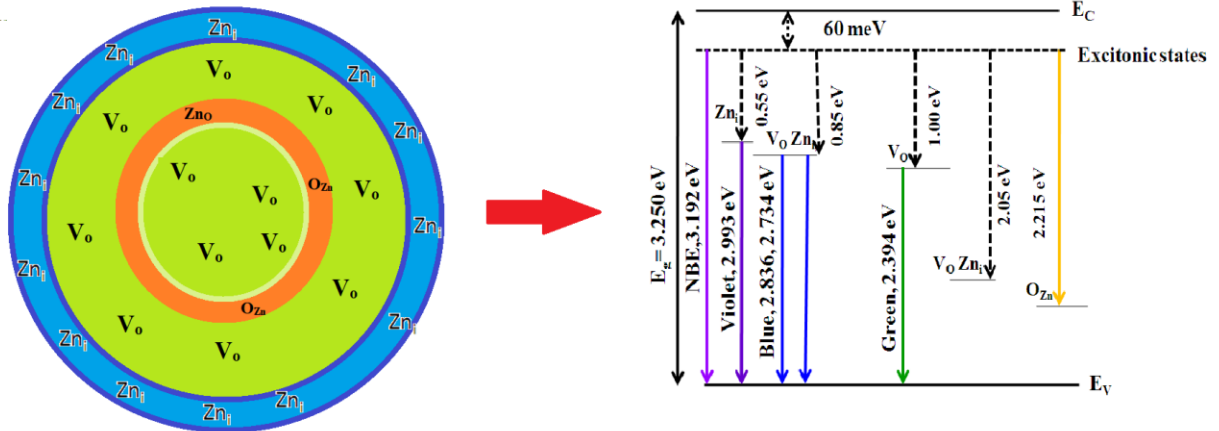
REFERENCES

1. N Kondal and S. K Tiwari, "Selectively enhanced oxygen vacancies in undoped polycrystalline ZnO as a consequence of Multi-Step Sintering", *Ceramic International*, vol. 43, no. 13, pp. 10347–10352, 2017.
2. J. Wang and L. L. Shaw, "*Morphology-enhanced low-temperature sintering of nanocrystalline hydroxyapatite*", *Advanced Materials*, vol. 19, no. 17, pp. 2364–2369, 2007.
3. B. N. Kim, K. Hiraga, and K. Morita, "*Kinetics of normal grain growth depending on the size distribution of small grains*", *Materials transactions*, vol. 44, no. 11, pp. 2239–2244, 2003.
4. J. Wang and L. Gao, "*Photoluminescence properties of nanocrystalline ZnO ceramics prepared by pressureless sintering and spark plasma sintering*", *Journal of the American Ceramic Society*, vol. 88, no. 6, pp. 1637–1639, 2005.
5. B. B. Straumal, A. A. Mazilkin, S. G. Protasova, A. A. Myatiev, P. B. Straumal, G. Schütz, P. A. Van Aken, E. Goering, and B. Baretzky, "*Magnetization study of nanograined pure and Mn-doped ZnO films: Formation of a ferromagnetic grain-boundary foam*", *Physical Review B*, vol. 79, no. 20, pp. 1–6, 2009.
6. K. Ramakanth, *Basics of X-ray Diffraction and its Application* (I.K. International Publishing House Pvt. Ltd.: New Delhi: 2007).
7. W. I. F. David and J. C. Matthewman, "*Profile refinement of powder diffraction patterns using the Voigt function*", *Journal of applied crystallography*, vol. 18, no. 6, pp. 461–466, 1985.
8. B. D. Cullity, "*Elements of X-ray Diffraction*", 2nd Ed, Addison-Wesley Publishing Company Inc. (1978).
9. H. H. Tian and M. Atzmon, "*Comparison of X-ray analysis methods used to determine the grain size and strain in nanocrystalline materials*", *Philosophical magazine A*, vol. 79, no. 8, pp. 1769–1786, 1999.
10. P. Erhart and K. Albe, "*Diffusion of zinc vacancies and interstitials in zinc oxide*", *Appl. Applied Physics Letters*, vol. 88, no. 20, pp. 23–25, 2006.

11. Z. B. Fang, Z. J. Yan, Y. S. Tan, X. Q. Liu, and Y. Y. Wang, “*Influence of post-annealing treatment on the structure properties of ZnO films*”, *Applied Surface Science*, vol. 241, no. 3–4, pp. 303–308, 2005.
12. G. W. Tomlins, J. L. Routbort, and T. O. Mason, “*Oxygen Diffusion in Single-Crystal Zinc Oxide*”, *Journal of the American Ceramic Society*, vol. 81, no. 4, pp. 869–876, 2005.
13. R. F. K. Gunnewiek and R. H. G. A. Kiminami, “*Effect of heating rate on microwave sintering of nanocrystalline zinc oxide*”, *Ceramic . International*, vol. 40, no. 7 Part B, pp. 10667–10675, 2014.
14. W.F. Hosford, *Materials Science, An intermediate text*, Cambridge University Press; 2007. p. 7.
15. P. Erhart and K. Albe, “*First-principles study of migration mechanisms and diffusion of oxygen in zinc oxide*”, *Physical Review B*, vol. 73, no. 11, p. 115207, 2006.
16. M. F. Cerqueira, T. Viseu, J. Ayres De Campos, A. G. Rolo, T. De Lacerda-Aroso, F. Oliveira, I. Bogdanovic-Radovic, E. Alves, and M. I. Vasilevskiy, “*Raman study of insulating and conductive ZnO:(Al, Mn) thin films*”, *Physica status solidi (a)*, vol. 212, no. 10, pp. 2345–2354, 2015.

CHAPTER 3

“ORIGIN OF POLYCHROMATIC EMISSION AND DEFECT DISTRIBUTION WITHIN ANNEALED NANOCRYSTALLINE ZnO AND THEIR EFFECT ON MAGNETIC PROPERTIES AND SPIN-SPIN INTERACTION”



3.1 Introduction

Wurtzite ZnO has received incredible endorsements in the areas of spintronics and dilute magnetic semiconductors. Its high exciton binding energy makes it potential material for its application in nano lasers, blue LEDs, high temperature random laser, and various optoelectronic devices [1-4]. From the use of Zinc oxide in electrical, optical and spintronics devices, one needs to understand its growth mechanisms, defect distribution within the grains & its emission properties. The grain growth mechanism during conventional and multistep annealing has been explored extensively in Chapter 1. The different grain growth mechanism leads to different distributions of intrinsic defects within the grains. This redistribution of defects leads to tailoring of different defect related properties. Hence the study of defect related optical and magnetic properties are inevitable. Chemical vapor deposition (CVD), Pulsed laser deposition (PLD), e beam evaporation, sol-gel are very well known and explored ways of synthesis [5-8]. All the techniques possesses virtues & short comings but a method free of defects is till date hidden. Though existence and the interaction of intrinsic defects in ZnO plays key role in its several applications like light emitting diodes, field-effect transistors, gas sensors etc but in spite of widespread studies on defects, a lucid and clear chemical identification of defects is as yet controversial [9-11]. Beside the identifications of the intrinsic defects, their distribution inside the grains has been a moot point till date and there is no agreement on the origin and identification of these defects [12, 13]. Many authors attempted to correlate the defects distributions, grain size and defect related emissions. Several ideas have been put forward for different emission in visible regions, authors predicted that green emission is because of the transition between V_{O}^{+} and photo excited holes Where as many of them attributed it to transition between electron close to CBM and deeply trapped hole at V_{O}^{++} [14-16]. In a study based on 1st principle calculation of formation energy & electronic structure of intrinsic defects Kohan suggested that green emission is due to Zinc vacancies [17]. Halliburton et al. reported that oxygen vacancies are usually tailored by annealing specifically in Zinc or O rich environment or e-beam radiation [18]. The relation of effect of the intrinsic defects on luminescence properties becomes a tedious when the growth of particle is driven by annealing, because growth of Zn interstitial and oxygen vacancies is governed by Frenkel equation [$Zn_{Zn} \Leftrightarrow Zn_i + V_{Zn}$] and

Schottky equation $[O \Leftrightarrow V_{Zn} + V_o]$ [19]. Further ionization reaction of Zn_i [$Zn_i \Leftrightarrow Zn_i^+ + e^-, Zn_i^+ \Leftrightarrow Zn_i^{++} + e^-$] and oxygen vacancy [$V_o \Leftrightarrow V_o^+ + e^-, V_o^+ \Leftrightarrow V_o^{++} + e^-$] donate 2 electrons, and becomes tricky to distinct from each other. However, from all the defects Zn_i , V_{Zn} , and V_o^- and V_o-Zn_i complexes are major intrinsic defect in ZnO. Zn_i^+ , V_o^- and O_i^- are the only defects which are paramagnetic in nature and are easily detected by Electron Paramagnetic Resonance spectroscopy. Lin et al. calculated electronic energy state of almost all defect centers and found that the energy gap from the Zn_i energy state to valence band is 2.9 eV. “Kroger and Bylander” reported that energy state of Zn_i is 0.22 eV below the conduction band edge [20- 22] and that of V_o is ~ 1 eV below the conduction band edge. Xions et al. on correlating grain size, intrinsic defects and luminescence made out that V_o does not change appreciably with grain size or annealing [23]. Nicks and Daniel though observed direct correlation between V_o , green emission and surface, but did not see any relationship between green luminescence & excitonic emissions [24, 25]. Hence, chapter-III consist of investigations of the most favorable spectral positions of defects due to CA. We also investigate chemical nature of the defects by means of EPR and discover the cause for ferromagnetism in it.

3.2 Experimental details

Commercially available pure (99.99%) Zinc Oxide was CA in air atmosphere in muffle furnace. To study the optical properties the absorption curve was deduced from reflectance measurements in the wavelength ranging from (350-750 nm) by a “UV–Visible spectrophotometer (Perkin-Elmer $\lambda 750$)”. Defect related optical luminescence was recorded at RT using “Florescence spectrometer (PerkinElmer-LS55)”. The EPR experiment was performed for pure undoped and 1000°C annealed sample with microwave frequency 9.412 GHz, and 2mW power (Bruker BioSpin) in temperature range of 125K-RT for 400°C, 800°C and 1100°C annealed sample. The g value was calculated using DPPH (2,2-Diphenyl, 1-picryl hydrazyl, $g= 2.0036$) as a reference. The magnetic nature of the annealed ZnO nanoparticles was investigated using Vibrating Sample Magnetometry (VSM).

3.3 Result and discussions

3.3.1 Optical excitation and polychromatic emission

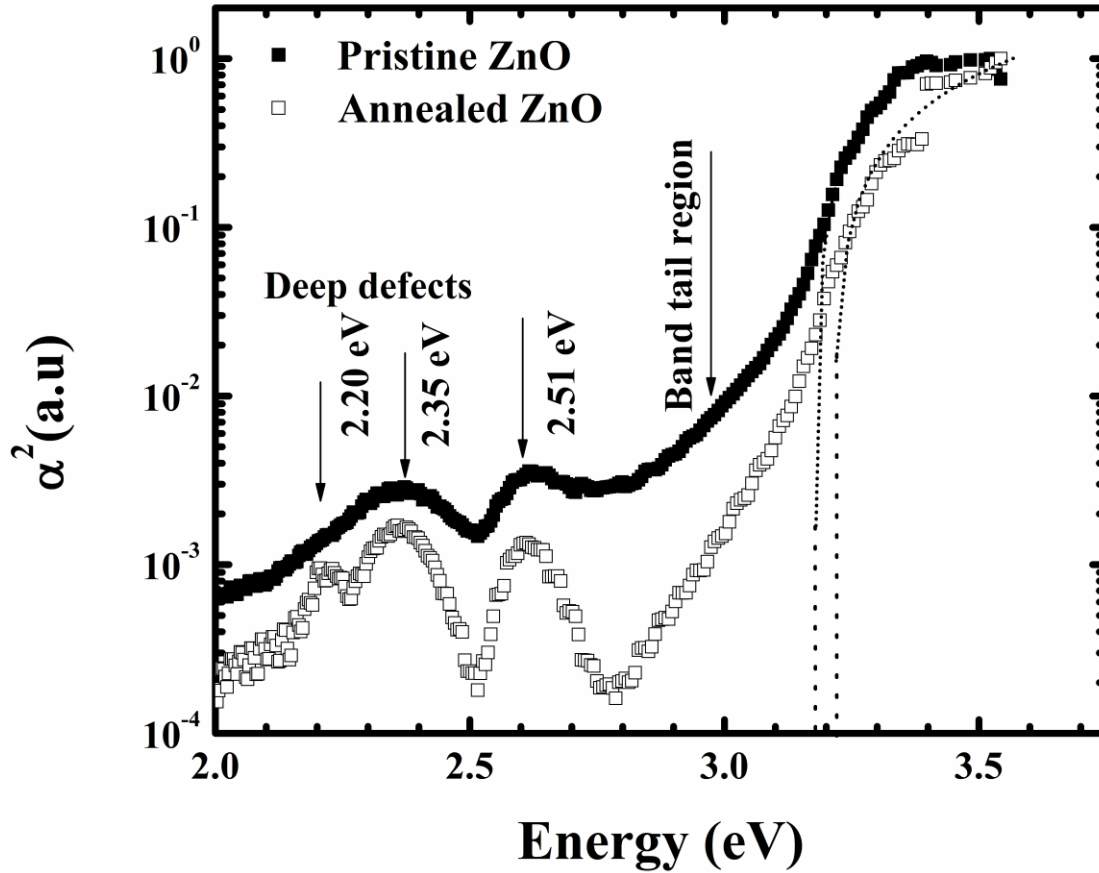


Figure 3.1: Square of absorption coefficient (α) plotted with photon energy.

To study the band absorption & absorption of the various defects lying in the band gap reflectance measurements were made. The absorption coefficient was calculated from:

$$2\alpha t = \ln\left[\frac{R_{max}-R_{min}}{R-R_{min}}\right] \quad (3.1)$$

Where t is the thickness, R is the reflectance for any intermediate photon energy, The reflectance decays from R_{max} to R_{min} due to absorption of light by sample [26]. Variation α^2 with incident photon energy for undoped & CA samples are shown in figure 3.1. E_g was

estimated from Tauc fit to experimental data depicted by dotted lines in figure 3.1. The absorption coefficient for direct transitions is given by

$$\alpha = \frac{A}{h\nu} (h\nu - E_g)^m$$

Where, $h\nu$ is the photon energy,

E_g is the band gap energy,

$m = \frac{1}{2}$ for allowed direct band transitions.

There is no effectual variation in band gap. It signifies that grain size subsist in feeble “exciton confinement range”, where exciton wave function coherence is anticipated to accomplish some enhancement of oscillator strength and bulk ZnO properties may begin. Therefore, the grain size between 65 nm - 90 nm as calculated by XRD is the appropriate range where trapping of surface defects, quenching & the dead layer effect become prominent [27]. Broad band tails with low energy peak at 2.51 eV and 2.35 eV in pristine and an additional peak at 2.20 eV in CA sample is observed. The formations of band tails are attributed to existence of stress in the sample. The absorption peaks in visible region are attributed to “ V_o ”, “ V_o^+ ” and “ V_{Zn} ”. These band tails are formed due to inhomogeneous spatial distribution of defects. The distribution produces an inhomogeneous local pressure within the sample which leads to fluctuations of band gap energy. These fluctuations in E_g emerges as band tails in absorption curves. This result is in good agreement with a report based on spin polarized local LDA along with corrected Hubbard parameter (U) for s orbital, p orbital and d orbital of Zn in ZnO, where authors predicted that presence of V_o and/ or V_{Zn} strongly contribute in optical absorption in visible region of electromagnetic spectra [29]. V_o and V_{Zn} exhibit strong absorption peak at 2.73 eV (453 nm), 2.42 eV (511 nm), and 2.24 eV (553 nm), V_o^- shows absorption peak at 2.81 eV (440 nm) and 2.73 eV (453 nm). Hence to explore emissions from these defects three different excitation energy at 3.54 eV (350 nm), 3.10 eV (400 nm) and 2.75 eV (450 nm) were chosen to excite ZnO samples for PL measurements.

Photoluminescence is emission of light from sample kept under optical excitation. It is based on the principle that electron hole pair (excitons) is created when light of adequate energy are

incident on the sample. The electrons jumps to CB and eventually relax to CBM and defect centers. If this relaxation is radiative in nature the emitted light is the photoluminescence signal. The PL spectra of ZnO are typically divided into two regions. Firstly, they exhibit the characteristic band to band transition called a near band edge emission (NBE) in Ultra violet region. The peak at 3.19eV called NBE. Secondly, they exhibit strong emission spectra in visible region from 400nm to 575nm which is attributed to intrinsic defect states lying between the VBM and the CBM. Luminescence in the visible region is ascribed to intrinsic defects of ZnO.

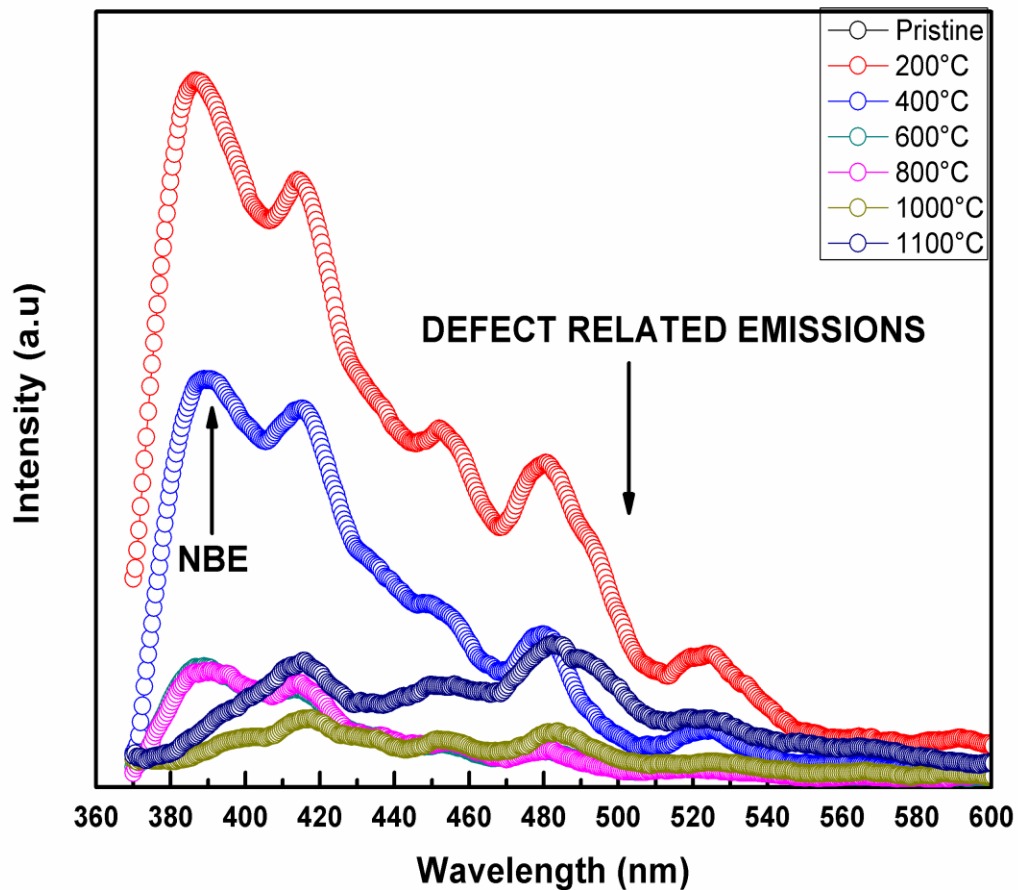
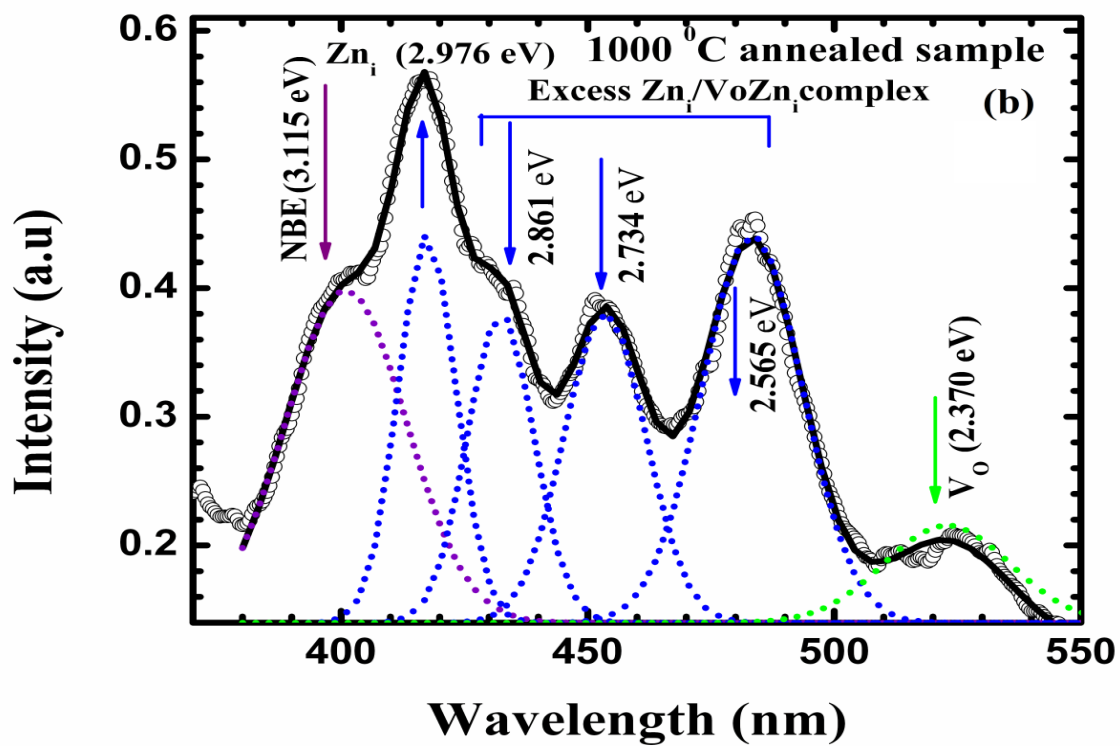
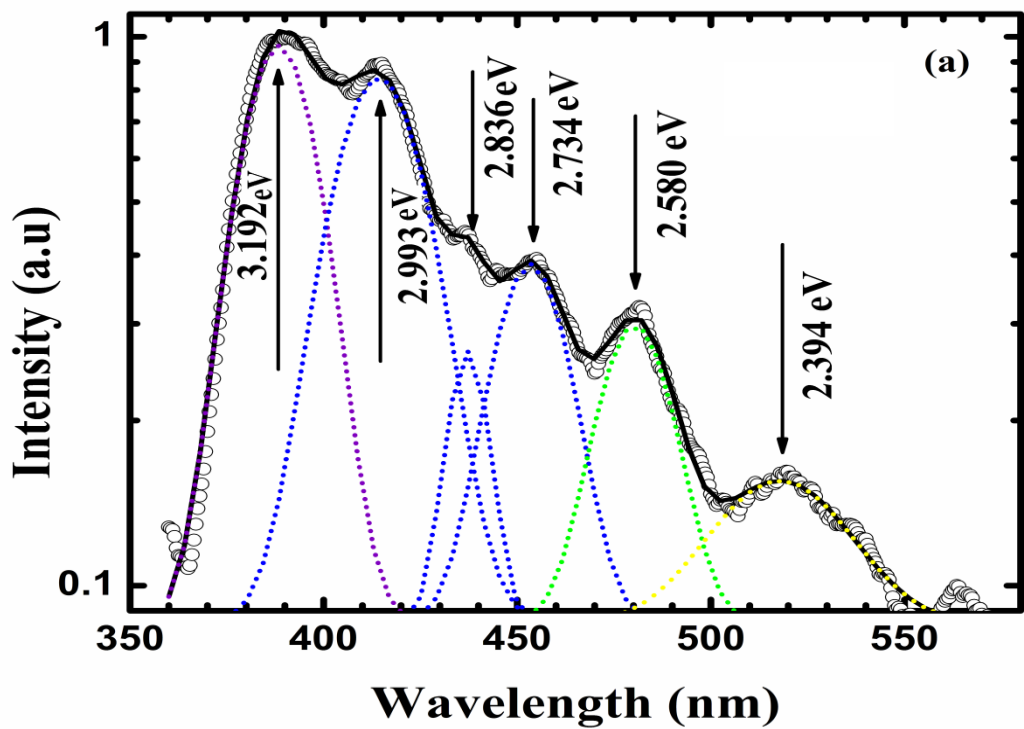


Figure 3.2: PL spectra of CA ZnO samples at excitation energy 3.54eV.



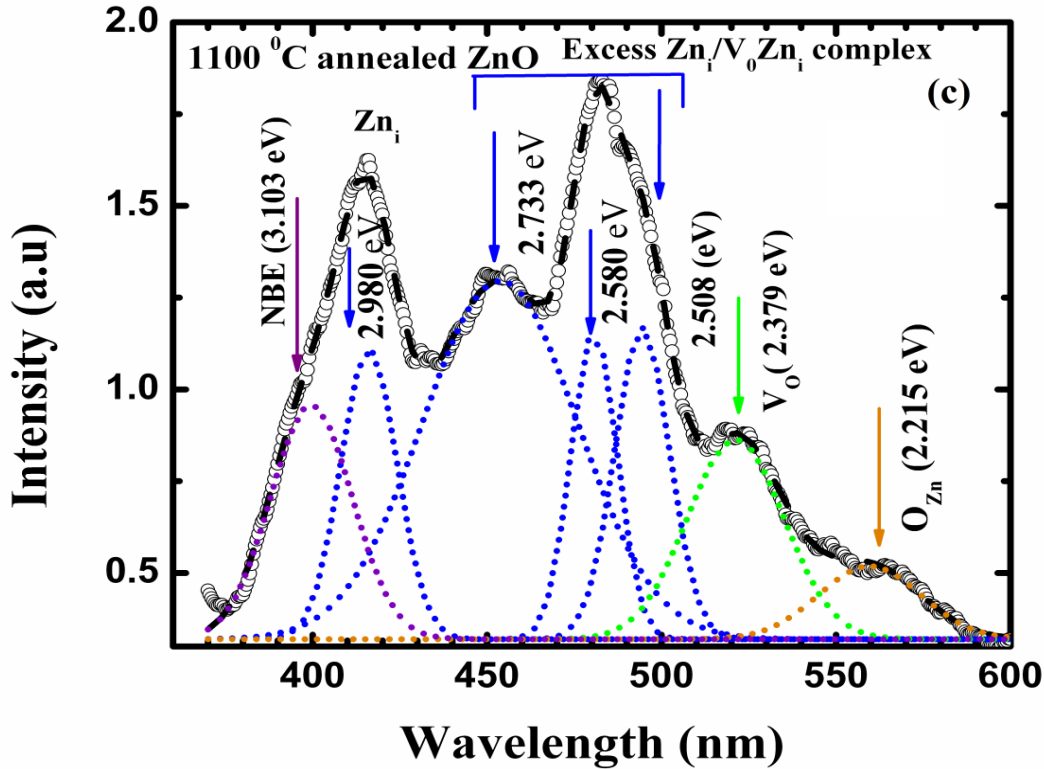


Figure 3.3: (a) Deconvoluted Photoluminescence spectra of 400°C CA ZnO at excitation wavelength 370nm, (b) Deconvoluted Photoluminescence spectra of 1000°C CA ZnO at excitation wavelength 370nm, (c) Deconvoluted Photoluminescence spectra of 1100°C CA ZnO at excitation wavelength 370nm.

The PL spectra has been deconvoluted and complete graph of 400°C CA sample is shown in figure 3.3 (a). Peaks were deconvoluted using Gaussian deconvolution, as shown in colored dotted lines and their positions have been marked with arrows. The interesting thing to observe that after CA at 1000°C in figure 3.3 (b) and 1100°C in figure 3.3 (c) the peak intensity of NBE (3.192, 3.115 and 3.103eV) decreases and that of defect related visible emission peaks enhances with a red shift of 20meV-30meV. This signifies increase in surface defects with respect to NBE due to high temperature CA ($T > 1000^\circ\text{C}$). The quenched NBE and enhanced defect related peaks in visible region could be due to oxidation of surface of grain. Figure 3.4 shows the variation of peak intensity of NBE/Zn defect and NBE/O defect with annealing temperature. The ratio of peak intensity increases with annealing temperatures which means that only surface defect are liable for enhanced defect related peaks.

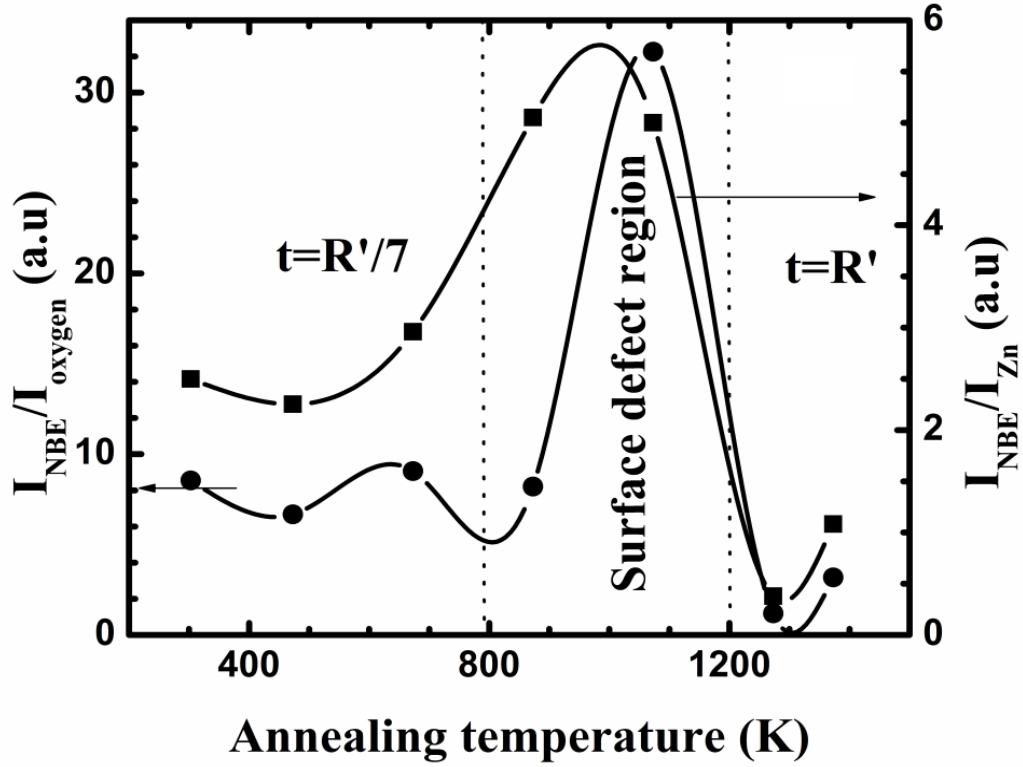


Figure 3.4: Variation of ratio of PL peak intensity of NBE/ Zn to O vacancy with annealing temperature.

These analyses reveal that defects become more effective at high temperature because concentration gradient between core and surface encourages the outward diffusion of Zn_i . The oxidation of Zn_i at surface causes formation of new layer of ZnO on pristine grains. This newly formed layer sets up a metal-semiconductor interface, which quenches NBE. These layers act as fresh new source of defect and recombination centre. It is exciting to note that grain size of pristine and 1000°C CA samples remains same whereas are different in distribution of defects. A model for explaining the dependence of peak intensity on the CA temperatures and grain size is explained below. The ratio of intensities of NBE/defects in visible region for “spherical grains of radii R” and “surface recombination thickness t” is given by [30],

$$\frac{I_{NBE}}{I_{visible(Zn/V_o)}} = C \left(\frac{R^3}{3R't'(R-t') + t'^3} - 1 \right) \quad (3.2)$$

Where, C is proportionality constant, comprising of oscillator strength & is independent of “R” and “t”. From equation 3.2 we can conclude that intensity ratio will acquire minimum value when the radius of grain and the thickness of surface layer becomes equal i.e. “R” = “t”. This means that highest annealing temperature for ZnO at its maximum growth is 1100°C. Further the separate region for temperature dependent grain growth and for dominant of surface defect are marked with dotted lines in figure 3.4. Dominance of surface defect takes place close to $\sim “t= R/7”$, hence range of surface recombination thickness can be taken as $“R”/7 < “t” < “R”$. Grain size results shows highest value of $“t” = R/2$. Further, absorption coefficient of Zinc Oxide at excitation wavelength (350 nm) is $“1.5 \times 10^7 \text{ m}^{-1}”$, the average optical penetration depth (α^{-1}) & thickness of excitation layer was nearly 66.67nm, somewhat close to calculated value of size of grain. Assuming “diffusion coefficient of electron $D_e = 5.2 \times 10^{-8} \text{ m}^2 \text{ sec}^{-1}$ ” and “exciton life time τ_{ex} in ZnO $\approx 10^{-9}$ second”, recombination layer thickness would be: $\sqrt{D_n \tau_n} \approx 7 \text{ nm}$. This specifies excitation is bulk process whereas recombination of photo excited electrons happens at surface.

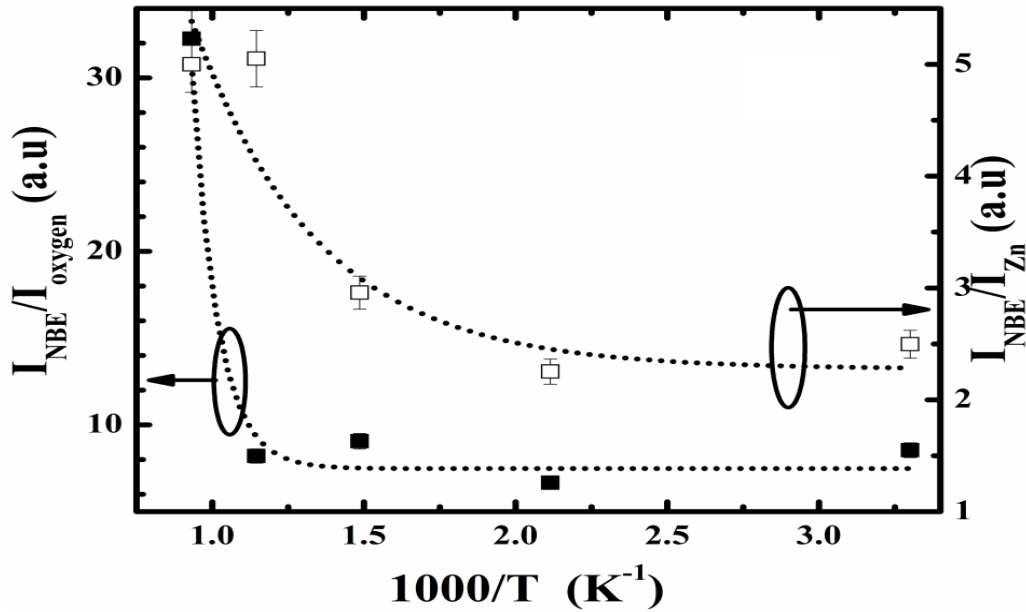


Figure 3.5: Variation of I_{NBE}/I_{Zn} and I_{NBE}/I_{Oxygen} with inverse of annealing temperature; dotted line shows the Arrhenius fit.

Activation energy (E_a) of defects on surface with respect to CBM was predicted from the Arrhenius equation. Variation of “ $I_{NBE}/I_{visible (Zn/Vo)}$ ” versus annealing temperature is plotted in

figure 3.5. E_a were calculated by fitting equation “ $I_{\text{NBE}}/I_{\text{visible}}(\text{Zn}_i/\text{V}_o) = a \exp(-E_a/k_B T)$ ” to the experimental data. Where, a , k_B , E_a are the pre-exponential factor, Boltzmann constant and activation energy of the defects respectively. The activation energy was 0.5eV for Zn_i and 2.65eV for V_o . For Zinc interstitial it reasonably agree with the results reported by Xu et al. whereas, for oxygen vacancies it is large. Gavryushin et al. has reported activation energy for oxygen vacancy is $\sim 1.2\text{eV}$ [31-34]. In comparison of experimental and theoretical result (dotted lines in figure 3.5) it is concluded that $E_a \sim 2.65\text{eV}$ belongs to antisite Zn and $\text{V}_o\text{-Zn}_i$ complex. Since, $\text{V}_o\text{-Zn}_i$ complex or DAP signature are predicted to take place at low temperature. Hence, peak in yellow region centered at 2.215eV is because of recombination of conduction electron with hole at O_{Zn} site. Therefore, cause of different luminescence (depicted by solid lines) in visible region can be mapped as shown in figure 3.6.

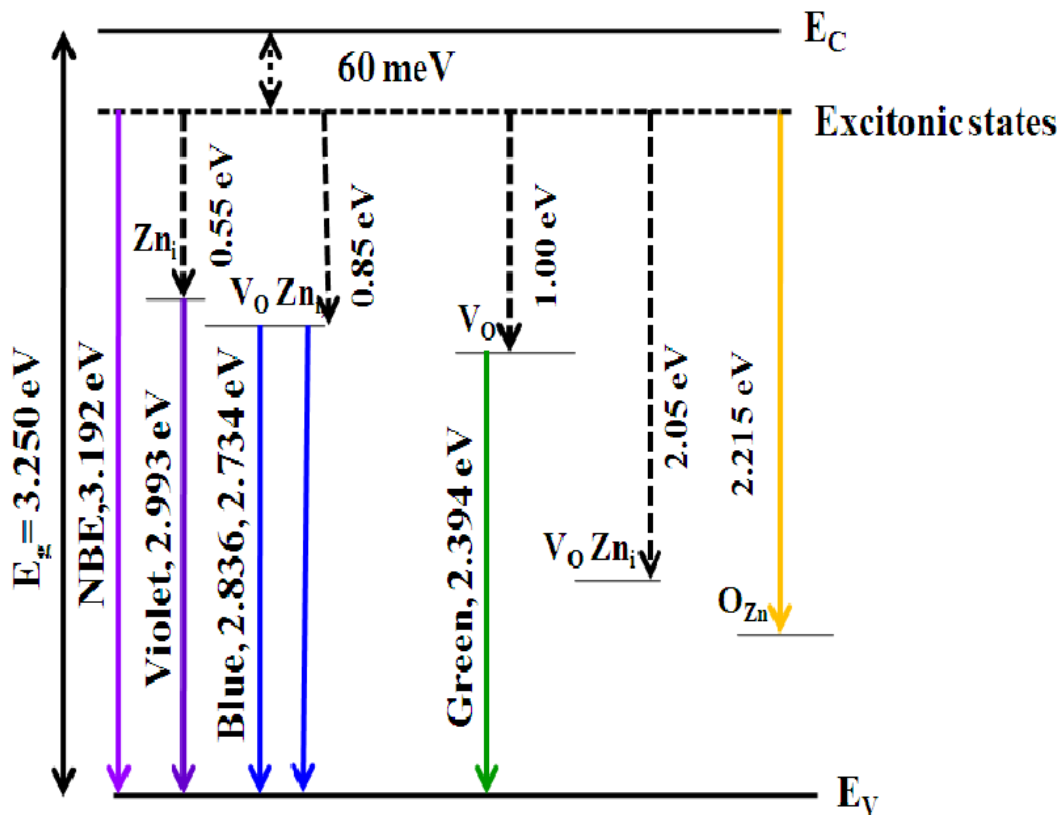
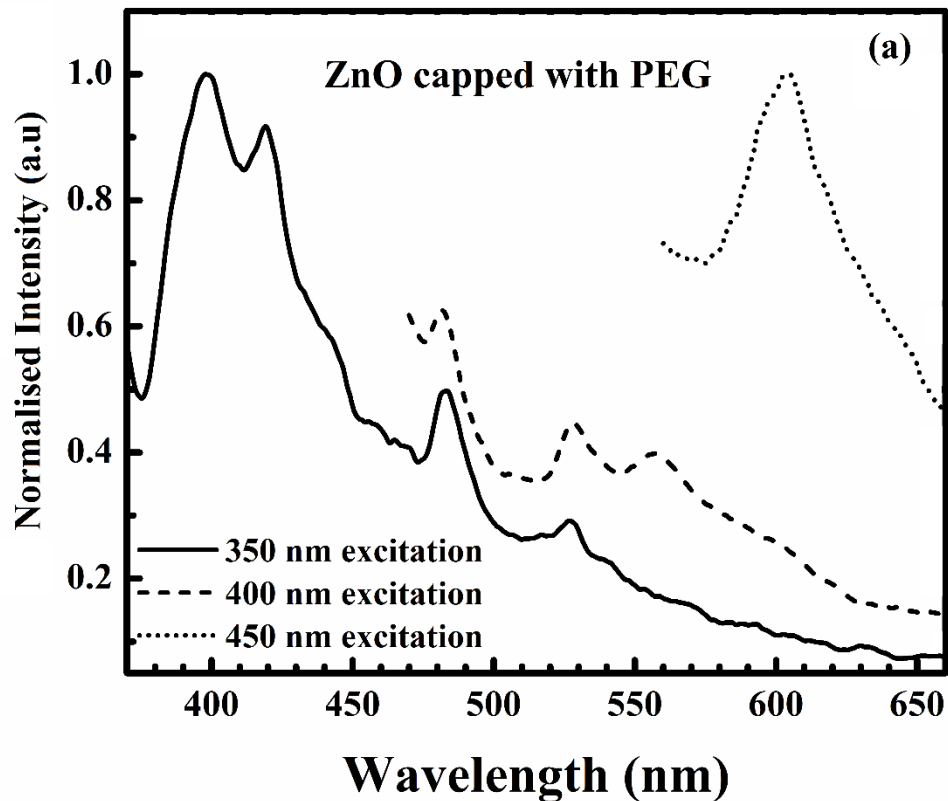


Figure 3.6: Schematic of visible emission transitions from ZnO.

These analysis shows that emission in blue region i.e. from Zn_i reside in a small area of the surface; so any modifications in surface will effect modification in luminescence spectra of Zn_i along with band bending that occur at surface. The emissions associated with oxygen vacancies (green) & complexes (yellow) reside in the core of grain and will remain unaffected.

To find out the consequences of surface modification on different luminescence regions, the CA sample at 1000°C were capped with “polyethylene glycol (PEG)” and “polyvinyl alcohol (PVA)”. PL spectroscopy was repeated with same excitation energy. PL emission spectra of surface modified ZnO sample is shown in figure 3.7 (a) and figure 3.7 (b). After capping the particles by polymers the blue emission from Zn_i decreases significantly and NBE starts enhancing and dominating again. PL peaks related to bulk (V_o and O_{Zn}) remain unaffected. This means that ZnO annealed at 1000°C was rich in surface defects.



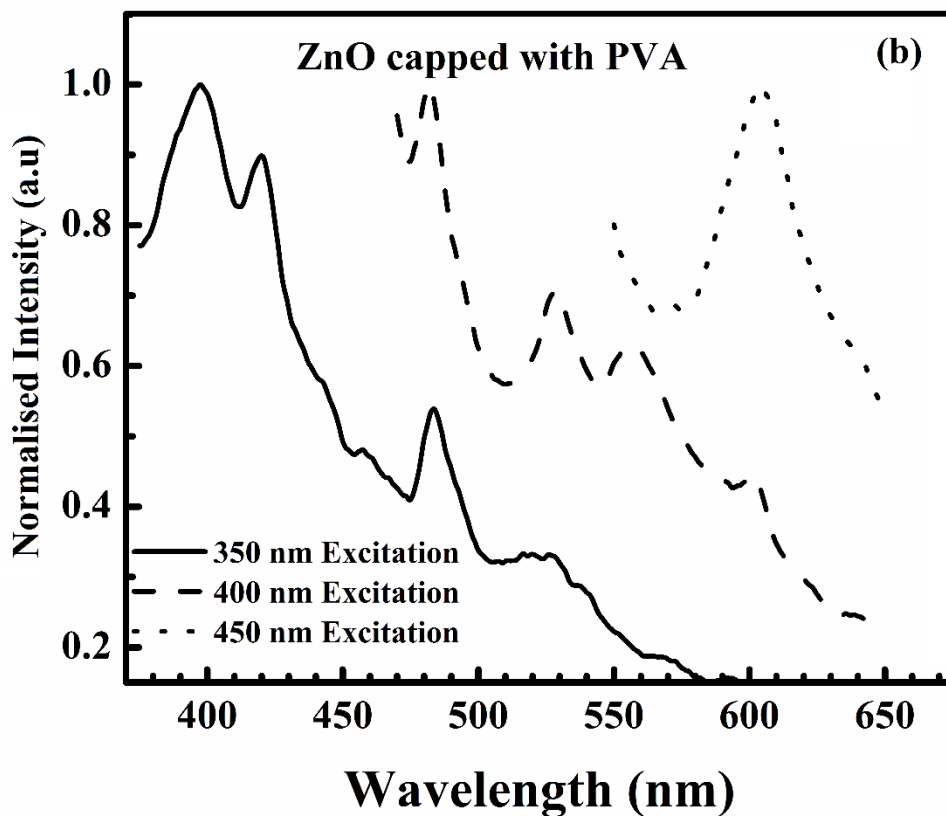
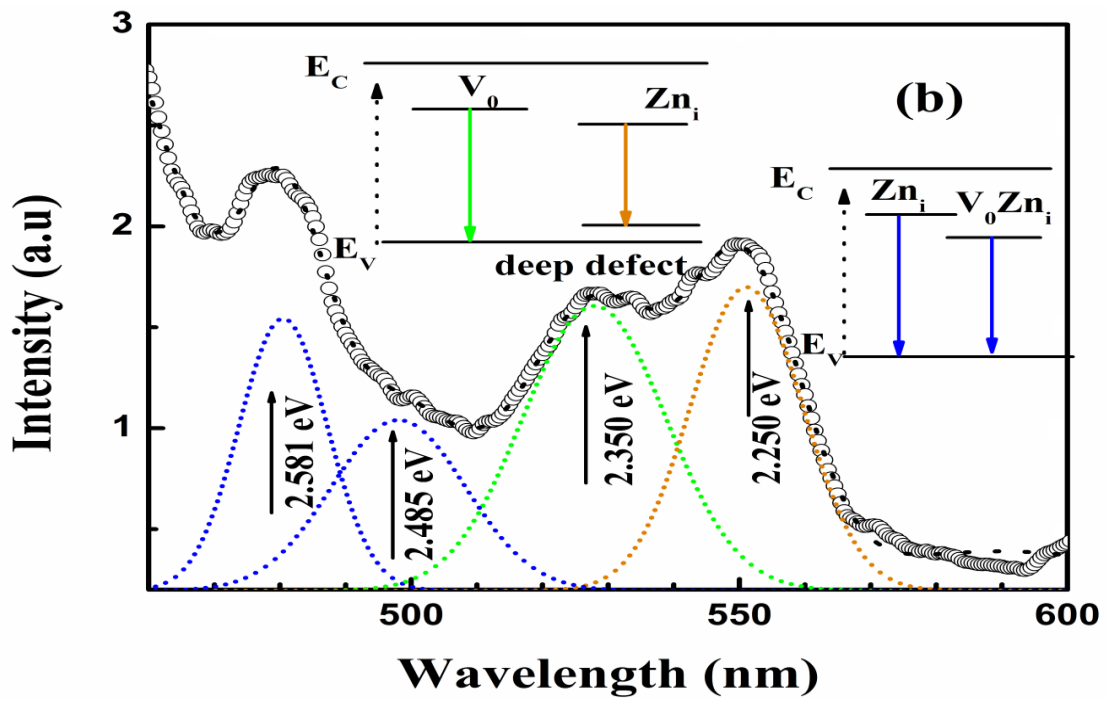
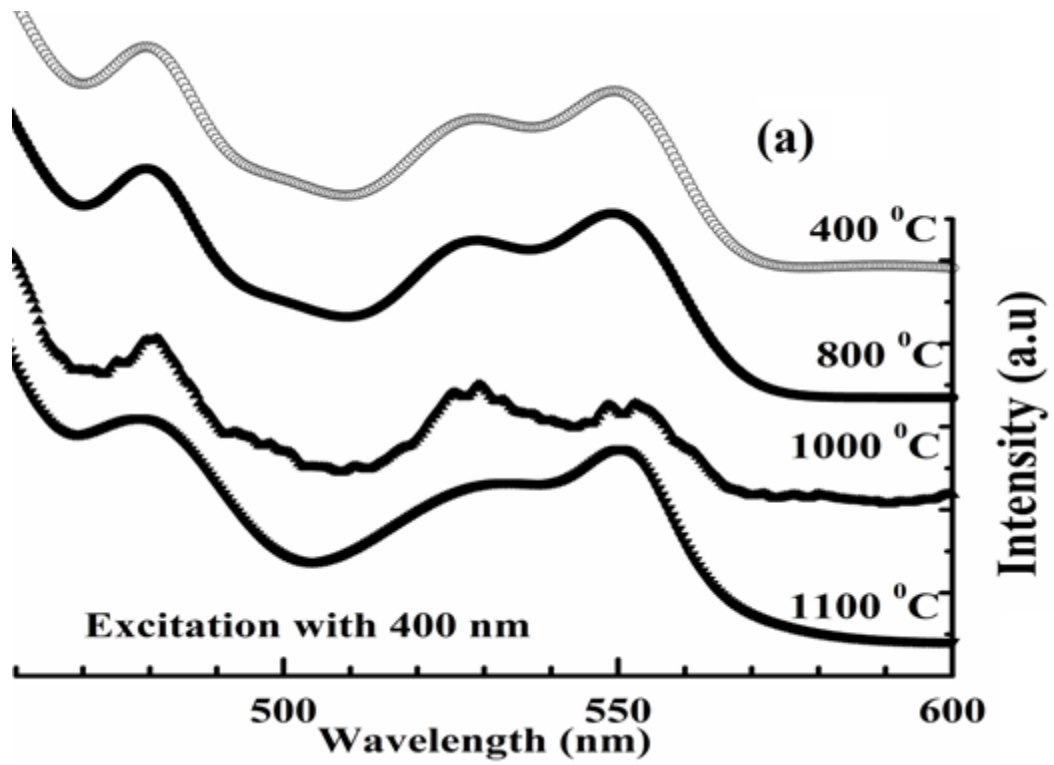


Figure 3.7: (a) PL spectra of CA 1000°C A capped with PEG and surface modified ZnO at different excitations, (b) PL spectra of CA 1000°C A capped with PVA and surface modified ZnO at different excitations.

3.3.2 Sub band excitation and emissions

To observe the effect of thickness of surface layer and its role in PL emission spectrum, CA ZnO nanoparticles were excited with photons of energy $< E_g$ i.e. 400nm (3.10eV) and 450nm (2.75eV). The sub band emission spectra is shown in figure 3.8 (a), (b), (c) and (d).



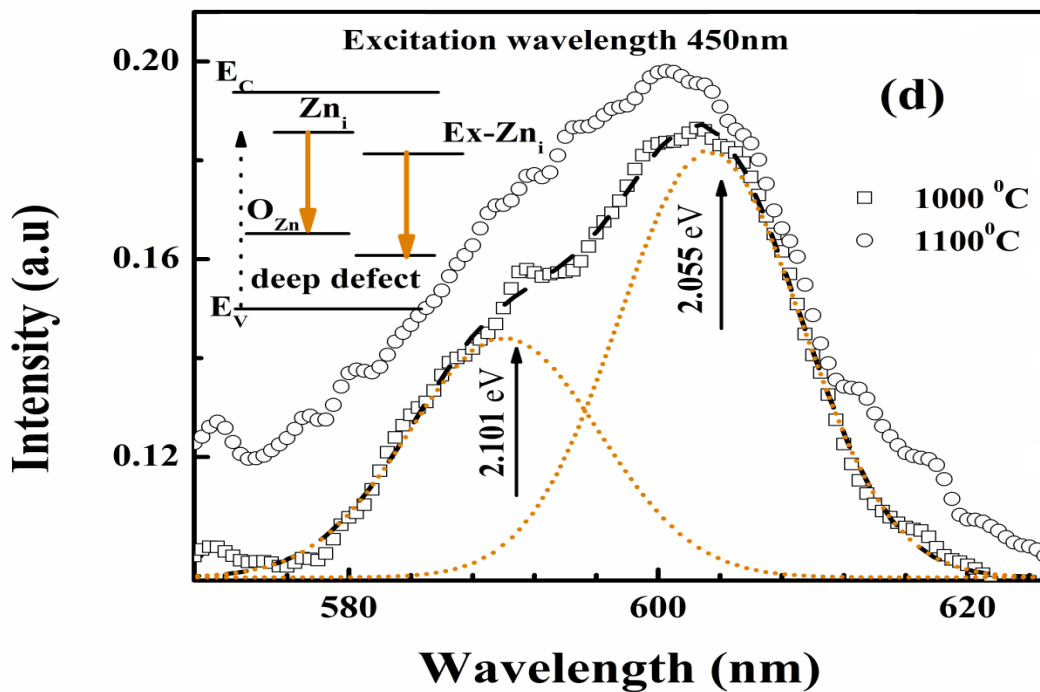
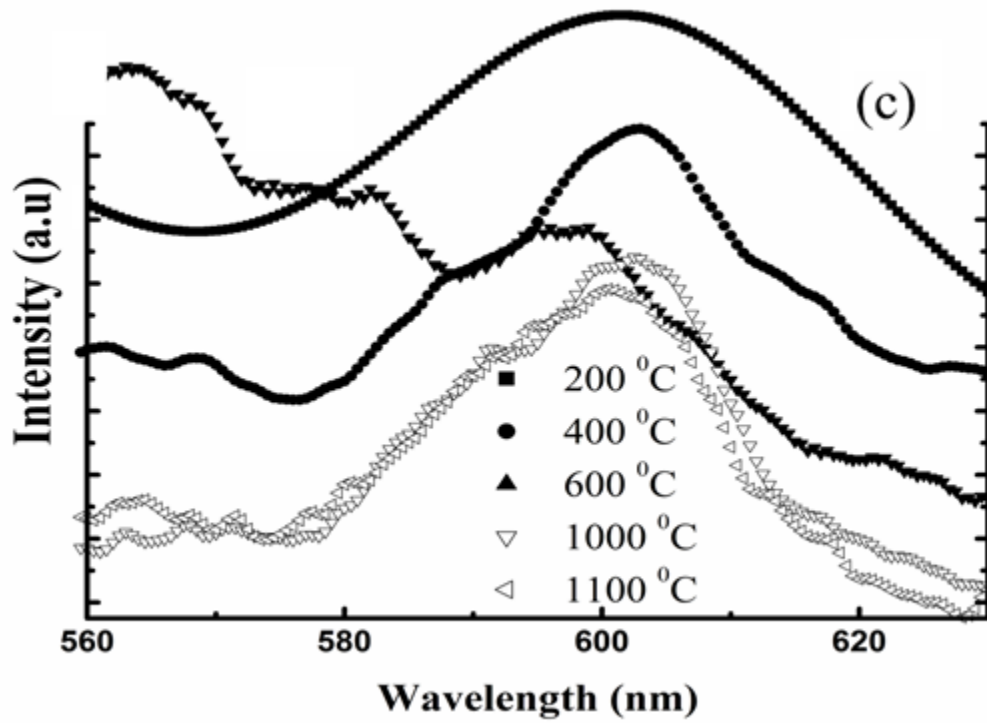


Figure 3.8: (a) PL spectra at 400nm excitation energy, (b) Extended spectra of 400°C CA samples, (c) PL spectra at excitation 450nm excitation energy, (d) Extended spectra of 450°C CA samples.

The luminescence spectra of ZnO sample CA at various temperatures at excitation wavelength 400 nm (3.10 eV) is shown in figure 3.8 (a). The complete graph for 400°C CA sample is shown in figure 3.8 (b). The experimental data are shown by open circles and the dotted lines shows the Gaussian deconvoluted peaks. It is fairly noticed that defect related emission peaks are clearly visible with little lower intensity than sample excited with excitation wavelength 350 nm. The emission peak at 480 nm (2.581 eV) seems pinned and three new peaks appear at 2.485, 2.350, and 2.250 eV respectively. Figure 3.8 (c) depicts the PL emission spectra recorded at excitation wavelength 450 nm (2.75eV). Figure 3.8(d) is just extension of the same. For the excitation with lower energy the PL peaks are noticeably visible and gets red shifted by $\sim 195\text{meV}$. Most exciting part is that deep lying defects can be excited with lower energy. The stability from different excitation annealing temperature was confirmed from the pinning of the PL emission peak at 2.581eV e.g. once Zn_i reaches the surface of grain it either gets oxidized or remains rigid at surface. The reason of co-emission from various colors is shown in inset of Figure 3.8(b).

When photon energy is sufficient enough to excite the electrons up to the Zn_i energy level, but not to the CB, majority of electrons get trapped at Zn_i states & induce effective transition from Zn_i energy level to VB. As CA does not alter the band gap & Zn_i the blue emission is fixed. Concurrently, because of steady state excitation, and RT thermal energy comparable number of excited electrons get transferred to the energy level of closely spaced $\text{V}_o\text{-Zn}_i$ complexes. Radiative transition from these $\text{V}_o\text{-Zn}_i$ complexes to VBM gives emission at 2.48 eV. In contrast to previous reported results [35], green emissions are still significant under low energy excitation. Thus, we propose that green luminescence is due to radiative recombination from triplet state of V_o ($S=1$) to singlet ground state of V_o ($S=0$). Whereas, orange luminescence centered on 2.250 eV is because of transition of electron from Zn_i to deep defect states. Later on by excitation with much lower photon energy i.e. 2.75 eV, where electrons are pumped to the excess Zn_i energy state, only orange luminescence is observed. This is because of transition from excess $\text{Zn}_i/\text{V}_o\text{-Zn}_i$ complexes to deep defect states, and from Zn_i energy level to O_{Zn} defect or effective role from both. Therefore, combined result of XRD, growth mechanism, interband and sub band PL emission, the spatial distribution of defects in spherical grains can be visualized.

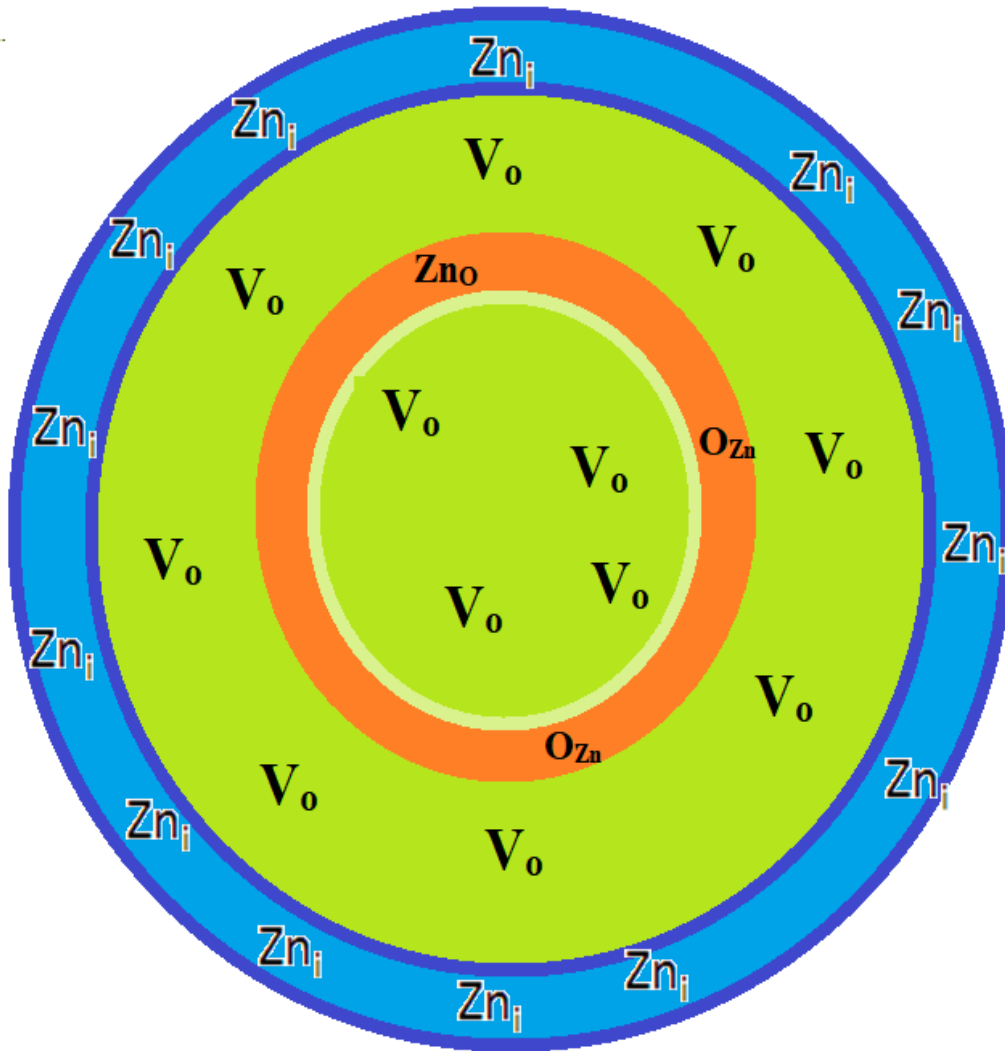


Figure 3.9: Spatial distribution of defects and their emissions within the grains.

The spatial position of defects responsible for blue and green emission within grains is shown by figure 3.9. Spatial distribution was further confirmed by fluorescence imaging method using Nikon fluorescence microscope equipped with triple band excitation filter DAPI, FITC, TRITC combined with appropriate set of dichromatic mirror. These excitation filters are narrow band pass filters in wavelength range of 385-400 nm, 475-490 nm and 545-565 nm respectively.

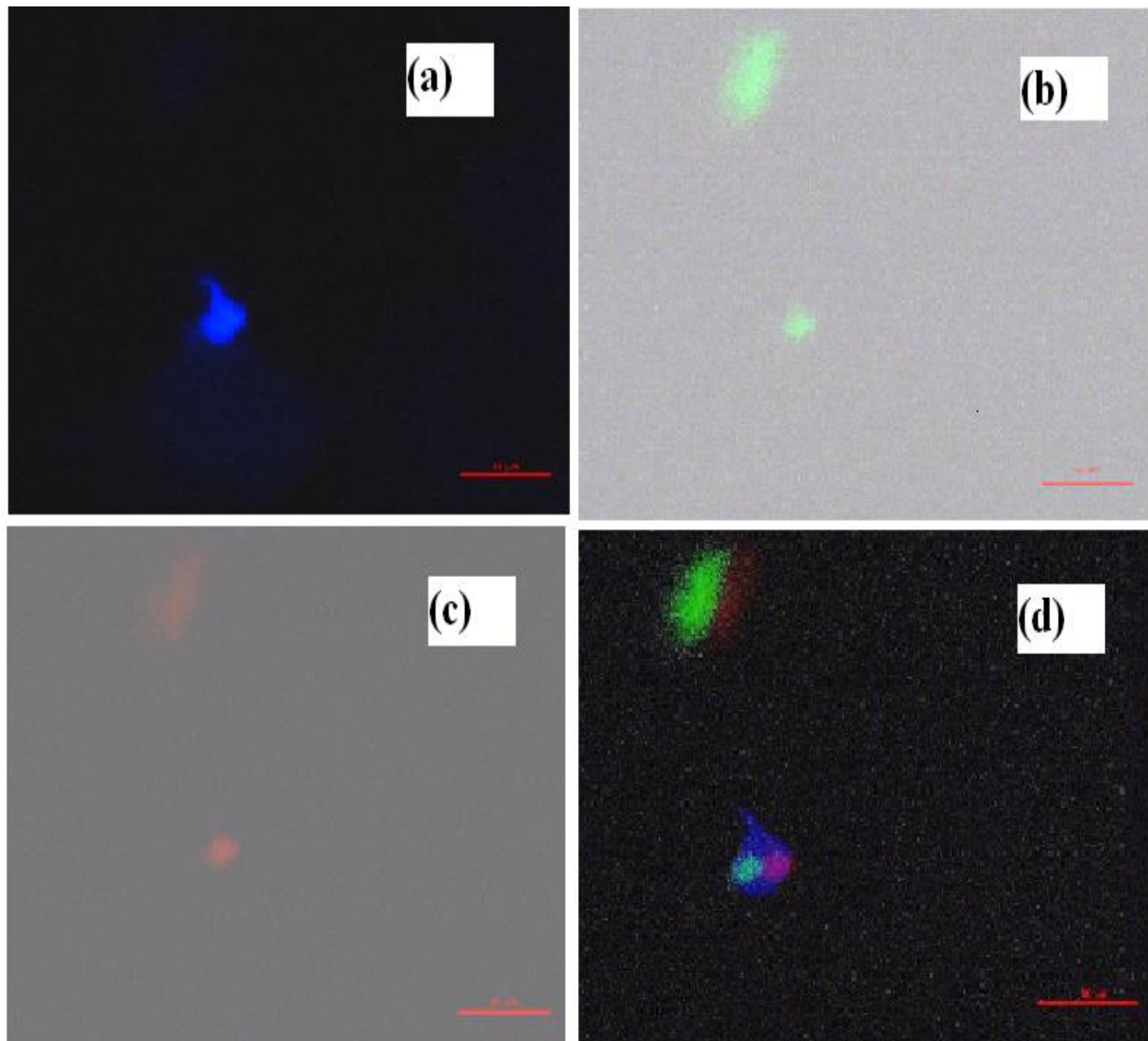


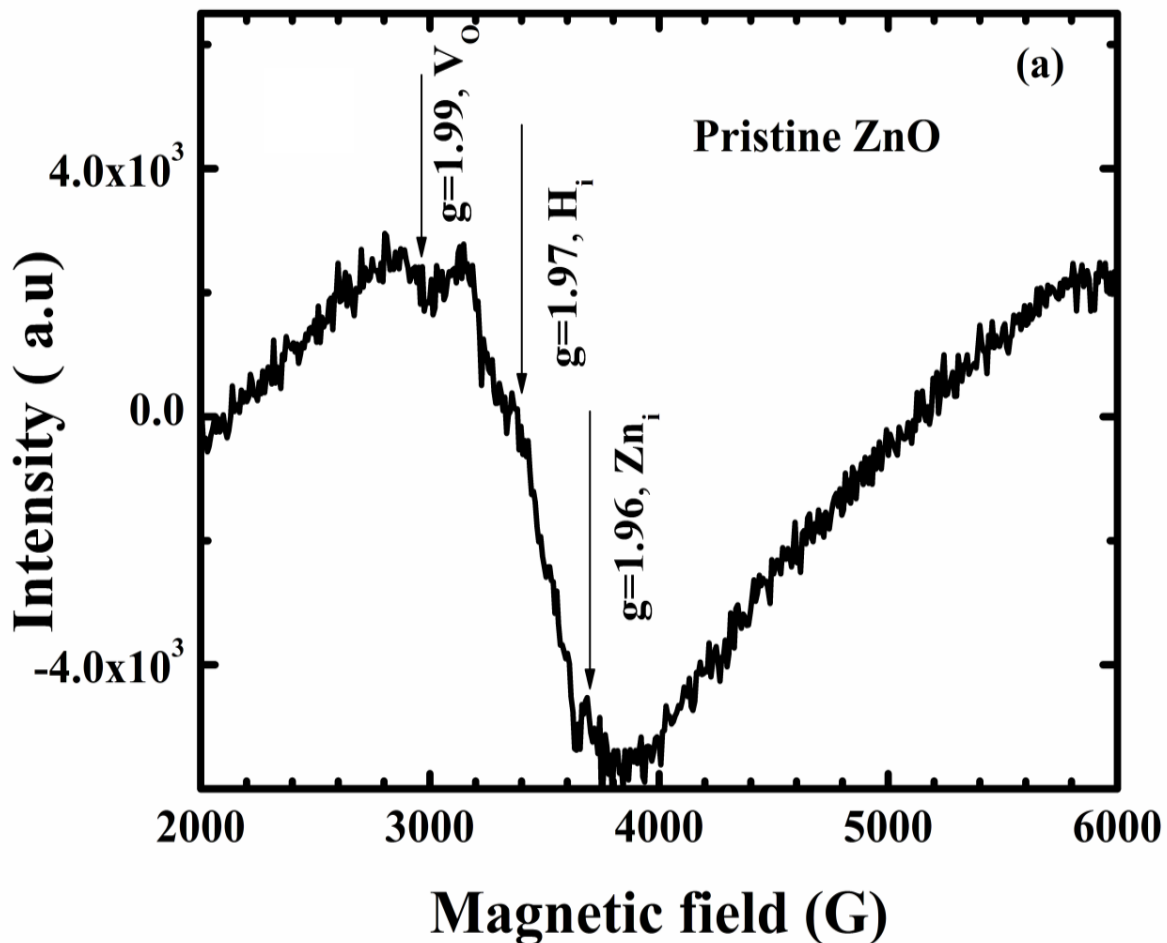
Figure 3.10: Fluorescence image of ZnO with various excitations (a) DAPI, (b) FITC, (c) TRITC, (d) Combined fluorescence image of grain.

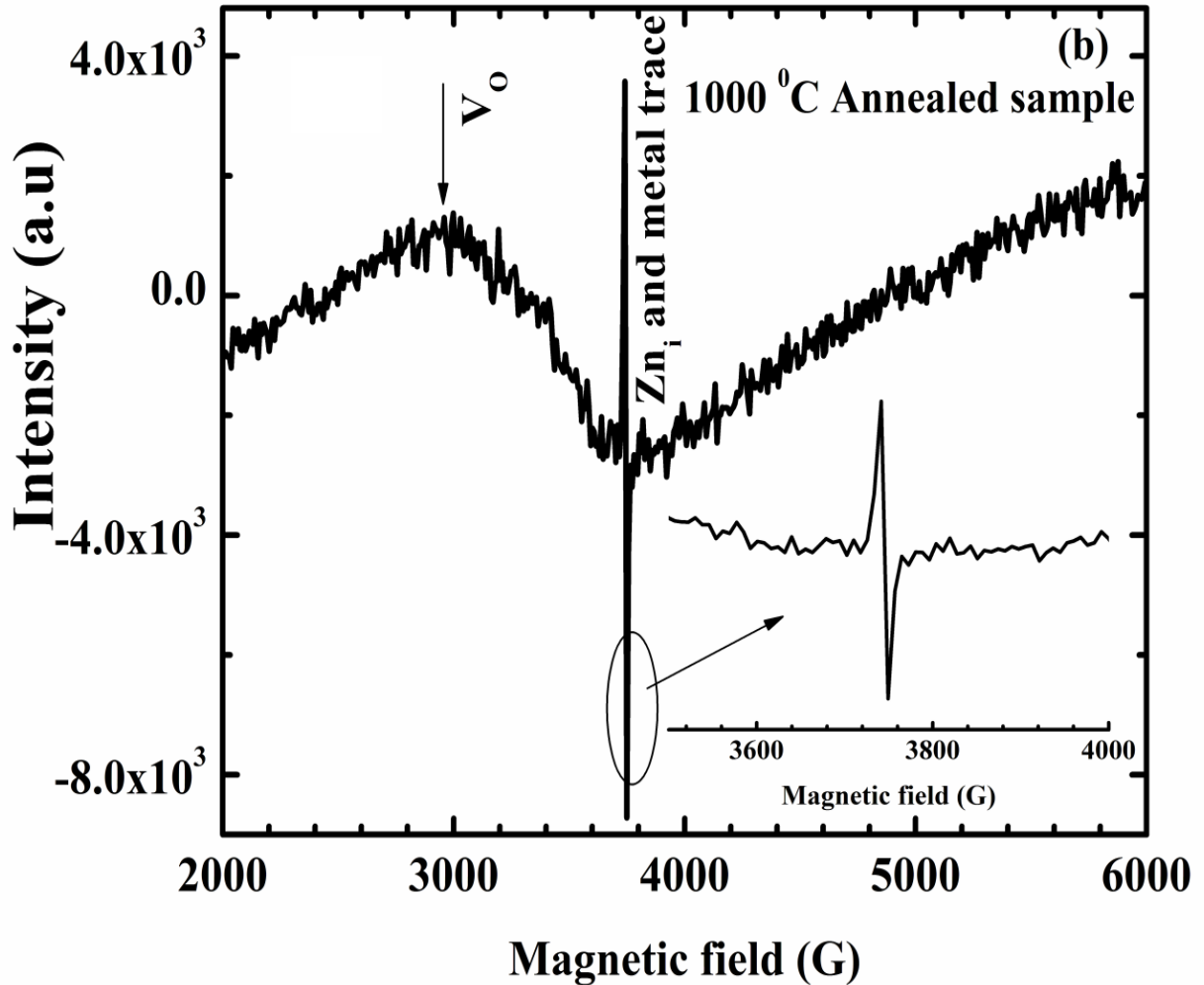
Figure 3.10 (a), (b), (c) shows the fluorescence imaging of CA ZnO grains corresponding to DAPI, FITC, and TRITC. The combined image of grain is shown in figure 3.10 (d). It can be observed from the imaging that blue emission seems to come from the whole grain where as green and red emission is constrained in small regions. Hence, from the results of fluorescence and theoretical model of growth it can be concluded that controlled annealing especially

annealing in steps will tailor the defect distributions within the grain and will change its luminescence properties.

3.3.3 EPR measurements and magnetic studies

For the technological applications, the chemical nature of these defects must be identified. EPR spectroscopy is one of the most potent methods to identify the chemical & ionic nature of defects/impurity in materials. EPR measurements were performed at RT for undoped unannealed and 1000°C CA ZnO samples. The EPR spectra of pristine and 1000°C CA ZnO samples are shown in figure 3.11 (a) & figure 3.11 (b).





The EPR spectra of pristine ZnO seem broad and superimposed. However, 3 distinct peaks are marked at $g = 1.99$, $g = 1.97$ and $g = 1.96$. They correspond to V_o , Hydrogen interstitials (H_i) and Zn_i respectively [36-39]. It is exciting to notice that H_i disappears rapidly on CA and merge together with Zn_i as observed by emerging of new strong signal at $g=1.96$, which is shown in inset of figure 3.11 (c). This is because of mixture of signal from Zn_i complexes, H_i , and metal trace present in the sample. Since, Zn_i and H_i signals seem to be merged at RT, EPR measurement were also performed at low temperature in range of 300K to 100K.

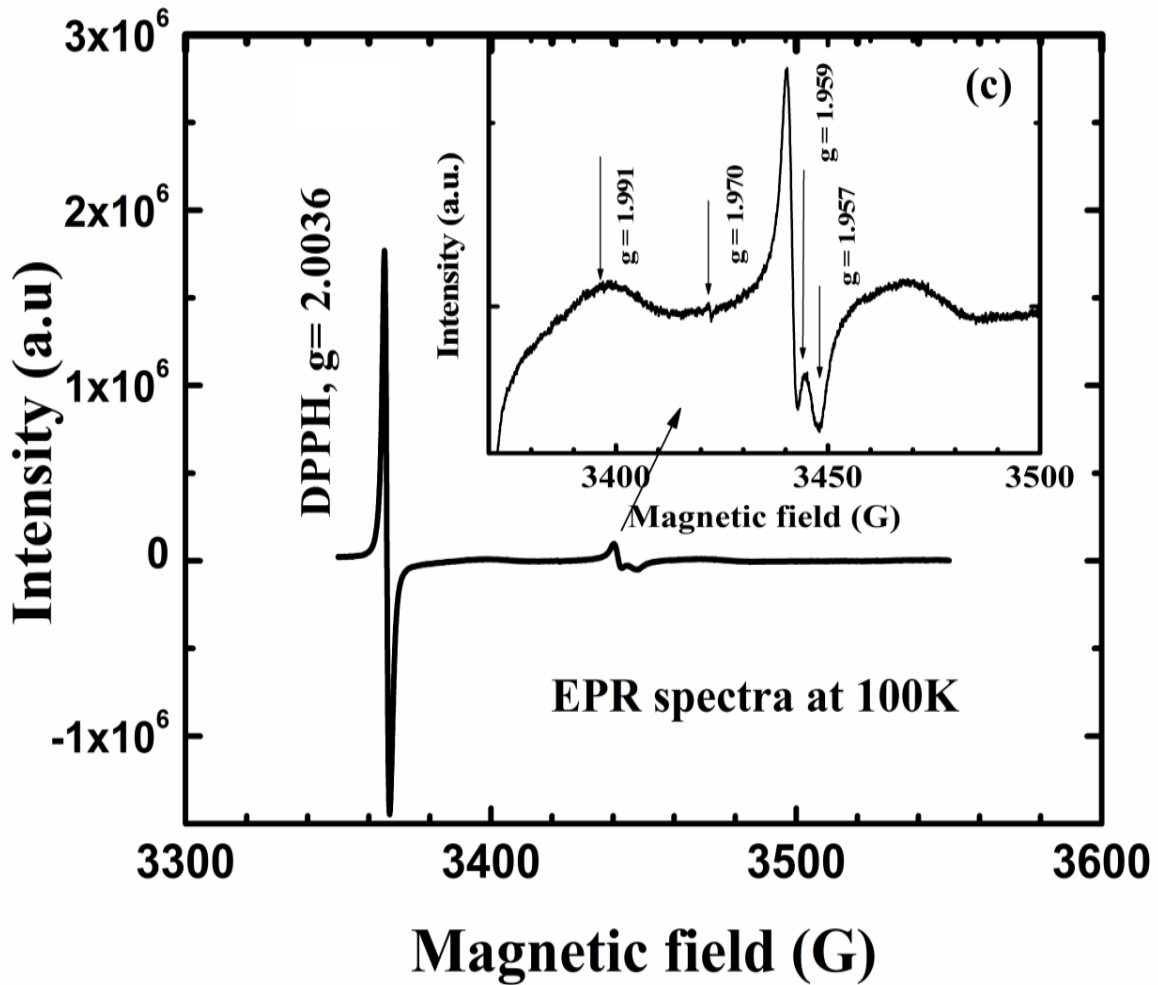


Figure 3.11: (a) Room temperature EPR spectra of Pristine ZnO, (b) Room temperature EPR spectra of CA sample at 1000°C, (c) EPR spectra obtained at 100K with reference DPPH, inset shows enhanced spectra.

EPR spectra at 100K show distinctive signature, and for exactness it is re-plotted in figure 3.11 (c) with standard reference sample DPPH (2,2-Diphenyl, 1-picryl hydrazyl, $g= 2.0036$), where inset shows elaborate spectra. It comprises of 4 peaks centered at g value 1.957 (1), 1.959 (2), $g=1.970$ (3) and $g = 1.991$ (4). These peaks were credited to Zn_i^+ , Zn_i^+ complexes with H_i and ionized V_o [38, 39]. Zn_i exhibits two distinct g values because it produces a local magnetic field inside the crystal lattice which in turn leads to production of anisotropy and indicate that Zn_i resides in two different structural environments.

LDA along with correlation energy (LDA+U) supports anisotropy in ZnO, as it has been proved that structural relaxations around V_o are large and different in various charge states of V_o, V_o^+ &

V_o^{++}). For V_o , the 4 nearest neighbor Zn are dislocated inward by 12% of equilibrium Zn-O bond length. Whereas, for V_o^+ and V_o^{++} the dislocations are outward by 2% and 23%. There are numerous reports which argue the assignment of EPR signal at $g = 1.96$, Vanheusden et al. reported that $g=1.96$ correspond to V_o^+ , whereas, Block et.al reported that $g = 1.96$ is due to neutral shallow donors and signal at $g = 1.99$ is due to V_o^+ [37-39]. EPR results prove that Zn_i and V_o stay together in sample even after annealing at 1000°C , and Zn_i lie in different structural environment which could be either oxygen or zinc. It also signify the formation of O_{Zn} defect. Exchange interaction between these defects will give interesting magnetic properties which were measured with VSM at RT as shown in figure 3.12.

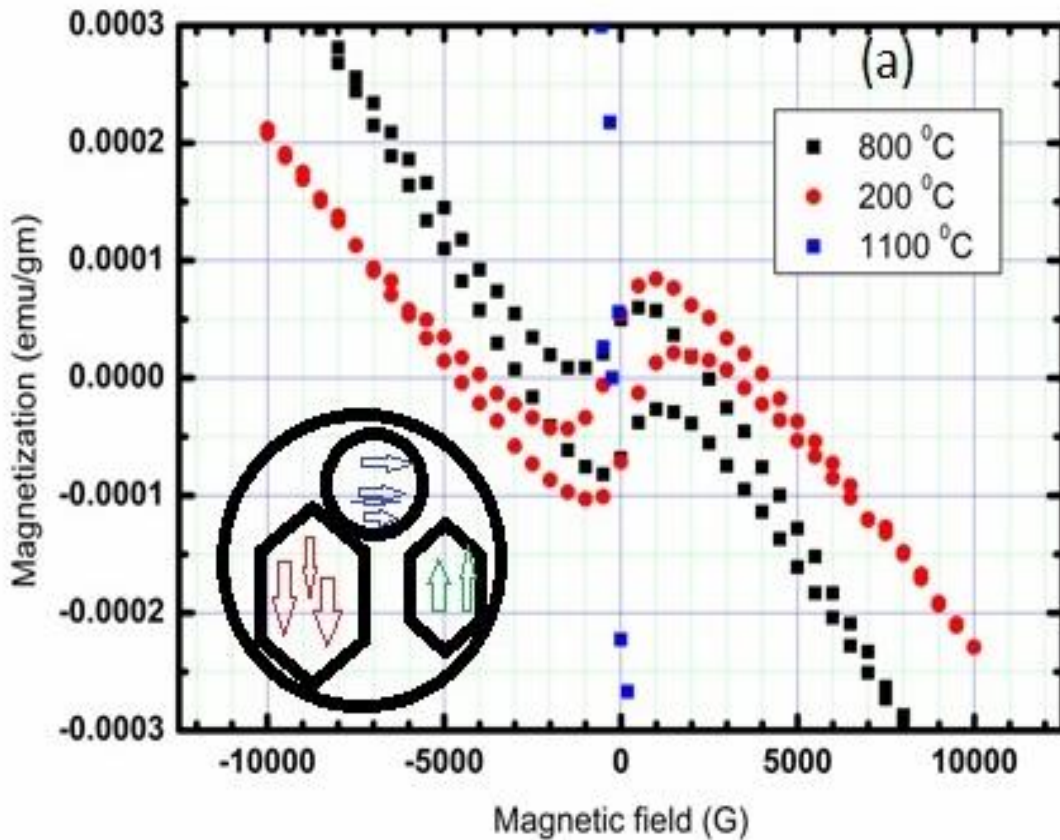
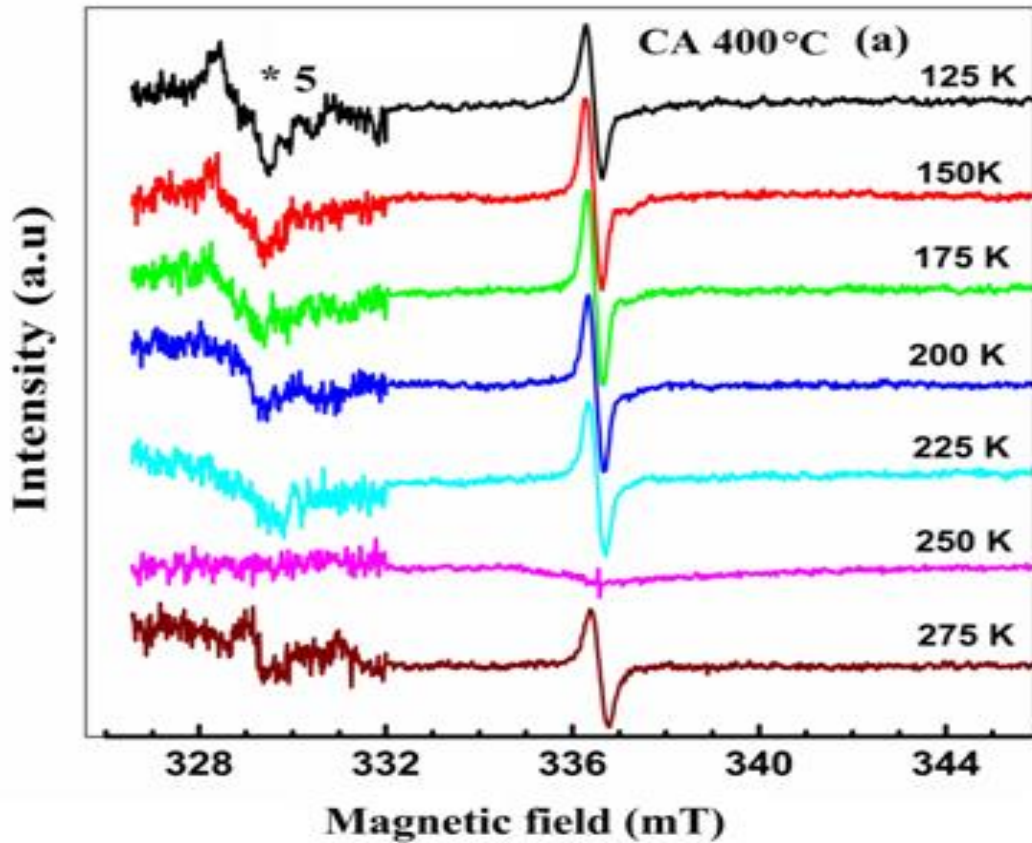


Figure 3.12: M-H curve of CA sample at 200°C , 800°C and 1100°C .

CA sample at 200°C and 800°C showed the ferromagnetic nature but CA sample at 1100°C exhibited a pure diamagnetic signal. The sample at 200°C and 800°C were though ferromagnetic

in nature but were saturated at a very less value of magnetic field ≈ 1500 Gauss. Low saturation implies the existence of defect clusters or the defect pair formation.

To further explore the cause for ferromagnetism and then transition to diamagnetism in CA samples we performed ESR measurements in temperature range of 125K to 275K on 400°C, 800°C and 1100°C annealed samples. 400°C annealed samples are very rich in defects and 800°C shows enhanced surface properties.



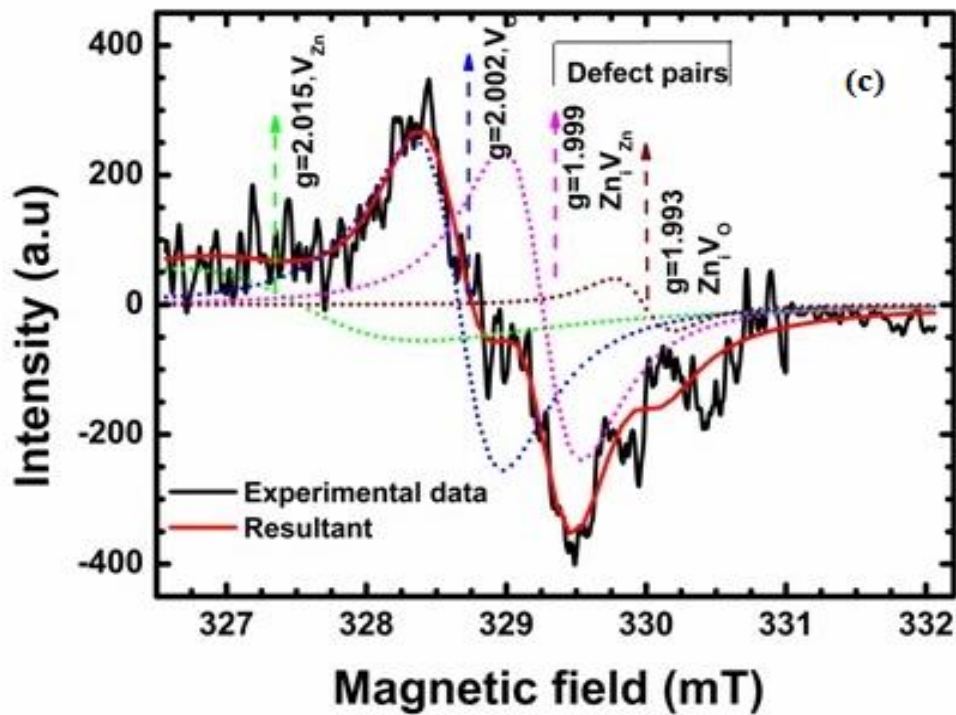
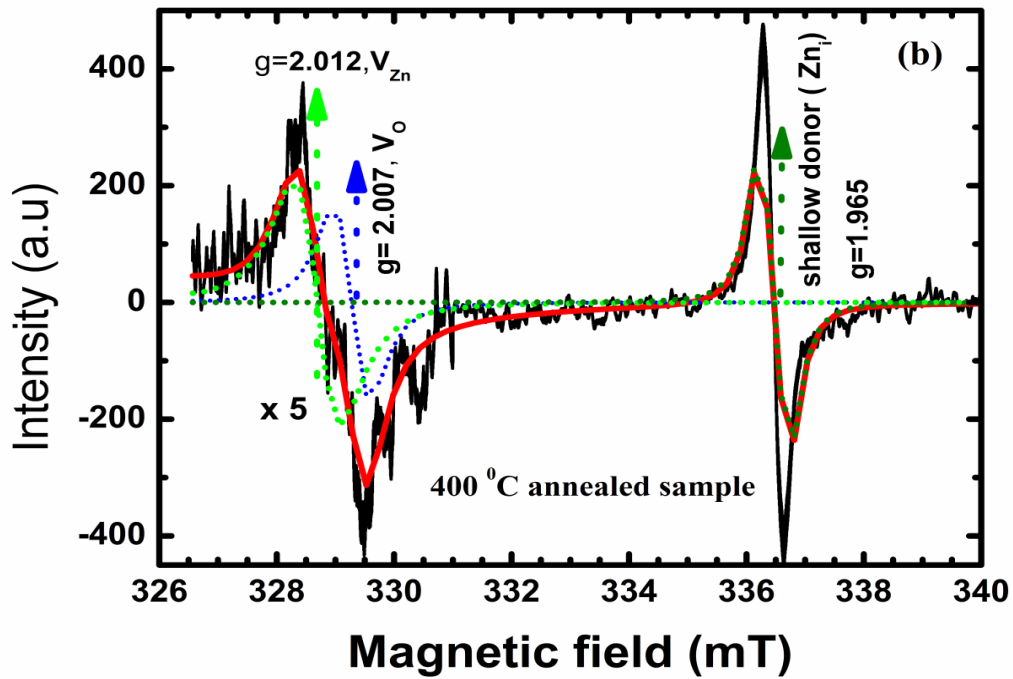


Figure 3.13: (a) Low temperature ESR spectra of CA at 400°C, (b) Deconvoluted shows the low temperature ESR spectra of CA at 400°C, (c) Deconvoluted shows the low temperature ESR spectra of CA at 400°C.

Figure 3.13 (a) shows the low temperature ESR spectra of 400°C annealed samples from 275K to 125K. It's deconvoluted spectra show the peaks at g value at 1.965, 2.007 & 2.012 which means the presence of ionized Zn_i , V_o and V_{Zn} defects respectively. This signal from Zn_i could be from surface or from bulk. The peaks at g value 2.007 seem broad and superimposed. It was then again deconvoluted using Lorentzian fits and clear signals at $g = 2.002$, 1.999 & 1.993 has been observed. These signal at $g = 1.999$ & $g = 1.993$ are attributed to ionized defects pairs Zn_iV_{Zn} & Zn_iV_o respectively. It confirms the interaction between intrinsic defects and hence the existence of defect complexes.

Figure 3.14 shows the ESR spectra of CA at 800°C at low temperatures. Interestingly ESR spectra of 800°C show one broad and asymmetric Lorentzian line, rather a Dysonian line shape.

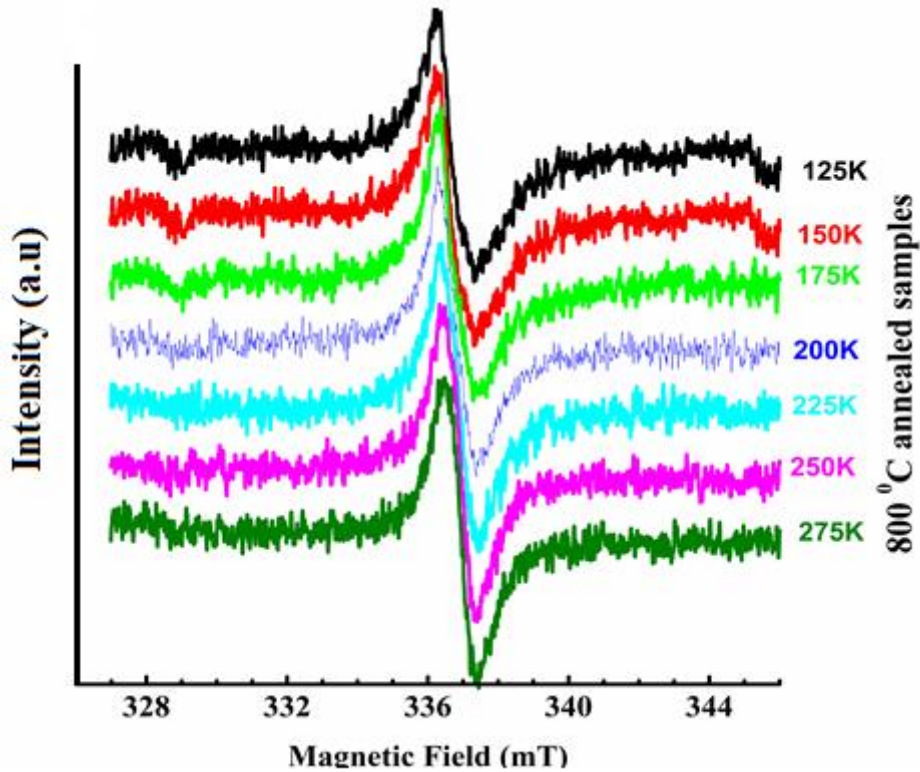
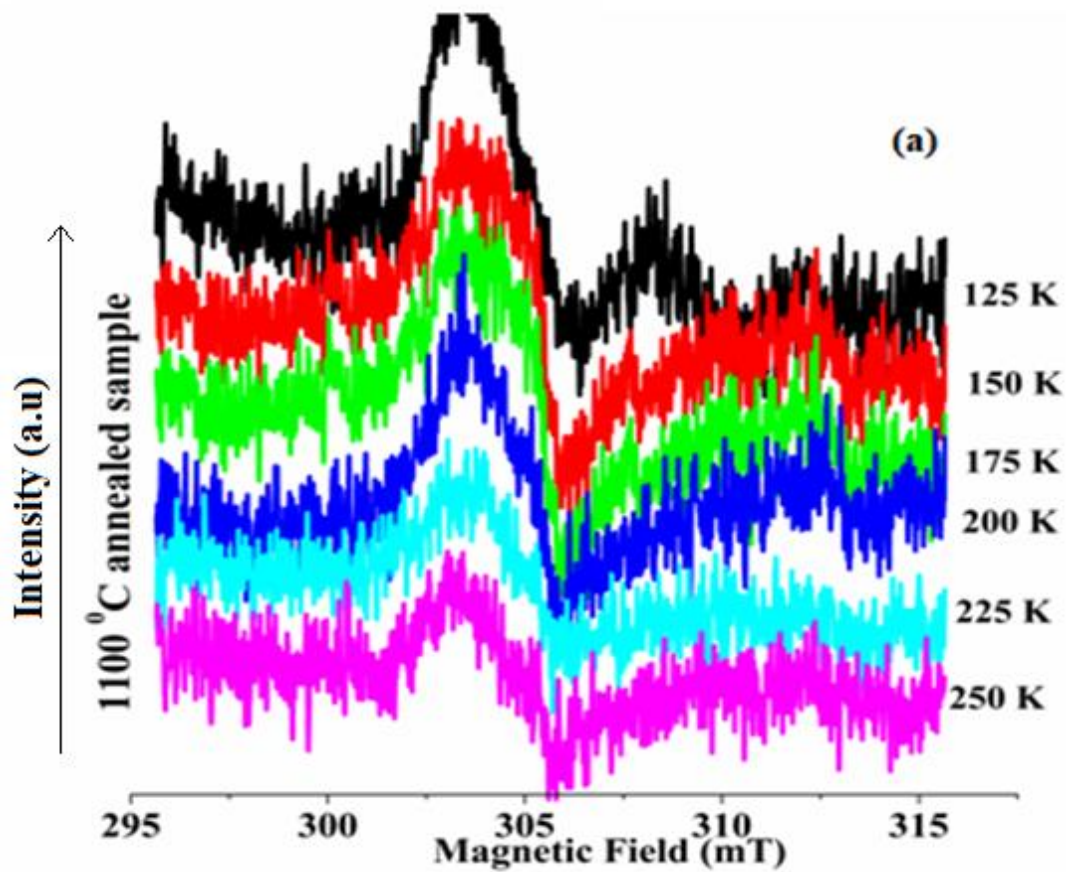


Figure 3.14: Low temperature ESR spectra of 800°C.

This line shape usually arises when skin effect drives the electric and magnetic microwave component out of phase in the sample and lead to an admixture of dispersion component into absorption one. But in our case penetration depth is of the order of few micrometers i.e. larger than grain size so the dispersion component must not be coming from there. Rather a Dysonian line shape may occur because of disproportionate surface effects [40]. Hence, signal at $g = 1.966$ indicates that Zn_i is located in surface region or at the grain boundaries.

Therefore it is expected that ferromagnetic nature of undoped annealed ZnO is due to presence of multi domains schematically shown in inset of figure 3.12. Direct interaction between Zn_i and V_{Zn} or defect pair via conduction electrons causes ferromagnetism in CA undoped ZnO samples. At 1100°C the CA ZnO turned out to be diamagnetic in nature.



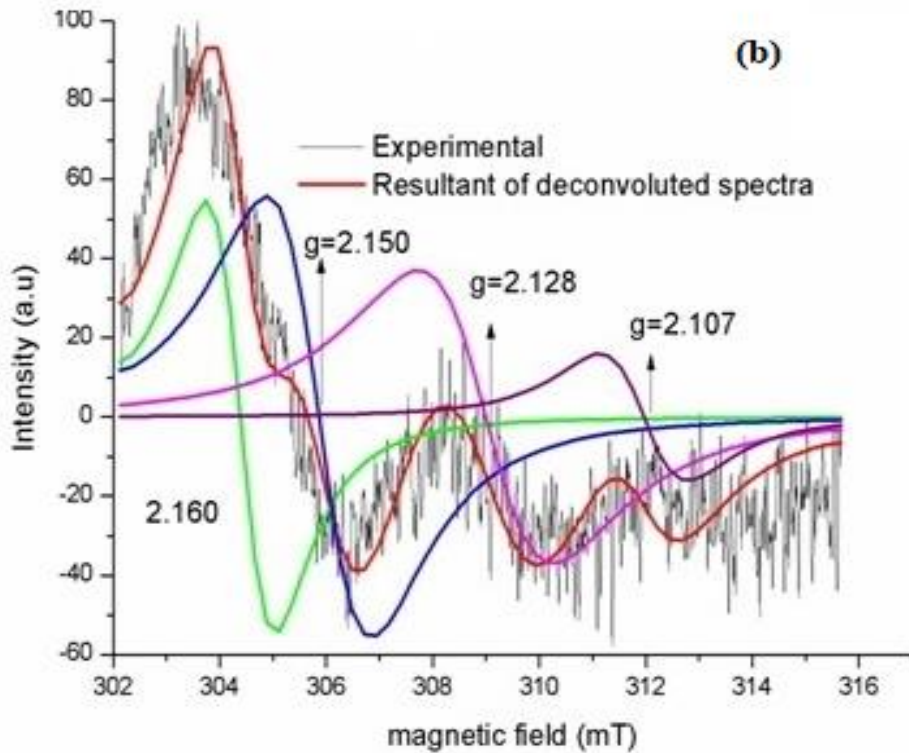


Figure 3.15: (a) Low temperature ESR spectra of 800°C at , (b) Deconvoluted ESR spectra at 125K.

This result is further supported by ESR spectra of 1100°C where there is no signature of Zn_i . Only the deep defects pairs were observed at g value. These Zn_i which served as mediators for enhanced coupling between shallow donors were absent and hence could not induce FM. Hence, samples at 1100°C turned diamagnetic in nature.

The variation of g value with low temperature is plotted in figure 3.16 & figure 3.17. The g value of Zn_i for 400°C and 800°C decreased with the increasing temperature where as the g value for V_o increased with increasing temperature. This implies effect of spin orbit coupling and crystal field on Zn_i defects is very opposite to each other at both the temperatures. The increase in g value means the increased spin orbit interaction. It clearly signifies that Zn_i lie in different spatial environment for both the temperatures and experience different SO and CF.

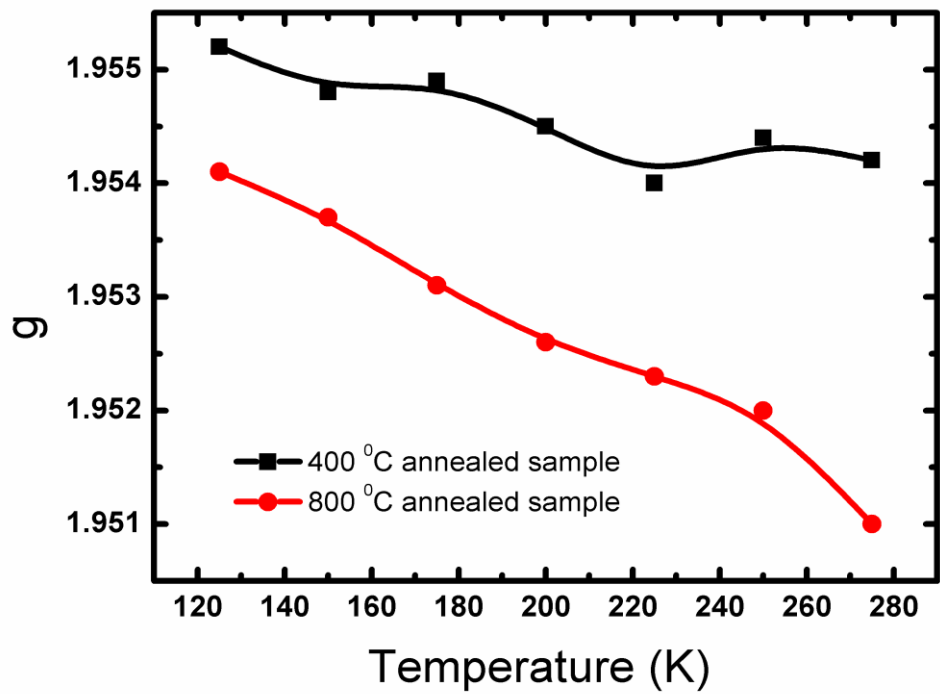


Figure 3.16: The g value of Zn_i plotted with temperatures.

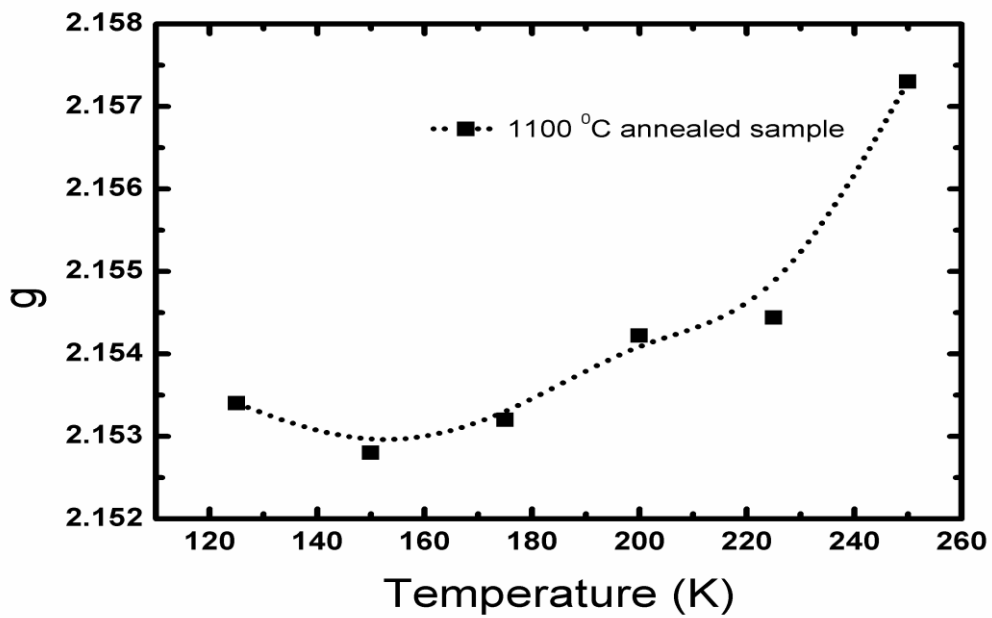


Figure 3.17: The g value of V_o plotted with temperatures.

3.4 Conclusion

The defect related optical & magnetic properties have been discussed briefly in this chapter. The defect related properties has been investigated using reflectance measurements & PL spectroscopy. It suggests the enhanced emissions from core of the grains while growing where as on the breaking of grains the enhanced emission from surface has been detected. The spatial distribution of defects inside grains has been recorded by Fluorescence imaging implies that the Zn_i are distributed throughout the surface whereas the O defects remained in the core. The paramagnetic centres have been detected by EPR spectroscopy & magnetic measurements were made using VSM measurements. The EPR spectra at 100K suggest the existence of Zn_i at surface as well as core. The VSM suggests that the CA samples exhibit RTFM till 1000°C but suddenly changes to diamagnetic at 1100°C. The Zn_i has been attributed to mediated FM in the annealed samples. The absence of Zn_i at 1100°C has been reasoned for the absence of FM in samples.

REFERENCES

- [1] D. C. Look, “*Recent advances in ZnO materials and devices*”, Materials Science and Engineering: B, vol. 80, no. 1–3, pp. 383–387, 2001.
- [2] D. M. Bagnall, Y. F. Chen, Z. Zhu, T. Yao, S. Koyama, M. Y. Shen, and T. “*Optically pumped lasing of ZnO at room temperature*”, Applied Physics Letters, vol. 70, 2230-2232, 1997.
- [3] Z. P. Wei, Y. M. Lu, D. Z. Shen, Z. Z. Zhang, B. Yao, B. H. Li, J. Y. Zhang, D. X. Zhao, X. W. Fan, and Z. K. Tang , “*Room temperature p-n ZnO blue-violet light-emitting diodes*”, Applied Physics Letters, vol. 90, no. 4, pp. 4–7, 2007.
- [4] T. Dietl, H. Ohno, F. Matsukura, J. Cibert, and D. Ferrand, “*Zener model description of ferromagnetism in zinc-blende magnetic semiconductors*”, Science (80), vol. 287, no. 5455, pp. 1019–1022, 2000.
- [5] A. Tsukazaki, A. Ohtomo, T. Onuma, M. Ohtani, T. Makino, M. Sumiya, K. Ohtani, S. F. Chichibu, S. Fuke, Y. Segawa, H. Ohno, H. Koinuma, and M. Kawasaki, “*Repeated temperature modulation epitaxy for p-type doping and light-emitting diode based on ZnO*”, Nature. Materials, vol. 4, no. 1, pp. 42–45, 2005.
- [6] M. Kasuga and S. Ogawa, “*Electronic Properties of Vapor-Grown Heteroepitaxial ZnO Film on Sapphire*”, Japanese journal of applied physic, vol. 22, pp. 794–798, 1983.
- [7] T. Sekiguchi, S. Miyashita, K. Obara, T. Shishido, and N. Sakagami, “*Hydrothermal growth of ZnO single crystals and their optical characterization*”, Journal of crystal growth, vol. 214, pp. 72–76, 2000.
- [8] N. R. Aghamalyan, I. A. Gambaryan, E. K. Goulanian, R. K. Hovsepyan, R. B. Kostanyan, S. I. Petrosyan, E. S. Vardanyan, and A. F. Zerrouk, “*Influence of thermal annealing on optical and electrical properties of ZnO films prepared by electron beam evaporation*”, Semiconductor science and technology, vol. 18, pp. 525–529, 2003.
- [9] H. Cao, Y. G. Zhao, S. T. Ho, E. W. Seelig, Q. H. Wang, and R. P. H. Chang, “*Random laser action in semiconductor powder*”, Physical Review Letters, vol. 82, no. 11, pp. 2278–2281, 1999.

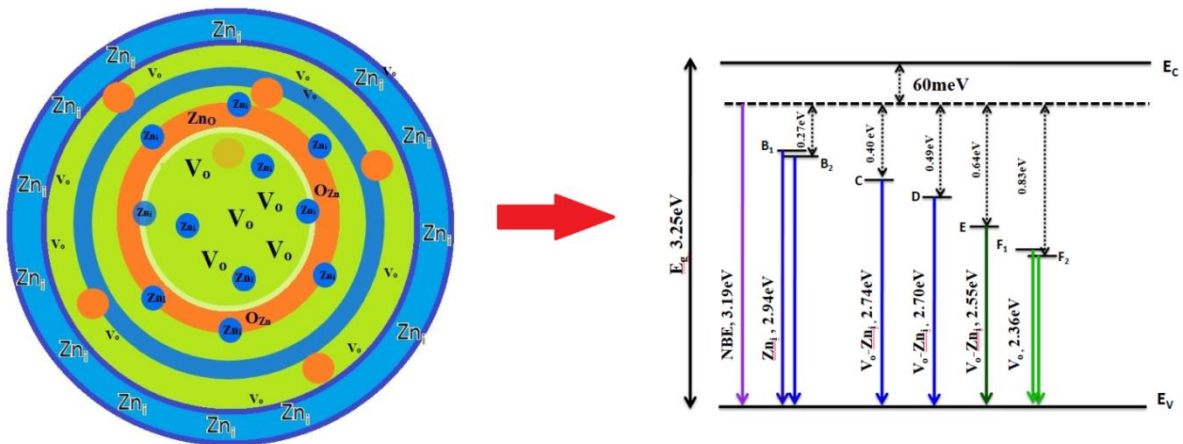
- [10] H. Cao, Y. G. Zhao, H. C. Ong, S. T. Ho, J. Y. Dai, J. Y. Wu, and R. P. H. Chang, “*Ultraviolet lasing in resonators formed by scattering in semiconductor polycrystalline films*”, *Applied Physics Letters*, vol. 73, no. 25, pp. 3656–3658.
- [11] D. Chu, Y. Masuda, T. Ohji, and K. Kato, “*Formation and photocatalytic application of ZnO nanotubes using aqueous solution*”, *Langmuir*, vol. 26, no. 4, pp. 2811–2815, 2010.
- [12] Ü. Özgür, Y. I. Alivov, C. Liu, A. Teke, M. A. Reshchikov, S. Doğan, V. Avrutin, S. J. Cho, and H. Morkoç, “*A comprehensive review of ZnO materials and devices*”, *Journal of Applied Physics*, vol. 98, no. 4, pp. 1–103, 2005.
- [13] L. Schmidt-Mende and J. L. MacManus-Driscoll, “*ZnO - nanostructures, defects, and devices*”, *Materials Today*, vol. 10, no. 5, pp. 40–48, 2007.
- [14] K. Vanheusden, W. L. Warren, C. H. Seager, D. R. Tallant, J. A. Voigt, and B. E. Gnade, “*Mechanisms behind green photoluminescence in ZnO phosphor powders*”, *Journal of Applied Physics*, vol. 79, no. 10, pp. 7983–7990, 1996.
- [15] S. B. Zhang, S. H. Wei, and A. Zunger, “*Intrinsic n-type versus p-type doping asymmetry and the defect physics of ZnO*”, *Physical Review B*, vol. 63, no. 7, 2001.
- [16] S. a Studenikin, N. Golego, and M. Cocivera, “*Fabrication of green and orange photoluminescent, undoped ZnO films using spray pyrolysis*” *Journal of Applied Physics*, vol. 2287, no. 1998, pp. 22–24, 2012.
- [17] A. F. Kohan, G. Ceder, D. Morgan, and C. G. Van de Walle, “*First-principles study of native point defects in ZnO*”, *Physical Review B*, vol. 61, no. 22, pp. 15019–15027, 2000.
- [18] L. E. Halliburton, N. C. Giles, N. Y. Garces, M. Luo, C. Xu, L. Bai, and L. A. Boatner, “*Production of native donors in ZnO by annealing at high temperature in Zn vapor*”, *Applied. Physics Letters*, vol. 87, no. 17, pp. 1–3, 2005.
- [19] D.J Binks, PhD thesis, University of Surrey, 1999.
- [20] B. Lin, Z. Fu, and Y. Jia, “*Green luminescent center in undoped zinc oxide films deposited on silicon substrates*”, *Applied Physics Letters*, vol. 79, no. 7, pp. 943–945, 2001.
- [21] F.A. Kroger, *The chemistry of imperfect crystals* 2nd edition, North Holland Amsterdam 1974.
- [22] E. G. Bylander, “*Surface effects on the low-energy cathodoluminescence of zinc oxide*”, *Journal of Applied Physics*, vol. 49, no. 3, pp. 1188–1195, 1978.

- [23] G. Xiong, U. Pal, and J. G. Serrano, “*Correlations among size, defects, and photoluminescence in ZnO nanoparticles*”, *Journal of Applied Physics*, vol. 101, no. 2, 2007.
- [24] M. L. Singla, M. Shafeeq M, and M. Kumar, “*Optical characterization of ZnO nanoparticles capped with various surfactants*”, *Journal of Luminescence*, vol. 129, no. 5, pp. 434–438, 2009.
- [25] N. S. Norberg and D. R. Gamelin, “*Influence of surface modification on the luminescence of colloidal ZnO nanocrystals*”, *The Journal of Physical Chemistry B*, vol. 109, no. 44, pp. 20810–20816, 2005.
- [26] V. Kumar, S. K. Sharma, T. P. Sharma and V. Singh, *J. Optical materials*, 21, 115 (1999)
- [27] C. G. Van De Walle and J. Neugebauer, “*First-principles calculations for defects and impurities: Applications to III-nitrides*”, *Journal of Applied Physics*, vol. 95, no. 8, pp. 3851–3879, 2004.
- [28] A. L. Taylor, G. Filipovich, and G. K. Lindeberg, “*Electron paramagnetic resonance associated with Zn vacancies in neutron-irradiated ZnO*”, *Solid State Communications*, vol. 8, no. 17, pp. 1359–1361, 1970.
- [29] R. M. Sheetz, I. Ponomareva, E. Richter, A. N. Andriotis, and M. Menon, “*Defect-induced optical absorption in the visible range in ZnO nanowires*”, *Physical Review B*, vol. 80, no. 19, pp. 1–4, 2009.
- [30] I. Shalish, H. Temkin, and V. Narayanamurti, “*Size-dependent surface luminescence in ZnO nanowires*”, *Physical Review B*, vol. 69, no. 24, pp. 1–4, 2004.
- [31] P. S. Xu, Y. M. Sun, C. S. Shi, F. Q. Xu, and H. B. Pan, “*The electronic structure and spectral properties of ZnO and its defects*”, *Nuclear Instruments and Methods in Physics Research Section B: Beam Interactions with Materials and Atoms*, vol. 199, pp. 286–290, 2003.
- [32] T. K. Gupta and W. D. Straub, “*Effect of annealing on the ac leakage components of the ZnO varistor. I. Resistive current*”, *Journal of Applied Physics*, vol. 68, no. 2, pp. 845–850, 1990.
- [33] H. S. Kang, J. S. Kang, J. W. Kim, and S. Y. Lee, “*Annealing effect on the property of ultraviolet and green emissions of ZnO thin films*”, *Journal of Applied Physics*, vol. 95, no. 3, pp. 1246–1250, 2004.

- [34] V. Gavryushin, G. Račiukaitis, D. Juodžbalis, A. Kazlauskas, and V. Kubertavičius, “*Characterization of intrinsic and impurity deep levels in ZnSe and ZnO crystals by nonlinear spectroscopy*”, *Journal of Crystal Growth*, vol. 138, no. 1–4, pp. 924–933, 1994.
- [35] H. Zeng, G. Duan, Y. Li, S. Yang, X. Xu, and W. Cai, “*Blue luminescence of ZnO nanoparticles based on non-equilibrium processes: Defect origins and emission controls*”, *Advanced Functional Materials*, vol. 20, no. 4, pp. 561–572, 2010.
- [36] N. Y. Garces, L. Wang, L. Bai, N. C. Giles, L. E. Halliburton, and G. Cantwell, “*Role of copper in the green luminescence from ZnO crystals*”, *Applied Physics Letters*, vol. 81, no. 4, pp. 622–624, 2002.
- [37] D. M. Hofmann, A. Hofstaetter, F. Leiter, H. Zhou, F. Henecker, B. K. Meyer, S. B. Orlinskii, J. Schmidt, and P. G. Baranov, “*Hydrogen: A Relevant Shallow Donor in Zinc Oxide*”, *Physical Review Letters*, vol. 88, no. 4, p. 4, 2002.
- [38] N. G. Kakazey, T. V. Srećković, and M. M. Ristić, “*Electronic paramagnetic resonance investigation of the evolution of defects in zinc oxide during tribophysical activation*”, *Journal of materials science*, vol. 32, no. 17, pp. 4619–4622, 1997
- [39] B. V. Ischenko, S. Polarz, D. Grote, V. Stavarache, K. Fink, and M. Driess, “*Zinc Oxide Nanoparticles with Defects*”, *Advanced Functional Material*, vol. 15, no. 12, pp. 1945–1954, 2005.
- [40] J. P. Joshi and S. V. Bhat, “*On the analysis of broad dysonian electron paramagnetic resonance spectra*”, *Journal of Magnetic Resonance*, vol. 168, no. 2, pp. 284–287, 2004.

CHAPTER 4

“SELECTIVELY ENHANCED DIFFERENT DEFECTS IN NANOCRYSTALLINE ZnO: A PATH TO MAKE P-TYPE ZnO WITHOUT DOPING BY MULTISTEP ANNEALING”



4.1 Introduction

As discussed in schematic of CA and MSA annealing figure 2.1 the diffusion constants in case of multistep annealing will change in every step of annealing. The different distribution of defects was initially presumed from the XRD result for same annealing temperatures, for CA and MSA the XRD peaks varied differently. The mechanism of multistep annealing has been discussed briefly in Chapter-II. It suggests that the kinetics of grain growth and diffusion of defects are totally different from CA. The stress generated out of diffusion of Zn_i along c axis was different in nature for both the cases. Hence, we conclude that MSA will lead to different type of defect distribution within the grain. In CA we concluded that Zn_i will migrate to surface and will reside on both the core as well as on surface. But in case of MSA Zn_i will migrate to surface till 200°C but after that when the diffusion coefficients change, the spatial location of Zn_i and V_o will be difficult to predict because they will diffuse anisotropically. The breaking of grain at 800°C implies that the concentration of defects at surface become more than core i.e. the defects diffused rigorously towards surface as compared to CA. To investigate for the magnetic, electrical and optical properties of MSA ZnO it is desirable to understand how a little change in microstructures can lead to different spatial distribution of defects and hence can tailor various different properties of the material. Therefore the understanding of the annealing process i.e. annealing time, annealing temperature, heating rate is vital to understand above said properties. Different groups have reported various annealing techniques like rapid thermal heating, conventional annealing, two step sintering, hot pressing or spark plasma sintering etc and have reported very different results [1-5]. Conventional annealing technique has been used for ample research in ZnO. Spark plasma sintering, a hot press technique with very high heating rate $\sim 100^\circ\text{C}/\text{min}$ was found to be effective in powder sample to achieve densification in nano crystalline ZnO. This process allows achieving higher annealing temperatures in very few minutes. Hence, to tailor different properties we first need to understand how the defects are spatially distributed in ZnO. The question to be answered in this chapter is how this spatial distribution is different to CA ZnO and how it tailors the optical and magnetic properties. We performed reflectance measurements and PL spectroscopy to investigate the electronics states of the defects. To detect the paramagnetic centers in the sample we performed EPR spectroscopy at low temperatures.

4.2 Result and discussions

4.2.1 Optical excitation and polychromatic emission

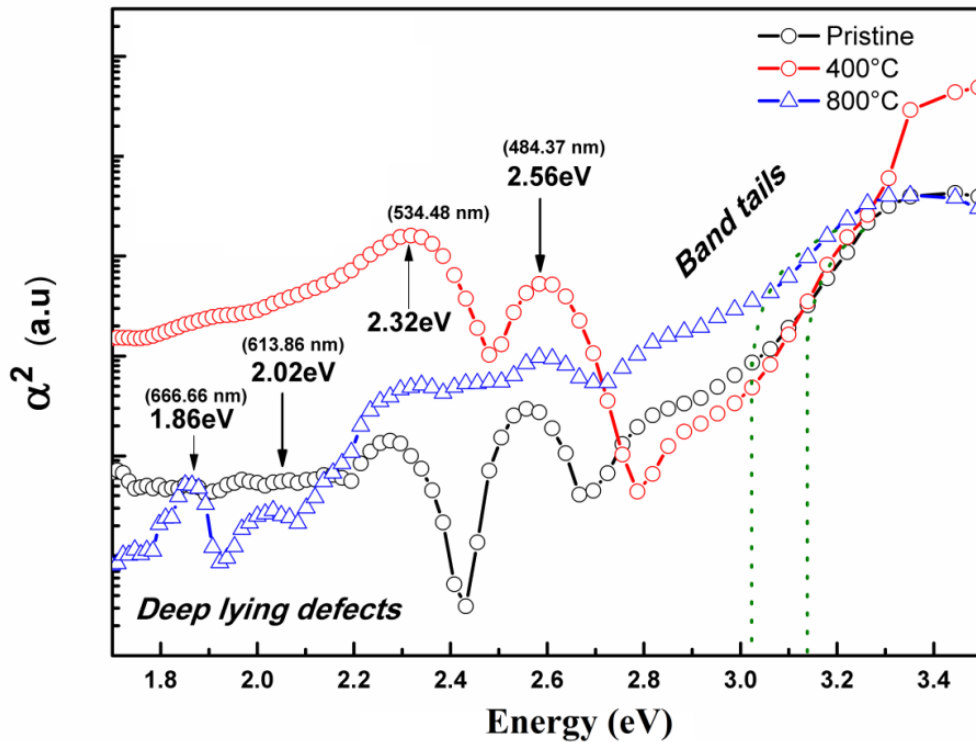


Figure 4.1: Square of absorption coefficient (α) versus with incident photon energy.

To study the absorption from the various defects lying in the band gap we made reflectance measurements for MSA ZnO samples. Variation of square of absorption coefficient (α) with incident photon energy for pristine and MSA samples at 400°C and 800°C is shown in figure 4.1. The optical band gap was predicted from Tauc fit to the experimental data shown in the dotted lines. A little change in band gap (E_g) was seen. The band gap decreases at 800°C by 96meV w.r.t pristine ZnO. Band gap narrowing at 800°C without any extrinsic doping is an important result, as band gap tuning has always been reported by doping ZnO by transition metal. Wang et al has reported band contraction because of increase in concentration of V_o in ZnO [6]. The oxygen vacancies must have increased in MSA process and ended up in contraction of E_g as it was validated by enhancement of

the phonon mode due to O vibration in Raman spectra. They winded up by saying that band gap doesn't change if the V_o are less in concentration but in case when the concentration is more the defect states becomes delocalized and overlap with the VBM and lift the position of the VB resulting in shrinking of E_g . The existence of surplus oxygen vacancies at MSA 800°C is figured out. It was even confirmed by Raman spectroscopy with the appearance and broadening of longitudinal optical (LO) phonon mode. The band tails like in CA were also noticed in MSA as a result of inhomogeneous distribution of defects within the sample [7]. The band tails at 800°C were broader than at other two MSA temperatures. Absorption at 2.56 eV, 2.32 eV and 2.02 eV and 1.86 eV are attributed to intrinsic deep lying defects of ZnO like V_o^+ , V_o , V_{Zn} . For 800°C annealed ZnO the peak centered at 2.32 eV is wide & may due to the existence surplus of oxygen vacancies in the sample.

Firstly to see the emissions from intrinsic defects, the samples were excited from excitation wavelength 300 nm and 400 nm respectively i.e. the excitation with energy more than and less than the band gap energy.

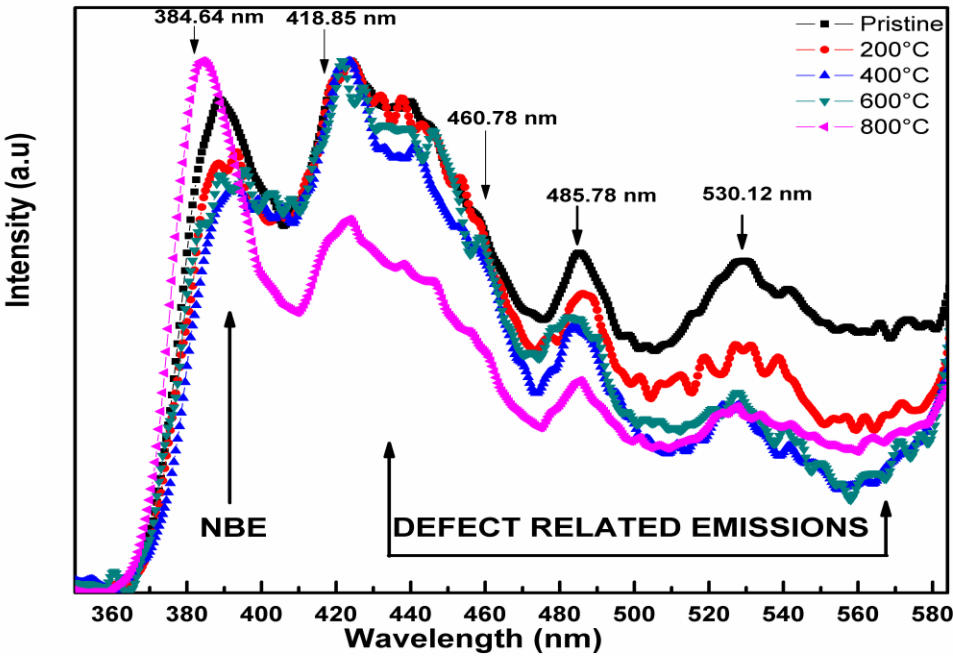
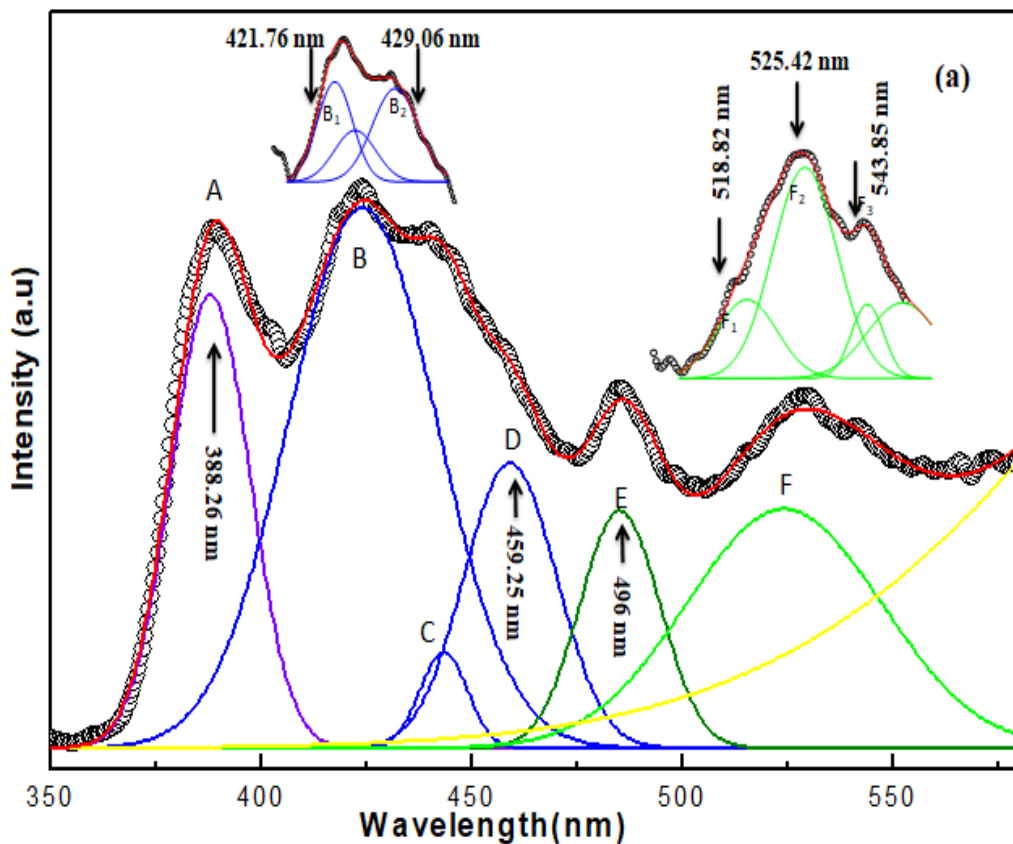


Figure 4.2: Photoluminescence spectra of MSA samples.

As discussed earlier the PL spectra typically consist of NBE and defect related peaks in the visible region. The peak centered at 384.64 nm is from the band to band transition (NBE). The NBE is quenched at 200°C, 400°C and 600°C and unexpectedly enhances at 800°C. NBE peak position shifts from Pristine (384.64 nm) to 800°C (389.33 nm) implying the little shift in band gap energy. The band gap narrows at 800°C by 96meV.

As suggested in the grain growth mechanism that the defects distributions inside the grains for MSA are very different to the CA so their emissions will also be very different. The emission from the native defects lying between the VBM and the CBM is observed in visible region from 400 nm to 575 nm in the PL spectra.



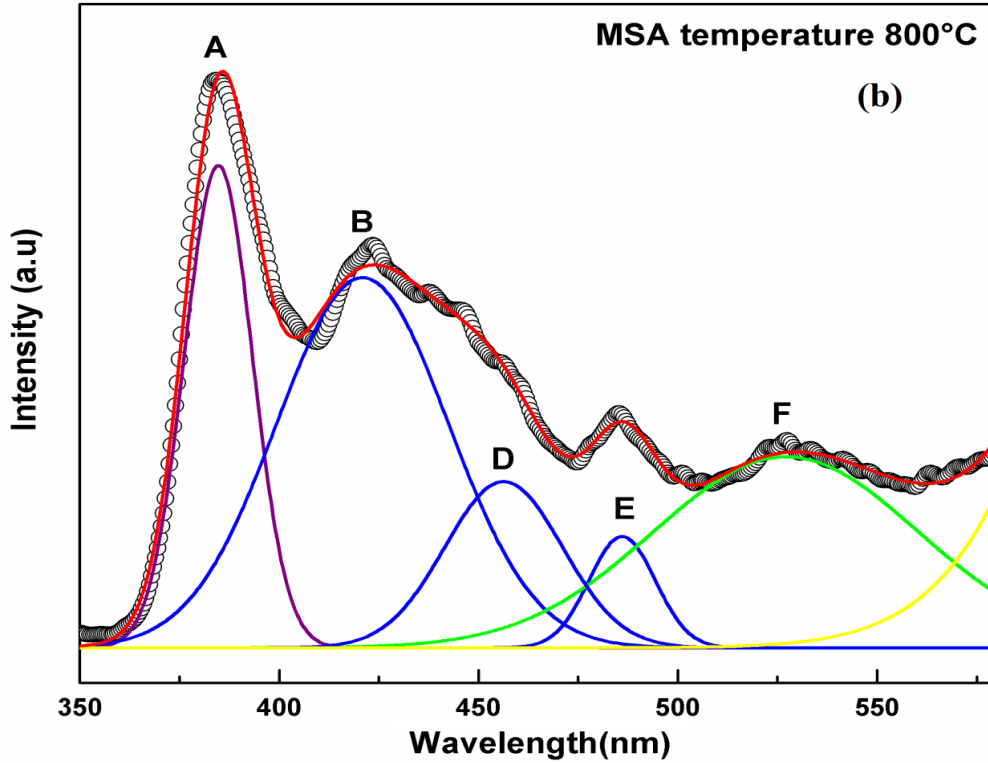


Figure 4.3: (a) Deconvoluted PL spectra of 400°C MSA sample, (b) Deconvoluted PL spectra of 800°C MSA sample.

The deconvolution of PL spectra of 400°C and 800°C of MSA sample was done. The presence of blue emission is denoted by peak B. This peak B is associated with shallow donors i.e. Zn_i . Its position lies 0.27 eV below the CBM. The wide peak “B” is further deconvoluted into peak B_1 (2.94 eV) and B_2 (2.89 eV) and that is due to Zn_i or Zn_i clusters i.e. the existence of different states of Zn_i [8].

The green luminescence has been allocated to O related defects. It is V_o lies 0.9 eV below the CBM. Peak labeled F positioned 0.83 eV below the CBM is related to oxygen vacancies. It is further deconvoluted into 3 distinct peaks i.e. F_1 (2.39 eV), F_2 (2.36 eV) and F_3 (2.28 eV). Three possible states of V_o exist: neutral oxygen vacancy (V_o), single ionized oxygen vacancy V_o^+ and doubly ionized oxygen vacancy V_o^{++} . Liao et al reported the emission from V_o^{++} is in yellow region [9]. So the V_o^{++} cannot be responsible for emission of F_2 . The dominant of all the three peaks is F_2 and is attributed directly to single ionized oxygen vacancy.

In MSA samples the concentrations of defects becomes high and defect-defect interaction becomes obligatory to be taken into account. There can be 3 kinds of interactions as reported by Kim et al [10]: (i) Columbic repulsion between Zn_i-Zn_i (ii) Interaction between V_o-V_o (iii) Interaction between the V_o-Zn_i and formation of complexes. V_o-Zn_i is the most favorable complexes because of their low formation energy. They lie somewhere between the energy states of V_o and Zn_i . The peak C (2.80), D (2.7ev) and E (2.5ev) are attributed to the complexes of V_o-Zn_i . Minor differences in the energies of these complexes arise from their varying separations in the ZnO lattice. The defect evolution was investigated by plotting intensity ratio of F, E, B peaks with respect to NBE versus annealing temperature as shown in figure 4.4. The nature of Zn_i and V_o-Zn_i complexes were derived. It was found that the variation of peak F was different from the nature of peak B and peak E implying that the V_o were found to be varying strongly with MSA temperature meaning thereby that the diffusion of oxygen vacancies were rigorous.

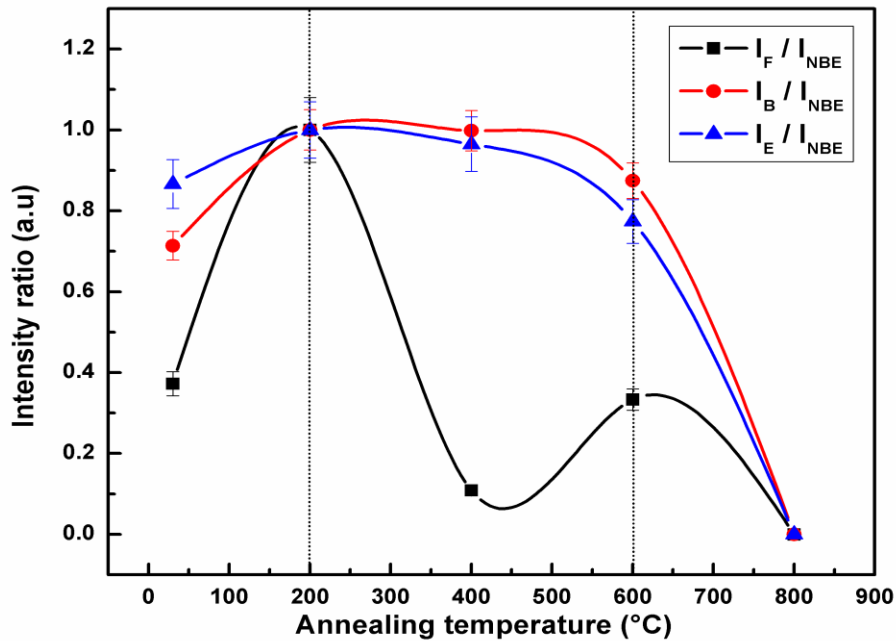


Figure 4.4: Variation of Intensity ratio of defect complexes with respect to NBE versus multistep annealing temperature.

4.2.2 Sub band excitation and emissions

To authenticate the stability of V_o - Zn_i and defects lying within the band gap we did PL measurements by sub band excitations. Further from the excitation wavelength of 400nm the samples were excited and PL was recorded. The results which aroused the curiosity were the stable emissions from V_o - Zn_i and existence of intensified emissions from oxygen vacancies at 800°C as shown in figure 4.5. The luminescence from V_o asserted exceptionally wide luminescence peak and dominated the emissions from V_o - Zn_i . The enlarged & wide luminescence confirms the subsistence of excess V_o in the sample. Zn_i are shallow defects usually lying on the surface as well as the bulk of the grains so they can be easily tailored by CA where as oxygen vacancies lie somewhere in the deep and hence cannot be easily tailored. Therefore, one can conclude that MSA can provide plenty enough energy to V_o so that they can migrate and diffuse throughout the grains. After 400°C in MSA process, the formation of Zn_i stopped; V_o made complexes with Zn_i till 600°C and then at 800°C when the complexes formation saturated only the V_o increased.

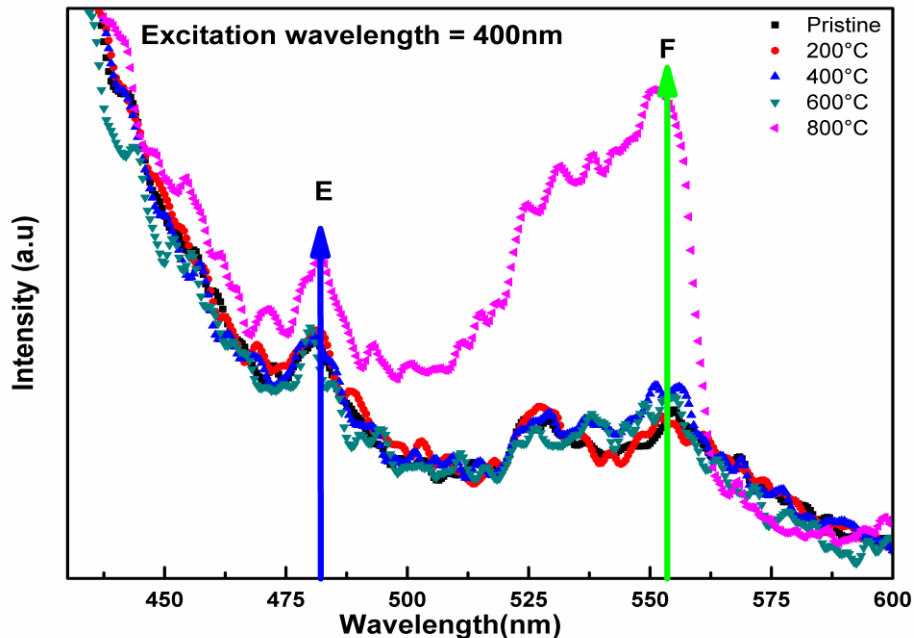


Figure 4.5: PL spectra at excitation wavelength of 450nm.

4.2.3 EPR measurements and magnetic studies

To investigate magnetic studies of MSA samples we performed Room Temperature VSM as shown in figure 4.6.

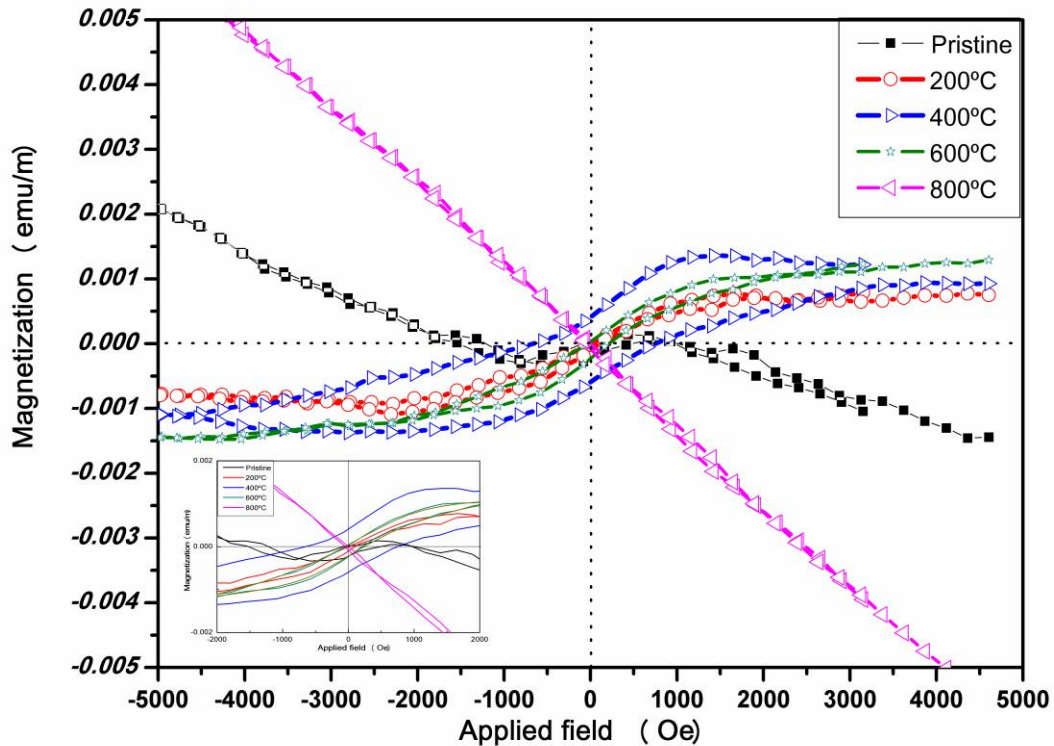


Figure 4.6: M-H curve of all the MSA samples.

It was observed that the MSA ZnO samples till 600°C shows a pure ferromagnetic behavior. The inset shows small but significant value of coercive field and remnant magnetization. The MSA samples annealed at 800°C shows a pure diamagnetic behavior and MSA samples at 400°C shows the maximum magnetization. Figure 4.7 shows variation of saturation magnetization with annealing temperature. It is maximum at 400°C and minimum 800°C. The transition from FM to diamagnetism occurred at 800°C in case of MSA.

Hence, we choose two temperatures 400°C (FM) and 800°C (diamagnetism) for EPR at low temperatures till 125K.

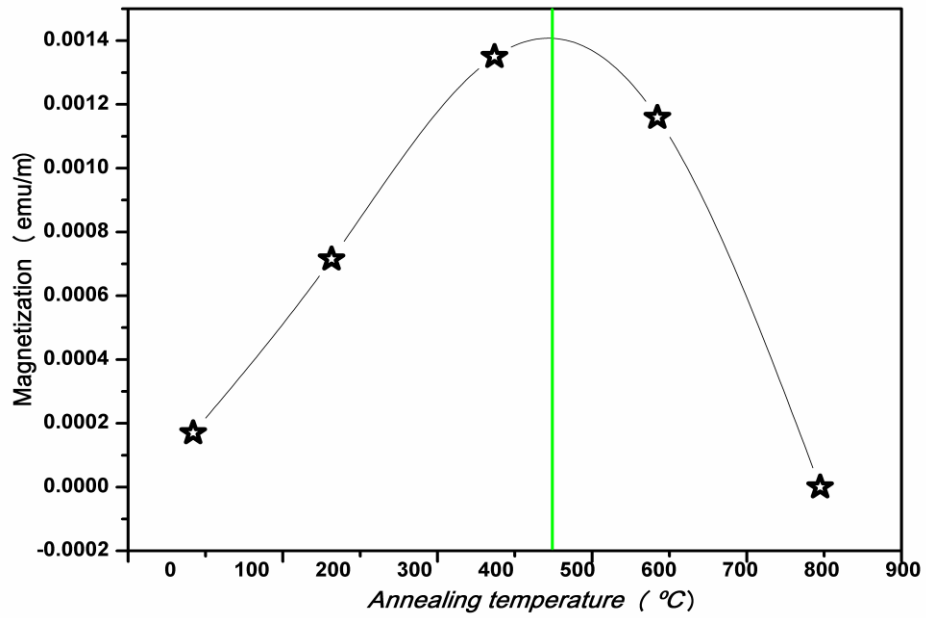
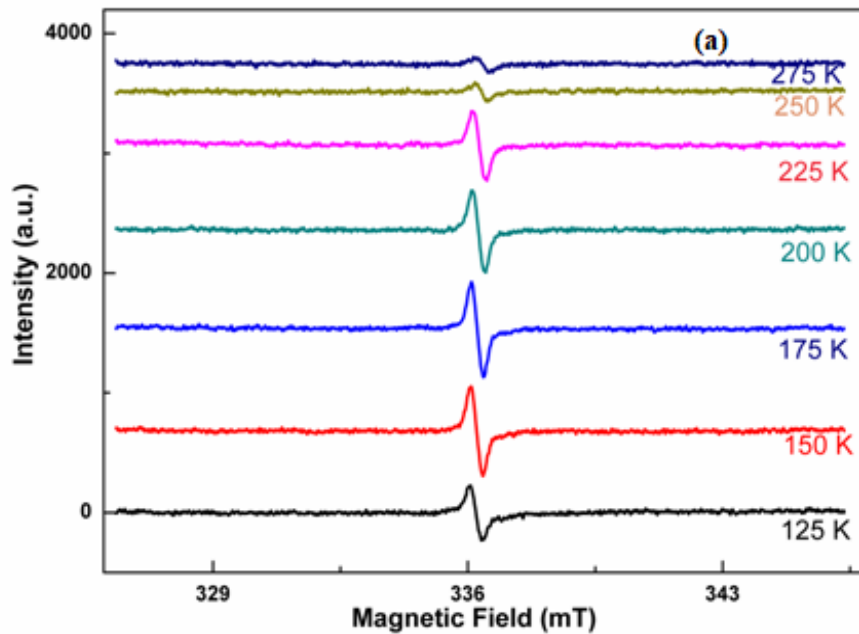


Figure 4.7: Magnetization versus MSA temperature.

Figure 4.8 (a) and (b) shows the low temperature ESR spectra for MSA 400°C and 800°C samples at various temperatures.



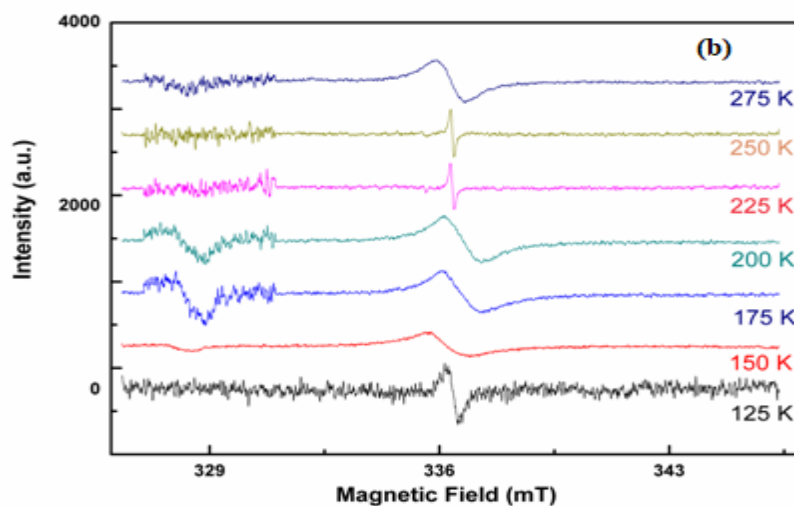
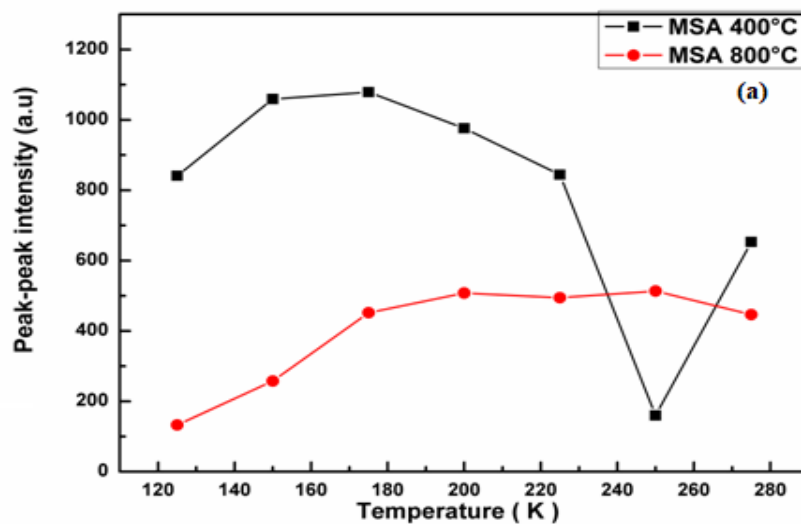


Figure 4.8: (a) ESR spectra of 400°C MSA sample from 275K to 125K, (b) ESR spectra of 800°C MSA sample from 275K to 125K.

The ESR spectra of 400°C show one and only signal centered at g value 1.965 which is attributed to Zn_i . The signal coming from Zn_i lies in the core as well as the surface. The peak to peak intensity of this peak as shown in figure 4.9 (a) decreases with increasing temperature after 200K, where as peak to peak intensity at 800°C increases by a very less value. Contrary to this the line width of Zn_i at 400°C remains unchanged but at 800°C it changed significantly.



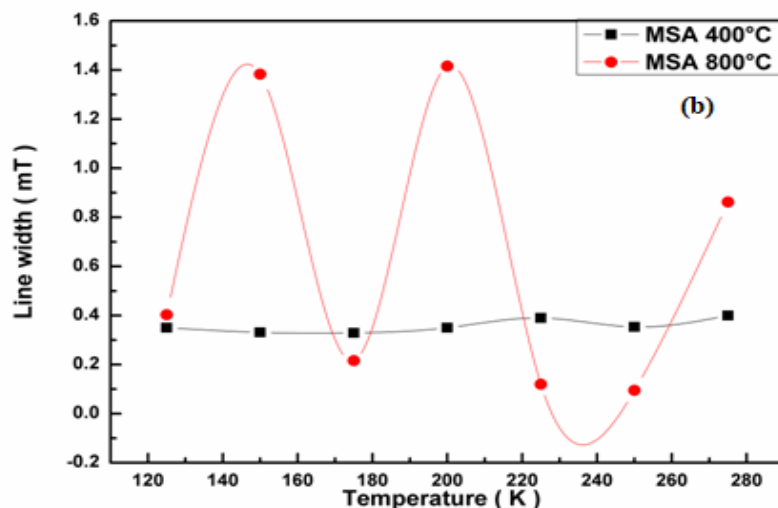


Figure 4.9: (a) Variation of peak to peak intensity of MSA 400°C and 800°C with temperature, (b) Variation of line width of MSA 400°C & MSA 800°C with temperature.

Significant change in line width implies that the spin lattice interaction. Samples at MSA 800°C are rich in surface defects as proved by structural studies, grain breaks and increases the surface defects. The ESR signal seems very asymmetric at 800°C. This could be attributed to anisotropy due to breaking of grains and defect diffusions. The line width is almost constant in case of 400°C as compared to 800°C. This could be attributed to increased spin lattice interactions at 800°C as the grain breaks.

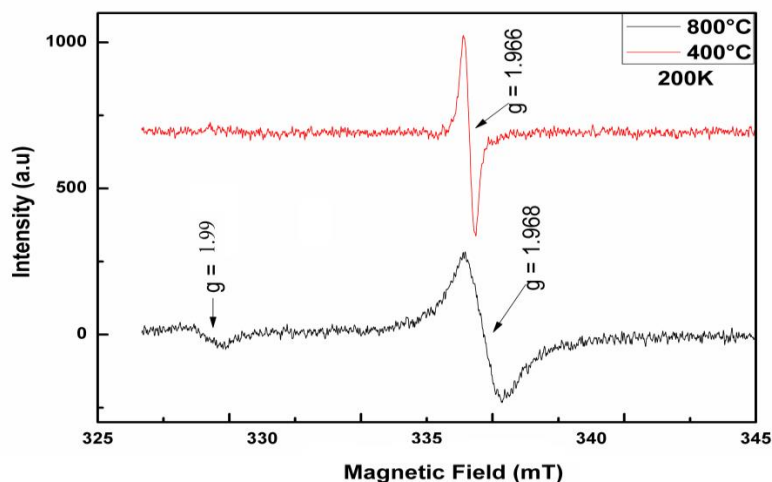


Figure 4.10: ESR spectra at 200K for 400°C and 800°C MSA sample.

We then plotted EPR of both the temperatures at 200K. Figure 4.10 clearly shows that at 400°C there is only signal attributed to Zn_i whereas at 800°C there are signals from Zn_i as well as V_o . The signal at 800°C is asymmetric and has a Dysonian line shape. Hence, the ferromagnetism at 400°C is clearly attributed to Zn_i defects at the surface as well as the core.

4.3 Comparative study of conventional and Multi step annealing

With the help of different characterization techniques the different analysis based on defect related studies has been made. The conclusion and differences in both the studies are made as following:

4.3.1 Mechanisms

In CA annealing the diffusion coefficients and the diffusion barriers are constant where as in case of MSA the diffusion constants of the defects are not fixed. They change in each step of annealing which means that the diffusion of defects in MSA does not remain isotropic during the process. The defect diffusion takes place differently in each step and defects relocate differently within the grains. The schematic of grain growth and distributions of various defects is shown in figure 4.11. According to grain growth model of in CA the Zn_i diffuse to surface and V_o remain in the core of the grain. The concentration of Zn_i at surface becomes more but in case of MSA the defects migrates randomly in each part of the grain.

A uniform distribution of defects does not take place as the diffusion constant of defects keep changing in every step of MSA. Hence, it becomes very difficult to spot the actual site of the defects within the grain. Defects interact with each other. The complex formation of Zn_i with V_o has also been observed with help of photoluminescence spectroscopy.

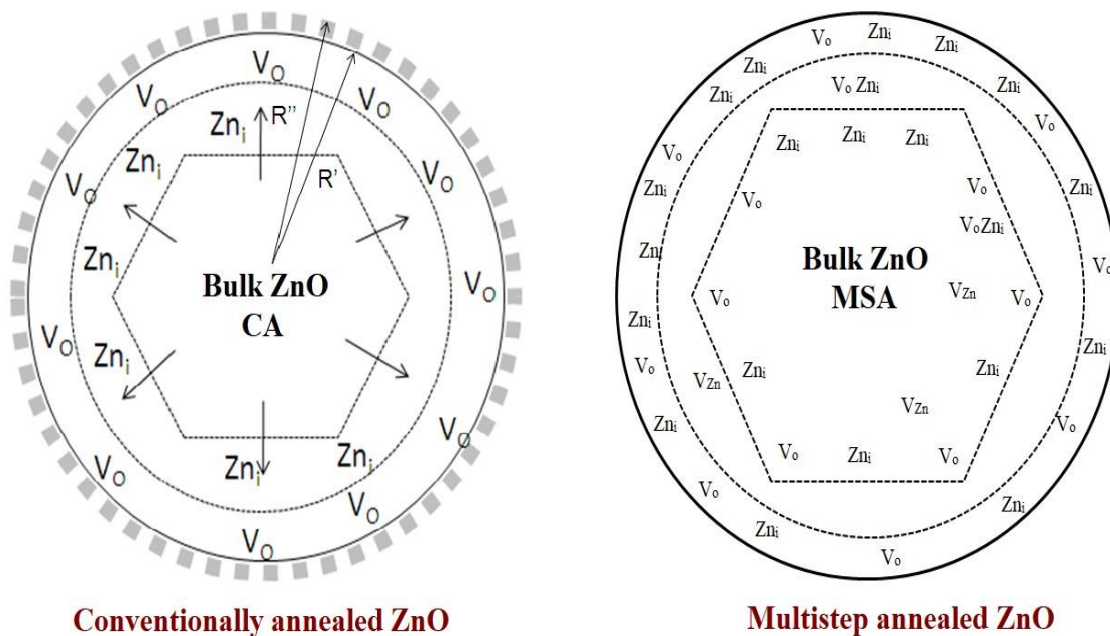


Figure 4.11: Schematic of distribution of defects within the grains in CA and MSA process.

4.3.2 Morphological studies

From the FESEM studies, as shown in figure 4.12 (a) and (b) we found that at temperature 400°C the shape of grains was perfectly spherical in case of CA where as in case of MSA the grains were cylindrical rod like structures and hexagonal shaped grains. It implied that the defects diffusion was not isotropic in all directions but was directional in case of MSA. As the MSA temperature increased the rods started becoming thicker and thicker and finally converted into spherical structures. Diffusion equation was further solved in spherical coordinate system for CA where as in cylindrical coordinate system for MSA which implemented very different results and different distributions.

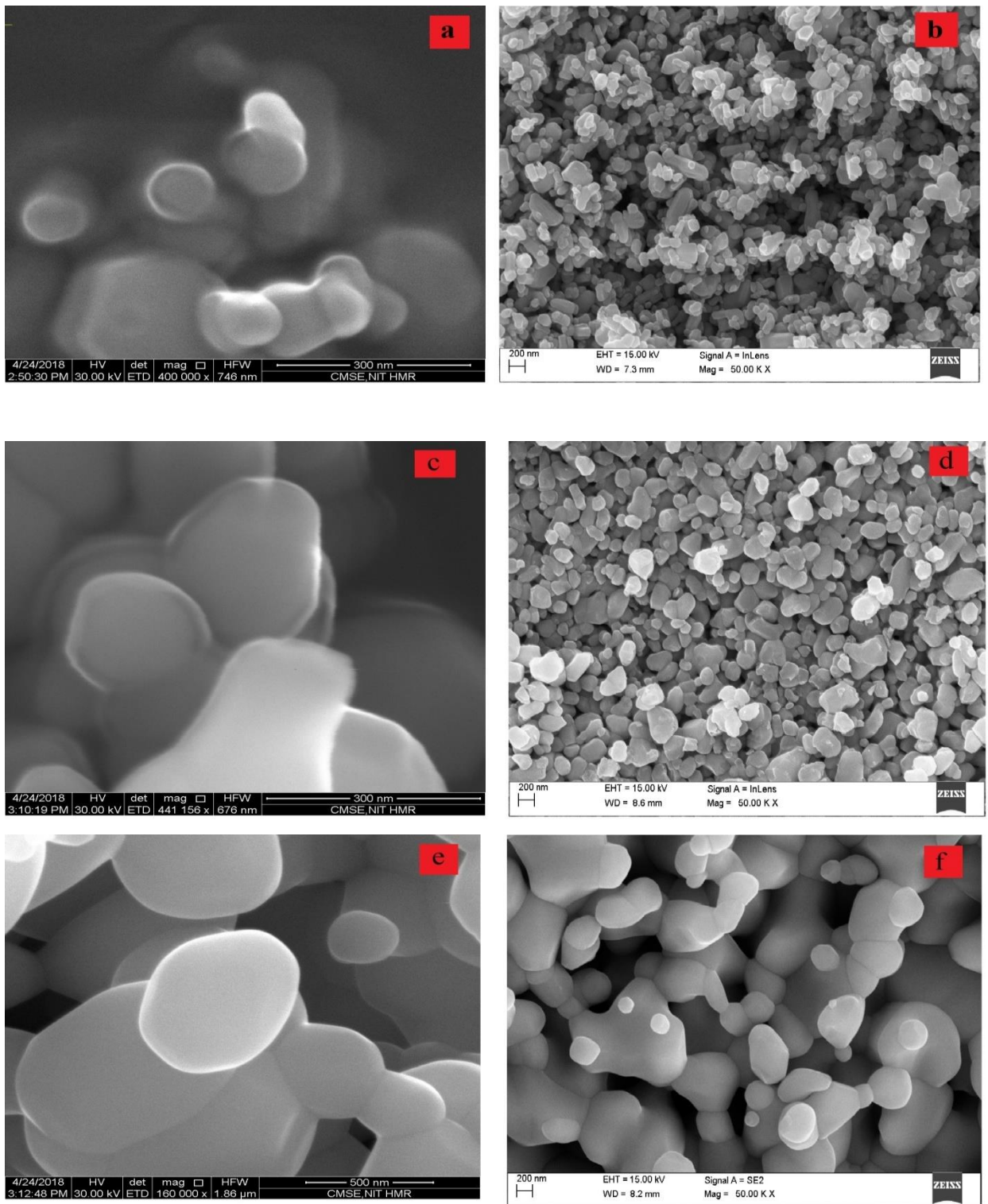
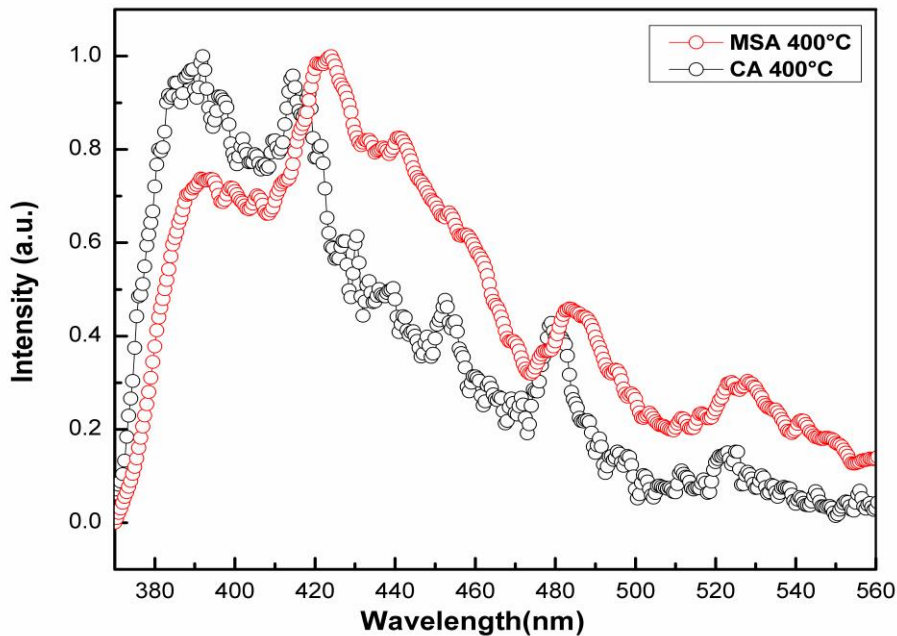


Figure 4.12: (a) FESEM image of CA 400°C, (b) FESEM image of MSA 400°C, (c) FESEM image of CA 600°C, (d) FESEM image of MSA 600°C, (e) FESEM image of CA 800°C, (f) FESEM image of MSA 800°C

Figure 4.12 (c) and (d) shows the FESEM images of 800°C CA and MSA samples. We see that at 800°C the grains due to MSA transformed into spherical grains where the grain boundary formation is clearly seen. The defects at grain boundaries, their interactions and their influence on magnetic properties are of great importance.

4.3.3 Photoluminescence studies

The different distributions of defects during CA and MSA can be visualized by photoluminescence emissions from defect states. There exist a huge difference between the emission at 400°C from CA and MSA. According to the spatial distributions of defects within the grain as discussed in chapter-II emission in NBE is attributed to defects in the core whereas defects in green and blue visible region are attributed to defects on the surface. The NBE seems enhanced in case of CA whereas it seems quenched for MSA with respect to defects related visible emissions. This means that concentration of defects in CA due to 400°C was more in the core of the grain whereas for MSA the defects at surface were more.



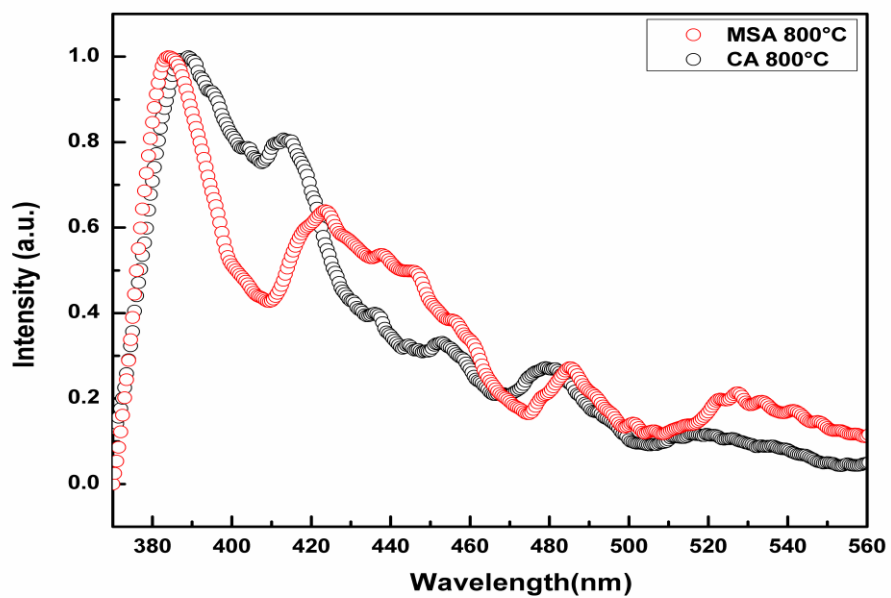
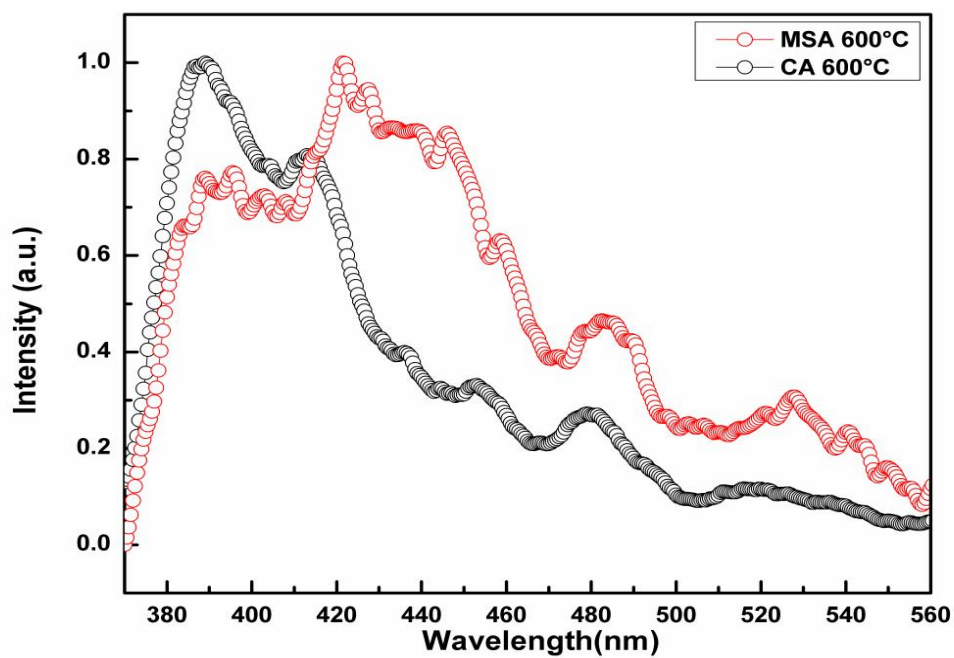


Figure 4.13: (a) PL spectra of CA and 400°C MSA sample (b) PL spectra of CA and 600°C MSA sample, (c) PL spectra of CA and MSA at 800°C.

From figure 4.13 (b) we see again the defects related visible emission was more and NBE was quenched where as at MSA 800°C. At 800°C the grain size reduced and surface defects were expected to be more but contraction prevailed in PL. This means that defects were randomly distributed in the grains in contrast to the systematic distribution in CA. Hence, we conclude by saying that annealing at one temperature by two different techniques leads to very different distributions of defects within the grain and hence will tailor all the defect related properties within.

4.3.4 EPR and Magnetic studies

For the identification of chemical nature of the intrinsic defects we performed EPR spectroscopy. We found that as the defect distribution was different found from PL spectroscopy the EPR spectra were also very different for CA and MSA. In figure 4.14 we see the EPR spectra at 125K for 400°C & 800°C. For CA there was a clear signal for Zn_i ($g = 1.96$) and V_o ($g = 1.99$) whereas for MSA there was no signal for V_o . Similarly, in case for 800°C the EPR signal is for both Zn_i as well as V_o . The Zn_i signal in CA appears broad and asymmetric can be thought as Dysonian line shape which particularly arises from the surface effects. This signal could be arising from Zn_i at the surface as well the core.

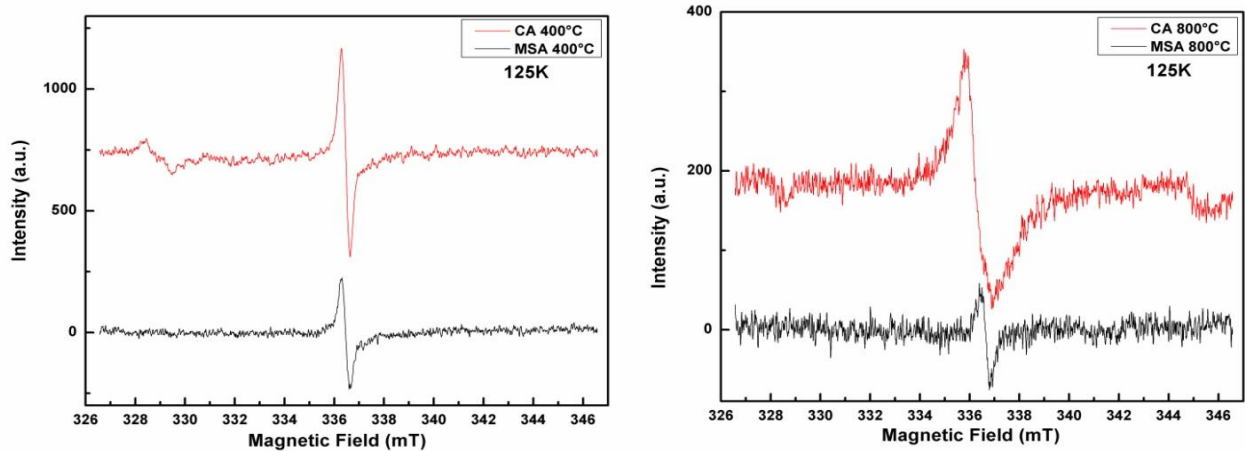


Figure 4.14: EPR spectra of CA and MSA at 400°C and 800°C.

When the magnetic properties of the CA samples were studied it was found that transition from ferromagnetism to diamagnetism occurs at 1100°C where as in case for MSA this transition occurred at 800°C as shown in figure 4.15. The Zn_i acted as mediators for mediating

ferromagnetism in CA where as in case of MSA there was the existence of Zn_i and V_o when the samples exhibited diamagnetism.

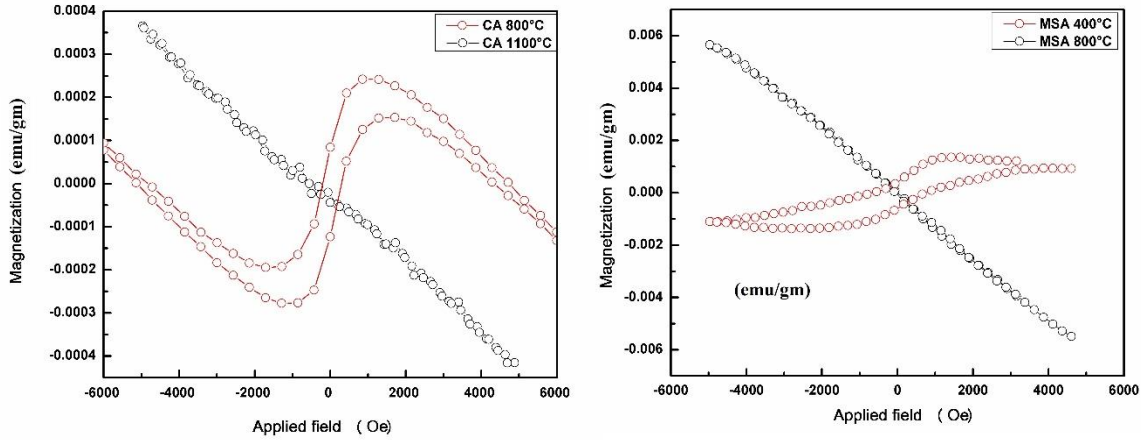


Figure 4.15: M-H curve of MSA and CA of 800°C and 1100°C.

4.4 Conclusion

The defect related optical & magnetic properties have been discussed briefly in this chapter. The emissions from core as well as defects from the surface have been recorded in ZnO. From the sub band excitation the deep defects are also excited and it was found that green emission was due to transition from triplet to singlet state. The MSA samples exhibited RTFM but showed diamagnetic behaviour at 800°C. This means that two annealing techniques lead to two different mechanisms of grain growth which inturn altered almost all properties.

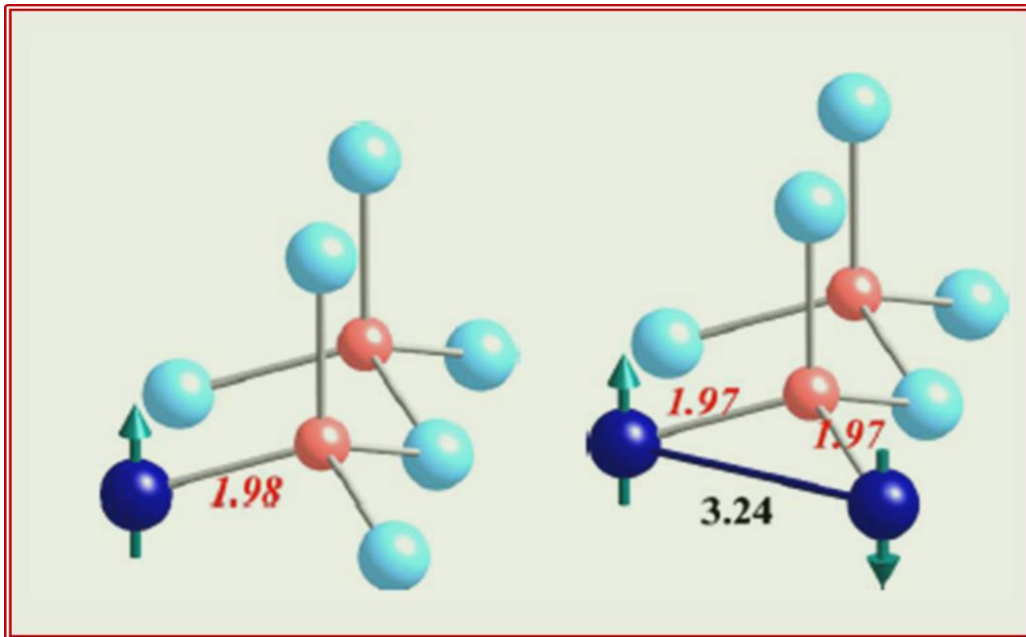
REFERENCES

- [1] I. W. Chen and X. H. Wang, “Sintering dense nanocrystalline ceramics without final-stage grain growth”, Nature, vol. 404, no. 6774, pp. 168–171, 2000.
- [2] M. Mazaheri, A. M. Zahedi, and S. K. Sadrnezhad, “Two-step sintering of

- nanocrystalline ZnO compacts: Effect of temperature on densification and grain growth*”, Journal of the American Ceramic Society, vol. 91, no. 1, pp. 56–63, 2008.
- [3] J. Wang and L. Gao, “*Photoluminescence properties of nanocrystalline ZnO ceramics prepared by pressureless sintering and spark plasma sintering*”, Journal of the American Ceramic Society, vol. 88, no. 6, pp. 1637–1639, 2005.
- [4] P. Durán, J. Tartaj, and C. Moure, “*Fully dense, fine-grained, doped zinc oxide varistors with improved nonlinear properties by thermal processing optimization*”, Journal of the American Ceramic Society, vol. 86, no. 8, pp. 1326–1329, 2003.
- [5] E. Olsson, G. Dunlop, and R. Österlund, “*Development of Functional Microstructure during Sintering of a ZnO Varistor Material*”, Journal of the American Ceramic Society, vol. 76, no. 1, pp. 65–71, 1993.
- [6] J. Wang, Z. Wang, B. Huang, Y. Ma, Y. Liu, X. Qin, X. Zhang, and Y. Dai, “*Oxygen vacancy induced band-gap narrowing and enhanced visible light photocatalytic activity of ZnO*”, ACS applied materials & interfaces, vol. 4, no. 8, pp. 4024–4030, 2012..
- [7] P. Leyral, D. Bois, and P. Pinard, “*Strain-Associated Band Tailing Effect in Semiconductors*”, Physica Status Solidi (b), vol. 73, no. 1, pp. 187–192, 1976.
- [8] P. S. Xu, Y. M. Sun, C. S. Shi, F. Q. Xu, and H. B. Pan, “*The electronic structure and spectral properties of ZnO and its defects*”, Nuclear Instruments and Methods in Physics Research Section B: Beam Interactions with Materials and Atoms, vol. 199, pp. 286–290, 2003..
- [9] Z. M. Liao, H. Z. Zhang, Y. B. Zhou, J. Xu, J. M. Zhang, and D. P. Yu, “*Surface effects on photoluminescence of single ZnO nanowires*”, Physics Letters A, vol. 372, no. 24, pp. 4505–4509, 2008.
- [10] Y. S. Kim and C. H. Park, “*Rich variety of defects in ZnO via an attractive interaction between O vacancies and Zn interstitials: Origin of n-type doping*”, Physical review letters, vol. 102, no. 8, pp. 1–12, 2009.

CHAPTER 5

“DEVELOPMENT OF CoO AND NiO DOPED ZnO BASED DMS: A PROMISING MATERIAL FOR SPIN ALIGNER”



5.1 Introduction

Crucial point to ensure the development of spintronics device is the development of the spin aligner material which is ferromagnetic at RT and act as a source of spin polarised electrons. There comes the concept of DMS which comprises of doping of host semiconductor material with very small concentrations of dopant. DMS is formed by substituting the cations of III–V or II–VI nonmagnetic semiconductors by ferromagnetic/antiferromagnetic Mn, Fe, Co and Ni, which exhibits exceptional magneto-optical and magneto-transport properties [1-4]. Room temperature ferromagnetism (RTFM) in transition metal (TM) doped ZnO has been predicted by numerous groups, Rath et al. studied the magnetic property of ZnO: Co nanoparticles and reported that the material exhibits paramagnetic behavior. Rao et al. explored the structural, optical and electrical properties of ZnO thin films prepared by spray pyrolysis technique. Bappaditya Pal et al reported RTFM in Co doped ZnO by solvo -thermal route. Song et al reported RT FM and a high T_c of 750 K for the Co doped ZnO ferromagnetic films [5-8]. Among all transition metals, NiO doped ZnO is one of the controversial topic, though $Zn_{1-x}Ni_xO$ ($x=1-4\%$) has shown ferromagnetism at high temperatures. There remains a great deal of controversy on the origin of ferromagnetism in $Zn_{1-x}Ni_xO$, W. Yu et al reported RTFM in $Zn_{1-x}Ni_xO$ thin films at $x = 1,3,5\%$, meanwhile T. Wakano et al. reported superparamagnetism at $x= 25\%$. In immediate contrast to this, other authors have reported the absence of ferromagnetism in $Zn_{1-x}Ni_xO$ [9-11]. Satyarathi et al. reported the coexistence of intrinsic and extrinsic origin of RTFM in Ni ion implanted ZnO film. Singhal et al. reported the FM in hydrogenated and vacuum annealed Ni doped ZnO disappear upon long reheating in air at very high temperature of 700°C and 800°C respectively [12]. TM (like in Co it is $1s^2, 2s^2, 2p^6, 3s^2, 3p^6, 4s^2, 3d^7$) VB electron in 4s orbital and have partially filled d orbital. The first theory dealing with FM is driven by exchange interaction between carriers and localized magnetic moment was first proposed by Zener. It predicts that direct super exchange between carriers and magnetic ions does not give rise to ferromagnetism but indirect super exchange does. Hence, DMS are typically identified by exchange interaction between localized electrons of d shell of magnetic ions (Co, Fe, Ni etc) and delocalized band state of s and p origin i.e. zinc interstitial and oxygen atom. Several theoretical models have also been put forward to explain the ferromagnetism as carrier mediated exchange interaction, bound magnetic polaron etc [13, 14]. It is very difficult to detect the local

structure of magnetic ion their microscopic cluster formation in host material. In this chapter we report the local structure variation around Co and Ni ions in ZnO host lattice by XRD and Raman scattering measurement and magnetic properties by room temperature VSM and ESR measurement. In order to probe local micro-cluster formation of dopants, low temperature ESR (5K - 85K) measurement were carried out.

5.2 Experimental details

Polycrystalline TM doped ZnO were prepared by solid state reaction method. High purity CoO and NiO were used for doping. These materials were carefully mixed by their weight percents and were crushed in mortar pestle for 3 hours. The powder was then annealed by CA method at 1100°C for 2 hours. As the CA ZnO was diamagnetic in nature at 1100°C so we chose this particular temperature. The CoO doping was done for 1, 2, 4, 6, 8 and 10% and NiO doping for 0.5, 1, 1.5, 2, 2.5, 3 and 3.5%. For structural characterization and local crystal structure around dopants, XRD and Raman scattering had been employed. VSM was employed for magnetic characterizations. To investigate the unpaired spins we performed EPR at RT as well as at low temperature.

5.3 Result and discussions

5.3.1 X-Ray diffraction studies of $Zn_{1-x}Co_xO$

Figure 5.1 shows the XRD spectra of CoO doped ZnO for various doping concentrations. All the diffraction peaks viz (100), (002), (101) corresponds to hexagonal wurtzite structure ZnO crystal and hence implies that $Zn_{1-x}Co_xO$ was successfully prepared. It should be noted that no secondary peak related to Co cluster or any other metal oxide or impurity was observed.

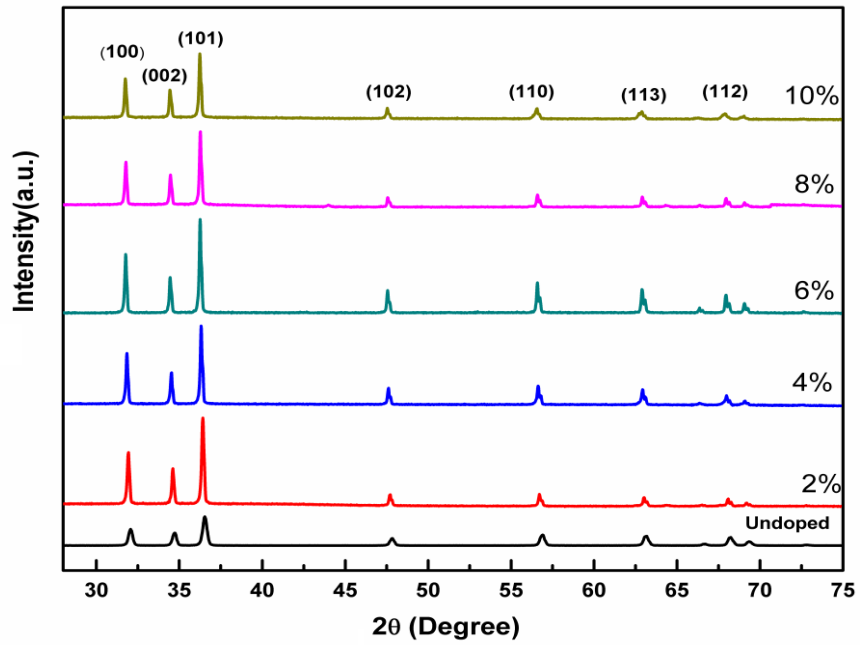


Figure 5.1: XRD pattern for undoped and CoO doped ZnO annealed conventionally at 1100°C.

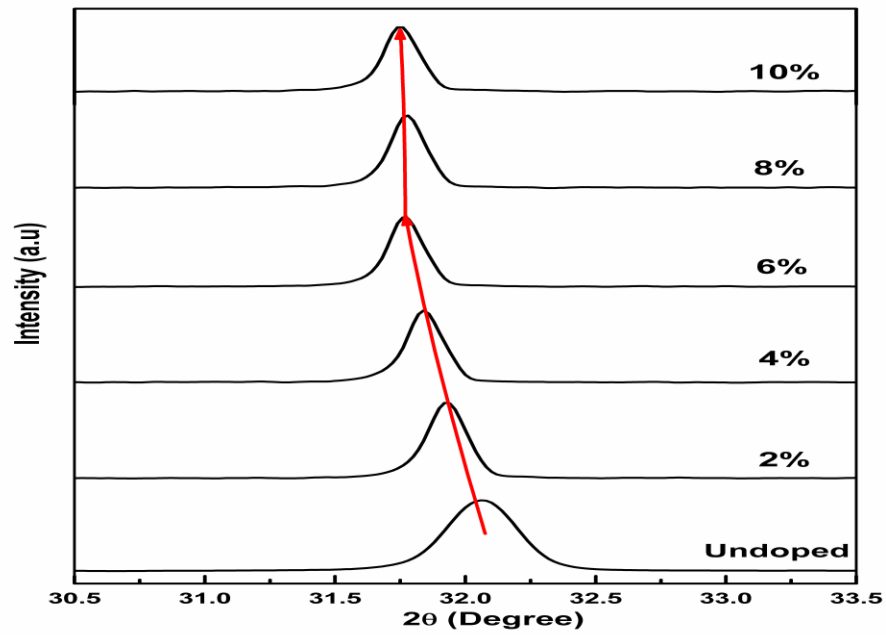


Figure 5.2: Variation of peak 100 with 2θ of all $Zn_{1-x}Co_xO$ ($x=0, 2,4,6,8, 10\%$) samples.

Although a clear shift of diffraction peaks towards lower angles with increase of % doping (marked with red line) is clearly depicted in figure 5.2, suggests the existence of tensile stress inside the grains. The lattice parameters “a”, “c” for hexagonal ZnO were calculated by

$\frac{1}{d^2} = \frac{4}{3} \left(\frac{1}{a^2} \right) + \frac{1}{c^2}$. The cell volume “V” of the unit cell was calculated by lattice parameters as $V = 0.866 * a^2 * c$.

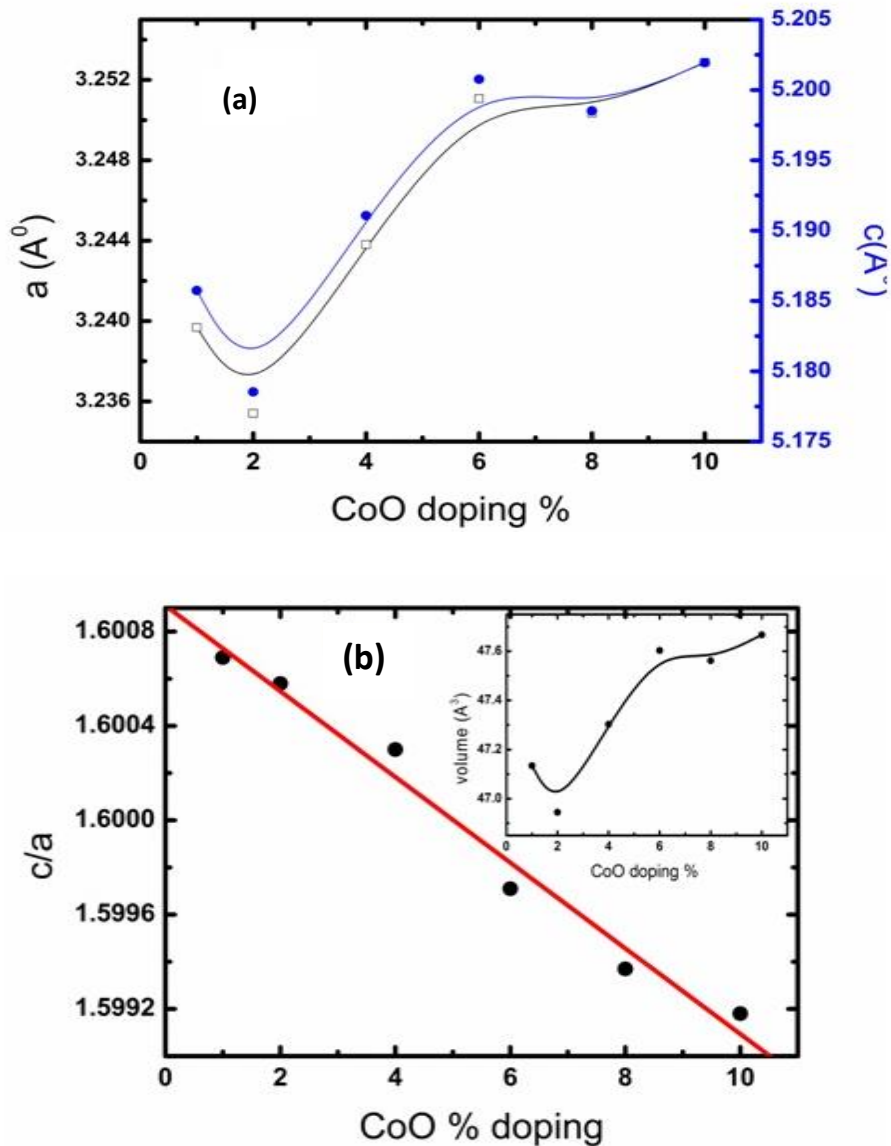


Figure 5.3: (a) Variation of lattice parameter a and c with CoO doping, (b) Variation of ratio of c/a with CoO doping %; Inset shows the variation of volume with % doping.

It is observed from figure 5.3 (a) and (b) that lattice parameters a , c first decreases then increases for $> 2\%$ doping, because for 1% CoO doped sample annealing cause diffusion of Co along crystal c -direction and suppresses further diffusion along c axis. The Co^{2+} can either go to either tetrahedral site or octahedral site. Although, a , c and volume increases with the $\%$ doping but this change seems nominal e.g. of the order of difference of ionic radii of Co^{2+} and Zn^{2+} (Zn^{2+} 0.60\AA , and Co^{2+} 0.58\AA). The minimal change exhibited in a , c proves that Co ions are not at the octahedral site of wurtzite structure as it would lead to significant increase in these quantities because octahedral divalent Co has radius between 0.65\AA (low spin) and 0.75\AA (high spin).

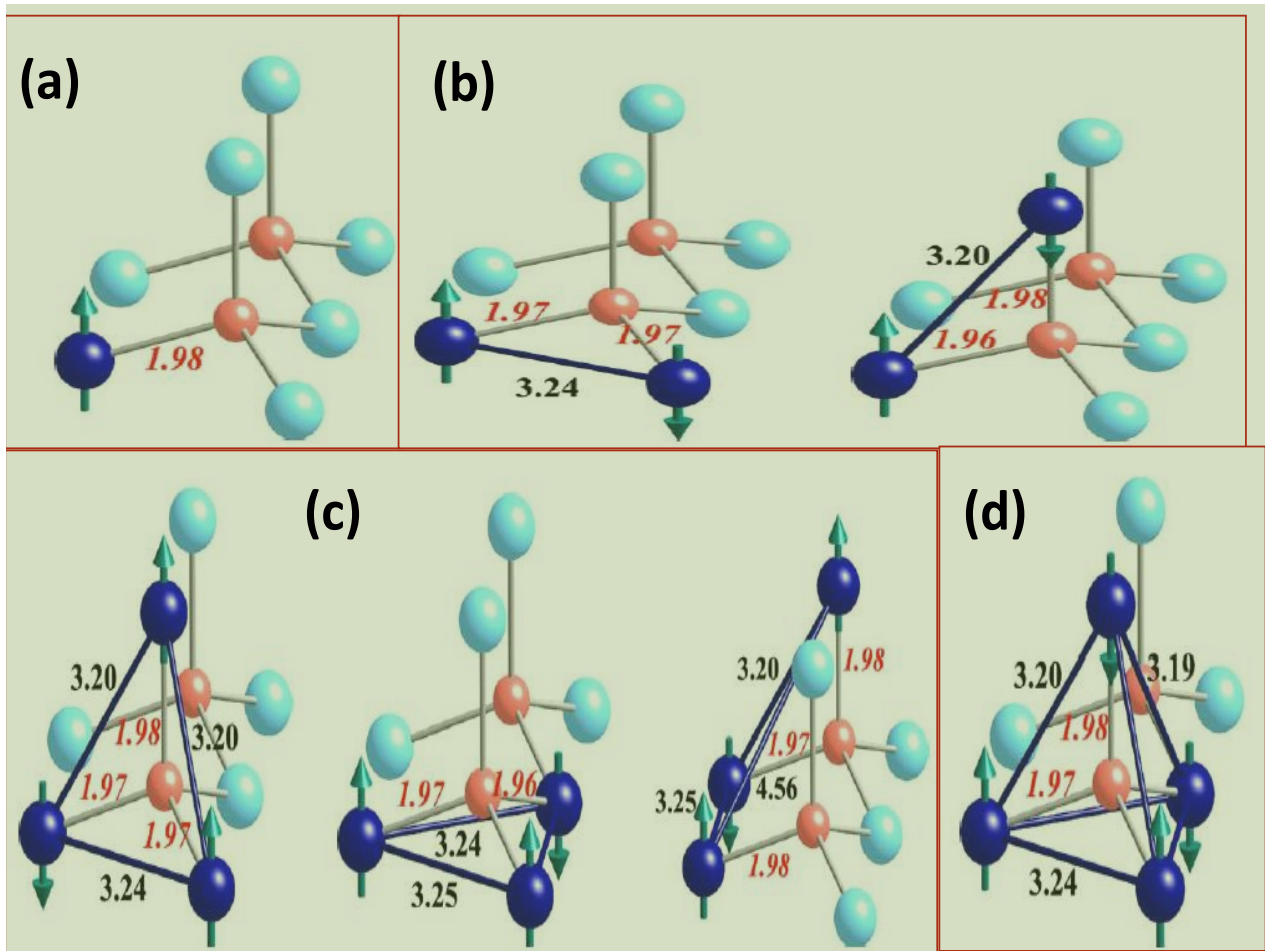


Figure 5.4: Microscopic picture of Co clustering, when Co occupied tetrahedral position in ZnO [16].

5.3.2 Magnetic properties of $Zn_{1-x}Co_xO$

To investigate the magnetic properties of the Co doped samples we performed Room temperature VSM as shown in figure 5.5.

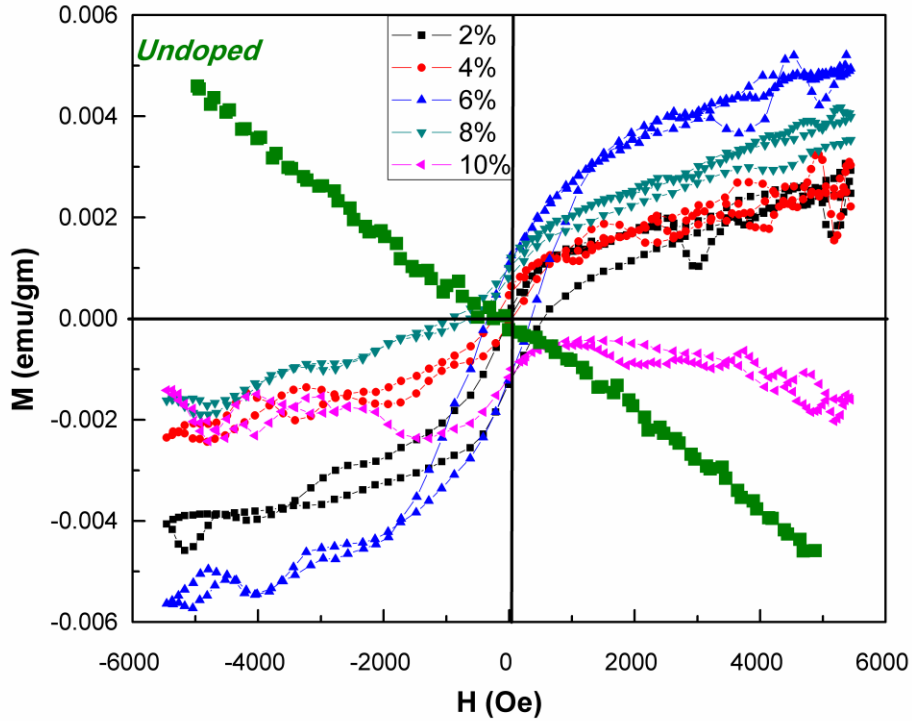
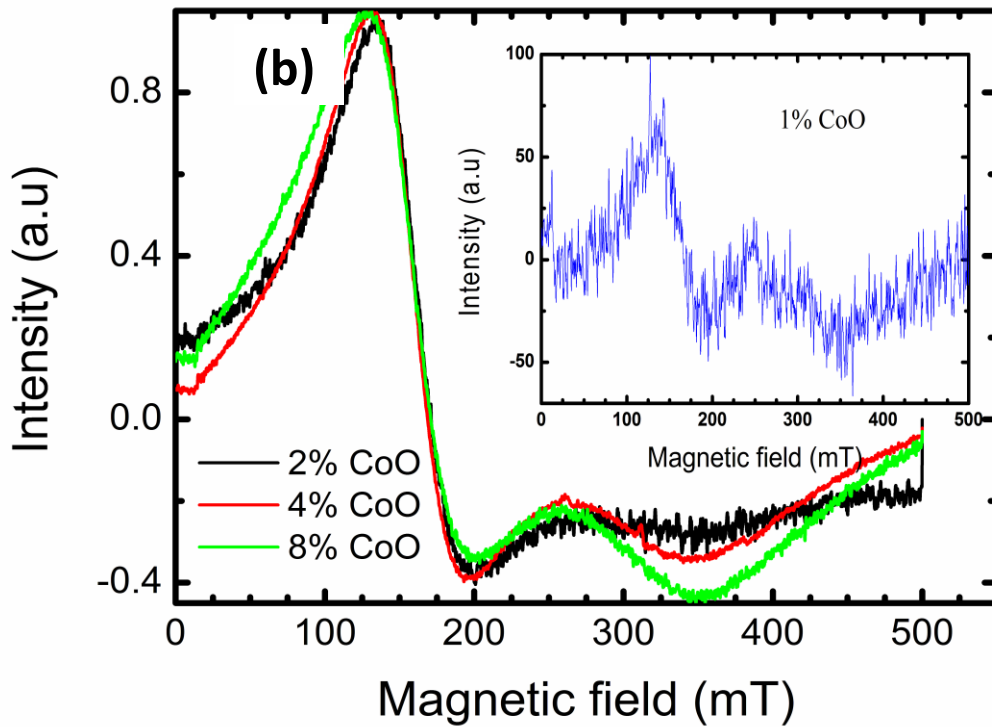
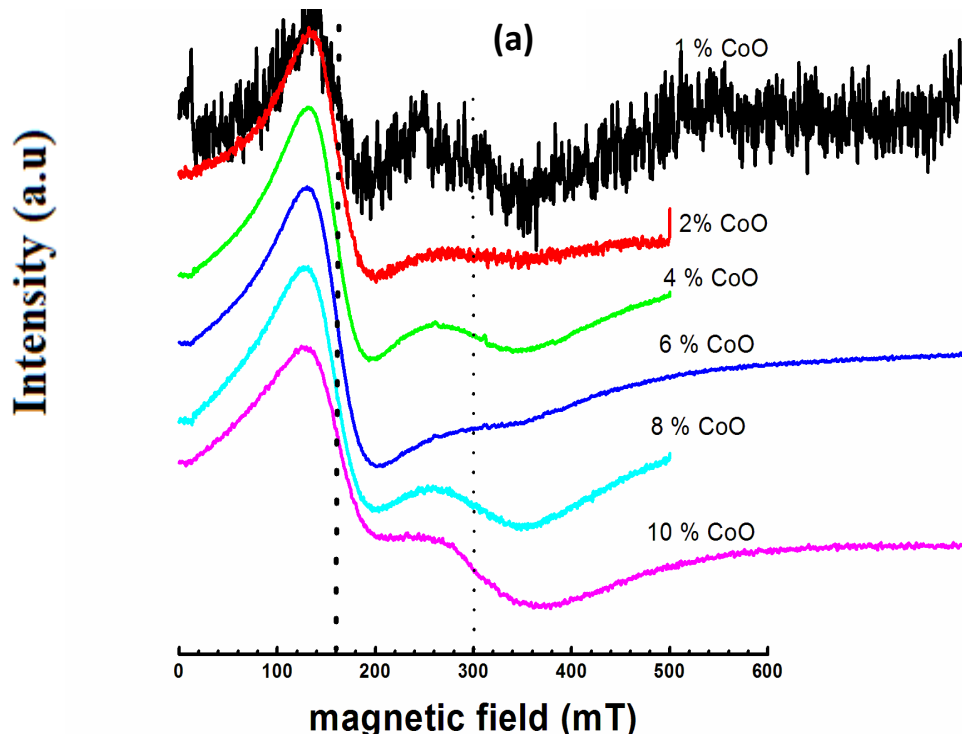


Figure 5.5: M-H curve of $Zn_{1-x}Co_xO$ at $x = 2, 4, 6, 8, 10\%$.

We found that all the Co doped ZnO samples exhibited the ferromagnetic behavior except for that of undoped ZnO. This ferromagnetism could be attributed to Co incorporation in the lattice. Ferromagnetism can arise from existence of Co-Co direct interaction, or Co-Co interaction via some mediator like V_o or Zn_i . To investigate the paramagnetic centers we readily employed EPR measurement at room temperature as well as at low temperatures both.



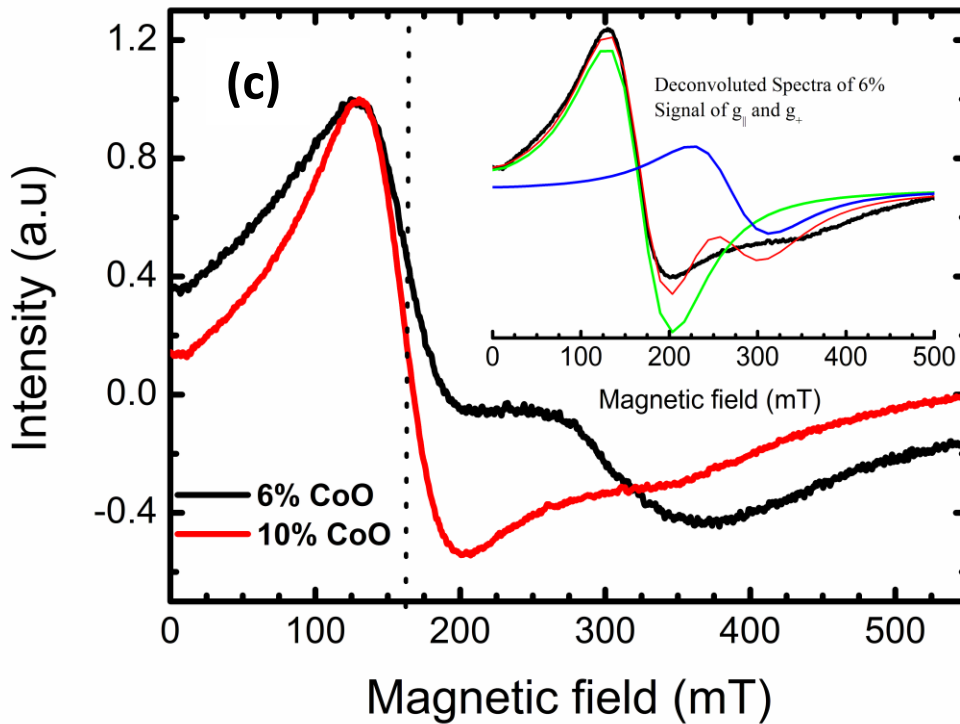


Figure 5.6: Normalized room temperature ESR spectra of CoO doped ZnO. Dotted lines show constant resonance (No g shift with doping (a) All doping percentages (b) CoO doping 2%, 4% & 8%: inset shows EPR spectra for 1% doping (c) CoO doping 6% & 10%.

RT EPR is shown in figure 5.6, for different doping percentage. It is clear from figure 5.6 (a) that resonance g value is not changing with doping percentage (shown by dotted line), although normalized EPR shows significant broadening of resonance line at 300 mT. Broadening of EPR lines occurs due to dipolar exchange or spin-lattice interaction. The EPR spectra of Co-doped ZnO at 1% recorded at 5K is shown at the inset of figure 5.6 (b). These lines are characteristics of spin $\frac{1}{2}$ coupled with nuclear spin $\frac{7}{2}$ of Co^{+2} . Only 1 % CoO doped ZnO reveals hyperfine interaction. Our sample is a powder sample, polycrystalline in nature hence it shows signal for both magnetic field perpendicular to c axis and parallel to c axis corresponding to two different values of Lande's g factor; $g_{||}$ ($H \parallel c$) at 2.24 and g_{\perp} ($H \perp c$) 4.28 simultaneously. These values of $g_{||}$ and g_{\perp} are very close to previously obtained value for single crystals [15]. Interesting, hyperfine splitting is found only in the case when magnetic field parallel to c axis. It is absent in

case of perpendicular configuration. Rest of the sample does not show any signature of hyperfine interaction as shown in figure 5.7 (b). Although, they exhibit a clear peak at $g_{\parallel} = 2.24$ and $g_{\perp} = 4.28$ respectively. Inset of figure 5.7 (b) shows variation of peak to peak width of resonance line with doping percentage, EPR line width increases linearly with increase of doping fraction. This reveals strong spin-spin and spin lattice relaxations. The line width of the EPR signal can be written as $\Delta B \propto \frac{1}{T_{1e}} + \frac{1}{T_{2e}}$, Where T_{1e} is the spin lattice relaxation time T_{2e} spin-spin relaxation time. Both spin-spin and spin-lattice relaxations contribute to EPR signal i.e. when the system returns to equilibrium it involve the spin flips to lower energy state and excess energy is lost to surrounding in form of heat.

Going back to VSM and XRD measurement, VSM indicates the increase of saturation magnetization till 6% and decrease after that. Noticeable point is saturation occurs at very low magnetic field ~ 2000 Oe, this could be signature of Co clustering. Whereas, XRD measurement indicate that Co ion is replacing Zn ion in tetrahedral geometry, and with increase of doping percentage XRD peak shifts towards lower angle till 6% which becomes constant after that. Shifting of XRD peaks towards lower angle implies development of tensile stress/strain within the grains, hence, increase of SO coupling. Microscopic origin of Co clustering in ZnO can be visualized as shown in figure 5.4. In this figure Co atom is indicated by dark blue ball with spin as arrow, Zn atom with turquoise light, and O atom with red in color respectively. The bond length between atoms was taken from Local spin density approximation combined with Hubbard parameter U (LSDA+U). Microscopic picture of Co clustering in ZnO can be packed into following points.

- (i) Single Co atom in unit cell irrespective of in plane and out plane configuration as shown in figure 5.4 (a). In this particular case, bond length between Co and oxygen atom is 1.98 Å, and Co induces a positive spin polarization on the neighboring oxygen atoms. Electronically, unit cell is now enriched with three different atomic orbital's (d orbital's from Co, s orbital from Zn, and p orbital's from O). Therefore, FM in lightly doped DMS (<1%) can be taken as due to sp-d exchange.
- (ii) Second possibility is two Co atoms substituting two Zn atoms in same unit cell, which is shown in figure 5.4 (b). Co atoms can take position in plane or out of the

- plane. Distance between Co-Co atoms are 3.20 Å and 3.24 Å for out of plane and in plane configuration respectively. This difference of separation of Co atoms is almost $\sim .04\text{Å}$, therefore anti-ferromagnetic and FM states are supposed to be degenerate. This also indicates a very short ranged magnetic interaction between Co atoms together with smallest cluster formation.
- (iii) Third possibility is occurrence of three Co atoms in single unit cell. This give total three possible arrangement of Co atoms in tetrahedral geometry as shown in figure 5.4 (c). Out of these structures, ground state structure according to LSDA+U is close triangular configuration in which first two Co atoms lies in x-y plane, while third lies out of the plane. Although, the difference in configuration energy of these three geometries is only few meV, hence any of the configurations can be picked up for explaining micro clustering. For large percentage doping or in extreme case one can assume all Zn atom is being replaced by Co in unit cell, in this case, most common or favorable geometry will be pyramidal structure, figure 5.4 (d). It is important to mention that in plane or out plane Co atoms are coupled anti ferromagnetically, hence, formation of Co trimmers or tetramers in single unit cell will result in decrease of resultant ferromagnetic coupling as compared to monomer and dimer Co atoms. Therefore, it is reasonable to expect that saturation magnetization will decrease with increase of cluster size or particle size.

In this particular case of micro cluster formation, Co spin align itself in such a way that distance between coupled Co atoms decreases in plane, whereas out of the plane distance increases. Since, metallic clusters are difficult to observe by XRD measurement it is difficult to measure Co-Co distance. Although, it is quite intuitive that decrease or increase of in plane or out plane Co-Co distance will result in significant increase of Zn-Zn distance, because of their difference in ionic radii. Zn-Zn in plane distance (a) increases with cluster formation which is shown in figure 5.3 (b). Further in order to confirm Co-Co dimer formation low temperature ESR at 5K were performed in rising field and falling field as shown in figure 5.8 (a) and (b).

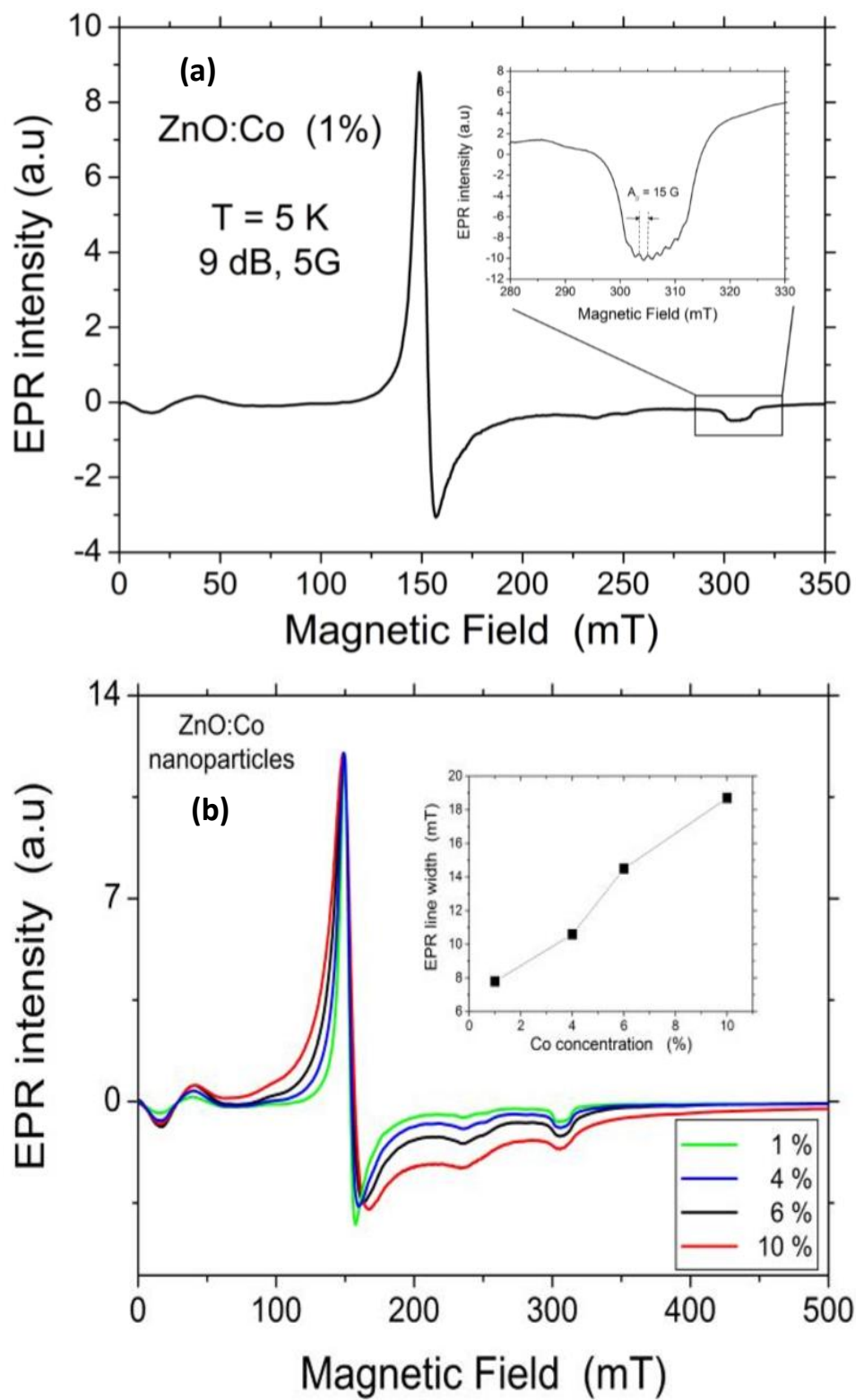


Figure 5.7: EPR spectra of Co doping at 1% performed at 5K.

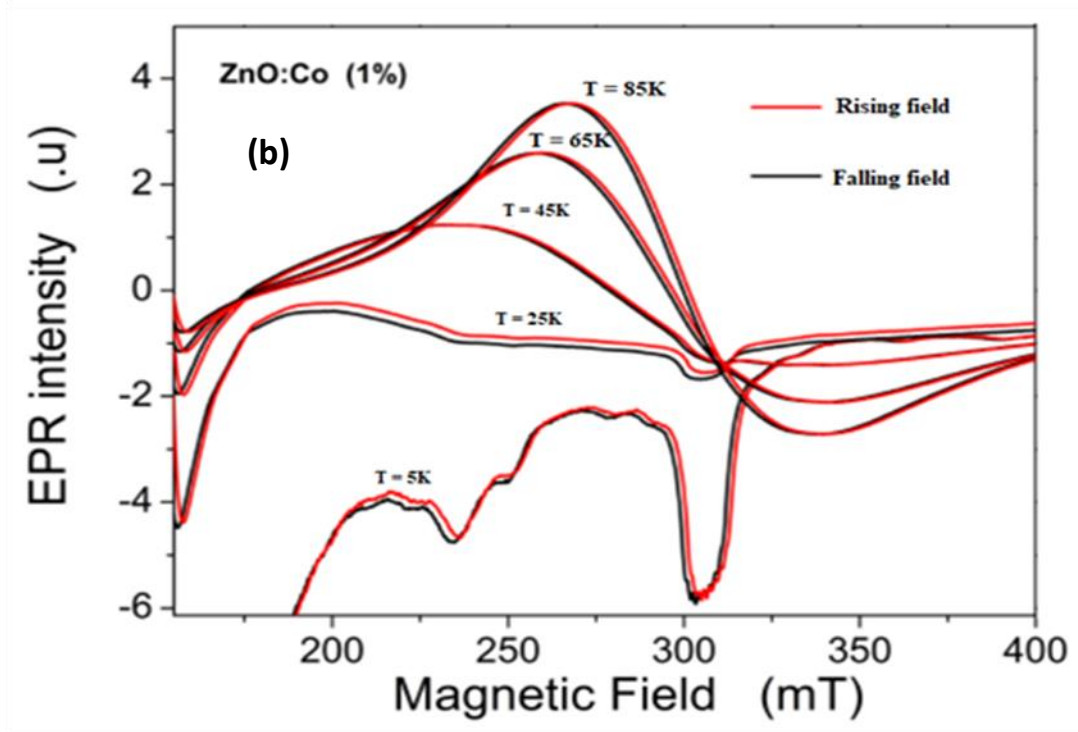
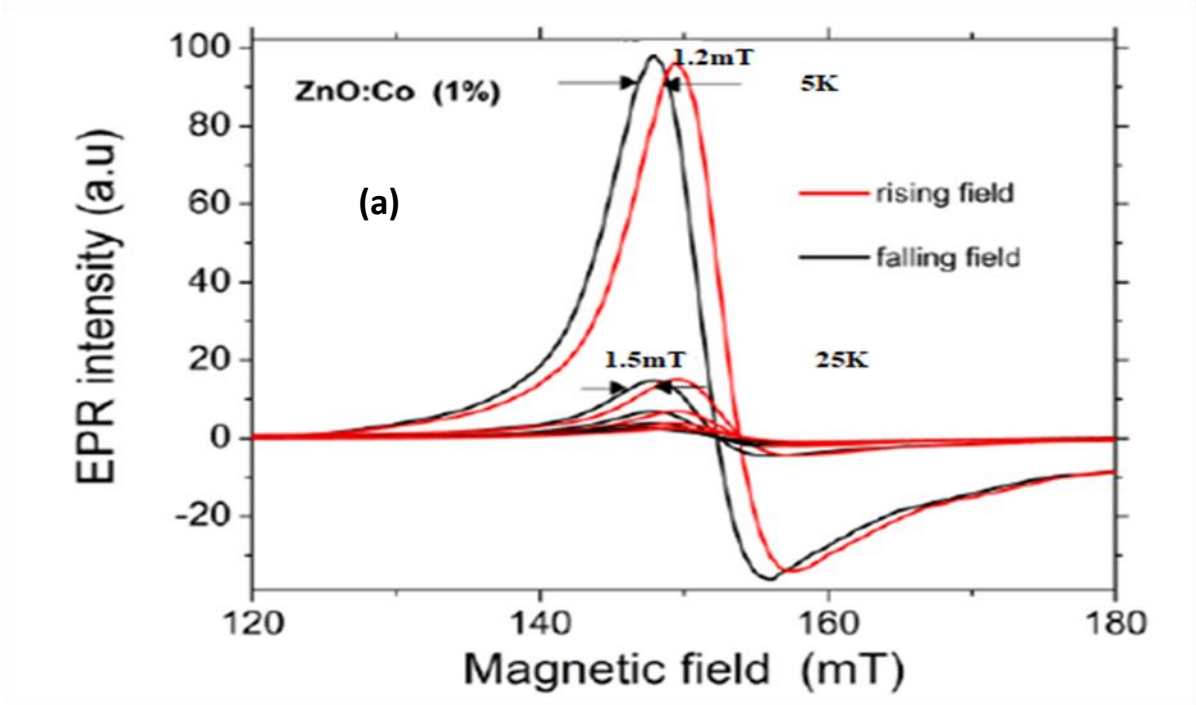
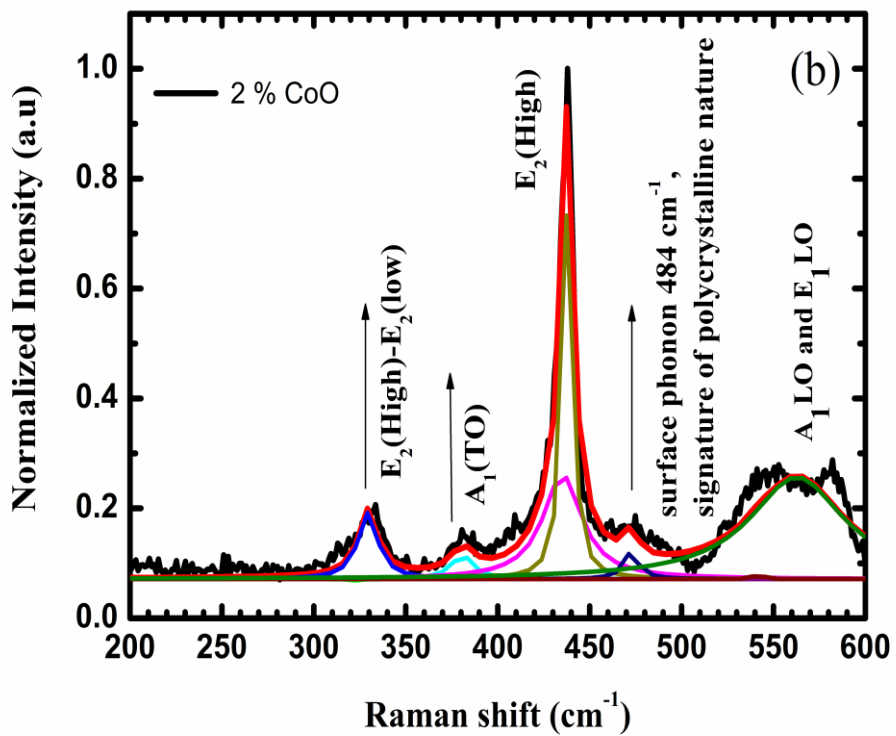
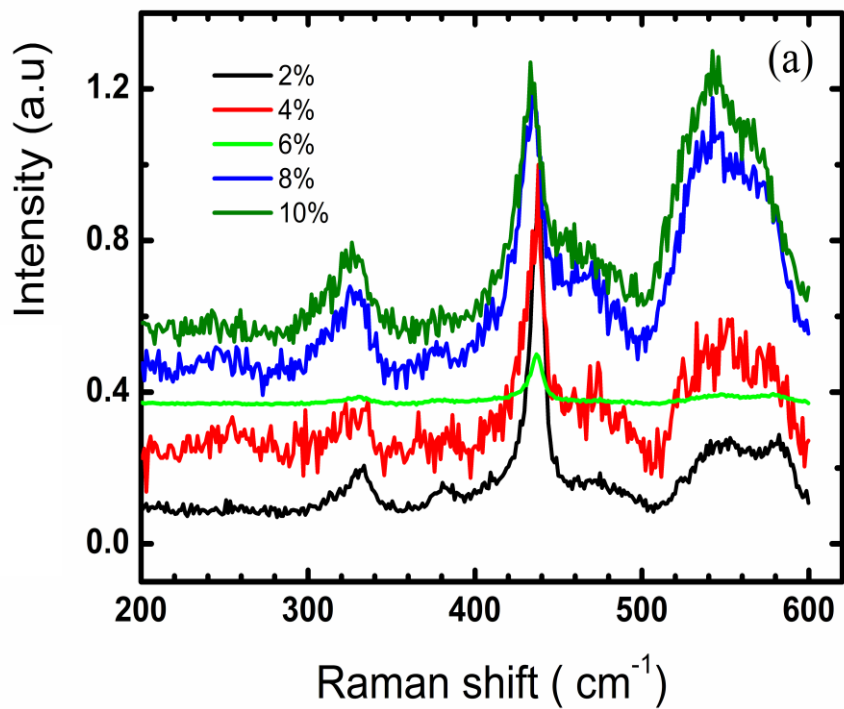


Figure 5.8: (a) EPR spectra of Co doping at 1% for g_{\perp} performed at 5K and 25K, (b) EPR spectra of Co doping at 1% for g_{\parallel} performed at 5K, 25K, 45K, 65K and 85K.

This shows a shift of EPR signal by 12 Gauss which indicates a small amount of metallic Co cluster which shifts the resonance line when magnetized. This shift was observed only in the case of the g_{\perp} resonance line at 155 mT. It reveals information about the existence of Co metallic clusters along the c axis. Meaning thereby that at 1% doping Co diffused along the c axis and formed clusters. It inhibited the further growth of Co towards this axis and for doping % > 1% Co diffused along the a axis i.e. perpendicular to the c-axis.

Microscopically, the effective internal field for parallel and perpendicular orientation of the crystal axis c and applied magnetic field B must be different, and magnetization of micro clusters should shift the resonance line towards higher values for parallel ($B \parallel c$) and lower values for perpendicular ($B \perp c$) respectively. Only 12 G shift for $B \perp c$ and negligible shift for $B \parallel c$, although a red line in figure 5.8 (b) seems to be inclined towards higher field is observed. Shift of 12 G is very small as compared to the shift from pure paramagnetic clusters. This also confirms the occurrence of micro clusters of Co atoms in the sample. This was further confirmed from Raman scattering measurement as shown in figure 5.9. In addition to the regular Raman mode from the undoped sample, a comparatively weak and broad Raman band at 484 cm^{-1} was observed due to surface phonons. With the doping two interesting facts were noticed (i) The enhancement and broadening of phonon modes (ii) Sharpening of phonon bands after 6% doping. The broadening of phonon modes reflects the deterioration of the host lattice by the distortion of local atomic arrangement around magnetic impurity and sharpening of peaks resembles the phonon modes of Co_2O_4 e.g. CoO clusters which were not detected by XRD measurement. Therefore, the origin of intrinsic ferromagnetic nature in ZnO based DMS is questioned by Raman and easily gets answered by spin measurement. Because if cluster formation takes place Co-Co dimers are more likely to occur but we did not observe any signature of dimers in ESR. This shows a negligible amount of Co_2O_4 phase.



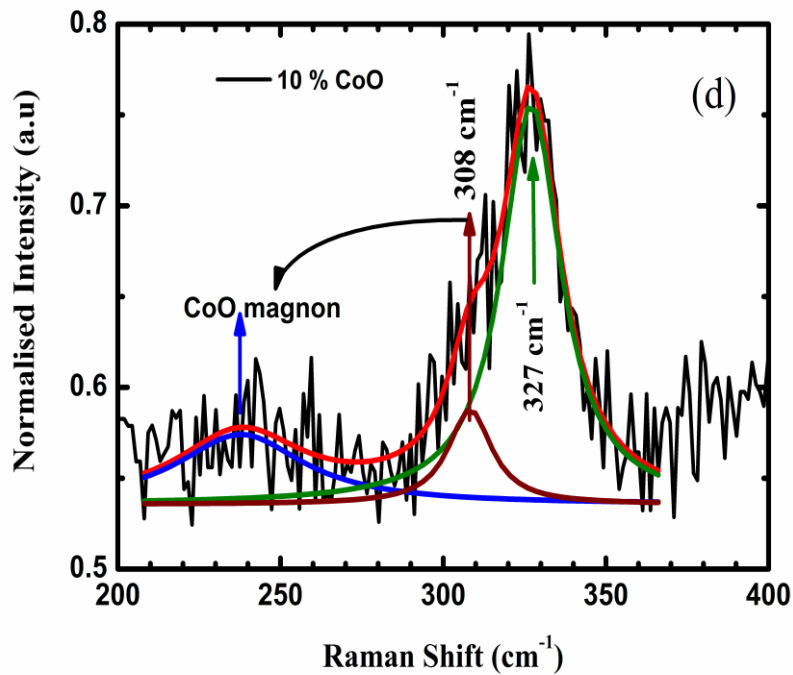
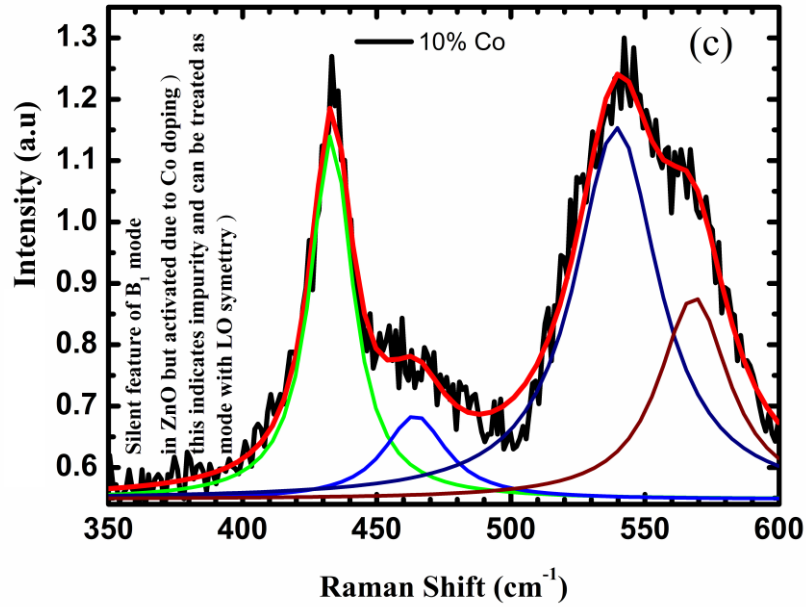


Figure 5.9: (a) Raman spectra with increasing doping percentage, (b) De-convoluted of 2% CoO doped sample, (c) De-convoluted of 10% CoO doped sample in 350-600 cm^{-1} range, (d) De-convoluted of 10% CoO doped sample in 200-400 cm^{-1} range.

5.3.3 Magnetic properties of $Zn_{1-x}Ni_xO$

All the $Zn_{1-x}Ni_xO$ doped samples show a pure ferromagnetic behavior with respect to undoped ZnO, as shown in figure 5.10. It also reflect same trend as of CoO doping in terms of magnetization. Saturation magnetization first increases with increase of NiO doping then decreases.

Figure 5.11 shows EPR spectra of 0.5% NiO doped ZnO. In this figure, we recognize the Co^{2+} powder signal by its form and its position (150 mT). The big structure around 340 mT is recognized as Mn^{2+} powder signal because of its global position. Another point allowing identification is that Co^{2+} relax very quickly because of its big spin-lattice coupling, so that the EPR intensity is expected to decrease rapidly with temperature, whereas, on the contrary, Mn^{2+} ions relaxes slowly, and have a weak temperature dependence of their EPR lines. It is important to mention that host material was 99.99 % pure and CoO and NiO were 99.5 and 99 % pure (as claimed by Sigma Aldrich), even though we observe strong magnetic and ESR signal from impurity.

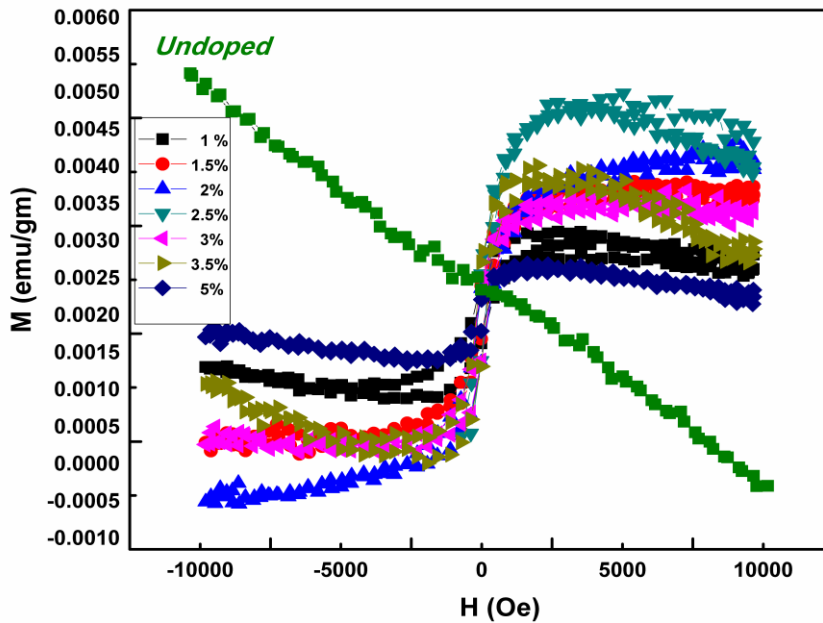


Figure 5.10: M-H curve of $Zn_{1-x}Ni_xO$ at $x = 0.5, 1, 1.5, 2, 2.5, 3$ and 3.5 %.

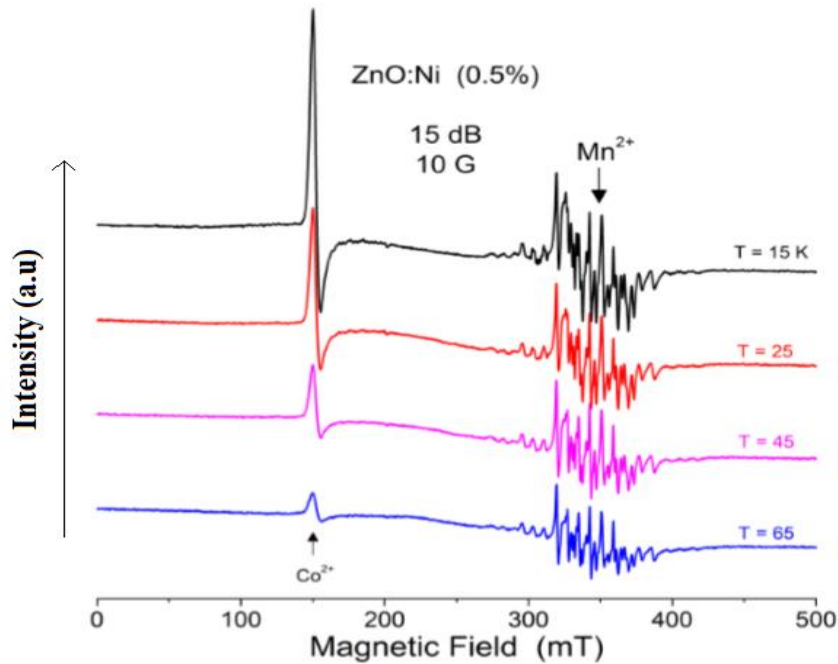


Figure 5.11: EPR spectra for Ni doping at 0.5% at 15K, 25K, 45K and 65K.

Therefore, it is difficult to reach at microscopic origin of ferromagnetism in Ni doped samples. Although, VSM measurement indicates clustering of Ni atoms in host material, as magnetization get saturated at very low magnetic field. Spatial position of Ni in host material (tetrahedral or octahedral) is also not known.

5.4 Conclusion

In conclusion, transition metal doped bulk sample always tend to form metallic microscopic clusters in host material which is difficult to get detected by XRD spectra. For spintronics applications, much lower doping fraction is needed i.e. less than 2% for Co and < 5% Ni. Although, CoO maintains crystal structure and enhances silent feature of Raman modes but Raman modes of Ni doped samples are very complex, and shows enhancement of surface phonon mode. Hence, powder samples grown by wet chemical method or sol-gel techniques and thin film made by spin coating will not be good material for making spintronic devices. Only thin films made by atomic layer deposition (ALD) method or pulsed laser deposition (PLD) methods at high substrate temperature can be suitable method for making spin based devices.

REFERENCES

- [1] Q. Pan, K. Huang, S. Ni, F. Yang, S. Lin, and D. He, “*Photoluminescence and magnetism in Co-doped ZnO powder,*” *Journal of Physics D: Applied Physics*, vol. 40, no. 21, pp. 6829–6833, 2007.
- [2] T. Dietl, H. Ohno, F. Matsukura, J. Cibert, and D. Ferrand, “*Zener model description of ferromagnetism in zinc-blende magnetic semiconductors,*” *Science* (80), vol. 287, no. 5455, pp. 1019–1022, 2000.
- [3] M. H. F. Sluiter, Y. Kawazoe, P. Sharma, A. Inoue, A. R. Raju, C. Rout, and U. V. Waghmare, “*First principles based design and experimental evidence for a ZnO-based ferromagnet at room temperature,*” *Physical Review Letter*, vol. 94, no. 18, pp. 3–6, 2005.
- [4] P. Mallick, C. Rath, R. Biswal and N. C. Mishra, “*Structural and Magnetization Behaviours of Ni Substituted Li-Mg Ferrites*”, *Indian J. Phys*, vol.1, no. 5, pp.128-132. 517, 2009.
- [5] C. Rath, S. Singh, P. Mallick, D. Pandey, N. P. Lalla, and N. C. Mishra, “*Effect of cobalt substitution on microstructure and magnetic properties in ZnO nanoparticles,*” *Indian Journal of Physics*, vol. 83, no. 4, pp. 415–421, 2009.
- [6] T. Prasada Rao, M. C. Santhosh Kumar, and V. Ganesan, “*Effect of annealing on the structural, optical and electrical properties of ZnO thin films by spray pyrolysis,*” *Indian Journal of Physics*, vol. 85, no. 9, pp. 1381–1391, 2011.
- [7] B. Pal, S. Dhara, P. K. Giri, and D. Sarkar, “*Room temperature ferromagnetism with high magnetic moment and optical properties of Co doped ZnO nanorods synthesized by a solvothermal route,*” *Journal of Alloys and Compounds*, vol. 615, pp. 378–385, 2014.
- [8] C. Song, F. Zeng, K. W. Geng, X. B. Wang, Y. X. Shen, and F. Pan, “*The magnetic properties of Co-doped ZnO diluted magnetic insulator films prepared by direct current reactive magnetron co-sputtering,*” *Journal of magnetism and magnetic materials*, vol. 309, no. 1, pp. 25–30, 2007.
- [9] K. Sato and H. Katayama-Yoshida, “*Material Design for Transparent Ferromagnets with ZnO-Based Magnetic Semiconductors Express Letter Material Design for Transparent*

- Ferromagnets with ZnO-Based Magnetic Semiconductors,*” Japanese Journal of Applied Physics. vol. 39, no. 6B, pp. 555–558, 2000.
- [10] W. Yu, L. H. Yang, X. Y. Teng, J. C. Zhang, Z. C. Zhang, L. Zhang, and G. S. Fu, “*Influence of structure characteristics on room temperature ferromagnetism of Ni-doped ZnO thin films,*” Journal of Applied Physics, vol. 103, no. 9, 2008 , T. Wakano, N. Fujimura, Y. Morinaga, N. Abe, A. Ashida, and T. Ito, “Magnetic and magneto-transport properties of ZnO : Ni ylms,” Physica E: Low-Dimensional Systems and Nanostructures, vol. 10, pp. 260–264, 2001
- [11] V. Jayaram and B. Sirisha Rani, “*Soft chemical routes to the synthesis of extended solid solutions of wurtzite ZnO-MO (M = Mg, Co, Ni),*” Materials Science and Engineering: A, vol. 304–306, no. 1–2, pp. 800–804, 2001.
- [12] R. K. Singhal, S. C. Sharma, P. Kumari, S. Kumar, Y. T. Xing, U. P. Deshpande, T. Shripathi, and E. Saitovitch, “*Study of electronic structure and magnetization correlations in hydrogenated and vacuum annealed Ni doped ZnO,*” Journal of Applied Physics, vol. 109, no. 6, 2011.
- [13] D. Coey, M. Venkatesan, and C. B. Fitzgerald, “*Donor impurity band exchange in dilute ferromagnetic oxides,*” Nature materials, vol. 4, no. 2, pp. 173–179, 2005.
- [14] G. Cabe, T. Fries, M. Liu, Y. Shapira, and L. Ram-Mohan, “*Bound magnetic polarons in-type,*” Physical Review B, vol. 56, no. 11, pp. 6673–6680, 1997.
- [15] W. C. Holton, J. Schneider, and T. L. Estle, “*Electron paramagnetic resonance of photosensitive iron transition group impurities in ZnS and ZnO,*” Physical Review, vol. 133, no. 6A. 1964.
- [16] Iuşan D, Kabir M, Grånäs O, Eriksson O, & Sanyal B, “*Microscopic picture of Co clustering in ZnO*”, Physical review B, vol 79 no 12, pp. 125202, 2009.

CHAPTER 6

“SUMMARY AND FUTURE SCOPE”

6.1 Summary

Dilute Magnetic Semiconductors have numerous applications in spintronics and optoelectronics due to magnetic and electric properties of the host and the dopant in it. Many research groups synthesize and characterize ZnO and transition metals (TM) doped ZnO bulk/thin films and nanostructures by various methods but most of them achieved RTFM due to impurity phases or metallic clusters. The successful insight of most spintronics applications depend critically on the ability to create spin-polarized charge carriers in a conventional semiconductor in a device structure. ZnO turn out to be a potential material in terms of wide direct band gap material having high exciton binding energy and various defect related optical and magnetic properties. In this thesis we extensively studied the host material before doping it with transition metal ion. The defects inside pure ZnO have been primarily studied by processing it with annealing. The effect of annealing on structure of ZnO has been studied by X-Ray diffraction technique, the morphologies by Field emission Scanning electron microscopy, defect related studies by U-V visible spectroscopy and photoluminescence spectroscopy, magnetic studies by vibrating sample magnetometer and detection of unpaired electrons by EPR.

In the first objective i.e. **Chapter-II** of the thesis, ZnO has been annealed using two different techniques viz CA and MSA techniques at high heating rate using a muffle furnace for 2 hours. Based on fundamentals it is proposed that the mechanism of both the techniques is different in terms of the varying diffusion constants. The diffusion of intrinsic defects of ZnO depends highly on the diffusion coefficients and diffusion barriers. The diffusion barriers in case of CA remains constant where as in case of multistep annealing they differ at each step of annealing leading to anisotropic distribution of defects within the grains. The XRD results reveals that in CA the strain oscillates from compressive to tensile whereas in case of MSA exactly opposite happens. The defect migrates in different directions and hence distributes differently in both the cases. To understand the diffusion of defects within the grains diffusion equation was solved in spherical and cylindrical polar coordinates. The FESEM images of CA suggest that shape of grains after annealing are perfectly spherical where as for MSA grains have different shapes such as cylindrical, hexagonal as well as spherical. For MSA we found that with increasing the annealing temperature the rods started becoming thicker and gradually transformed into spheres.

Solving the diffusion equation for spherical coordinates we proposed a grain growth model which suggests that grain growth during CA involves the diffusion of Zn_i towards surface of the grains. When the concentration of Zn_i on the surface becomes more than the concentration at core the densification start taking place and grain breaks. The grain breaking leads to excess surface defects. For CA this happens at 1100°C and for MSA it happen 800°C.

In the second objective i.e. **Chapter-III** of the thesis the defects and defect related optical and magnetic properties of CA annealed ZnO were investigated. Photoluminescence spectroscopy has been employed to locate the defect states within the bang gap. The samples were excited from the excitation energy more than the band gap energy and characteristics band to band transitions and defect related visible emissions were recorded. The NBE was supposed to come up from the core of grains where as the defect related emissions were from surface as well as the bulk. The blue emission related to Zn defects and green emission related to V_o was observed. Initially for all the temperatures till 1000°C the NBE seemed dominating over all other defects where as for 1100°C the emission from the near band was found to be quenched. This approved the grain growth model for CA that the excess surface defects lead to enhanced visible emissions. To see the chemical nature of defects we performed EPR and found the existence of Zn_i , V_o and hydrogen related defects. On annealing at 1000°C the EPR signals from Zn_i which was a secondary proof to our grain growth model seemed enhanced meaning thereby that the signal came from both the bulk as well as the core. To further resolve the different signals from Zn_i the EPR was performed at 100K. This EPR suggested two clearly resolved signals from Zn_i at the surface as well as the core. The interaction of these paramagnetic centres gives rise to RTFM. When the M-H curves of the CA samples were investigated it was found that all pristine samples were diamagnetic in nature. With annealing temperature the samples exhibited FM till 800°C and then showed diamagnetism at 1100°C. To investigate the cause of FM we performed low temperature EPR for sample CA 400°C (ferromagnetic) and 1100°C (diamagnetic). The existence of Zn_i , V_o , V_{Zn} , Zn_i-V_{Zn} (donor-acceptor pair) and Zn_i-V_o was found at 400 °C whereas for 1100°C no signal for Zn_i was observed. It was found that there were signals from V_o and V_{Zn} but not the Zn_i . Hence for this it is concluded the absence of Zn_i leads to diamagnetism means that Zn_i act as mediators between V_o and V_{Zn} to produce FM. There absence leads to no carrier mediated FM. Further the Fluorescence image of CA ZnO grains corresponding to DAPI, FITC,

and TRITC were taken to represent combined image of the grain. It was visually clear that blue emission was distributed within entire grain, whereas green and red emissions are confined in small region. The blue emission was attributed to presence Zn_i and green to oxygen vacancies. Hence, theoretical model of growth and fluorescence images proves the model for defect distribution within the grain. It was therefore concluded that more controlled annealing; specially two or three step annealing will greatly change the defect distribution and their emission properties. Hence, it will lead to tailoring of various optical and magnetic properties.

In the third objective i.e. **Chapter - IV** of the thesis we performed the same characterizations for MSA samples as we did for CA samples. The defects were investigated by PL spectroscopy and EPR measurements. The absorption curve implies the change in the E_g at MSA temperature at V_o and V_{Zn} at 800°C. The change in the E_g has previously been reported by various authors and has been attributed to enhanced oxygen vacancies in the sample. From the PL measurements we found that the spatial distributions of defects within the grains were not uniform. The defects were randomly distributed all over the grains. The defect related emissions seemed enhanced for all the MSA samples which mean that there were defects present due to MSA. When the sub band excitations were performed it was found that the emission from the defects clusters and complexes were almost constant for all the temperatures. The emission from the oxygen vacancies were found to be enhanced at 800°C. These enhanced oxygen vacancies were attributed to narrowing of band gap. It was then confirmed by Raman spectroscopy also when the E_1 (LO) phonon mode due to oxygen vacancies was found to be enhanced.

In the fourth objective i.e. **Chapter-V** of the thesis, a material for spin aligner has been developed i.e. the ZnO based DMS has been studied. Host material ZnO has been dilute doped by TM oxides CoO and NiO by solid state reaction. In the Co doping for 1% the hyperfine interaction between Co-Co ions has been detected at 5K by low temperature EPR measurements. As the sample was polycrystalline in nature the magnetic field was applied parallel and perpendicular to c axis simultaneously. The Co-Co hyperfine interaction was observed in case of magnetic field applied perpendicular to c axis. From XRD an appreciable shift in lattice parameters of Co doped samples was not observed. The EPR spectra of low temperature were then recorded in rising and falling fields. It was observed that the difference in EPR signal differed by a value of 1.2 mT for field in the direction parallel to c axis. This lead to a conclusion

that there was existence of Co clusters along c axis. The lattice parameter had decreased for 1% Co doped samples and then increased for all other doping concentrations. This means that Co initially diffused along c axis and formed clusters. When the concentration of Co ion was further increased it diffused along channel perpendicular to c axis.

6.2 Future Scope

- Electroluminescence measurement and spin Hall measurement on this proposed device can give possibility of future use of ZnO based DMS in spintronics devices. It will also open new window for making spin based FET and MOSFET for use in electronic industries
- Measure/calculate spin coherence distance and time in n-ZnO, p-ZnO and ZnO based DMS to optimize thickness of device.
- Fabrication of Spin light emitting diode using Pulsed Laser Deposition.

BIBLIOGRAPHY

- [1]. A. B. Djurisić and Y. H. Leung, “*Optical properties of ZnO nanostructures,*” *Small*, vol. 2, no. 8–9, pp. 944–961, 2006.
- [2]. A. Studenikin, N. Golego, and M. Cocivera, “*Fabrication of green and orange photoluminescent , undoped ZnO films using spray pyrolysis Fabrication of green and orange photoluminescent , undoped ZnO films using spray pyrolysis,*” *Journal of Applied Physics*, vol. 2287, no. 1998, pp. 22–24, 2012.
- [3]. Fang, Z. J. Yan, Y. S. Tan, X. Q. Liu, and Y. Y. Wang, “*Influence of post-annealing treatment on the structure properties of ZnO films,*” *Applied Surface Science*, vol. 241, no. 3–4, pp. 303–308, 2005.
- [4]. Straumal, A. A. Mazilkin, S. G. Protasova, A. A. Myatiev, P. B. Straumal, G. Schütz, P. A. Van Aken, E. Goering, and B. Baretzky, “*Magnetization study of nanograined pure and Mn-doped ZnO films: Formation of a ferromagnetic grain-boundary foam,*” *Physical Review B* , vol. 79, no. 20, pp. 1–6, 2009.
- [5]. B. Zhang, S. H. Wei, and A. Zunger, “*Intrinsic n-type versus p-type doping asymmetry and the defect physics of ZnO,*” *Physical Review B* , vol. 63, no. 7, 2001.
- [6]. Bland, L. Kiyoungh, and S. Steinmüller, “*The spintronics challenge,*” *Physics World*, vol. 21, no. 1, pp. 24–28, 2008.
- [7]. Holton, J. Schneider, and T. L. Estle, “*Electron paramagnetic resonance of photosensitive iron transition group impurities in ZnS and ZnO,*” *Physical Review*, vol. 133, no. 6A. 1964.
- [8]. C. Look, “*Recent advances in ZnO materials and devices,*” *Materials Science and Engineering: B*, vol. 80, no. 1–3, pp. 383–387, 2001..
- [9]. Cao, Y. G. Zhao, H. C. Ong, S. T. Ho, J. Y. Dai, J. Y. Wu, and R. P. H. Chang, “*Ultraviolet lasing in resonators formed by scattering in semiconductor polycrystalline films,*” *Applied Physics Letters* , vol. 73, no. 25, pp. 3656–3658, 1998.
- [10]. Cao, Y. G. Zhao, S. T. Ho, E. W. Seelig, Q. H. Wang, and R. P. H. Chang, “*Random laser action in semiconductor powder,*” *Physical Review Letters*, vol. 82, no. 11, pp. 2278–2281, 1999.

- [11]. Chappert, A. Fert, and F. N. Van Dau, “*Spin storage: the convergence of spin electronics and magnetic recording*,” vol. 3, no. 1, pp. 1–36, 1988.
- [12]. Chu, Y. Masuda, T. Ohji, and K. Kato, “*Formation and photocatalytic application of ZnO nanotubes using aqueous solution*,” *Langmuir*, vol. 26, no. 4, pp. 2811–2815, 2010.
- [13]. Cullity, “*Elements of X-ray Diffraction*”, 2nd Ed, Addison-Wesley Publishing Company Inc. (1978).
- [14]. D. M. Bagnall, Y. F. Chen, Z. Zhu, T. Yao, S. Koyama, M. Y. Shen, and T, “*Optically pumped lasing of ZnO at room temperature*”, *Applied Physics Letters*, no. 70, pp.2230-2232, 1997.
- [15]. D.J Binks, PhD thesis, University of Surrey, 1999.
- [16]. Dietl, H. Ohno, F. Matsukura, J. Cibert, and D. Ferrand, “*Zener model description of ferromagnetism in zinc-blende magnetic semiconductors*,” *Science*, vol. 287, no. 5455, pp. 1019–1022, 2000.
- [17]. Durán, J. Tartaj, and C. Moure, “*Fully dense, fine-grained, doped zinc oxide varistors with improved nonlinear properties by thermal processing optimization*,” *Journal of the American Ceramic Society*, vol. 86, no. 8, pp. 1326–1329, 2003.
- [18]. Halliburton, N. C. Giles, N. Y. Garces, M. Luo, C. Xu, L. Bai, and L. A. Boatner, “*Production of native donors in ZnO by annealing at high temperature in Zn vapor*,” *Applied Physics Letters*, vol. 87, no. 17, pp. 1–3, 2005
- [19]. Erhart and K. Albe, “*Diffusion of zinc vacancies and interstitials in zinc oxide*,” *Appl. Applied Physics Letters*, vol. 88, no. 20, pp. 23–25, 2006.
- [20]. Erhart and K. Albe, “*First-principles study of migration mechanisms and diffusion of oxygen in zinc oxide*,” *Physical Review B*, vol. 73, no. 11, p. 115207, 2006.
- [21]. Cerqueira, T. Viseu, J. Ayres De Campos, A. G. Rolo, T. De Lacerda-Aroso, F. Oliveira, I. Bogdanovic-Radovic, E. Alves, and M. I. Vasilevskiy, “*Raman study of insulating and conductive ZnO:(Al, Mn) thin films*,” *Physica status solidi (a)*, vol. 212, no. 10, pp. 2345–2354, 2015.

- [22]. F. K. Gunnewiek and R. H. G. A. Kiminami, “*Effect of heating rate on microwave sintering of nanocrystalline zinc oxide,*” *Ceramic . International*, vol. 40, no. 7 PART B, pp. 10667–10675, 2014.
- [23]. F. Kohan, G. Ceder, D. Morgan, and C. G. Van de Walle, “*First-principles study of native point defects in ZnO,*” *Physical Review B*, vol. 61, no. 22, pp. 15019–15027, 2000.
- [24]. F.A. Kroger, *The chemistry of imperfect crystals* 2nd edition, North Holland Amsterdam 1974.
- [25]. Bylander, “*Surface effects on the low-energy cathodoluminescence of zinc oxide,*” *Journal of Applied Physics*, vol. 49, no. 3, pp. 1188–1195, 1978.
- [26]. G. Kakazey, T. V. Srećković, and M. M. Ristić, “*Electronic paramagnetic resonance investigation of the evolution of defects in zinc oxide during tribophysical activation,*” *Journal of materials science*, vol. 32, no. 17, pp. 4619–4622, 1997.
- [27]. G. Thomas, “*Interstitial Zinc in Zinc Oxide,*” *Journal of Physics and Chemistry of Solids*, vol. 3, pp. 229–237, 1957.
- [28]. G. Thomas, “*The exciton spectrum of zinc oxide,*” *Journal of Physics and Chemistry of Solids*, vol. 15, no. 1–2, pp. 86–96, 1960.
- [29]. G. Van De Walle and J. Neugebauer, “*First-principles calculations for defects and impurities: Applications to III-nitrides,*” *Journal of Applied Physics*, vol. 95, no. 8, pp. 3851–3879, 2004.
- [30]. Galland and A. Herve, “*Temperature dependence of the ESR spectrum of the zinc vacancy in ZnO,*” *Solid State Communications*, vol. 14, no. 10, pp. 953–956, 1974.
- [31]. Gavryushin, G. Račiukaitis, D. Juodžbalis, A. Kazlauskas, and V. Kubertavičius, “*Characterization of intrinsic and impurity deep levels in ZnSe and ZnO crystals by nonlinear spectroscopy,*” *Journal of crystal growth*, vol. 138, no. 1–4, pp. 924–933, 1994.
- [32]. F. Sluiter, Y. Kawazoe, P. Sharma, A. Inoue, A. R. Raju, C. Rout, and U. V. Waghmare, “*First principles based design and experimental evidence for a ZnO-*

- based ferromagnet at room temperature,*” Physical review letters, vol. 94, no. 18, pp. 3–6, 2005.
- [33]. H. H. Tian and M. Atzmon, “*Comparison of X-ray analysis methods used to determine the grain size and strain in nanocrystalline materials,*” Philosophical magazine A, vol. 79, no. 8, pp. 1769–1786, 1999.
- [34]. H. Henry and D. V. Lang “*Nonradiative capture and recombination by multiphonon emission in GaAs and GaP*” Physical Review B, vol.15, no. 2, pp. 989-1016, 1977.
- [35]. H. S. Kang, J. S. Kang, J. W. Kim, and S. Y. Lee, “*Annealing effect on the property of ultraviolet and green emissions of ZnO thin films,*” Journal of Applied Physics, vol. 95, no. 3, pp. 1246–1250, 2004.
- [36]. H. Zeng, G. Duan, Y. Li, S. Yang, X. Xu, and W. Cai, “*Blue luminescence of ZnO nanoparticles based on non-equilibrium processes: Defect origins and emission controls,*” Advanced Functional Materials, vol. 20, no. 4, pp. 561–572, 2010.
- [37]. F. David and J. C. Matthewman, “*Profile refinement of powder diffraction patterns using the Voigt function,*” Journal of applied crystallography, vol. 18, no. 6, pp. 461–466, 1985.
- [38]. Wang and L. Gao, “*Photoluminescence properties of nanocrystalline ZnO ceramics prepared by pressureless sintering and spark plasma sintering,*” Journal of the American Ceramic Society, vol. 88, no. 6, pp. 1637–1639, 2005.
- [39]. J. Wang and L. Gao, “*Photoluminescence properties of nanocrystalline ZnO ceramics prepared by pressureless sintering and spark plasma sintering,*” Journal of the American Ceramic Society, vol. 88, no. 6, pp. 1637–1639, 2005.
- [40]. J. Wang and L. L. Shaw, “*Morphology-enhanced low-temperature sintering of nanocrystalline hydroxyapatite,*” Advanced Materials, vol. 19, no. 17, pp. 2364–2369, 2007
- [41]. J. Wang, Z. Wang, B. Huang, Y. Ma, Y. Liu, X. Qin, X. Zhang, and Y. Dai, “*Oxygen vacancy induced band-gap narrowing and enhanced visible light photocatalytic activity of ZnO,*” ACS applied materials & interfaces, vol. 4, no. 8, pp. 4024–4030, 2012.

- [42]. J. Xie, H. Deng, Z. Q. Xu, Y. Li, and J. Huang, “*Growth of ZnO photonic crystals by self-assembly,*” *Journal of Crystal Growth*, vol. 292, no. 2, pp. 227–229, 2006.
- [43]. Janotti and C. G. Van De Walle, “*Native point defects in ZnO,*” *Physical Review B*, vol. 76, no. 16, pp. 1–22, 2007.
- [44]. Janotti and C. G. Van De Walle, “*Oxygen vacancies in ZnO,*” *Applied Physics Letters*, vol. 87, no. 12, pp. 1–3, 2005.
- [45]. Jayaram and B. Sirisha Rani, “*Soft chemical routes to the synthesis of extended solid solutions of wurtzite ZnO-MO (M = Mg, Co, Ni),*” *Materials Science and Engineering: A*, vol. 304–306, no. 1–2, pp. 800–804, 2001.
- [46]. Ramakanth, *Basics of X-ray Diffraction and its Application* (I.K. International Publishing House Pvt. Ltd.: New Delhi: 2007).
- [47]. K. Sato and H. Katayama-Yoshida, “*Material Design for Transparent Ferromagnets with ZnO-Based Magnetic Semiconductors Express Letter Material Design for Transparent Ferromagnets with ZnO-Based Magnetic Semiconductors,*” *Japanese Journal of Applied Physics*. vol. 39, no. 6B, pp. 555–558, 2000.
- [48]. K. Singhal, S. C. Sharma, P. Kumari, S. Kumar, Y. T. Xing, U. P. Deshpande, T. Shripathi, and E. Saitovitch, “*Study of electronic structure and magnetization correlations in hydrogenated and vacuum annealed Ni doped ZnO,*” *Journal of Applied Physics*, vol. 109, no. 6, 2011.
- [49]. K. Vanheusden, W. L. Warren, C. H. Seager, D. R. Tallant, J. A. Voigt, and B. E. Gnade, “*Mechanisms behind green photoluminescence in ZnO phosphor powders,*” *Journal of Applied Physics*, vol. 79, no. 10, pp. 7983–7990, 1996
- [50]. Koudelka, J. Horák, and P. Jariabka, “*Morphology of polycrystalline ZnO and its physical properties,*” *Journal of materials Science*, vol. 29, no. 6, pp. 1497–1500, 1994.
- [51]. Kumar, S. K. Sharma, T. P. Sharma and V. Singh, “*Optical, electrical and structural investigations on Cd_{1-x}Zn_xSe sintered films for photovoltaic applications*” *J. Optical materials*, 21, 115 (1999)

- [52]. Schmidt-Mende and J. L. MacManus-Driscoll, “ZnO - nanostructures, defects, and devices,” *Materials today*, vol. 10, no. 5, pp. 40–48, 2007.
- [53]. L. Taylor, G. Filipovich, and G. K. Lindeberg, “*Electron paramagnetic resonance associated with Zn vacancies in neutron-irradiated ZnO*,” *Solid State Communications*, vol. 8, no. 17, pp. 1359–1361, 1970.
- [54]. L. Wu, G. G. Siu, C. L. Fu, and H. C. Ong, “*Photoluminescence and cathodoluminescence studies of stoichiometric and oxygen-deficient ZnO films*,” *Applied Physics Letters*, vol. 78, no. 16, pp. 2285–2287, 2001.
- [55]. Lin, Z. Fu, and Y. Jia, “*Green luminescent center in undoped zinc oxide films deposited on silicon substrates*,” *Applied Physics Letters*, vol. 79, no. 7, pp. 943–945, 2001.
- [56]. D. Coey, M. Venkatesan, and C. B. Fitzgerald, “*Donor impurity band exchange in dilute ferromagnetic oxides*,” *Nature materials*, vol. 4, no. 2, pp. 173–179, 2005
- [57]. M. Kasuga and S. Ogawa, “*Electronic Properties of Vapor-Grown Heteroepitaxial ZnO Film on Sapphire*,” *Japanese journal of applied physic*, vol. 22, pp. 794–798, 1983.
- [58]. M. L. Singla, M. Shafeeq M, and M. Kumar, “*Optical characterization of ZnO nanoparticles capped with various surfactants*,” *Journal of Luminescence*, vol. 129, no. 5, pp. 434–438, 2009.
- [59]. M. Law, L. E. Greene, J. C. Johnson, R. Saykally, and P. Yang, “*Nanowire dye-sensitized solar cells*,” *Nature materials*, vol. 4, no. 6, pp. 455–459, 2005.
- [60]. M. Liao, H. Z. Zhang, Y. B. Zhou, J. Xu, J. M. Zhang, and D. P. Yu, “*Surface effects on photoluminescence of single ZnO nanowires*,” *Physics Letters A*, vol. 372, no. 24, pp. 4505–4509, 2008.
- [61]. M. Mazaheri, A. M. Zahedi, and S. K. Sadrnezhad, “*Two-step sintering of nanocrystalline ZnO compacts: Effect of temperature on densification and grain growth*,” *Journal of the American Ceramic Society*, vol. 91, no. 1, pp. 56–63, 2008.
- [62]. M. N. Baibich, J. M. Broto, A. Fert, F. N. Van Dau, F. Petroff, P. Eitenne, G. Creuzet, A. Friederich, and J. Chazelas, “*Giant magnetoresistance of (001)Fe/(001)Cr magnetic superlattices*,” *Physical review letters*, vol. 61, no. 21, pp. 2472–2475, 1988.

- [63]. M. Whitaker, S. T. Ochsenein, V. Z. Polinger, and D. R. Gamelin, “*Electron Confinement Effects in the EPR Spectra of Colloidal n-Type ZnO Quantum Dots,*” *Journal of Physical Chemistry C*, vol. 98195, pp. 14331–14335, 2008
- [64]. McCabe, T. Fries, M. Liu, Y. Shapira, and L. Ram-Mohan, “*Bound magnetic polarons in-type,*” *Physical Review B*, vol. 56, no. 11, pp. 6673–6680, 1997.
- [65]. Morazzoni, R. Scotti, P. Dinola, C. Milani, and D. Narducci, “*Electron-Paramagnetic Resonance Study of the Interaction of the ZnO Surface with Air and Air Reducing Gas-Mixtures,*” *Journal of the Chemical Society, Faraday Transactions*, vol. 88, no. 12, pp. 1691–1694, 1992.
- [66]. Kim, K. Hiraga, and K. Morita, “*Kinetics of normal grain growth depending on the size distribution of small grains,*” *Materials transactions*, vol. 44, no. 11, pp. 2239–2244, 2003
- [67]. N. S. Norberg and D. R. Gamelin, “*Influence of surface modification on the luminescence of colloidal ZnO nanocrystals,*” *The Journal of Physical Chemistry B*, vol. 109, no. 44, pp. 20810–20816, 2005.
- [68]. Olsson, G. Dunlop, and R. Österlund, “*Development of Functional Microstructure during Sintering of a ZnO Varistor Material,*” *Journal of the American Ceramic Society. Soc*, vol. 76, no. 1, pp. 65–71, 1993.
- [69]. Leyral, D. Bois, and P. Pinar, “*Strain-Associated Band Tailing Effect in Semiconductors,*” *Physica Status Solidi (b)*, vol. 73, no. 1, pp. 187–192, 1976.
- [70]. Mallick, C. Rath, R. Biswal and N. C. Mishra, (2009) 517, “*Structural and Magnetization Behaviours of Ni Substituted Li-Mg Ferrites*”, *Indian J. Phys*, vol.1, no. 5, pp.128-132.
- [71]. Meyer B.K, Alves H, Hofmann D.M, Kriegseis W, Forster D, Bertram F, Christen J, Hoffmann A, Straßburg M, Dworzak M, and Haboeck U, “*Bound exciton and donor–acceptor pair recombinations in ZnO.*” *Physica status solidi (b)*” vol 241.2, pp 231-260,2004.
- [72]. N. Kondal and S. K. Tiwari, “*Selectively enhanced oxygen vacancies in undoped polycrystalline ZnO as a consequence of Multi-Step Sintering*”, *Ceramic International*, vol. 43, no. 13, pp. 10347–10352, 2017.

- [73]. N. Kondal and S. K. Tiwari, “*Origin of polychromatic emission and defect distribution within annealed ZnO nanoparticles*”, Material Research. Bulletin, vol. 88, no. December, pp. 156–165, 2017.
- [74]. Ohno H, “*Making Nonmagnetic Semiconductors Ferromagnetic*”, Control and uses od fects vol. 281, Issue 5379, pp. 951-956.
- [75]. P. S. Xu, Y. M. Sun, C. S. Shi, F. Q. Xu, and H. B. Pan, “*The electronic structure and spectral properties of ZnO and its defects,*” Nuclear Instruments and Methods in Physics Research Section B: Beam Interactions with Materials and Atoms, vol. 199, pp. 286–290, 2003.
- [76]. P. Wei, Y. M. Lu, D. Z. Shen, Z. Z. Zhang, B. Yao, B. H. Li, J. Y. Zhang, D. X. Zhao, X. W. Fan, and Z. K. Tang, “*Room temperature p-n ZnO blue-violet light-emitting diodes,*” Applied Physics Letters, vol. 90, no. 4, pp. 4–7, 2007.
- [77]. P.W. Anderson “Magnetism” ed G Rado and H Suhl (New York) Chapter 2 (1963) 25
- [78]. Pal, S. Dhara, P. K. Giri, and D. Sarkar, “*Room temperature ferromagnetism with high magnetic moment and optical properties of Co doped ZnO nanorods synthesized by a solvothermal route,*” Journal of Alloys and Compounds, vol. 615, pp. 378–385, 2014.
- [79]. Q. Pan, K. Huang, S. Ni, F. Yang, S. Lin, and D. He, “*Photoluminescence and magnetism in Co-doped ZnO powder,*” Journal of Physics D: Applied Physics, vol. 40, no. 21, pp. 6829–6833, 2007.
- [80]. Aghamalyan, I. A. Gambaryan, E. K. Goulanian, R. K. Hovsepyan, R. B. Kostanyan, S. I. Petrosyan, E. S. Vardanyan, and A. F. Zerrouk, “*Influence of thermal annealing on optical and electrical properties of ZnO films prepared by electron beam evaporation,*” Semiconductor science and technology, vol. 18, pp. 525–529, 2003.
- [81]. M. Sheetz, I. Ponomareva, E. Richter, A. N. Andriotis, and M. Menon, “*Defect-induced optical absorption in the visible range in ZnO nanowires,*” Physical Review B, vol. 80, no. 19, pp. 1–4, 2009.
- [82]. Rainey, J. Chess, J. Eixenberger, D. A. Tenne, C. B. Hanna, and A. Punnoose, “*Defect induced ferromagnetism in undoped ZnO nanoparticles,*” Journal of Applied Physics, vol. 115, no. 17, 2014

- [83]. Rath, S. Singh, P. Mallick, D. Pandey, N. P. Lalla, and N. C. Mishra, “*Effect of cobalt substitution on microstructure and magnetic properties in ZnO nanoparticles,*” *Indian Journal of Physics*, vol. 83, no. 4, pp. 415–421, 2009.
- [84]. E. Harrison, “*Conductivity and Hall effect of ZnO at low temperatures,*” *Physical Review*, vol. 93, no. 1, pp. 52–62, 1954.
- [85]. S. Kim and C. H. Park, “*Rich variety of defects in ZnO via an attractive interaction between O vacancies and Zn interstitials: Origin of n-type doping,*” *Physical review letters*, vol. 102, no. 8, pp. 1–12, 2009.
- [86]. Sato K, Yoshida H.K, “*First principles materials design for semiconductor spintronics*”, *Semiconductor Science and Technology*”, vol. 17, pp. 367-376, 2002
- [87]. Sato K, Yoshida H.K, —*Material Design for Transparent Ferromagnets with ZnO-Based Magnetic Semiconductors*”, *Japanese Journal of Applied Physics*, vol. 39, pp. L555-L558, 2000
- [88]. Shalish, H. Temkin, and V. Narayanamurti, “*Size-dependent surface luminescence in ZnO nanowires,*” *Physical Review B* , vol. 69, no. 24, pp. 1–4, 2004.
- [89]. C. Song, F. Zeng, K. W. Geng, X. B. Wang, Y. X. Shen, and F. Pan, “*The magnetic properties of Co-doped ZnO diluted magnetic insulator films prepared by direct current reactive magnetron co-sputtering,*” *Journal of magnetism and magnetic materials*, vol. 309, no. 1, pp. 25–30, 2007.
- [90]. Dietl, H. Ohno, F. Matsukura, J. Cibert, and D. Ferrand, “*Zener model description of ferromagnetism in zinc-blende magnetic semiconductors,*” *Science* (80), vol. 287, no. 5455, pp. 1019–1022, 2000. A.
- [91]. T. K. Gupta and W. D. Straub, “*Effect of annealing on the ac leakage components of the ZnO varistor*”. I. Resistive current,” *Journal of Applied Physics*, vol. 68, no. 2, pp. 845–850, 1990.
- [92]. T. M. Børseth, B. G. Svensson, A. Y. Kuznetsov, P. Klason, Q. X. Zhao, and M. Willander, “*Identification of oxygen and zinc vacancy optical signals in ZnO,*” *Applied Physics Letters*, vol. 89, no. 26, 2006.

- [93]. T. Prasada Rao, M. C. Santhosh Kumar, and V. Ganesan, “*Effect of annealing on the structural, optical and electrical properties of ZnO thin films by spray pyrolysis,*” *Indian Journal of Physics*, vol. 85, no. 9, pp. 1381–1391, 2011.
- [94]. T. Sekiguchi, S. Miyashita, K. Obara, T. Shishido, and N. Sakagami, “*Hydrothermal growth of ZnO single crystals and their optical characterization,*” *Journal of crystal growth*, vol. 214, pp. 72–76, 2000.
- [95]. Tsukazaki, A. Ohtomo, T. Onuma, M. Ohtani, T. Makino, M. Sumiya, K. Ohtani, S. F. Chichibu, S. Fuke, Y. Segawa, H. Ohno, H. Koinuma, and M. Kawasaki, “*Repeated temperature modulation epitaxy for p-type doping and light-emitting diode based on ZnO,*” *Nature materials*, vol. 4, no. 1, pp. 42–45, 2005.
- [96]. Ü. Özgür, Y. I. Alivov, C. Liu, A. Teke, M. A. Reshchikov, S. Doğan, V. Avrutin, S. J. Cho, and H. Morkoç, “*A comprehensive review of ZnO materials and devices,*” *Journal of Applied Physics*, vol. 98, no. 4, pp. 1–103, 2005.
- [97]. Chen and X. H. Wang, “*Sintering dense nanocrystalline ceramics without final-stage grain growth,*” *Nature*, vol. 404, no. 6774, pp. 168–171, 2000.
- [98]. Smith, M. D. Tokach, R. D. Goodband, J. L. Nelssen, and B. T. Richert, “*Effects of the Interrelationship between Zinc Oxide and Copper Sulfate on Growth Performance of Early-Weaned Pigs,*” *Journal of animal science*, vol. 75, no. 7, pp. 1861–1866, 1997.
- [99]. Sperlich A, “*Electron paramagnetic resonance spectroscopy of conjugated polymers and fullerenes for organic photovoltaics.*” (2013).
- [100]. Tomlins, J. L. Routbort, and T. O. Mason, “*Oxygen Diffusion in Single-Crystal Zinc Oxide,*” *Journal of the American Ceramic Society*, vol. 81, no. 4, pp. 869–876, 2005
- [101]. W.F. Hosford, *Materials Science, An intermediate text*, Cambridge University Press; 2007. p. 7.
- [102]. Weckhuysen, Bert M, Ralf Heidler, and Robert A. Schoonheydt. “*Electron spin resonance spectroscopy*”, *Characterization I*. Springer, Berlin, Heidelberg, 2004. 295-335.

- [103]. Zhao, P. Klason, M. Willander, H. M. Zhong, W. Lu, and J. H. Yang, “*Deep-level emissions influenced by O and Zn implantations in ZnO,*” Applied Physics Letters, vol. 87, no. 21, pp. 1–3, 2005.
- [104]. Xiong, U. Pal, and J. G. Serrano, “*Correlations among size, defects, and photoluminescence in ZnO nanoparticles,*” Journal of Applied Physics, vol. 101, no. 2, 2007.
- [105]. Yosida K, -Theory of Magnetism, Springer, Berlin, 1996.
- [106]. Yu P Y and Cardona M 2005 Fundamentals of Semiconductors 3rd edn (Berlin: Springer).
- [107]. Yu, L. H. Yang, X. Y. Teng, J. C. Zhang, Z. C. Zhang, L. Zhang, and G. S. Fu, “*Influence of structure characteristics on room temperature ferromagnetism of Ni-doped ZnO thin films,*” Journal of Applied Physics, vol. 103, no. 9, 2008 , T. Wakano, N. Fujimura, Y. Morinaga, N. Abe, A. Ashida, and T. Ito, “Magnetic and magneto-transport properties of ZnO : Ni films,” Physica E: *Low-Dimensional Systems and Nanostructures*, vol. 10, pp. 260–264, 2001.
- [108]. Zener, “*Interaction between the d shells in the transition metals,*” Physical Review, vol. 81, no. 3, pp. 440–444, 1951.